



Open your mind. LUT.
Lappeenranta University of Technology

Markku Nikku

Three-dimensional modeling of biomass fuel flow in a circulating fluidized bed furnace

Thesis for the degree of Doctor of Science (Technology) to be presented with due permission for public examination and criticism in the Auditorium 1382 at Lappeenranta University of Technology, Lappeenranta, Finland on the 25th of June, 2015, at noon.

Acta Universitatis
Lappeenrantaensis 644

Supervisors Professor Timo Hyppänen
Department of Energy Technology
Faculty of Technology
Lappeenranta University of Technology
Finland

Associate Professor Jouni Ritvanen
Department of Energy Technology
Faculty of Technology
Lappeenranta University of Technology
Finland

Reviewers Professor Ryszard Bialecki
Institute of Thermal Technology (ITT)
Silesian University of Technology
Poland

Assistant Professor David Pallarès
Department of Energy and Environment
Chalmers University of Technology
Sweden

Opponent Docent Esa Muurinen
Department of Environmental and Chemical Engineering
University of Oulu
Finland

ISBN 978-952-265-809-8
ISBN 978-952-265-810-4 (PDF)
ISSN-L 1456-4491
ISSN 1456-4491
Lappeenrannan teknillinen yliopisto
Yliopistopaino 2015

Abstract

Markku Nikku

Three-dimensional modeling of biomass fuel flow in a circulating fluidized bed furnace

Lappeenranta 2015

99 pages

Acta Universitatis Lappeenrantaensis 644

Diss. Lappeenranta University of Technology

ISBN 978-952-265-809-8, ISBN 978-952-265-810-4 (PDF), ISSN-L 1456-4491,

ISSN 1456-4491

The reduction of greenhouse gas emissions in the European Union promotes the combustion of biomass rather than fossil fuels in energy production. Circulating fluidized bed (CFB) combustion offers a simple, flexible and efficient way to utilize untreated biomass in a large scale. CFB furnaces are modeled in order to understand their operation better and to help in the design of new furnaces. Therefore, physically accurate models are needed to describe the heavily coupled multiphase flow, reactions and heat transfer inside the furnace.

This thesis presents a new model for the fuel flow inside the CFB furnace, which acknowledges the physical properties of the fuel and the multiphase flow phenomena inside the furnace. This model is applied with special interest in the firing of untreated biomass. An experimental method is utilized to characterize gas-fuel drag force relations. This characteristic drag force approach is developed into a gas-fuel drag force model suitable for irregular, non-spherical biomass particles and applied together with the new fuel flow model in the modeling of a large-scale CFB furnace. The model results are physically valid and achieve very good correspondence with the measurement results from large-scale CFB furnace firing biomass.

With the methods and models presented in this work, the fuel flow field inside a circulating fluidized bed furnace can be modeled with better accuracy and more efficiently than in previous studies with a three-dimensional holistic model frame.

Keywords: biomass, fuel flow, modeling, circulating fluidized beds

Acknowledgements

The work presented in this thesis has been done partially in the ERA-NET Bioenergy framework project *Advanced Biomass Combustion Modelling for Clean Energy Production*. I would like to express my thanks for the partners involved in the project.

I would like to express my thanks to several people who contributed one way or the other to the process of creation and finalization of this thesis.

I am grateful for Professor Ryszard Bialecki and Assistant Professor David Pallarès for pre-examining the thesis and for their comments on how to improve this work. Huge thanks are expressed to Professor Esa Muurinen who agreed to act as my opponent.

Special thanks are extend to Professor Timo Hyppänen for believing in me and letting me find my own way. I am grateful for several persons within our organization: Jouni Ritvanen, for support and guidance of the thesis work, publications and related matters. Kari Myöhänen, for continued co-operation in research and participation to the work done over the years. Payman Jalali, for finding a peculiar way of getting me to begin and for excellent courses on the multiphase flows. Esa Vakkilainen, for on- and off-topic discussions and education about biomass and power plants. Jaakko Ylätaalo, for setting the example (that it just requires some work), as well as continued and much needed peer-support along with Srujal Shah, Alexander Maximov, Petteri Peltola, Heikki Suikkanen, Ville Rintala, Arto Ylönen, Matti Koski, Antti Rantakaulio, Timo Merisaari, Jussi Saari and others; we have to understand and remember the basics! Thanks are also in order for Markku Autio, Kari Ihaksi, Juha Karppinen and other support staff for their efforts in the laboratory in designing, building and maintaining the equipment used in this and all the other works not mentioned here. Thanks are extended to the whole department of Energy Technology for a nice atmosphere and community to work in and to be a part of. Thanks are also due to Marko Lyytikäinen, Ari Kettunen and all other persons at Amec Foster Wheeler for cooperation during the years.

Finally, my greatest appreciation goes to my wife, family and friends, who keep me in touch with “normal life” and its wonders. Much love and eternal gratitude for being there for me!

Markku Nikku
June 2015
Lappeenranta, Finland

Know thy fuel.

Contents

Abstract

Acknowledgements

Contents

List of publications	11
Nomenclature	13
1 Introduction	17
1.1 Background	17
1.2 Objectives and methods.....	18
1.3 Description of content	20
2 Literature review	21
2.1 Biomass	21
2.1.1 Origins.....	21
2.1.2 Chemical and mechanical properties	22
2.1.3 Benefits, challenges, remedies and costs	25
2.2 Fluidized beds.....	28
2.2.1 Fluidization	28
2.2.2 Forces in fluidized beds	33
2.2.3 Circulating fluidized bed boilers.....	38
2.3 Modeling of fluidized beds.....	40
2.3.1 General modeling approaches	41
2.3.2 Conservation equations	41
2.3.3 Peculiarities in the modeling of fluidized beds	44
3 Modeling of fuel flow in a large-scale circulating fluidized bed furnace	47
3.1 Previous works	47
3.1.1 CFD studies.....	47
3.1.2 Holistic models	49
3.2 Development of the fuel flow model.....	49
3.2.1 Model frame description	49
3.2.2 Solids flow field	50
3.2.3 Gas flow field.....	51
3.2.4 Flow of fuel	52
4 Characterization of gas-fuel drag force	55
4.1 Characterization experiment.....	55
4.2 Image analysis and results	57
4.3 Analysis of characterization results.....	60

5	Drag force model development	65
5.1	Temperature scaling	65
5.2	Selection of the voidage function	66
5.3	Empirical drag force model	67
6	Simulations of CFB furnaces	69
6.1	Sensitivity analysis	69
6.2	Large scale simulations	72
6.2.1	Test case	72
6.2.2	A large scale CFB unit	75
6.3	Model validation and discussion	78
7	Conclusions	85
	References	87

List of publications

This thesis is based on the following papers. The rights to include the papers in the dissertation have been granted by the publishers. Additional results outside the following works are presented. This content is presented in parts of chapter 4 related on the characterization analysis, the whole chapter 5 on the drag force model development and parts of chapter 6 related to the modeling and validation with the developed drag force model.

- I. Nikku, M., Jalali, P., Ritvanen, J. and Hyppänen, T. (2014). Characterization method of average gas–solid drag for regular and irregular particle groups. *Powder Technology*, 253, pp. 284-294.
- II. Nikku, M., Myöhänen, K., Ritvanen, J. and Hyppänen, T. (2014). Modeling of fuel flow in circulating fluidized bed furnaces. In: Jinghai Li, Fei Wei, Xiaojun Bao and Wei Wang ed., *Proceedings of 11th International Conference on Fluidized Bed Technology*, 14.-17.5.2014, Beijing, China.
- III. Nikku, M., Myöhänen, K., Ritvanen, J. and Hyppänen, T. (2014). Three-dimensional modeling of fuel flow with a holistic circulating fluidized bed furnace model. *Chemical Engineering Science*, 117, pp. 352-363.
- IV. Nikku, M., Myöhänen, K., Ritvanen, J., Hyppänen, T. and Lyytikäinen, M. (2015). Modelling and validation of fuel flow in CFB furnace. *Proceedings of 22th conference of Fluidized Bed Conversion*, 14.-17.6.2015, Turku, Finland.

I was the corresponding author and principal investigator in all the journal and conference papers presented above.

In publication I, I participated in the planning and commissioning of the experimental device, planning of the test matrix and carrying out the characterization experiments. I was responsible for the post-processing and analysis of the image analysis data and for the characterization analysis.

In publication II and III, I tested the new fuel flow model before implementation to the model frame. I was responsible for sensitivity analysis, defining, conducting, post-processing and analyzing all the simulations.

In publication IV, I participated in the measurements on the boiler used in the validation and was responsible for the simulations and the model validation.

For the work presented in the thesis, I developed the new drag force model from the data presented in publication I (presented in chapter 5), including the temperature scaling approach. Additionally, I did the simulations and validation, presented in chapter 6.

Nomenclature

Latin alphabet

<i>A</i>	area	m^2
B	buoyant force	N
C_D	drag coefficient	–
<i>D</i>	dispersion/diffusion coefficient	$\text{m}^2 \text{s}^{-1}$
F	force	N
G	gravitational force	N
<i>H</i>	height	m
<i>K</i>	momentum exchange coefficient	$\text{kg m}^{-3} \text{s}^{-1}$
<i>P</i>	flow potential	$\text{kg m}^{-1} \text{s}^{-1}$
<i>R</i>	mass and species source term	$\text{kg m}^{-3} \text{s}^{-1}$
<i>T</i>	temperature	K, °C
<i>V</i>	volume	m^3
<i>a</i>	coefficient	–
<i>b</i>	coefficient	–
<i>c</i>	coefficient	–
<i>d</i>	diameter	m
<i>f</i>	target profile	–
g	gravitational acceleration	m s^{-2}
g_0	radial dispersion function	–
<i>h</i>	specific enthalpy	J kg^{-1}
<i>k</i>	comminution coefficient	–
<i>p</i>	pressure	Pa
<i>r</i>	roundness	–
<i>t</i>	time	s
v	velocity	m s^{-1}
<i>w</i>	mass fraction	–
<i>x</i>	distance, x-coordinate (width)	m
<i>y</i>	y-coordinate (depth)	m
<i>z</i>	z-coordinate (height)	m

Greek alphabet

Γ	source term	kg s^{-1}
Φ	energy source term	$\text{J m}^{-3} \text{s}^{-1}$
Ω	momentum source term	Pa s^{-1}
β	macroscopic or characteristic drag coefficient	$\text{s}^{-1}, \text{kg m}^{-3} \text{s}^{-1}$
δ	temperature scaling factor	–
ε	volume fraction	–
θ	wall layer momentum thickness	m
λ	conductivity	$\text{W m}^{-1} \text{K}^{-1}$

μ	viscosity	$\text{kg s}^{-1} \text{m}^{-1}$
ρ	density	kg m^{-3}
τ	shear stress	Pa
ϕ	source term in potential flow	$\text{kg m}^{-3} \text{s}^{-1}$
φ	switch function	–

Dimensionless numbers

Ar	Archimedes number
Re	Reynolds number

Superscripts

*	reference
---	-----------

Subscripts

D	drag
E	Ergun
WY	Wen-Yu
bed	bed
btm	bottom
c	cold
dil	dilute
e	electricity
g	gas
h	hot
f	fluid
fu	fuel
fri	friction
i, j	indexes
max	maximum
mean	mean
mf	minimum fluidization
mp	multiparticle
p	particle
res	restitution
rm	relative velocity correlation
s	solid
susp	suspension
th	thermal
top	top
tot	total
trans	transition

Abbreviations

1D	one-dimensional
2D	two-dimensional
3D	three-dimensional
BFB	bubbling fluidized bed
CFB	circulating fluidized bed
CFD	computational fluid dynamics
DDPM	dense discrete phase model
DEM	discrete element method
DNS	direct numerical simulation
EU	European Union
EMMS	Energy-minimization multi-scale
GHG	greenhouse gas
H-G	Huilin-Gidaspow
HHV	higher heating value
LES	large eddy simulation
MP-PIC	multiphase particle-in-cell
PSD	particle size distribution
RANS	Reynolds averaged Navier-Stokes
SD	standard deviation
SOB	Syamlal-O'Brien

1 Introduction

1.1 Background

The climate change has led to demands and policies that require reductions in greenhouse gas (GHG) emissions in energy production. In recent years the main focus has been on decreasing the carbon dioxide emission released from fossil fuel combustion due to implications of global warming and climate change. While the mechanisms behind the climate change are not clear, preventative actions have been implemented globally. At the same time, scientific research along with ideologically and politically colored discussions on the topic is continued.

The European Union (EU) has set guidelines for reductions in GHG emissions and utilization of renewable energy sources, such as biomass (European commission, 2005). The target for the reductions is 20% (compared the level in the 1990) by 2020 while increasing the share of renewable energy production to 20% of energy consumption in the EU (European Commission, 2008). More recently, targets were published for 2030, with 40% reductions in GHG emissions and 27% minimum share of renewables (European Commission, 2014). These and other political actions have a strong influence on the energy production sector and the related research.

In Finland, a large share of renewable energy has been and is still produced with biomass derived from forests and peat, as seen in Figure 1, which presents a comparison of the total energy production in Finland in years 2005 and 2012. From 2005 to 2013, the use of renewable fuels was more than doubled in district heating and cogeneration in Finland (Finnish Energy Industry, 2014a; Finnish Energy Industry, 2014b). The increased utilization of renewable energy sources can be seen also in the rapid development of wind energy generation and increased interest in solar energy generation, while their share is still marginal. Hydroelectric production has not increased due to lack of new power stations and the role of hydroelectric generation in grid load balancing. Significant sources of renewable energy are industrial biomass utilization, peat, recovered fuels, and demolition wood. (Finnish Energy Industry, 2014b) Therefore, efficient and increased utilization of biomass resources in energy production is imperative to meet the set targets for renewable power generation and for increasing domestic production.

There are various approaches in the world for the utilization of biomass as an energy source, depending on the intended use. While small-scale combustion in stoves and fireplaces is the most commonly utilized method globally, in this work the focus is on the large-scale heat and electricity production, where the simplest method is direct combustion in a power plant furnace. The characteristics of solid biomass differ greatly from solid fossil fuels, which could cause difficulties in direct combustion in certain types of furnaces. There are combustion applications, fluidized beds, which can be designed to utilize untreated biomass as the only fuel. Many circulating and bubbling fluidized bed (CFB and BFB) boilers firing biomass are in operation around the world. The CFB

technology has been successfully scaled up to 460 MW_e, with a 550 MW_e unit to be commissioned in 2015, while BFB capacities are below 150 MW_e (Jäntti et al., 2012; Koornneef et al., 2007). Currently the largest biomass firing CFB is 190 MW_e with concept plants scaled up to 400 MW_e (Nevalainen et al., 2012). Therefore, CFB technology is a very good candidate, if not the only one, in large-scale utilization of untreated biomass.

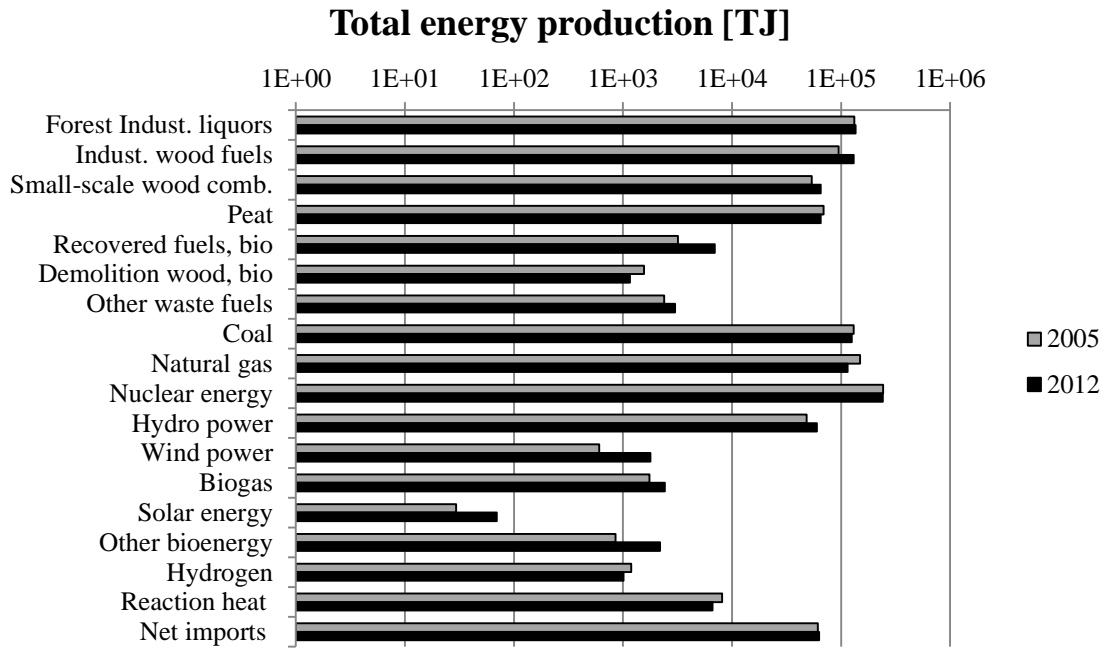


Figure 1. Total energy production (in TJ, with logarithmic scale) in Finland during 2005 and 2012 by selected energy sources (Statistics Finland, 2014).

1.2 Objectives and methods

Multiphase flow, thermochemical reactions and heat transfer taking place simultaneously inside a CFB furnace occur on many different time- and length-scales and strongly coupled with each other. Due to this complexity, detailed analysis of these phenomena with computational fluid dynamics (CFD) is still extremely time-consuming. This is why the modeling approaches available for engineering purposes have been limited to simplified holistic models, which often contain empirically derived correlations for the modeling of hydrodynamics and/or reactions.

The fuel flow determines where the thermochemical reactions take place in the furnace, affecting the temperature and gaseous species distributions, as well as the performance and efficiency of the whole boiler. Therefore, correct estimation of the fuel flow is essential for furnace design and analysis. Typically the fuel flow in holistic models has been considered dispersive, though evidence of convective nature of fuel mixing and behavior has been presented by Pallarès & Johnsson (2008). These models often require

inputs which could be difficult to predetermine for new fuels. While the dispersive fuel mixing approach is suitable for fossil fuels, which have more comparable properties to the bed material in CFBs, this approach might not be suitable for the lighter and more heterogeneous biomass material. The heterogeneous nature of biomass poses challenges in the determination of material properties, such as particle size, which is important in chemical conversion and fluidization characteristics.

The objective of this work is to develop models for the fuel flow inside the CFB furnace, which acknowledge the physical properties of the fuel and the multiphase flow phenomena inside the furnace. A new fuel flow model is applied in the firing of untreated biomass, but it can be utilized also with other fuels. With the method presented in this work, the fuel flow field inside CFB furnace could be modeled with better accuracy and more efficiently than in previous works by utilizing a convective fuel flow model (using the momentum-type approach) within a three-dimensional holistic CFB model frame.

The gas-solid drag force can be determined for different materials, such as biomass, with laboratory experiments. These results can be utilized in the modeling of the fuel flow inside large-scale CFB furnaces when the experimental results are scaled. The results can be scaled by taking into consideration the changes in the drag force due to the changing state of the gas, from cold to hot conditions, and the volume fraction of the solids, from a single particle to a multiparticle system.

The presented models can be utilized in the design and analysis of large-scale CFB furnaces. The validity of the fuel flow model and the experimental gas-solid drag force model can be estimated by comparing the modeled results with measurements obtained from operational CFB furnaces.

To enable the consideration of convective fuel flow, a convective fuel flow model was developed by implementing a simplified, size-fractional momentum equation for the fuel. This model considers forces such as gravity, buoyancy, inertia, and drag force from the gas and solid phases. Fick's law type of diffusion behavior was utilized in the modeling of mixing. The momentum equation -based approach allows free formation of fuel concentration profiles based on the fuel properties, depending on the furnace hydrodynamics and fuel reactions, and without a need for predetermined inputs.

An experimental method was utilized in the determination of gas-fuel drag force relations. The method allows the determination of an average characteristic drag coefficient for a material fraction through a simple laboratory test procedure, rather than meticulous analysis of the shapes and sizes of individual particles, which are required in traditional determination of the drag coefficient. Image analysis was utilized to obtain information on the shape and size distributions of the studied materials, allowing comparison between the characteristic and traditional drag coefficients.

The characteristic drag force approach was developed into a gas-fuel drag force model suitable for irregular, non-spherical biomass particles and applied together with the new

fuel flow model in the modeling of a large-scale CFB furnace. The model results are physically valid and achieve very good correspondence with the measurement results from a large-scale CFB furnace firing biomass.

1.3 Description of content

Chapter 2 presents a literature review. Biomass and its properties are examined with respect to its utilization in energy production and especially firing in CFB boilers. The benefits, disadvantages, possible solutions and costs of biomass utilization are illustrated. A summary of fluidization and the related phenomenon is given to illustrate the mechanisms affecting CFB furnaces and boilers, which are also discussed. Mathematical modeling and numerical simulation in general are presented, and some more specific issues related to the modeling of fluidized beds are presented.

Chapter 3 contains a summary of previous efforts in large-scale CFB furnace modeling. A brief description of the model frame utilized in this work is included, along with a description of the developed fuel flow model. In chapter 4, the experimental approach and the results of fluidization characterization are presented. The heterogeneous nature of biomass is demonstrated by image analysis. Also the obtained characteristic drag coefficient are compared with the traditional drag coefficients. In chapter 5, the experimental results are developed into a drag force model, and the developed model is compared with the drag force models presented in the literature. In chapter 6, different simulation cases are presented to illustrate the functionality of the new fuel flow model with comparison to the old one. Sensitivity analysis, along with large-scale CFB furnace simulations are presented by utilizing the drag force models found in the literature and the experimentally derived drag force model. Validation of the models is done with comparison to measurements from an operational CFB furnace firing biomass. Finally, conclusions and suggestions for further research are offered in chapter 7.

2 Literature review

2.1 Biomass

2.1.1 Origins

Biomass is renewing natural, plant or animal -derived solid fuel, whereas biogas and liquid biofuels are not considered in this work. Biomass is commonly classified by its origin or properties and subcategorized in numerous ways. (Vassilev et al., 2010) Typical Finnish biomasses are forest-derived wood-based materials and swamp-derived peat (decayed vegetation or organic material), which are the biomasses considered and later discussed in this work. The formal status of peat is that while it is a biomass, it is considered as a fossil fuel rather than (slowly) renewable. As seen in Figure 2, in Finland the tree trunks are typically utilized in the forest industry (lumber, pulp and paper production), leaving the bark, branches, stumps, leaves and needles for other uses, such as energy production, or as waste. Figure 2 also illustrates other sources of wood-based materials used as directly or as a precursor for biomass fuels. (Alakangas, 2005; Khan et al., 2009) Figure 1 gives information on the volume of the Finnish energy production from different wood-based sources.

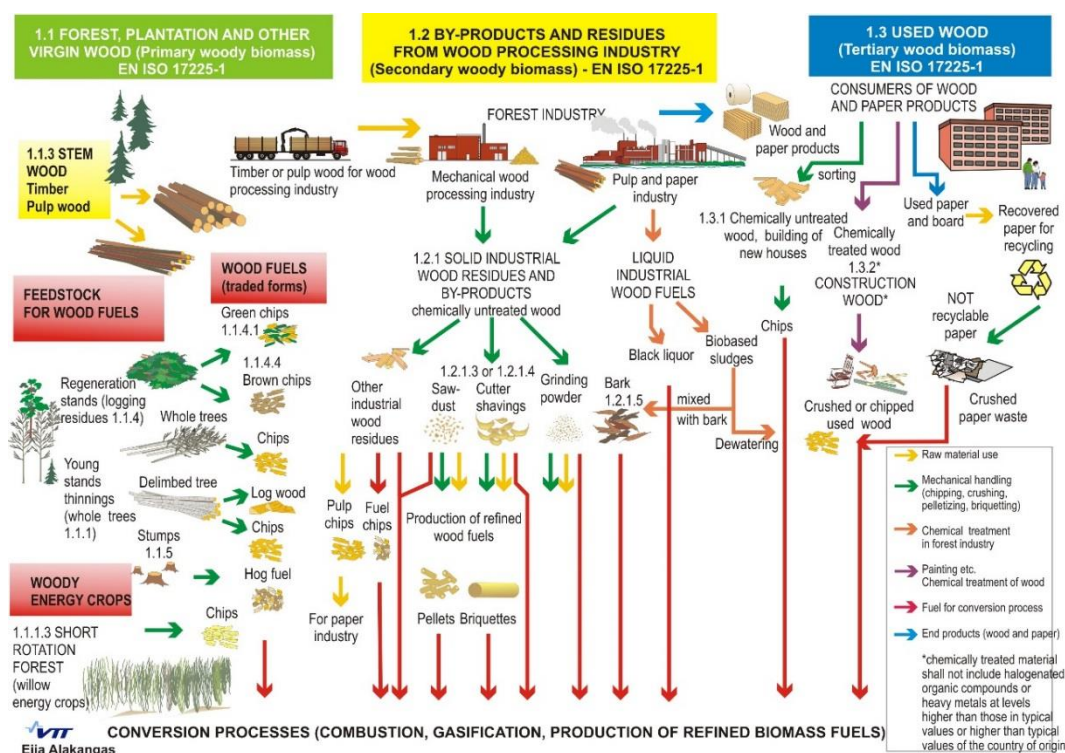


Figure 2. Wood and wood-based material sources of biomass fuels. The image courtesy of Eija Alakangas, VTT.

In the following sections, the properties of biomasses are discussed and compared with solid fossil fuels, such as coals. Note that the properties of biomass can vary greatly for example between different types of plants, the same type of plants of different age and growing location, and different parts of the same plant (Alakangas, 2005; Vassilev et al., 2010).

2.1.2 Chemical and mechanical properties

Compared to coals, raw biomasses have higher moisture and volatile content and lower char and ash content, leading to lower energy density and heating value. The low heating value translates directly to a need to burn many times larger amount of raw biomass to obtain the same amount of energy as received from one unit of coal. (La Nauze, 1987; Vassilev et al., 2010) Figure 3 presents carbon and hydrogen content in relation to heating value for different fuels. The approaches to improve biomass properties are discussed in chapter 2.1.3. The chemical properties also make biomass more reactive than coal (Vassilev et al., 2010), and some biomasses are known to decay and even spontaneously combust while in storage, due to biological and thermochemical reactions (Van Loo & Koppejan, 2010). The high moisture content may also make the fuel freeze in cold storage (Mattsson, 1990).

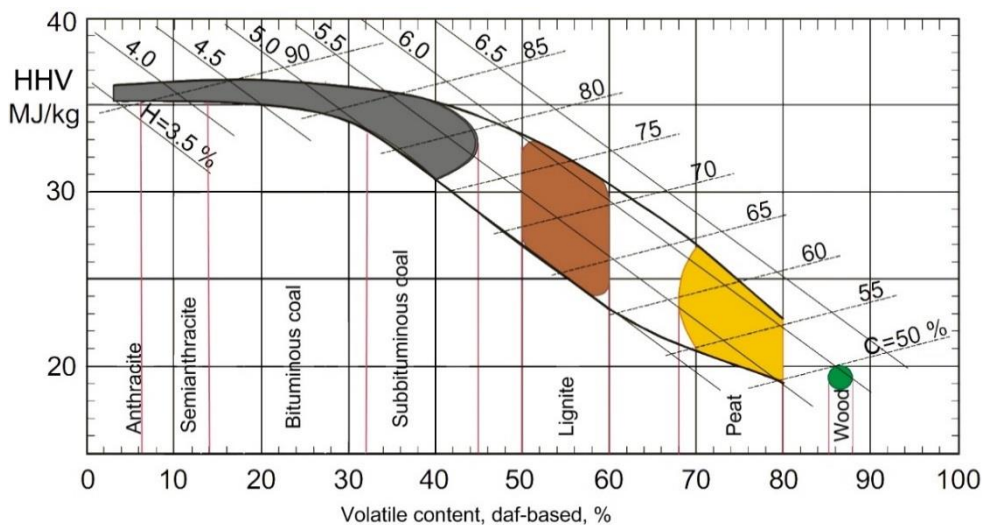


Figure 3. Comparison of volatile, carbon and hydrogen contents of fuels with respect to the higher heating value. Figure after Eija Alakangas (2005) with permission.

The chemical composition is a fundamental aspect of any fuel, and it is strongly linked with the reaction characteristics and possible reaction products. The chemical composition of biomass depends on for example the type, place of harvest and part of plant utilized. Sulfur, nitrogen, alkali, chlorine, polycyclic aromatic hydrocarbons, and heavy metal content of the biomass are of special interest as they can form compounds harmful to the boiler or the environment. Another issue is the ash behavior, as a low ash

melting temperature is not desirable in combustion applications. (Khan et al., 2009; Vassilev et al., 2010)

The mechanical properties affect the storage and transport of the biomass, and also the fuel feeding system of the combustor (La Nauze, 1987). The main mechanical properties are particle size, shape and density, while other properties are not often considered if the biomass is not pelletized to a fixed size where it is wished to remain. Compared to coal, biomass is softer as a bulk, which is largely due to loose packing, but also due to lower strength of the material. The main challenge with biomass is typically maintaining the flowability, which is strongly affected by the irregular particle size and shape and the high moisture content (mechanical and liquid bridging) along with the angle of repose as well as internal and external friction factors. (Mattsson, 1990; Wu et al., 2011)

Miao et al. (2011) report that the energy consumption of grinding increased with the decreasing particle size. The effect of moisture content did not affect the comminution energy requirements with large particles, while having a significant impact with smaller particles. Specific comminution energy consumption could be significant compared to the fuel heating value when producing fine powders. (Miao et al., 2011) While the breaking of the largest fuel particles might be desirable, the generation of very fine fuel dust is not, as it poses health issues and increased difficulties in transportation and fuel feeding (Dai et al., 2012; Van Loo & Koppejan, 2010).

2.1.2.1 Particle size and shape distributions

For utilization in energy production, the fuel has to be processed into a suitable size range for the application. This means grinding or milling to achieve suitable particle size distribution (PSD) for the fuel feeding and specific combustion method. The particle size and shape distributions depend on the type of biomass and the (pre)treatment, such as cutting, shaving, or grinding, for example. To minimize fuel processing costs, the fuel is ground down (if necessary) only to a particle size which is manageable by the fuel transport and feeding systems (Van Loo & Koppejan, 2010). Due to these reasons, the PSD of biomass can be very wide, from very fine (order of μm) to very coarse particles (order of 10 cm) (Publication I ref. data).

The determination of particle shape is not a simple task, unless dealing with regularly shaped particles (such as spheres, tetrahedrons, cylinders or hexahedrons) which can be expressed with a few different dimension parameters. A classification of particle shape by Mandø & Rosendahl (2010) is presented in Table 1. It has been shown that mineral material, such as coal and sand (Figure 4) has a rather spherical, though irregular shape with a narrow distribution, with average roundness or circularity around 0.6. (Publication I ref. data; Ulusoy & Igathinathane, 2014). For biomass, several authors, have reported wide distributions of irregular and non-spherical shape (Cui & Grace, 2007; Doroodchi et al., 2013; Guo et al., 2012; Guo et al., 2014; Mattsson, 1990; Miao et al., 2011).

Table 1. Classification of particle shape (Mandø & Rosendahl, 2010).

	Spherical	Non-spherical
Regular	Polygons, low aspect ratio spheroids	Cubes, cylinders, disks, tetrahedrons, high aspect ratio spheroids
Irregular	Pulverized coal, sand, many powders, particulate matter	Pulverized biomass, flakes, splinters, agglomerates

For irregular particles, several dimensions can be measured, and ultimately these particles require 3D measurement to determine their shape, surface area and volume accurately. Several 2D and 3D shape factors have been presented in the literature (and summarized in Publication I) to reduce the shape to a single number, which typically describes how much the particle deviates from a circle or a sphere of the same surface area or volume. Recently full 3D laser scanning of irregular particles has been presented by Bagheri et al. (2015) to obtain the true particle shape. The method took 2 hours per particle to obtain the shape information (Bagheri et al., 2015).

Rosendahl et al. (2007) have presented an example of milling straw and the resulting particle size and shape distributions. Guo et al. (2012) have studied the effect of grinding to shape of biomass, and they found that the particles retained their elongated, stick-like shape throughout the grinding process. The particle elongation was reduced as the particle size reduced. This result was related to plant growth direction and the anisotropic cell bond strength, resulting in an elongated shape. Similarly, coal particles break along grain boundaries, leading to retention of a roughly similar spherical shape. (Guo et al., 2012)

Mattsson (1990) points out that irregularly shaped biomass particles can be “hooked”, heavily curved particles, which tend to interlock with other particles, causing interlocking and bridging. Zulfiqar et al. (2006) have studied the co-firing of coal with sawdust and woodchips, and report the “physical form” of the biomass (shape and size) to be a major contributor to the flowability of the coal-biomass-mixture. Mattsson & Kofman (2002) state that particle shape is the most important factor in fuel flowability, as the long, thin and hooked particles are more prone of bridging and blocking. Guo et al. (2014) report findings on the angle of repose of blends of spherical material and biomass (images of particles illustrated in Figure 4), stating that differences in surface roughness, size and shape contribute to the flowability of the mixture. The measured angles of repose increased linearly as a function of the biomass share in the mixture. While the smaller biomass particle typically increased flowability, the sawdust surface roughness was attributed to decreasing the flowability in the mixture, despite the fine particle size. (Guo et al., 2014)

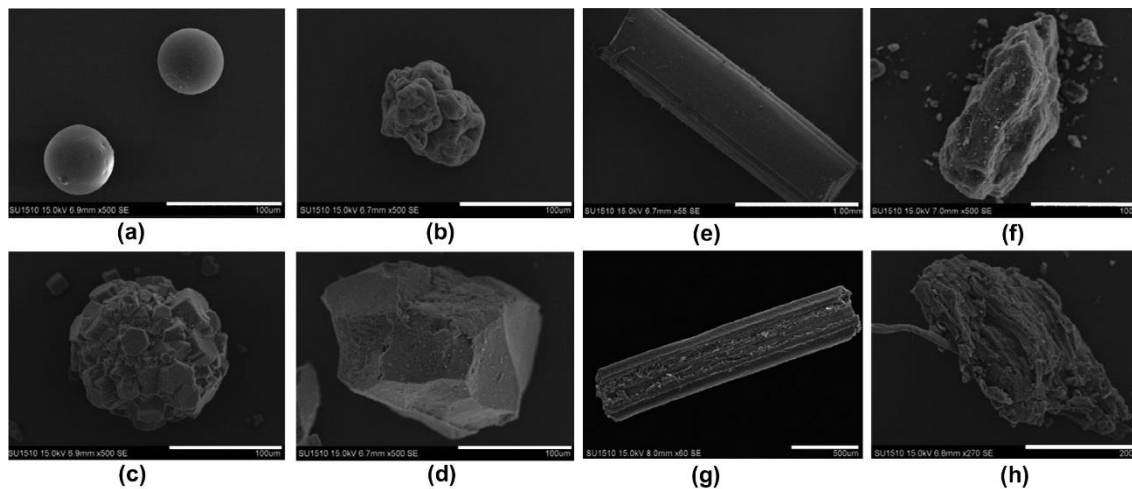


Figure 4. Scanning electron microscope images of granular material. (a) Glass beads. (b) PVC. (c) Al_2O_3 . (d) Quartz sand. (e) String. (f) Coal. (g) Rice straw. (h) Sawdust (Guo et al., 2014).

2.1.2.2 Density

The irregular shape of biomass particles and their ability to absorb water make the measurement of particle or material density challenging. Biomass density is often reported as bulk density, which is affected by the particle packing (shape and size distributions), moisture content and external pressure applied. (Miao et al., 2011) Therefore, while more difficult to measure, material density should be utilized. Examples of material densities are presented in Table 2 for biomasses and coal. Compared to coal, biomasses have typically lower density, which is partially explained by a low ash content. The moisture content also increases the biomass density, dry biomass being lighter than wet biomass. The results presented by Miao et al. (2011) indicate that both the material and bulk densities are affected by the particle size, the effect being larger for bulk density.

Table 2. Examples of reported material densities from Green & Perry (1997).

Material	Birch, yellow	Fir, Douglas	Pine, Norway	Spruce, white	Pine charcoal
Average material density [kg/m³]	705	510	545	450	370
Material	Oak charcoal	Peat	Limestone	Anthracite (coal)	Lignite (coal)
Average material density [kg/m³]	530	370	2450	1550	1250

2.1.3 Benefits, challenges, remedies and costs

2.1.3.1 Benefits and detriments, challenges and remedies

Vassilev et al. (2010) list the major benefits that can be achieved with biomass utilization. Many biomasses are considered as renewable energy sources, which means that they cannot be depleted with sustainable utilization unlike fossil (or slowly renewing) energy

sources. The current classification of biomass as *carbon neutral* gives advantages in public acceptance (Kraxner et al., 2009), and possibly in climate change prevention (Vassilev et al., 2010). Lower ash, heavy metal, carbon, sulfur and nitrogen content correlate with lesser gaseous and solid emissions, while high volatile content generally indicates higher reactivity and easier firing (Vassilev et al., 2010). According to Van Loo & Koppejan (2010) the share of biomass of global primary energy production was 3.5% in 2006. Parikka (2004) estimates global utilization to be 38% of available biomass resources, indicating increase potential in biomass-based energy production. Biomass can be an inexpensive option if it is locally available, and it can reduce the dependency on imported fossil fuels (Khan et al., 2009), as is the case in Finland. Also construction waste (such as demolition wood) can be utilized in power generation rather than landfilled as waste (Vassilev et al., 2010).

On the other hand, high moisture content and low density of biomass lead to low energy density, which increases the transportation and storage costs. Alkali and chlorine content can cause agglomeration and corrosion problems in furnaces and boilers. Ethical and political issues can arise from the utilization of food crops or their farming land in energy production. There are also debates on the environmental impact of biofuel agriculture. (Brown, 2011; Vassilev et al., 2010)

Low energy density is probably the main problem of biomass when aiming at utilizing it as a replacement for fossil fuels. In order to obtain the same amount of energy from biomass, several times more material has to be harvested, transported and utilized, which increases the costs. This is why ways of “energy densifying” are much sought after in the research related to biomass.

Drying is one of the most significant ways to increase the energy density of biomass. Bringing the moisture content from 40-60% down to 10-20% can mean huge savings in the amount of fuel needed. However, the cost of drying should be as low as possible in order to maintain profitability. In Finland, old drying method is to pile and leave the harvested material to dry in the open air, which is time consuming. (Alakangas, 2005) In some cases, the piles have to be monitored, as the decay may cause spontaneous ignition of the pile. Over time, the decay leads to degradation of the biomass as fuel, especially in improper storage conditions. (Van Loo & Koppejan, 2010).

Along with energy densifying, biomass can also be densified to increase the mass-to-volume ratio to lower the transportation and storage costs. Compressing biomass into pellets or briquettes also removes moisture and helps tackle the matter of irregular size and shape, alleviating the resulting problems. (Chen et al., 2015)

In order to utilize biomass in other applications than fluidized beds, such as internal combustion engines, gas turbines and pulverized combustion plants, pretreatment and/or conversion processes are required, as direct utilization is often not feasible or reasonable. With pulverized coal plants, a small share of biomass could be utilized in co-combustion with proper pre-treatment to control the particle size in fuel feeding.

Gasification, under stoichiometric combustion, and pyrolysis, thermal decomposition in oxygen free conditions, are ways to derive gaseous biofuels. The aim is to extract the maximum amount of volatiles and char from the biomass as gas, which can be further processed into a gaseous fuel containing for example hydrogen, methane and carbon monoxide, or further processed to liquid fuels such as methanol, ethanol or biodiesel. (Brown, 2011)

Torrefaction aims at producing an improved solid fuel, so called biochar out to raw biomass by removing moisture and volatiles, thus increasing the energy density and allowing its usage also in non-fluidized bed combustion applications. The manufactured biochar can be used for example to replace fossil coal. (Chen et al., 2015)

2.1.3.2 Costs

The matter of costs is important in all commercial activities, also in energy production. The costs determine the price of energy to the producer and consumer, with the legislation offering possible subsidies for the selected energy production methods. The costs of energy production can be divided into three categories - investment costs needed to build a power plant, fixed costs, such as land lease, for example, and variable costs which depend on the operations, such as fuel costs. The costs are affected by several factors, which make comparisons between technologies challenging. This leads to a situation where cost analysis is case-dependent. Here a brief summary is presented of the biomass utilization options and their approximate costs. Brown (2011) has estimated the costs of different methods of power production with biomasses. Direct combustion had the lowest investment costs (\$/kW) and could be extended up to 400 MW_{th} plants, while gasification and pyrolysis had significantly higher investment costs (\$/kW) and maximum scale of 25-50 MW_{th}. Essentially, the higher investment cost of gasification and pyrolysis were due to the need to build additional processing units (if not already available). (Brown, 2011)

The investment cost depends on the type of plant, whereas it can be argued that other fixed costs do not vary greatly between different types of combustion technologies. According to Koornneef et al. (2007), fuel costs make up a significant share of the total plant costs, from 15% to 31% depending on the technology and the fuel. The fuel costs comprise the fuel price, transport and processing costs. Alakangas et al. (2002) present examples on fuel prices, which vary between countries, fuels and with time. The prices change for example due to demand, taxation and subsidy policy changes (Alakangas et al., 2002). The main factors affecting the fuel price seem to be domestic production vs. import costs together with the method and distance of transportation and the level of refinement. Van Loo & Koppejan (2010) provide cost information on fuel processing and transportation costs. The bulk density correlates with the specific transportation cost; the lower the bulk density, the less fuel is transported and the higher the cost. Table 3 presents biomass processing costs. It can be summarized that the costs increase as the level of processing increases (reduction of size and moisture content, increases in uniformity and energy density). (Van Loo & Koppejan, 2010)

Table 3. Processing costs of biomass by Van Loo & Koppejan (2010).

Process	Costs [€/ton of input material]
Breaking/chipping	6.00
Grinding	12.50
Pulverization	31.00
Sieving	9.50
Pelletization, briquetting	7.50-25.00
Mechanical dewatering	3.00
Drying (wood)	7.00
Thermal drying (sludge)	31.00 (per ton of water evaporated)

There are several different methods for biomass utilization, which have been proven to work. The question remains, whether they are economically viable options. The production costs from solid biomass should be covered by the subsidy free price of the produced energy or fuel. The pretreatment and conversion processes typically require energy, reducing the net energy gain, as mentioned by Miao et al. (2011). Ever-present conversion losses mean that only a part of the original amount of the energy reaches the final product. According to Campbell et al. (2009) and Ohlrogge et al. (2009), greater mileage and fewer GHG emissions could be obtained by producing electricity for electric cars with direct combustion of biomass, rather than ethanol conversion for internal combustion engines.

The cheapest and most energy-efficient way of utilizing biomass is direct combustion of air-dried biomass in a large CFB boiler (especially in combined heat and power generation), if the fuel can be found within reasonable distance of the place of utilization. Obviously, these issues need to be evaluated separately for each existing plant and new project, and changing policies of subsidies and taxation can create challenges in biomass utilization and selection of the right fuel and combustion technology.

2.2 Fluidized beds

Fluidization is interaction between a fluid flow and a bulk of solid material, commonly referred to as a *bed* or *bed material*, regardless of its fluidization state. This process is examined in this chapter, starting from fundamentals and ending in an application in circulating fluidized bed boilers.

2.2.1 Fluidization

2.2.1.1 Packed and fluidized beds

Kunii & Levenspiel (1991, p. 1) define fluidization as an operation where a group of “solid particles are transformed into a fluid-like state” with fluid flow. Different fluidization states are illustrated in Figure 5. The fluidized state for solid, granular material can be achieved by blowing the fluid through a packed (or fixed) bed of material (Figure 5 a) until the bed becomes fluidized. The fluid flow passing through a packed bed

experiences a pressure drop due to the drag force over the bed, equated with the weight of the bed particles (Kunii & Levenspiel, 1991). Ergun (1952) has presented a correlation for pressure drop Δp over height of the bed H_{bed} (Equation 1) consisting of additive viscous and inertial parts. Niven (2002) has pointed out that this phenomenon can be explained by a simple contraction-expansion model of fluid moving in the channels between the particles. The numerical constants have been argued to derive from the particle shape and/or the test device, rather than being universal constants. (Arsenijevic et al., 1999)

$$\frac{\Delta p}{H_{\text{bed}}} \mathbf{g} = 150 \frac{(1 - \varepsilon_f)^2 \mu_f \mathbf{v}_f}{\varepsilon_f^3 d_s^2} + 1.75 \frac{(1 - \varepsilon_f) \rho_f \mathbf{v}_f^2}{\varepsilon_f^3 d_s} \quad (1)$$

where \mathbf{g} is gravitational acceleration, ε_f is fluid volume fraction, μ_f fluid viscosity, \mathbf{v}_f superficial velocity of fluid, d_s diameter of bed particles and ρ_f density of fluid. As the fluid flow is increased further, the bed expands and becomes fluid-like (Figure 5 b), and this transitional velocity is called the *minimum fluidization velocity*. Many correlations have been presented for this fundamental characteristic of a fluidized bed system. Wen & Yu (1966) have developed a dimensionless correlation for minimum fluidization from the Ergun equation (2) by including particle shape and bed voidage.

$$a \text{Re}_{\text{mf}}^2 + b \text{Re}_{\text{mf}} = \text{Ar} \quad (2)$$

where Re_{mf} and Ar are Reynolds number at minimum fluidization velocity and Archimedes number, respectively. Several values for coefficients a and b have been listed by Kunii & Levenspiel (1991), and a collection of other correlations has been presented by Oka & Anthony (2004). The reasons for several correlations may be related to difficulties in particle size and shape determination, as well as assumptions of forces affecting within the beds.

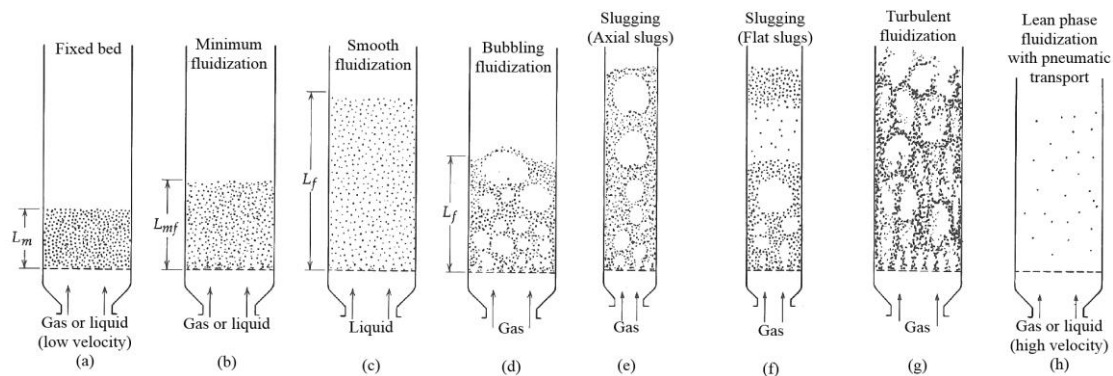


Figure 5. Modes of fluidization (Kunii & Levenspiel, 1991).

2.2.1.2 Characteristics of fluidized beds

The characteristic features of fluidized beds, which set them apart from packed beds, are illustrated in Figure 6. Fluidized beds share common features with liquids, for example a bubbling bed (Figure 5 d) resembles a boiling liquid with gas bubbles forming in the bottom and rising to the surface of the bed. Other liquid-like features are buoyancy, surface alignment to horizontal level and the analogy of pressure drop over the bed to hydrostatic pressure in liquids. (Basu, 2006; Kunii & Levenspiel, 1991)

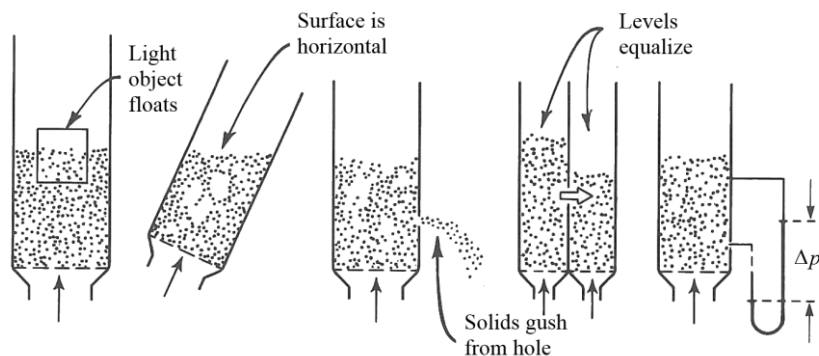


Figure 6. Hydrodynamic properties of fluidized beds (Kunii & Levenspiel, 1991).

The characteristics of fluidized beds depend on the solid and fluid properties and on the fluid flow rate. By increasing the fluid flow rate, several different fluidization regimes can be observed (Figure 5 c-h): bubbling, turbulent or pneumatic transport. The pressure drop of these different stages is presented in Figure 7 (Oka & Anthony, 2004).

Figure 8 illustrates the flow structure inside CFB units. As the fluid velocity increases, the particles start to be carried out of the fluidized bed reactor and to maintain the same number of particles in the system, new material has to be added or the exiting material returned. This exiting and back circulation of material is called external circulating CFBs. There is also an internal circulation of the material inside the reactor, where the solid particles are likely to rise in the middle or the *core* of the reactor, and flow down on the wall region or the *annulus*, where the fluid velocity is lower and the fluid flow cannot keep the particles fluidized. (Basu, 2006; Kunii & Levenspiel, 1991)

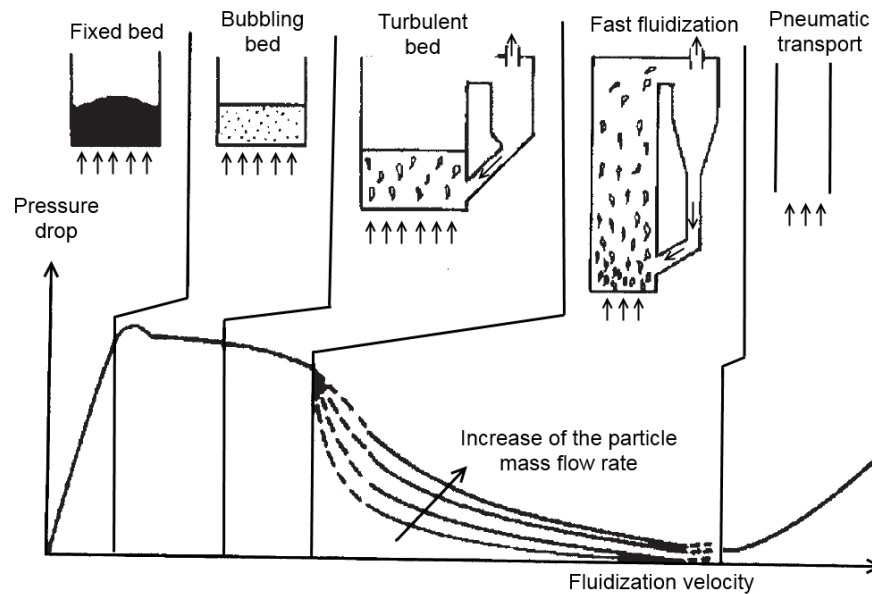


Figure 7. Pressure drop of different fluidization regimes (Oka & Anthony, 2004).

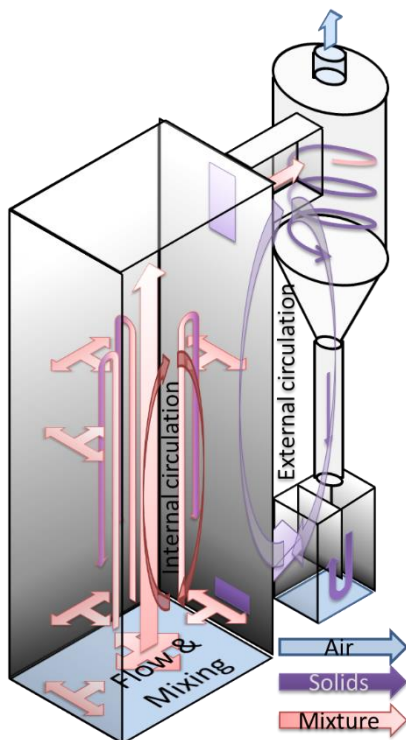


Figure 8. Simplified illustration of flow structures inside a circulating fluidized bed. The internal and external circulation are illustrated along with mixing mechanisms inside the furnace. One furnace wall and its flow indicators have been omitted for better visualization.

For the particles that are leaving the system, another important threshold velocity has been exceeded: *terminal velocity*, which can be theoretically defined from a single particle

force balance between gravity \mathbf{G} , buoyancy \mathbf{B} and drag force \mathbf{F}_D (Equation 3) (Basu, 2006). The terminal velocity of a particle surrounded by other particles is different from that of a single particle in only fluid flow. The concentration of particles causes a pressure drop over the particles (as illustrated in Figure 7), increasing the buoyant force (as discussed further in Chapter 2.2.2.1).

$$\mathbf{F}_D = \mathbf{G} - \mathbf{B} \quad (3)$$

When the fluidization velocity is the same as the terminal velocity of the particles, the particle is suspended in the fluid flow. Another interpretation is the maximum falling velocity of the particle falling in stationary fluid. When the fluid flow in the fluidized bed exceeds the terminal velocity of the particles, the particle will be entrained by the flow and can be elutriated from the system. For CFBs, terminal velocity is an important characteristic, as material elutriation and circulation are desirable phenomena. In the following chapters, the forces in fluidized beds and the effect of ambient conditions and reactions to fluidization are discussed.

Another characteristic behavior observed for fast fluidized beds, is that the particles go through constant formation of temporary groups, called *clusters*. These clusters are formed due to the effect of the particles on the gas flow field, also interparticle forces may play a role (M. Ye et al., 2005). Very different behavior can be observed in clusters compared to single particles. The gas flow causes clusters to change shape continuously and eventually break down, and new clusters can be formed from the same and new particles. (Basu, 2006) Clustering and bubbling are indications of the heterogeneous nature of the multiphase flow in a fluidized bed.

2.2.1.3 Determination of the fluidization regime

Several authors classified the different characteristics observed in fluidized beds on the basis of the properties of the particles and the fluid flow. Geldart (1973) has divided the particulate material into four groups (A, B, C and D) based on the average particle size and the density difference of the particles and fluid. He observed that different particles behaved in a distinctively different manner in fluidization, with different particle size and density. Very fine, group C particles are difficult to fluidize due to cohesion, while the easily fluidized group A and B particles are typical for fluidized beds, and the coarse group D are more difficult to fluidize and tend to channel or spout rather than fluidize evenly. Kunii & Levenspiel (1991), Cui & Chaouki (2004a) and Yang (2007) report that the changing ambient conditions and internal forces in the bed could change the bed behavior from one group to another. Yang (2007) expanded the Geldart classification to work in elevated pressures and temperatures.

Kunii & Levenspiel (1991) and Publication I list works which have mapped the different fluidization regimes and linked them with the Geldart groups, in order to be able to predict the fluidization regime from the particle and fluid properties and fluidization velocity. Dimensional and dimensionless plots are presented, which give approximate information

on the fluidization regime for the chosen operational conditions and materials. (Kunii & Levenspiel, 1991)

2.2.2 Forces in fluidized beds

To gain better understanding of the different fluidization regimes, it is necessary to understand the forces present in a fluidized bed. Considering a single particle, the force balance consists of gravity, buoyancy and drag force from the fluid (Basu, 2006). For a multiple particle system, the effect of other particles has to be considered, such as friction and normal forces in contact, as well as possible interparticle forces (Cui & Chaouki, 2004b). Electromagnetic forces are often neglected, though at least the electrostatic forces could play a role in cold and dry conditions with certain materials.

2.2.2.1 Gravity and buoyancy

Gravitational force between the earth and the particles in the fluidized bed is quite straightforward to determine. The weight of the bed can be measured without the fluid flow, and the fluid flow simply works against the gravity to fluidize the bed and then to elutriate the particles.

Unfortunately, the effect of buoyancy is difficult to determine experimentally in fluidized beds due to problems in distinguishing it from the drag force of the fluid flow. The equation of buoyancy and the combined force with gravity are presented in Equations 4 and 5, respectively. (Rasul, 1999)

$$\mathbf{B} = \rho \mathbf{g} V \quad (4)$$

$$\mathbf{G} - \mathbf{B} = (\rho_s - \rho) \mathbf{g} V \quad (5)$$

In the literature, two models for buoyancy force in fluidized beds are presented. According to Rasul (1999), several authors claim that the density ρ for the buoyant force is simply the density of the pure fluid ρ_f , while a number of authors present the suspension density ($\rho_{\text{susp}} = \varepsilon \rho_f + (1 - \varepsilon) \rho_s$) as the proper density formulation. Rasul (1999) presents results of liquid-solid fluidized beds indicating that the pure fluid density results match experimental results better. However, textbooks such as Basu (2006), Kunii & Levenspiel (1991) and Oka & Anthony (2004) refer to objects lighter than the bed floating and heavier ones sinking in gas-solid fluidization, and the effect of particles on the pressure inside the bed, neither of which support the conclusions by Rasul (1999). These might be the reasons why several authors utilize the suspension density model, rather than only gas density in modeling buoyancy in gas-solid fluidized beds, for example by Shabani et al. (2012).

Buoyancy studies in gas-solid systems found in the literature focus on bubbling fluidized beds. A study by Soria-Verdugo et al. (2011) suggests that the density (and particle size) difference does not so much affect the particle rising in the bubbling bed, but rather

prevents them from sinking under the bed surface. According to Rees et al. (2005) and Rees et al. (2006), biomass and waste particles have a positive buoyancy effect, which enables the fuel particles to rise to the surface of the bed. In BFB, the particles seem to rise in the wake of the bubbles as reported by Pallarés et al (2006). Bruni et al (2002) studied self-segregation of biomass particles, where devolatilized gas bubble from the particle would transport the particle to the surface of the bed. Rao (2009) has reviewed theoretical and empirical research on buoyancy in fluidized beds. He also reports experimental results finding significant buoyant force compared to the particle weight from a fluidized bed to a submerged large sphere. He has also studied the effect of the stagnation cap of defluidized particles resting over larger particles, adding to the gravity force. (Rao, 2009) Tee et al. (2008) have studied velocity fluctuations in fluidized beds, which they suspected to originate from density fluctuations. They also point out that particle segregation occurs not only by density, but due to different particle size. (Tee et al., 2008)

It can be summarized that there is evidence of a buoyancy force existing in fluidized beds, but unfortunately clear understanding and formulation for the buoyancy force in circulating fluidized beds is still missing.

2.2.2.2 Drag force

Drag force is described as “air resistance” in the case of an object moving through air, such as airplanes and cars, but moving fluid also exerts a force on a stationary or moving object, provided that the fluid and object have a non-zero relative velocity. Drag force can be divided into several different phenomena, though typically only two can be satisfactorily distinguished, pressure or shape drag and frictional drag. Drag and lift force are similar but in different directions, and here only drag force is discussed.

Skin friction or frictional drag is related to fluid flow around an object, which creates a boundary layer. The relative motion of the object and the fluid flow causes a velocity gradient and a shear force on the boundary layer, and this contact affects both the fluid and the object. Friction drag can be expressed as presented in Equation 6.

$$\mathbf{F} \equiv \frac{\tau}{0.5\rho_f \mathbf{v}_f^2} = 2 \frac{d\theta}{dz} \quad (6)$$

where τ is shear stress on the surface, \mathbf{v}_f is the free stream velocity of the fluid and θ and z are the momentum thickness and height of the boundary layer, respectively. The skin friction correlations can be found in Gudmundsson (2014) and White (2003), for example. The roughness of a surface has an effect on skin friction: the rougher the surface, the more friction there is between the fluid flow and the surface. (Gudmundsson, 2014; White, 2003)

Skin friction can only explain the drag force of a thin flat plate, while for other shapes, another type of drag force has to be acknowledged: the pressure or shape drag, which is related to the overall shape of the object. The point of the object (the nose) to contact the flow first acts as a “watershed”, dividing the fluid flow to move around the object and experiencing higher pressure from the flow. The flow starts to go around the object as laminar and transitions to turbulent according to the flow velocity and surface and object shape. Often the flow detaches from the surface of the object, which creates vortexes in the low pressure wake of the object. The high pressure on the nose and low pressure behind the object can be described as the shape or pressure drag. (Gudmundsson, 2014; White, 2003)

It can be seen in Figure 9 that the relation of pressure and frictional drag depends on the shape of the object. For a flat plate, the frictional drag dominates, while for a sphere or a cylinder, the shape drag is the dominant factor in the drag coefficient. (White, 2003)

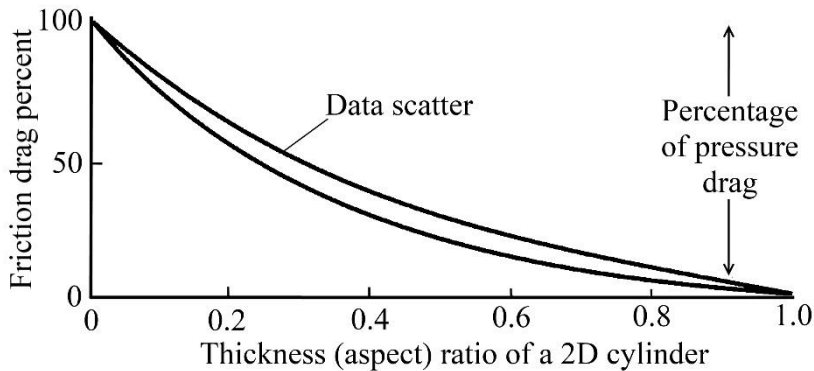


Figure 9. Ratio of pressure and friction drag on a 2D cylinder as a function of aspect ratio (cylinder width to height). (White, 2003)

For practical reasons, a common practice is to combine skin friction and shape drag together as a drag coefficient. The drag coefficient C_D is typically determined empirically due to difficulties or unfeasibility of theoretical determination. The drag coefficient can be considered as a characteristic function of the shape of the object and the relative velocity between the fluid and the object. (Gudmundsson, 2014; White, 2003) Standard drag coefficient curves are presented in the literature as a function of the Reynolds number for different regular shapes, for example by Lapple & Shepherd (1940).

The drag force between a particle and fluid flow can be defined as

$$\mathbf{F}_D = \frac{1}{2} \rho_f A_p C_D (\mathbf{v}_f - \mathbf{v}_p)^2 \quad (7)$$

For irregular particles and wide PSDs, the determination of drag coefficients or the planform (perpendicular to the flow) areas (A_p) would require a tremendous amount of measurements, as demonstrated by Bagheri et al. (2015). Due to this, the particles are often either assumed as spheres or average values are used to determine the drag

coefficient. For non-spherical particles, the drag coefficients are typically larger than for spheres with the same Reynolds number. van Wachem et al. (2015) found that non-spherical particles aligned their largest primary axis (if applicable) perpendicular to the flow, thus maximizing the cross-sectional area A_p . Other works, (e.g. Mandø & Rosendahl, 2010; Njobuenwu & Fairweather, 2015) have shown non-spherical particles constantly changing their orientation either with random or periodic rotation with respect to the flow. This also means changes in the cross-sectional area and the drag coefficient, which is difficult to take into consideration for example in modeling.

2.2.2.3 Interparticle forces

These are several different kinds of forces affecting between the particles in fluidized beds: Van der Waals, electrostatic, capillary, collisional, and frictional forces. Unfortunately, these forces are complex and not well understood, leading to several cases where only hydrodynamic forces are considered in fluidized beds. In this chapter interparticle forces are discussed briefly based on Cui & Chaouki (2004b), Li & Kato (2001) and Seville et al. (2000). Magnetic particles are not commonly used in fluidized bed combustion, and magnetic forces are omitted.

Rietema & Piepers (1990) credit interparticle forces for several phenomena in fluidized beds, which they claim cannot be explained by hydrodynamic forces. These are the electrical conductivity of a fluidized bed, a phenomenon of a tilted fluidized bed (as presented in Figure 6), where the bed surface shears off to the horizontal level only after a certain critical angle, and the “surpressure”, which is an additional pressure drop when moving from a packed bed to a fluidized bed (illustrated in Figure 7 as a small “bump”), instead of a smooth pressure drop curve in the transition. According to Seville et al. (2000), interparticle forces may affect the boundaries between Geldart groups.

Van der Waals forces are non-electrostatic forces, such as dipole forces and other forces between molecules and particles. They are relevant over very short distances (in the order of 10^{-10} m, i.e. order of molecular size), which makes them relevant for very fine particles (Geldart C group). The role of Van der Waals forces diminishes with increasing particle size and surface roughness due to increased distance between the surfaces.

Electrostatic forces exist between electrically charged and non-charged atoms and particles, and their effect is directly proportional to the strength of the charge. Particles can become charged through for example collisional or frictional contacts, or through thermionic emission in high temperatures. Electrostatic forces have been found to play a significant role with fine (group C) particles, while their relative strength is also reduced with increasing particle size. Variables affecting the generation of a charge in fluidized beds are the chemical composition, surface properties, particle shape and size, fluidization velocity and relative humidity. With low relative humidity, fluidized beds of small particles (C and A) have been shown to have significant amount of static electricity, an effect which is negated by increasing the relative humidity, as the water molecules in air appear to discharge the particles.

Collisional forces are often thought to dominate the interparticle forces in fluidized beds, especially inside a dense bed. The collisions can be considered either elastic (with no energy losses) or inelastic. In frictional collisions, the contact of particles is tangential rather than acting on the normal direction of the surface. Collisional and frictional forces are both dependent on the mechanical properties of particles, such as Young modulus, surface roughness and particle shape, as well as the relative velocities and angle of contact.

Capillary or liquid forces occur with high relative humidity as liquid bridges start to form between particles due to condensation and/or vapor adsorption. The effect of capillary forces are again stronger for fine particles (group C), though also larger particles are affected (group A and B). (Li & Kato, 2001)

2.2.2.4 The effect of ambient conditions

The fluid properties, namely density and viscosity are affected by the ambient conditions of the system; temperature and pressure. The effect of changes in ambient conditions on the fluidization behavior have been investigated and reported by several authors. Poletto et al. (1993) found the increasing pressure of the system to reduce the minimum fluidization velocity. In their work, the pressure had a major effect on the density of CO₂ while viscosity changes remained small (Poletto et al., 1993). Rowe (1984) reports about the role of particle size in elevated pressures. The results indicated that the minimum fluidization velocity of small particles (Geldart group A) was not affected by the increased pressure, due to the viscous flow regime, while larger particles (group B) experienced significant reduction in the minimum fluidization velocity (Rowe, 1984). Jiliang et al. (2013) report that the minimum fluidization velocities decrease with the increase of temperature in binary systems, as well as with a wide PSD. Yates (1996) claims that the terminal velocity decreases for small particles and increases for large particles with increasing temperature, while the pressure increase causes terminal velocity to decrease regardless of particle size (groups A, B and D).

The interparticle forces may also be affected by changes in pressure and temperature, which could also have affected the above mentioned findings. Changes in the bed voidage with temperature have been claimed to result from changing interparticle forces. According to Cui & Chaouki (2004a) the changes in interparticle forces with temperature are still poorly understood and the findings are divided. In cold conditions of laboratory devices, all interparticle forces can have a significant effect on the fluidization behavior of the fluidized bed system. In hot conditions, capillary forces should lose their effect as water is evaporated. Electrostatic forces have not been reported to play a significant role in high temperature fluidized beds. The collisional and frictional forces may change if the particle properties are affected by the increased temperature. It is typically considered that the collisional and frictional exchanges between particles are the dominant and most significant form of particle interaction in fluidized beds, while the effect of other interparticle forces are neglected.

2.2.2.5 The effect of reactions

So far the particles have been considered as inert. For bed material, this assumption could be suitable, though a limited number of chemical reactions may occur. The particle size can change due to mechanical grinding, or agglomeration due to ash softening/melting, which should be avoided.

For fuel, inert assumption is neither true nor desirable. When a fuel particle enters a hot fluidized bed, it is surrounded by hot gas and particles, which cause a rapid temperature rise, and fuel moisture is evaporated and leaves the fuel particle. The volatile material is released during devolatilization as the particle temperature increases, and finally only fuel char and ash remain. At this point, the fuel particle may have lost a majority of its weight and its density has changed. Certain fuels are known to shrink or even swell during drying and devolatilization. Alakangas (2005) mentions that drying reduces the volume of wood. The char can react in the gas atmosphere by combustion or gasification, during which the particle size and density can change, most likely simultaneously. (Magdziarz & Wilk, 2013; Yang et al., 2008) These changes affect the force balance of the particle. Mass loss increases the ratio of drag force to gravity, while changes in size affect the buoyancy and drag force. Considering a freshly fed, unreacted fuel particle, it is less likely to elutriate due to its larger mass and size than a dried, devolatilized or burning particle.

2.2.3 Circulating fluidized bed boilers

An overview of the development and history of circulating fluidized bed (CFB) boilers has been presented by Koornneef et al. (2007). The first patent of a fluidized bed was granted in 1922 for lignite gasification, and since then fluidized beds have been utilized in the chemical industry and energy production in for example catalytic cracking, gasification and combustion, with new concepts being designed for enriched oxygen combustion and carbon capture and sequestration. The number of units and the maximum capacity have steadily increased to approximately 400 units built worldwide and with the technology being scaled to supercritical utility CFB boilers with the duty of 550 MW_e (to be commissioned in 2015) (Jäntti et al., 2012). The needs for the development of CFB combustion vary in different countries from environmentally friendly utilization of high sulfur coals, to small-scale industrial heat production and utilization of biomass and other lower rank and/or domestic solid fuels. (Koornneef et al., 2007; Oka & Anthony, 2004)

Figure 10 presents a layout of a commercial CFB boiler. The furnace contains a bed of sand or fuel ash (commonly referred as bed material) and sorbent, which is fluidized with primary air blown through the grid on the bottom of the furnace. Secondary air, fuel and sorbent are fed to the lower furnace, and the upper furnace may contain additional heat transfer surfaces. From the upper furnace, the gas-particle suspension enters a cyclone separator where the solids are separated from the gas by centrifugal motion and gravity and returned to the furnace through a loop-seal and an optional external bubbling bed heat exchanger. The gas exits the separator and moves through the back-pass and fine particle

filter before the stack or flue gas treatment for carbon capture and sequestration, for example.

It should be noted that different parts of the boiler operate in different fluidization regimes. A dense bubbling, turbulent or fast fluidized bed is found in the lower furnace, with dilute suspension higher in the furnace, swirling flow is found in the cyclone, and the solids return system can be considered to operate in a moving packed bed and bubbling bed regimes. (Basu, 2006)

The main advantages of CFB combustion are high combustion efficiency, due to good mixing and material internal and external circulation, fuel flexibility, and the ability to utilize low rank fuels, due to the bed of inert material which acts also as a heat storage balancing the changes in the fuel properties. The furnaces are typically operated in temperatures below 950°C , which prevents ash melting and formation of thermal NO_x emissions, and enables the effective utilization of limestone or other sorbents in the furnace to reduce SO_x emissions. (Basu, 2006; Oka & Anthony, 2004)

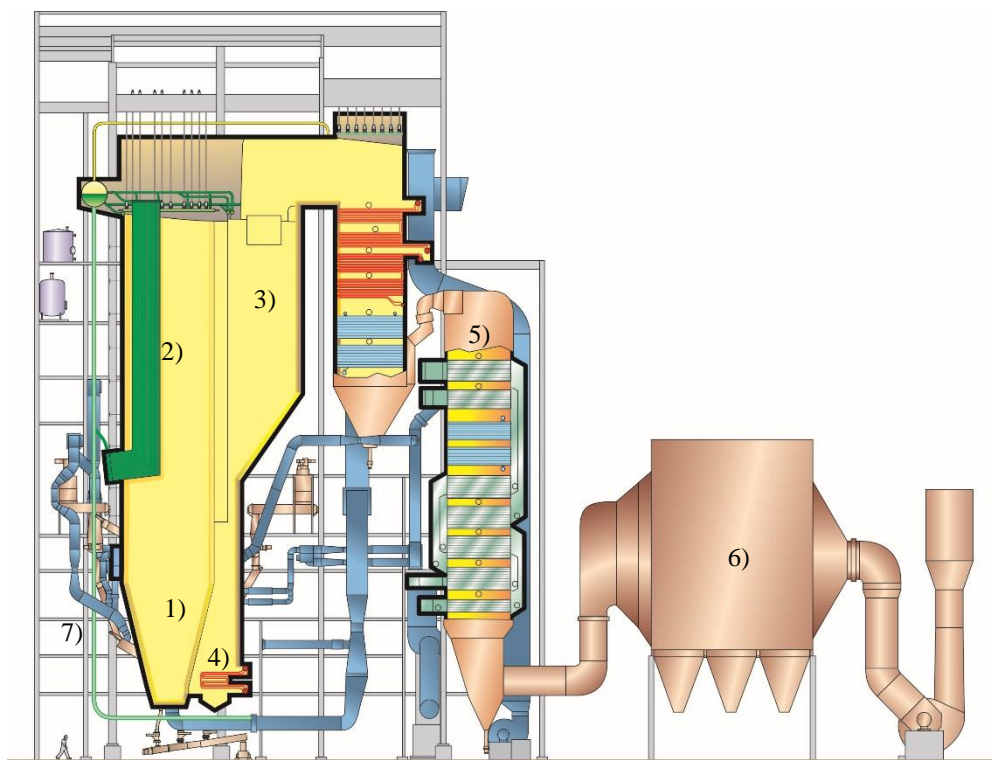


Figure 10. Kaukaan Voima Oy biomass firing $385 \text{ MW}_{\text{th}}$ CFB boiler in Lappeenranta, Finland. The image courtesy of Amec Foster Wheeler. The numbered parts are 1) furnace, 2) internal heat surface, 3) separator, 4) external heat exchanger and particle return to furnace, 5) back-passes with heat surfaces, 6) electrostatic particle filter, 7) fuel, sorbent and secondary air feeding.

The fuel is the main factor in the new furnace design process, as its properties determine, along with furnace hydrodynamics, the forming temperature and combustion product distributions. This affects the placement and sizing of the heat transfer surfaces, for

example. Understating and being able to predict the fuel behavior inside the furnace is thus extremely important for successful furnace design. In La Nauze (1987), an example of the effect of the fuel type on the forming temperature profiles can be found, as presented in Figure 11. The high volatile content of the wood chips and the resulting above-bed combustion is offered as an explanation for the clearly different temperature profile compared to coals.

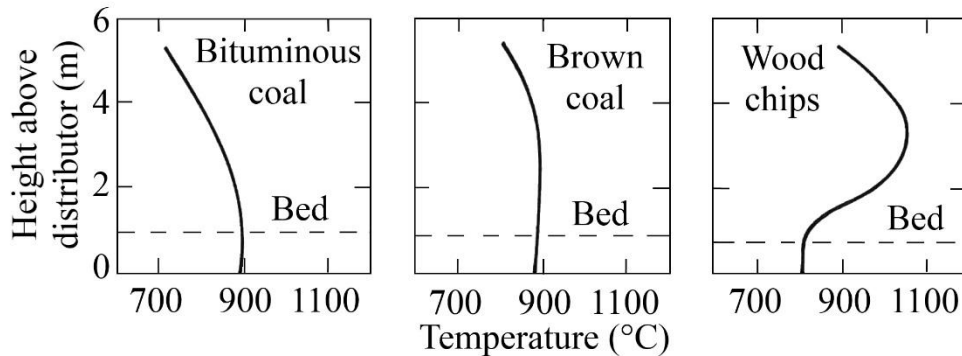


Figure 11. Effect of fuel type on the temperature profile of the CFB furnace. (La Nauze, 1987)

2.3 Modeling of fluidized beds

The need for modeling comes from the need to understand the process studied, and also from the infeasibility of measurements. Modeling offers more information about the process with great detail, it is a non-intrusive method, cheaper than comprehensive measurements, and applicable to a wide range of problems. Modeling enables the study of processes and devices before manufacturing, saving prototyping costs. Large CFB furnaces are modeled, as the system is too large (and challenging) for comprehensive measurements. Modeling is not restricted by physical limitations (lack of measurement ports), but rather by computational resources, validity of the models and boundary conditions, and the skills of the modeler. It should be kept in mind that when simulation results are obtained, estimation of their validity and accuracy is essential. Validation measurements are always required to confirm or refute the modeled results and models. (Patankar, 1980)

Numerical simulation of fluid flow, or computational fluid dynamics (CFD), is based on a numerical solution of physical conservation laws in a selected geometry. The geometry is a limited volume of space with relevant descriptions of boundaries, inlets and outlets. Both the conservation equations and the geometry are discretized for numerical calculations. The geometry is discretized by splitting the total volume into several smaller control volumes, creating a connected calculation mesh, in which the discretized conservation equations will be solved. The conservation equations are rewritten from their integral or vector form to reflect the discretization of the geometry and modeling scheme. The number of conservation equations to be solved depends on the number of

dimensions and phases simulated, as well as the modeling scheme. For most applications, 3D cases have to be considered. Depending on the process, the simulation can be time-dependent, or steady state, stating that time is not considered. In this chapter the different modeling approaches, especially related to the modeling of CFB furnaces, are presented.

2.3.1 General modeling approaches

There are two main approaches to the modeling of multiphase flows. The Eulerian approach considers each phase as continuous, selecting the computational cells larger than individual molecules or particles, so that it is effectively impossible to distinguish individuals from the bulk. This approach is typically used for gases and liquids, but can be extended to granular solid material. As a result, the Eulerian approach offers only the average value for the whole computational cell. Better resolution requires the use of more computational cells, which is eventually limited by computational resources. (Loth, 2008)

An alternative way for a particulate phase would be to consider every particle as a separate entity. The Lagrangian approach is a particle-tracking method considering the movement and force interaction of individual particles or molecules. (Loth, 2008) The benefit of the Lagrangian approach is good accuracy in the consideration of particle movement, and also the particle-particle collisions can be solved, with method called discrete element method (DEM). The main drawback is the computational costs deriving from the need to use a small time step in transient simulation combined with large amounts of particles, leading to a limited system size or number of particles. Grouping methods, such as the multiphase particle-in-cell method (MP-PIC) or dense discrete phase model (DDPM), offers a remedy to the problem with reduced resolution of details.

2.3.2 Conservation equations

CFD and numerical simulation of energy conversion systems are based on a numerical solution of fundamental conservation equations within the computational domain. These fundamental quantities are mass, species, momentum and energy. In addition to these, additional closure equations are needed to consider the interaction between the phases in a multiphase system. Together with suitable material properties, equations of state for fluids and boundary conditions, the system can be modeled. The following conservation equations are adapted from Ishii & Hibiki (2006) for the Eulerian approach.

2.3.2.1 Continuity equation and conservation of species

For the multiphase flow, the share of phase j in a computational cell is described with volume fraction ε_j . Sum of phases in a cell must fill the whole volume of the cell. Additionally, the sum of volume fractions of species i make up the total volume fraction of phase j , as described in Equation 8.

Continuity equation (9) describes the conservation of mass. The terms describe storage and flow of material of phase j , with ρ representing the density and \mathbf{v} the velocity vector (1-, 2- or 3-dimensional, depending on the system considered). The sources and sinks Γ , consist of inlets, outlets and phase change due to thermochemical reactions, for example evaporation or combustion.

$$\begin{cases} \sum_j \varepsilon_j = 1 \\ \sum_i \varepsilon_i = \varepsilon_j \end{cases} \quad (8)$$

$$\frac{\partial}{\partial t} (\varepsilon_j \rho_j) + \nabla \cdot (\varepsilon_j \rho_j \mathbf{v}_j) = \sum \Gamma_j \quad (9)$$

$$\frac{\partial}{\partial t} (\varepsilon_i \rho_j) + \nabla \cdot (\varepsilon_i \rho_j \mathbf{v}_j) = -\nabla \cdot (D_i \nabla \varepsilon_i \rho_j) + \sum \Gamma_i \quad (10)$$

Conservation of species i of phase j (Equation 10) is closely related to the conservation of mass, as it describes the mass balance of individual components, such as oxygen or fuel char, for example. Note the addition of the diffusion term with diffusion coefficient D , as the species can also be transported by diffusion as well as convection. The term diffusion is used for gaseous species and general discussion, while the term dispersion is used for solid material. The diffusion can be considered as only molecular diffusion or it can include also turbulent mixing, depending on the modeling approach. Different species of the same phase can share the continuity and momentum equations, and only the conservation of the species is solved separately, as presented above.

2.3.2.2 Momentum equation

Momentum equation (11) presents the conservation of momentum for phase j . The terms describe the storage and transport of momentum with velocity \mathbf{v} with respect to shear stresses $\boldsymbol{\tau}$, pressure p , gravity and source terms Ω , which also contain additional forces.

$$\frac{\partial}{\partial t} (\varepsilon_j \rho_j \mathbf{v}_j) + \nabla \cdot (\varepsilon_j \rho_j \mathbf{v}_j \mathbf{v}_j) = \nabla \cdot (\varepsilon_j \boldsymbol{\tau}_j) - \nabla (\varepsilon_j p_j) + \rho_j \mathbf{g} + \sum \Omega_j \quad (11)$$

The difficulties in the discretization and computation of the momentum equation arise from the non-linearity in the convective term ($\mathbf{v}\mathbf{v}$). The estimation and inclusion of the interfacial stresses on the surfaces of the computational cell, momentum exchange between phases, coupling between velocity and pressure, and the consideration of turbulence create additional challenges. There are methods to handle the non-linearity, formulation of stress-terms and pressure-velocity-coupling presented in the literature and they will not be discussed further, as they are not in the scope of this thesis. Turbulence is discussed in the following chapter, as its modeling method has a significant impact on the discretization of the equations and geometry.

2.3.2.3 Turbulence considerations

There are several methods available for modeling turbulence. In the case of laminar flow, turbulence modeling can be neglected, while this is rarely the case with industrial flow applications.

There are different Eulerian models available, differing by the resolution and accuracy. Direct numerical simulation (DNS) is the pinnacle of CFD, where the flow field can be solved without any modeling. Large eddy simulation (LES) solves the equations down to a certain filter (mesh) size and provides highly accurate results with lower computational costs than DNS. Currently these approaches are limited to small geometries due to high demand of computational resources. Reynolds averaged Navier-Stokes (RANS) models are applied for most industrial applications. While they offer poorer description of the fine structures of the flow (namely turbulence), the accuracy in modeling of the bulk movement is good and the method relatively fast and computationally inexpensive. While some modeling approaches (such as LES) solve the majority of the flow, the mesh resolution sets a boundary to what can be solved and what has to be modeled with so called subgrid-scale models.

For multiphase flow, the turbulence consideration becomes even more challenging due to multiple interconnected phases in which the turbulence can be independent or connected. For fluidized beds, the importance of turbulence is still unknown. van der Schaaf et al. (1999) report that gas-particle turbulence has a negligible effect on the pressure fluctuations found in a laboratory scale circulating fluidized bed. Sternéus et al. (1999) measured gas flow characteristics of CFB units similar to turbulent flows, although the mechanism behind these properties could not be determined. Most likely the particles act as a filter, breaking the large eddies to smaller ones that dissipate faster. Another possibility is that the movement of the particle phase reduces the visible effects of turbulence or create turbulence like effects by causing velocity/density fluctuations (van der Schaaf et al., 1999).

2.3.2.4 Energy equation

Conservation of energy is handled by energy equation (12), presented here as thermal energy conservation with enthalpy h , assuming that the mechanical energy of the flow has a negligible effect on the total energy. The terms are (from left to right) the storage and transport of energy by the flow, by diffusion and source terms Φ which consider the sources and sinks due to for example chemical reactions or heat transfer. Depending on the modeling approach, the phases can have separate energy equations or share a common one. In fluidized beds, the bed material has a significant effect on the storing of heat and heat transfer due to the larger mass of the bed and higher specific heat capacity.

$$\frac{\partial}{\partial t}(\varepsilon_j \rho_j h_j) + \nabla \cdot (\varepsilon_j \rho_j \mathbf{v}_j h_j) = \nabla \cdot (\lambda_j \nabla T_j) + \sum \Phi_j \quad (12)$$

2.3.3 Peculiarities in the modeling of fluidized beds

The challenges in the modeling of multiphase flows come from the interactions between the phases. The interactions are complex and occur in multiple time and length scales between the phases. Additionally, modeling the particle interaction within the particle phase is challenging. There are several types of models available in the literature for chemical reactions between phases (see for example Singh et al. (2013)). This chapter focuses on the gas-solid and solid-solid phase momentum interaction.

The interaction of phases are determined with coupling. For very dilute particle flows one-way coupling is used, and it can be considered that the particles do not affect the gas flow, but are affected by the gas flow. The threshold for this is particle volume fractions below 10^{-6} . For flows denser than this, two-way coupling should be used with true interaction between the phases. For dense flow, the interaction within the particle phase should be considered, as the particle-particle collisions start to play a significant role. This is called four-way coupling with the volume fractions of solid phase above 10^{-3} . (Alletto & Breuer, 2012; Crowe & Michaelides, 2006) The level of coupling has a notable effect on the computational costs of the simulation, one-way coupling being cheapest and fastest one, and complexity and costs increasing with the degree of coupling.

2.3.3.1 Gas-solid interaction

As discussed above, the drag force on a single, regularly shaped particle has been widely studied, while the drag force of an irregular non-spherical particle is more difficult to determine due to difficulties in the determination of particle size and shape. The drag force caused by a fluid flow on a system of multiple particles has even less complete understanding, due to phenomena rising from the multiphase flow.

One method to estimate the drag force in multiparticle system modeling is to use so-called voidage functions, which are derived from experiments. The average void fraction is correlated as a ratio of the drag force in the multiparticle system to a single particle drag force. Both liquid and gas fluidization have been utilized with the assumption of a homogeneous fluidization. The drag force between the fluid and particles increases with the increase of the volume fraction of the particles in the system. (Gidaspow & Ettehadieh, 1983; Lewis et al., 1949; Richardson & Zaki, 1954; Wen & Yu, 1966) A different view has been presented, where the drag force is reduced with the increased particle presence (Matsen, 1982; Nieuwland et al., 1994; Wang & Li, 2007). This is due to abandonment of the homogeneity assumption, which is known to be false due to the development of particle clusters and gas bubbles.

Equation 13 presents the gas-solid drag force \mathbf{F}_{g-s} for a control volume of volume V with K_{g-s} , the momentum exchange coefficient.

$$\mathbf{F}_{g-s} = K_{g-s} (\mathbf{v}_g - \mathbf{v}_s) V \quad (13)$$

There are a few models for gas-solid momentum interaction in Eulerian modeling. The Gidaspow & Ettehadieh (1983) model is a combination of the so-called Wen and Yu (1966) (Equation 14) and Ergun (1952) (Equation 15) models. The origin of the voidage function exponent (-2.65) in Equation 14 is not reported in the original publication by Gidaspow & Ettehadieh (1983), but is later Gidaspow et al. (1991) referred to as having an experimental origin without further reference or explanation. The exponent presented by Wen & Yu (1966) was -4.7 , so the origins of the name of the model are somewhat unclear. It has been shown that Wen and Yu's drag force model is actually a single particle drag coefficient relation to the Reynolds number, scaled with a voidage function (Yang et al., 1985). The drag coefficient of Schiller & Naumann (1935) is used in this formulation (Equation 18), which also has been expanded from the original for large Reynolds numbers. The Ergun model is derived from packed bed pressure drop experiments, and its use has been extended to threshold of fluidization and even beyond to fluidized beds. The Gidaspow model contains a discontinuity at the voidage of 0.8, at the interface of the Ergun and Wen and Yu models. To remedy this, Huilin & Gidaspow (2003) have presented a switch function φ (Equation 17) to smooth the transition between the models in Equation 16.

Table 4. The Huilin-Gidaspow model equations. (Huilin & Gidaspow 2003)

$$K_{\text{WY}} = \frac{3}{4} C_D \frac{\varepsilon_s \varepsilon_g \rho_g |\mathbf{v}_g - \mathbf{v}_s|}{d_s} \varepsilon_g^{-2.65} \quad \varepsilon_g > 0.8 \quad (14)$$

$$K_E = 150 \frac{\varepsilon_s (1 - \varepsilon_g) \mu_g}{\varepsilon_g d_s^2} + 1.75 \frac{\rho_g \varepsilon_s |\mathbf{v}_g - \mathbf{v}_s|}{d_s} \quad \varepsilon_g \leq 0.8 \quad (15)$$

$$K_{\text{g-s}} = \varphi K_E + (1 - \varphi) K_{\text{WY}} \quad (16)$$

$$\varphi = \arctan[150 \cdot 1.75 (0.2 - \varepsilon_s)] \pi^{-1} + 0.5 \quad (17)$$

$$C_D = \begin{cases} \frac{24}{\text{Re}} (1 + 0.15 \text{Re}^{0.687}) & \text{Re} \leq 1000 \\ 0.44 & \text{Re} > 1000 \end{cases} \quad (18)$$

The model of Syamlal et al. (1993) (Equation 19) has a similar form to the Gidaspow model, but includes the terminal velocity correlation \mathbf{v}_{tm} (Equation 21) by Garside & Al-Dibouni (1977) and uses the drag coefficient given by DallaValle (1948) (Equation 23). Note that this expression is only found in the second edition of the book, while the first edition (DallaValle & Klemin, 1943) offers another expression ($C_D = 0.40 + 24.4 \text{Re}^{-1}$), a form which is more comparable to the other drag coefficient correlations found in the literature. The reasons for the modification of the drag coefficient between editions, and the utilization of the drag coefficient of the second edition are unclear.

Also other momentum exchange models are found in literature (for example Gibilaro et al. (1985) and Hill, Koch, & Ladd (2001a, 2001b)), but further discussion is omitted here. While not an independent momentum exchange model, the energy-minimization multi-scale (EMMS) method by Li & Kwauk (1994) is a promising method for Eulerian

simulations, as it includes mesoscale structures (clusters) as their own entities and does not rely on the assumption of homogeneous fluidization. The multiphase flow is considered to consist of dense, dilute and gas phases, with a solution of their respective drag forces and velocity fields. (Shuai et al., 2011)

Table 5. The Syamlal et al. (1993) model equations.

$$K_{g-s} = \frac{3\varepsilon_g \varepsilon_s \rho_g C_D}{4\mathbf{v}_m^2 d_p} |\mathbf{v}_s - \mathbf{v}_g| \quad (19)$$

$$\mathbf{v}_m = 0.5 \left(a - 0.06 \text{Re} + \sqrt{(0.06 \text{Re})^2 + 0.12 \text{Re}(2b - a) + a^2} \right) \quad (20)$$

$$a = \varepsilon_g^{4.14} \quad (21)$$

$$b = \begin{cases} 0.8 \varepsilon_g^{1.28} & \varepsilon_g \leq 0.85 \\ \varepsilon_g^{2.65} & \varepsilon_g > 0.85 \end{cases} \quad (22)$$

$$C_D = (0.63 + 4.8 \text{Re}^{-0.5})^2 \quad (23)$$

2.3.3.2 Solid-solid interaction

Only a few models could be found for solid-solid momentum exchange in the literature as reviewed and discussed by Bell (2000). Syamlal (1985) has presented Equation 24 for the modeling of solid-solid momentum exchange coefficient $K_{s,i-s,j}$ between solid phases i and j with the radial distribution function g_0 by Lebowitz (1964) (Equation 25).

$$K_{s,i-s,j} = \frac{3(1 + c_{\text{res}})(\pi/2 + c_{\text{fri}}\pi^2/8)\varepsilon_{s,i}\varepsilon_{s,j}\rho_{s,i}\rho_{s,j}(d_{s,i} + d_{s,j})^2 g_0 |\mathbf{v}_{s,i} - \mathbf{v}_{s,j}|}{2\pi(\rho_{s,i}d_{s,i}^3 + \rho_{s,j}d_{s,j}^3)} \quad (24)$$

$$g_0 = \frac{1}{\varepsilon_g} + \frac{3d_{s,i}d_{s,j}}{\varepsilon_g^2(d_{s,i} - d_{s,j})} \left(\frac{\varepsilon_{s,i}}{d_{s,i}} + \frac{\varepsilon_{s,j}}{d_{s,j}} \right) \quad (25)$$

where c_{res} and c_{fri} are coefficients of restitution and friction, respectively. Bell (2000) has presented her own model for solid-solid interaction. One option would be to utilize computational methods to derive new models, for example discrete element method (DEM) simulations have shown promising results in the modeling of dense fluidized bed systems with differing results to the models mentioned above (Jalali & Hyppänen, 2010; Jalali et al., 2013). The benefit of this kind of an approach is a more physically correct solution, while the main drawbacks are the significant computational costs of using individual particles in the simulations. Some scholars (Makkawi et al., 2006; Weber & Hrenya, 2006; Weber & Hrenya, 2007; M. Ye et al., 2008) have included the cohesion effects of interparticular forces in their simulations.

3 Modeling of fuel flow in a large-scale circulating fluidized bed furnace

The general methodology of modeling has been applied in the modeling of fuel flow inside a large-scale CFB furnace. Previous works were discussed. The utilized model frame has been briefly introduced. A new fuel flow model has been developed, and fundamental differences to previous fuel flow modeling approaches are discussed below.

3.1 Previous works

A limited number of studies are presented in the literature on the fuel flow inside a CFB furnace, as reported by Pallarès & Johnsson (2008) who have reviewed fuel flow modeling in fluidized beds. Experimental and modeling studies of fuel flow were found for BFB, such as Farzaneh et al. (2013), Garcia-Gutierrez et al. (2015), Liu & Chen (2010), Olsson et al. (2012), and Sette et al. (2014), and they focus on the dispersive horizontal mixing with particle tracking.

Fewer studies of CFBs can be found in the literature due to difficulties in optical particle tracking as the particles obscure the view. Mixing and particle residence times in a CFB riser have been studied with an optical method by Wei & Zhu (1996) and Yan et al. (2009) and with radioactive tracers by Van de Velden et al. (2007, 2008). Van de Velden et al. (2007, 2008) used radiated radish seeds to represent biomass particles. These studies (Van de Velden et al., 2007, 2008; Wei & Zhu, 1996; Yan et al., 2009) can be referred to for further details and references on experimental studies of solids mixing in CFBs.

The difficulties encountered in experimental research can be overcome with modeling. Unfortunately, CFD analysis of a CFB furnace is computationally very expensive, especially if reaction modeling is included. This is why many CFD works on CFB are limited to studying the hydrodynamics or finer details of the multiphase flow. Even then, these studies have difficulties in predicting the horizontal pressure profile (i.e. the particle distribution) correctly, due to difficulties in the modeling of small and medium scale flow structures, such as particles and clusters. The most common application of CFD is to study the flow in a riser, which is often done in small scale, or even as 2D. Far fewer examples can be found of 3D riser studies and large furnace simulations. As the fuel flow and mixing inside a CFB furnace are inherently three-dimensional, the 1D and 2D simulations cannot be utilized in the study of fuel mixing, thus only 3D simulations are discussed further.

3.1.1 CFD studies

There are different approaches for fuel flow modeling in fluidized beds. The fuel can be modeled with the Eulerian approach as a separate solid phase, leading to flow with one

gaseous and two solid phases, or as a species of the solid phase in the two-phase flow. Another option is to use the Lagrangian approach, where the fuel particles or groups of particles are tracked.

Nikolopoulos et al. (2013) have simulated a small full loop of a CFB model in ambient temperatures. A full loop of 0.1 MW_{th} CFB pilot has been simulated by Adamczyk et al. (2014a) in cold conditions. Shah et al. (2010) have simulated a 374MW_{th} hot furnace without reactions. The same furnace was simulated later by Shah et al. (2015a) with different subgrid-scale drag force corrections. Another reactionless CFB furnace has been simulated by Shah et al. (2015b) by using 4 different particle size fractions. Man et al. (2010) have simulated a 300MW_e CFB full loop, but offer limited details on the models and methods. Zhang et al. (2010) have performed a transient EMMS simulation of a 150MW_e CFB full loop in hot conditions, but without reactions.

Tanskanen (2005) has studied the coal flow inside a section of a CFB furnace for coal in 2D and 3D without reactions. 1.2 MW_{th} pilot with fuel combustion with 3 Eulerian phases has been simulated by Nikolopoulos et al. (2009) and later by Nikolopoulos et al. (2014) with EMMS. Hartge et al. (2009) have simulated a pilot scale CFB riser hydrodynamics with different drag force models compared with measurements. Taivassalo et al. (2012) have performed time-averaged modeling of a 12MW_{th} CFB unit, including reactions and fuel particle tracking. A similar approach was later taken by Niemi et al. (2014) for the same unit and Peltola & Kallio (2013) for a 135MW_e CFB unit. Adamczyk et al. (2013) and Adamczyk et al. (2014b) have simulated a 460MW_e CFB furnace with hybrid Euler-Lagrange approach with dense discrete phase model (DDPM) in hot conditions with reactions. Weng et al (2011) simulated a 250MW CFB furnace combusting coal and animal derived biomass with MP-PIC method.

Adamczyk et al. (2014b) give information on computational times: utilizing 16 cores a month of wall time was required for obtaining a transient solution for 60 seconds of data for time-averaging. Inclusion of combustion is reported to triple the computational time. Shah et al. (2015b) report on 16 processor transient simulation of less than two minutes to have taken 1 week and 3 weeks with a coarse and fine mesh, respectively. This shows the current infeasibility of a CFD solution in the modeling of CFB furnaces for engineering purposes. With the developing computation power and methods, the feasibility has to be re-evaluated from time to time.

The cases where the fuel flow is modeled without reactions lead to overestimated fuel concentrations, as the fuel is not consumed by the reactions. In hot cases, the variation of temperature should be considered due to its effects on the reactivity and flow. As a summary, it can be stated that a holistic model considering the coupled phenomena inside a CFB furnace should be utilized in the modeling of the fuel flow.

3.1.2 Holistic models

Three-dimensional holistic models are commonly used in the modeling of CFB furnaces, as they consider all the fundamental aspects of CFB, namely hydrodynamics, reactions and heat transfer. Steady state, partially empirical (later semi-empirical) models are applied with coarser mesh structures, compared to CFD requirements, to keep the computational costs on an acceptable level for furnace design and analysis. (Lyytikäinen et al., 2014)

Currently there are three different 3D semi-empirical CFB furnace models that have been presented in the literature, 1) by Hyppänen et al. (1991) from Lappeenranta University of Technology, 2) Knoebig et al. (1999) from Hamburg University of Technology and 3) Pallarès & Johnsson (2008) from Chalmers University of Technology. These models have been later utilized in the modeling of CFB gasification, air- and oxy-combustion, as well as limestone behavior and radiation by 1) Bordbar et al. (2015), Koski et al. (2011), Lyytikäinen et al. (2014), Myöhänen & Hyppänen (2011), Myöhänen et al. (2014), Rahiala et al. (2014) and Publications II-IV, 2) Hartge et al. (2009), Luecke et al. (2004), Petersen & Werther (2005) and Wischniewski et al. (2010) and 3) Seddighi et al. (2013).

A comprehensive analysis of similarities and differences between the presented semi-empirical CFB furnace models has been presented by Myöhänen (2011). These furnace models share similar characteristics, such as a steady state solution and semi-empirical approach in the modeling of hydrodynamics, reactions and fuel flow. The fuel flow is considered as dispersive and can even be directed towards a fixed concentration profile. While this approach has been successfully applied in the modeling of coal combustion, this approach could be less suitable for the modeling of wider PSD and lower density biomass.

3.2 Development of the fuel flow model

An existing steady state holistic three-dimensional CFB furnace model frame has been utilized and further developed in this work. A brief description of the overall model frame is presented here, along with the description of the previous modeling approach of the fuel flow. After this, the development of the new fuel flow model is described. For more details on the model frame, see Myöhänen & Hyppänen (2011) and Myöhänen (2011) as they are the main references throughout the whole chapter.

3.2.1 Model frame description

The three-dimensional CFB furnace model frame used in this work is a steady state one and contains semi-empirical components in the determination of homogeneous and heterogeneous reactions of the fuel, sorbent and various gaseous species, fragmentation of solid material, convective and radiative heat transfer, and flow dynamics. The separators and possible external heat exchangers are modeled with separate submodels. The fuel consists of char, volatiles, moisture, and ash. When the fuel is fed into the furnace

in the model frame, it dries and releases the volatile material according to the reaction models, leaving the char to the fuel particle. Fragmentation of the fuel, sorbents and bed material is handled with comminution model for each solid species. The model frame utilizes a uniform block mesh with typical mesh size in the order of 100 000 cells for commercial CFB units. A single processor desktop PC can be utilized in the simulations and with typical simulation times in the order of hours. The model frame is illustrated in Figure 12.

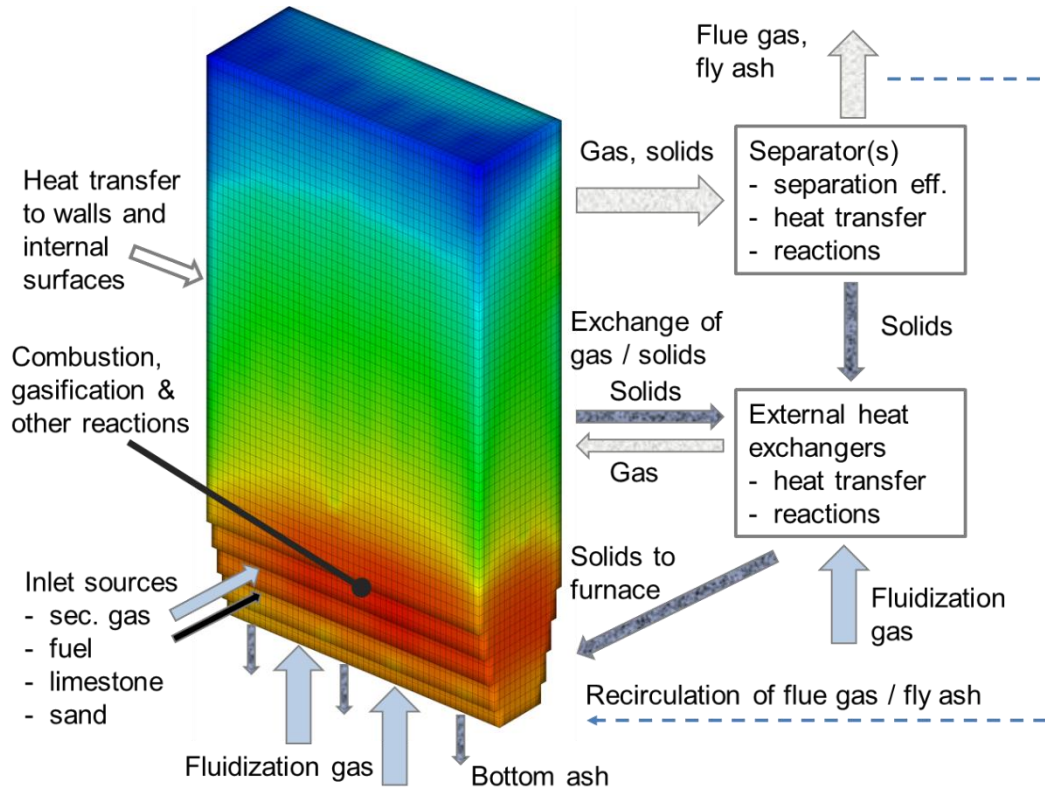


Figure 12. The model frame utilized in this work. The image courtesy of Kari Myöhänen.

3.2.2 Solids flow field

In the model frame, all solids material is divided into six size fractions. The solid species are ash, sorbent, make-up material, and fuel. The vertical concentration profile governing the solids concentration of all solids is based on the formulation by Johnsson & Leckner (1995). The total volume fraction of the bed material, fuel char and sorbents ε_s is fixed for each height H as a constant for the whole cross-section based on Equation 26 (Myöhänen, 2011).

$$\varepsilon_s(H) = (\varepsilon_{s,btm} - \varepsilon_{s,top} \exp(c_{dil} H_{tot})) \exp(-c_{trans} H) + \varepsilon_{s,top} \exp(c_{dil}(H_{tot} - H)) \quad (26)$$

where $\varepsilon_{s,btm}$ and $\varepsilon_{s,top}$ are solids concentrations at the bottom and top, respectively, H_{tot} the total furnace height, c_{dil} and c_{trans} are dilute and transition section decay constants, respectively. (Johnsson & Leckner, 1995; Myöhänen, 2011)

A wall layer is superimposed next to all vertical walls in the furnace. The wall layer exchanges solid material and energy with the furnace core and the walls, but the wall layer is currently not applied to gas or solid species (namely fuel or sorbent). This exchange enables the modeling of internal circulation by defining the exchange velocities between the dilute core and the dense wall layer. (Myöhänen, 2011)

The continuity and momentum equations for the solid material are presented in Equations 27 and 28. A potential flow approach is utilized for the solution of velocity and flow potential P_s , when the concentration of solids and the source term ϕ_s are solved based on a previously iterated solution or is fixed as inputs. The reaction source term R_s includes the effect of thermochemical reactions and phase change.

$$\oint_A \varepsilon_s \rho_s \mathbf{v}_s \cdot d\mathbf{A} = \int_V \phi_s dV + \int_V R_s dV \quad (27)$$

$$\varepsilon_s \rho_s \mathbf{v}_s = \nabla P_s \quad (28)$$

The continuity of the different solid material species are solved separately for each species but by utilizing the common momentum equation (28) and therefore the velocity profiles are uniform for each species.

3.2.3 Gas flow field

The continuity and momentum equations for the gas phase are presented in Equations 29 and 30.

$$\oint_A \varepsilon_g \rho_g \mathbf{v}_g \cdot d\mathbf{A} = \int_V \phi_g dV + \int_V R_g dV \quad (29)$$

$$\int_V \beta \varepsilon_s \rho_s (\mathbf{v}_g - \mathbf{v}_s) dV = - \int_V \varepsilon_s \nabla P dV \quad (30)$$

The momentum equation of the gas phase is simplified to consider only gas pressure (flow potential) P and equating it with the macroscopic drag of the solid phase, where β is the macroscopic drag coefficient between the gas and solid phases. Species conservation equation (31) is solved for each gas component i , where w is the weight fraction of species i within the phase. Thus, the gas flow is determined with the velocity from the total gas flow and Fick's law type of diffusion for each species.

$$\oint_A w_i \varepsilon_g \rho_g \mathbf{v}_g \cdot d\mathbf{A} - \oint_A \varepsilon_g \rho_g D_g \nabla w_i \cdot d\mathbf{A} = \int_V \phi_i dV + \int_V R_i dV \quad (31)$$

3.2.4 Flow of fuel

The fuel is divided into four components, which are treated separately inside the model frame: moisture, which evaporates to water vapor, volatiles, which are released as gaseous species in devolatilization, char, and inert ash, which is treated as the bed material. The releases and reactions of moisture, volatiles and char are handled with release and reaction models. The flow of evaporated moisture, devolatilized gaseous species and ash are governed by the momentum equations of total flow of gas and solids (Equations 30 and 28, respectively), while continuity equation is solved for each species and fraction separately. Equation 32 describes the continuity equation for fuel fraction i .

$$\oint_A \varepsilon_{fu,i} \rho_{fu,i} \mathbf{v}_{fu,i} \cdot d\mathbf{A} - \oint_A D_{fu,i} f_{0,i} \nabla \left(\frac{\varepsilon_{fu,i} \rho_{fu,i}}{f_{0,i}} \right) \cdot d\mathbf{A} = \int_V \phi_{fu,i} dV - \int_V \sum_{j,j \neq i} k_{fu,ij} \varepsilon_{fu,i} \rho_{fu,i} dV + \int_V \sum_{j,j \neq i} k_{fu,ji} \varepsilon_{fu,i} \rho_{fu,i} dV \quad (32)$$

where the variables are D_{fu} , the dispersion coefficient, ϕ_{fu} , the source term, and k_{fu} , the comminution coefficients from fraction i to j and vice versa. The terms from left to right are: convection and diffusion over computational cell faces, source term, and comminution to and from this fraction due to reactions, fragmentation and agglomeration. With the old fuel flow model, the velocity comes from the total solids velocity field (Equation 29), and the flow of each species is actually defined by the dispersion coefficient $D_{fu,i}$ and the target profile $f_{0,i}$ which follows the formulation of Equation 26. This means that the fuel tries to reach a predefined vertical average concentration with dispersion, which evens out the concentration differences by Fick's law.

In the new fuel flow model, a separate momentum equation for fuel is introduced and the term $f_{0,i}$ is given value 1 in the continuity equation (32), leading to Fick's law type of diffusion, negating any target profile functionality. The new momentum equation for the fuel fraction i is presented in Equation 33. The term on the left hand side is the inertia, with gravity, buoyancy, and drag force from gas and solids, respectively, on the right hand side of the equation. The solved fuel velocity is used in Equation 32 in the solution of the fuel continuity instead of the velocity of solved for other solid phases with Equation 28.

$$\oint_A \varepsilon_{fu,i} \rho_{fu,i} \mathbf{v}_{fu,i} \cdot d\mathbf{A} = \int_V \varepsilon_{fu,i} (\rho_{fu,i} - \rho_{susp}) \mathbf{g} dV + \int_V K_{g-fu} (\mathbf{v}_g - \mathbf{v}_{fu,i}) dV + \int_V K_{s-fu} (\mathbf{v}_s - \mathbf{v}_{fu,i}) dV \quad (33)$$

where the variables K_{g-fu} and K_{s-fu} are the momentum exchange coefficients between gas and fuel, and solids and fuel, and \mathbf{v}_g and \mathbf{v}_s , the gas and solids velocities, respectively. Buoyancy is considered with suspension density $\rho_{susp} = \varepsilon_g \rho_g + \varepsilon_s \rho_s$ to include the effect of both the gas and solid phases. For the drag force between the gas and fuel phases, the drag

force model of Huilin & Gidaspow (2003) presented in Table 4 was implemented in the first stage. For the solid-fuel drag force, the model of Syamlal et al. (1993) (presented in chapter 2.3.3.2) was adopted. The chosen models were taken from the literature, and the models consider the particles as perfect spheres. While this approach may not be well suited for biomass, it was selected here as both are common models in the literature. In the first stage, the model parameters have to be adjusted to make a correction for the non-spherical shape of the particles. In the second stage, this issue is treated with an experimental approach to determine the gas-fuel drag force, overcoming the need of making adjustment to the model.

The new solution of the fuel flow based on the momentum equation allows the furnace hydrodynamics (through their respective models) and fuel properties to determine the fuel concentration profiles, rather than relying on a predetermined target profile. The target profile formulation requires the highest concentrations to be at the grid level, while this may not be the case for very light and easily elutriated materials.

The mass, density, shape and size of the fuel particle can change in the furnace, due to thermochemical reactions. In the furnace model, the changing particle size of the reacting particles is considered with the comminution model. While currently the particle density remains constant in the model frame, additional models could be later implemented for the density change of the particles during reactions.

4 Characterization of gas-fuel drag force

Biomass fluidization was studied in laboratory facilities along with other materials to determine their fluidization characteristics. The effect of particle density, size and shape on fluidization was studied. The characteristic drag coefficient was computed from measurements and compared with the drag coefficient data published in the literature.

4.1 Characterization experiment

Fluidization characterization of materials was performed in order to investigate the average gas-particle drag force without having detailed information about the material properties. Experimental investigation was executed with a fluidization characterization test device, illustrated in Figure 13.

The device was operated with compressed air in ambient pressure and temperature, and it consisted of a glass tube riser to allow visual inspection of fluidization behavior, followed by a U-bend to the down comer. The total riser height was 2.3 m with an internal diameter of 0.11 m, and the device was capable of superficial air velocities between 0.3 and 10.5 m/s. The solid material sample was placed to the bottom of the riser above a fine mesh grid, and fluidized, and a part of the sample was elutriated from the riser. In the down comer, the pipe diameter was increased to lower the flow velocity, and a T-intersection was used to separate the elutriated sample from the air. The sample was collected in the collection vessel while air and the unseparated particles were led to a separator containing a bag filter. The flow rate in the test device was controlled with a mass flow controller, and the pressure drop over the riser was measured below the grid and before the U-bend. The temperature of the fluidizing air was measured before the grid to determine the correct fluidization air density.

Four dried samples of different materials were used in the tests: glass beads (silica), quartz sand, peat, and forest residue from South-Eastern Finland. The glass beads represented nearly spherical particles. The quartz sand represented a common make up material in CFB boilers. The two biomass samples were provided by a local power plant. The initial material PSD for the biomass samples was determined by sieving a part of the sample, for sand the PSD was provided by the supplier, and the mean diameter of glass beads was reported to be 250 μm by the manufacturer.

The densities of biomass samples were measured in fine powder, that of sand in water, and the density of the glass beads was provided by the supplier. Different particle sizes were utilized in the density measurements to achieve a more representative average value for the material. The average measured or provided density was used for the whole material, essentially assuming homogeneous density, while particle size may influence the material density, as reported by Miao et al. (2011).

The sand and biomass samples were fluidized for several minutes with steady superficial air velocity ranging from 1 to 5 m/s with 1 m/s increments, and for the forest residue an

additional velocity of 6 m/s was used to achieve enough elutriated material for the analysis. For the glass beads, velocities from 0.5 to 2.0 m/s with 0.5 m/s increments were used. The elutriated samples were collected, weighed to obtain the mass loss with each fluidization velocity, photographed and image analyzed.

In the presented approach several assumptions are made. Only the vertical drag force is considered between the gas and particles. No other forces than gravity, buoyancy and drag force are considered to affect in the system, as it is assumed that when fluidized, all particles will experience enough time in the dilute conditions to elutriate, the drag force-gravity-relations permitting, regardless of particle interaction or interparticle forces. As the gas velocity is increased incrementally, the exact elutriation velocity cannot be measured. Therefore an average of the fluidization velocities is used for the material elutriated between the fluidization velocity increments. The effect of the walls on the elutriation of the particles is considered negligible.

Static electricity caused some adhesion problems during the test runs, especially with sand, as small, charged particles made contact with the glass tube and would detach on their own later. The amount of material on the riser walls was small compared to the overall mass in the system, but the results showed that a small amount of fine quartz sand particles were present in the higher flow velocities, likely to have been detached from the walls (as seen in Figure 16).

The steady fluidized state was more difficult to achieve for biomass samples than for the more spherical and homogeneous sand and glass beads. The fluidization regimes varied during the biomass experiments due to the wide PSD; irregular shape and particle bridging made fluidization of particles difficult. This may have caused some of the smaller particles to elutriate at a higher fluidization velocity than they would in the absence of larger particles. It is difficult to estimate the amount of error caused by this, as the average particle sizes increased monotonically with the fluidization velocity. Figure 13 presents the cumulative mass loss of each sample with respect to fluidization velocity. Figure 14 presents a picture of the bulk of each of the tested material samples.

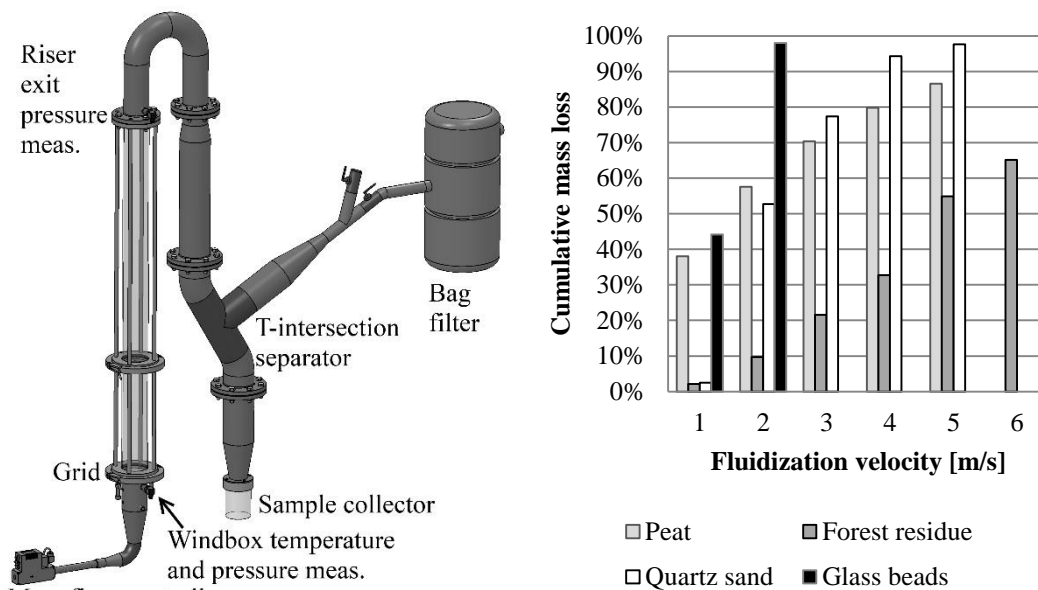


Figure 13. Fluidization device utilized in the characterization experiments, and cumulative mass loss of each sample with fluidization velocity.

4.2 Image analysis and results

Image analysis was performed for the elutriated samples to determine the size and shape distributions of the material. The particles were spread out and photographed at their presumed maximum projection surface area by using a system camera for large particles and a microscope for small particles. The glass beads and quartz sand particles were slightly transparent, but this did not interfere with the image analysis. A commercial software was used to detect and determine the particle shapes and sizes, although later several other shape factors were calculated from the measurement results due to the insufficient documentation by the software on shape determination. Insufficient documentation was also provided on details of the measurement process. From the image analysis, particle maximum, arithmetic mean and minimum dimensions were obtained, along with particle projection surface area and perimeter. More information on the image analysis procedure is presented by Korhonen (2012). The roundness by Pentland ($r_p = 4A_p\pi^{-1}d_{\max}^{-2}$) (Riley, 1941) was chosen as the shape factor for the analysis and data comparison. Although the particle thickness (the third dimension) was not measured, visual observations of the thickness were made.

Image analysis is sensitive to the total number of pixels in each particle, and the initial data suffered from a large scatter due to very small particles with too few pixels. For a more reliable shape analysis, detected particles with the projection surface area under 1 mm^2 for the system camera and under 0.01 mm^2 for the microscope photographs were excluded. This reduced the scatter dramatically.

Table 6 presents the image analysis results of elutriated samples fluidized with increasing velocities. Figure 15 offers an example of the particles elutriated with the fluidization velocity of 2 m/s, and Figure 16 illustrates the mean diameter-roundness relation between quartz sand and forest residue. It can be concluded from these results that the PSD of biomass is much wider than that of quartz sand and that the shape is very non-spherical. Both the shape and size portray large deviation with biomass within each velocity fraction, while less deviation is present for sand and the highly spherical glass beads. For the forest residue, roundness decreases with the mean particle diameter with exponential relation, supporting the findings of Guo et al. (2012). Contrary to this, the roundness of peat increases as the fluidization velocity increases, which is logical as more spherical particles have higher terminal velocity. More detailed results and analysis, including the image analysis of sieved samples, can be found in Publication I.

Table 6. Image analysis results of fluidized samples reported with standard deviations.

	Fluidization velocity [m/s]	Filtered average diameter [mm]						Roundness [-]	
		min	SD	mean	SD	max	SD	r	SD
Forest residue	1.0	1.405	0.702	2.518	1.310	2.858	1.460	0.378	0.192
	2.0	1.800	1.274	3.248	2.227	3.686	2.492	0.376	0.190
	3.0	5.793	5.312	11.768	10.111	13.191	11.154	0.273	0.180
	4.0	9.028	7.196	19.420	13.232	21.551	14.505	0.264	0.171
	5.0	11.695	9.545	24.911	19.996	27.799	22.116	0.288	0.187
	6.0	11.147	9.382	23.368	21.453	25.786	23.132	0.400	0.184
Peat	1.0	0.143	0.051	0.236	0.100	0.269	0.115	0.378	0.154
	2.0	1.787	0.925	2.852	1.761	3.249	1.972	0.483	0.181
	3.0	2.679	1.297	3.725	1.913	4.215	2.180	0.579	0.152
	4.0	3.943	2.333	5.291	3.145	5.916	3.501	0.616	0.163
	5.0	4.849	2.990	6.762	4.857	7.576	5.416	0.590	0.169
Quartz sand	1.0	0.140	0.026	0.181	0.033	0.202	0.039	0.639	0.107
	2.0	0.189	0.040	0.235	0.050	0.260	0.058	0.665	0.095
	3.0	0.459	0.102	0.573	0.135	0.633	0.158	0.672	0.103
	4.0	0.611	0.131	0.758	0.163	0.839	0.188	0.676	0.085
	5.0	0.384	0.289	0.478	0.355	0.530	0.395	0.664	0.098
Glass beads	1.0	0.204	0.026	0.211	0.026	0.216	0.028	0.926	0.021
	1.5	0.234	0.013	0.242	0.014	0.247	0.014	0.942	0.004
	2.0	0.242	0.017	0.250	0.017	0.256	0.017	0.926	0.024

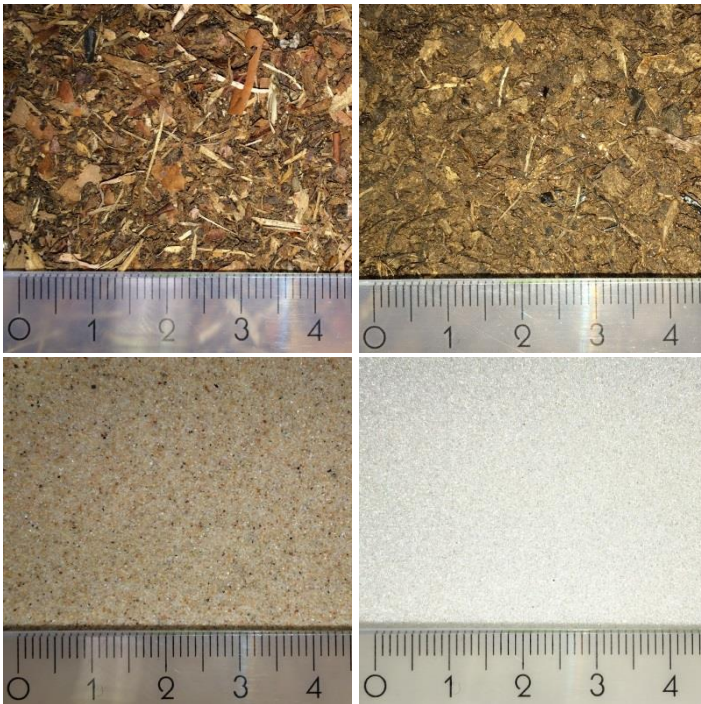


Figure 14. The characterized materials (from top left to bottom right): forest residue, peat, quartz sand and glass beads.

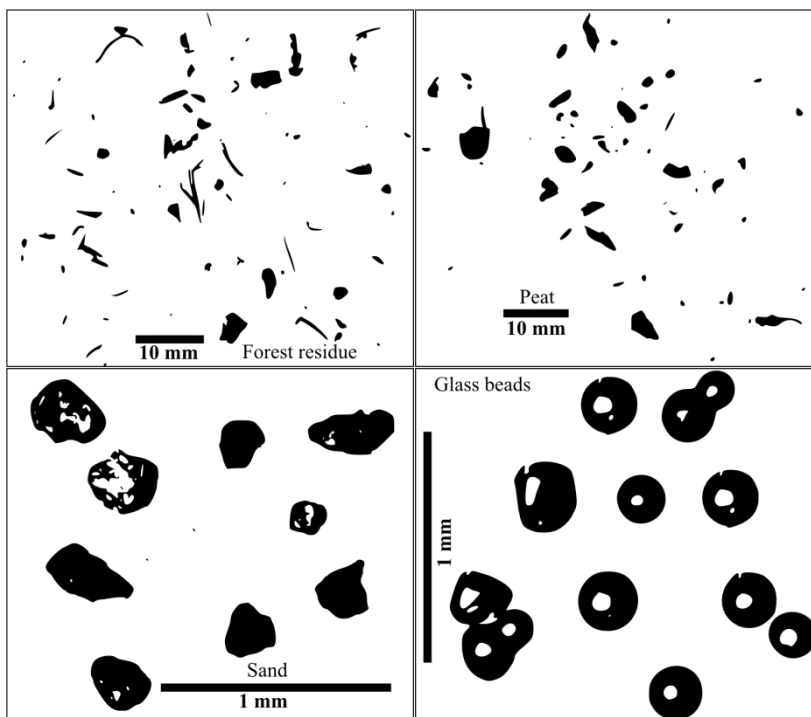


Figure 15. Samples of the image analysis pictures for each sample collected with the fluidization velocity of 2 m/s.

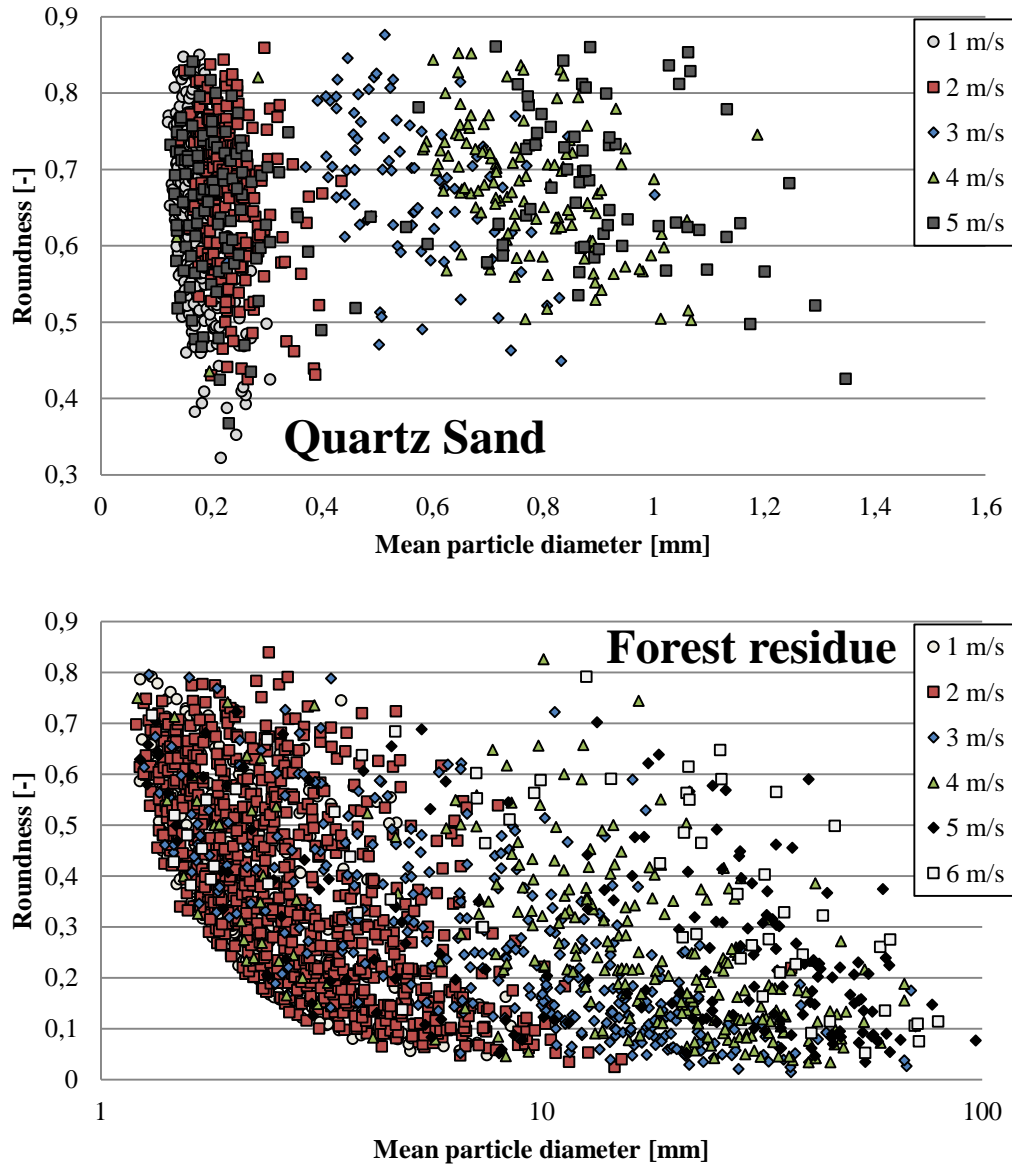


Figure 16. Mean particle diameter vs. roundness plots of quartz sand and forest residue.

4.3 Analysis of characterization results

Analysis of the experimental results was performed in order to determine the characteristic drag coefficient. It was assumed, that during an experiment given enough time for fluidization with steady gas velocity, all particles will experience enough time in dilute conditions to be free of the effect of other particles. In these conditions, all the particles of which terminal velocity is exceeded, are elutriated from the system due to a

drag force larger than the gravitational force of the particle. Material samples can be divided into velocity fractions based on their fluidization velocities in which they are elutriated. Similar but slightly different analysis of the characterization results is presented in Publication I, with the main difference that the buoyancy is included in to the force balance as presented below.

The force balance of a single particle presented in Equation 34 in a case of the gas flow velocity being the terminal velocity of the particle. A theoretical drag force on a single particle is presented in Equation 7. Additionally, a macroscopic drag force for a single particle or a group of particles is defined with Equation 36. Replacing the theoretical single particle drag force with the macroscopic drag force in the force balance and including the effect of gravity and buoyancy (Equation 35), the force balance can be expressed with Equation 37.

$$\mathbf{F}_D = \mathbf{G} - \mathbf{B} \quad (34)$$

$$\mathbf{G} - \mathbf{B} = (\rho_s - \rho_f) \mathbf{g} V \quad (35)$$

$$\mathbf{F}_D = \beta (\mathbf{v}_f - \mathbf{v}_s) V \quad (36)$$

$$\beta (\mathbf{v}_f - \mathbf{v}_s) = (\rho_s - \rho_f) \mathbf{g} \quad (37)$$

The velocity of the particle is zero when the gas velocity is the terminal velocity of the particle. This is the threshold which determines whether the particle will be elutriated, and it was used in the analysis of β . An average velocity was used in the analysis as the exact terminal velocity was not known. Due to the incremental fluidization velocity increase, several particles can be elutriated and therefore the method describes average elutriation behavior of a group of particles. Equation 38 was used to compute the velocity fractional average characteristic drag coefficient β from the experimental results.

$$\beta = \frac{(\rho_s - \rho_f) \mathbf{g}}{\bar{\mathbf{v}}_f} \quad (38)$$

For comparison with the traditional drag coefficient C_D , Equation 7 and 36 can be combined. The particle shape correction is included in the analysis as $d_p = r_p^{0.5} d_{\text{mean}}$ from the image analysis. The solved form of this combination is presented in Equation 39 and the comparison results are illustrated in Figure 17.

$$\beta = \frac{3}{4} \frac{\rho_f C_D}{d_p} (\mathbf{v}_f - \mathbf{v}_s) \quad (39)$$

The fractional average values of particle mean diameter and roundness (obtained with image analysis) density and characteristic drag coefficient are presented in Table 7. It can be seen in Figure 17 that good correspondence with the standard drag curves presented by Lapple & Shepherd (1940) was achieved with the spherical particles of glass beads and quartz sand. This supports the validity of the presented characterization approach.

The irregular non-spherical forest residue particles did not correspond with the data presented for spheres, cylinders or discs, which was to be expected for non-spherical particles. The good correspondence of peat with the drag curve of discs could be coincidental. Reasons for the mismatch are most likely due to inability to determinate the three-dimensional shape-size correctly with 2D image analysis. The 2D shape is good enough approximation for the 3D shape with highly spherical particles, but not with irregular non-spherical, as was pointed out by Cavarretta et al. (2009). Also the large deviation in the particle size and shape may have affected to the average fractional results obtained in the characterization experiments. Better agreement between the curves and data points could be achieved by utilizing the average minimum diameter from the image analysis. This indicates that the smallest (image analysis was performed on the maximum projection), not-measured third dimension has a significant effect on the drag force. To obtain accurate shape-size-information, three-dimensional shape should be determined. Based on the reasoning above and the results presented, it can be concluded that trying to predict the drag force for irregular shape particles with the literature correlations is quite difficult. In contrast, the characterization approach has a benefit of providing directly the characteristic drag force and also dividing a sample into different fractions based on their flow properties.

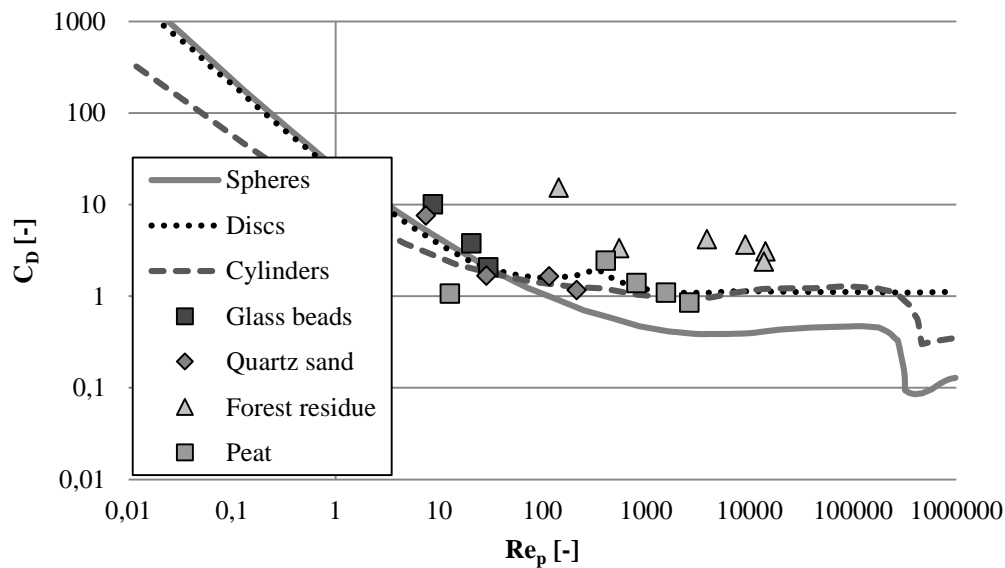


Figure 17. Comparison between standard drag curves by Lapple & Shepherd (1940) and the drag coefficient C_D computed from characterization test results with Equation 40.

Table 7. Fractional average properties of characterized materials.

		Glass beads			Forest residue					
<i>i</i>	1	2	3	1	2	3	4	5	6	
d_p	2.11E-04	2.42E-04	2.50E-04	2.52E-03	3.25E-03	1.18E-02	1.94E-02	2.49E-02	2.34E-02	
r_p	0.926	0.942	0.926	0.378	0.376	0.273	0.264	0.288	0.400	
ρ	2 730	2 730	2 730	510	510	510	510	510	510	
β	44 458	21 549	15 392	9 433	3 168	1 915	1 370	1 072	887	
		Quartz sand					Peat			
<i>i</i>	1	2	3	4	5	1	2	3	4	5
d_p	1.81E-04	2.35E-04	5.73E-04	7.58E-04	4.78E-04	2.36E-04	2.85E-03	3.73E-03	5.29E-03	6.76E-03
r_p	0.639	0.665	0.672	0.676	0.664	0.378	0.483	0.579	0.616	0.590
ρ	2 415	2 415	2 415	2 415	2 415	340	340	340	340	340
β	47 359	15 786	9 472	6 766	5 262	6 647	2 216	1 329	950	739

5 Drag force model development

This chapter describes the measures taken to develop the results of the characterization experiment into a drag force model and how to incorporate it with the new fuel flow model to be utilized in the existing three-dimensional model frame. To utilize the information derived from the characterization, the drag force in cold conditions was scaled to the hot conditions and to the presence of other particles. The developed drag force model was compared with models presented in literature.

5.1 Temperature scaling

A temperature scaling factor was developed to scale the results of the characterization experiment from the cold experimental condition to hot furnace conditions. The scaling factor, which was derived from the theory of the single particle drag force (Equation 7), considers the effect of varying gas density and viscosity with temperature and pressure. A widely used drag coefficient by Schiller & Naumann (1935) (Equation 40) was employed in the scaling, and it has an effect on the drag force only through the temperature scaling. Thus the temperature change has an effect through the gas density in Equation 7 and Reynolds number in drag coefficient in Equation 40. The approach also allows the gas composition to change from air to flue gas, for example.

$$C_D = \frac{24}{\text{Re}_p} \left(1 + 0.15 \text{Re}_p^{0.687} \right) \quad (40)$$

Glicksman (1984) presented scaling laws to maintain hydrodynamic similarity between different environmental conditions by changing the particle properties, such density and particle size. While this approach maintains the hydrodynamic similarity, it does not give information what happens to the drag force of a specific material when conditions change. Here, the focus is on determining how the particle drag force is affected by the changing environmental conditions. Unlike in the scaling of hydrodynamics similarity, here the particle properties are not modified but the drag force is scaled with changes in the gas properties (namely density and viscosity) when moving from the cold to hot conditions. This assumption is only limited to scaling of the characteristic drag force and is not considered for changes to particle properties caused by thermochemical reactions in the furnace.

By combining and simplifying the drag coefficient (Equation 40) and (Equation 7), the drag force of a single particle can be expressed with a single equation with respect to gas viscosity and density. The temperature scaling factor δ , which is defined as the ratio of the drag force in hot conditions to the drag force in cold conditions is presented in Equation 41. In Equation 41, two terms are found; viscous and inertial. Similar division of terms in fluidized bed pressure drop and drag force has been reported earlier by Ergun (1952) and Glicksman (1984), and based on the Reynolds number, the flow can be divided into viscous and inertia -dominated regions, as well as an intermediate region where both

terms play an important role in the drag force. Figure 18 illustrates the effect of temperature scaling on δ with respect to slip velocity, particle size, and Reynolds number.

$$\delta = \frac{\mathbf{F}_{D,h}}{\mathbf{F}_{D,c}} = \frac{3\mu_{g,h} + \frac{9}{20}(\rho_{g,h}d_p(\mathbf{v}_g - \mathbf{v}_s))^{0.687}\mu_{g,h}^{0.313}}{3\mu_{g,c} + \frac{9}{20}(\rho_{g,c}d_p(\mathbf{v}_g - \mathbf{v}_s))^{0.687}\mu_{g,c}^{0.313}} = \frac{\mu_{g,h}(1 + 0.15\text{Re}_h^{0.687})}{\mu_{g,c}(1 + 0.15\text{Re}_c^{0.687})} \quad (41)$$

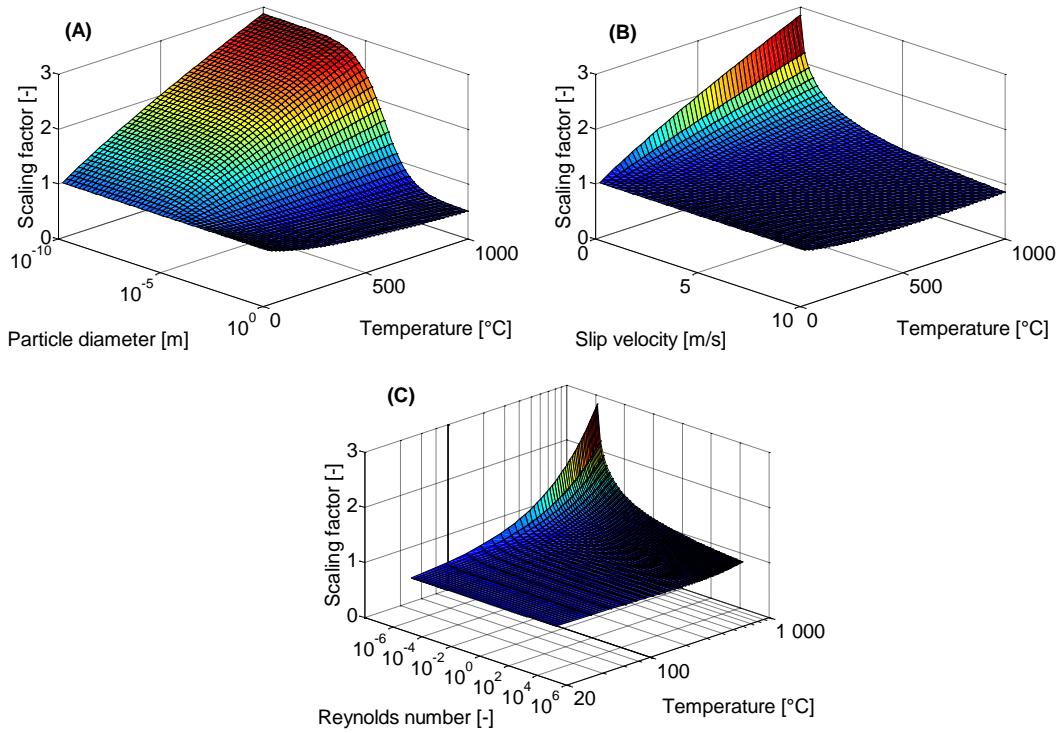


Figure 18. Temperature versus the scaling factor δ . (A) Constant slip velocity of 3 m/s on varying particle size. (B) Constant particle size of 300 μm with varying slip velocity. (C) Reynolds number varied between 10^{-6} and 10^6 . Temperature varied from 20°C to 1000°C in all cases.

It can be seen in Figure 18, that for viscous-dominant fine particles, the drag force in hot conditions is increased, while for inertia-dominated coarse particles, the drag force is reduced as the temperature increases. This result is supported by the findings reported by Yates (1996). The effect of slip velocity is high when the slip velocity (inertia) is low and the temperature high, while for higher (inertia) slip velocity values, the effect is minimal, regardless of the temperature.

5.2 Selection of the voidage function

As the characterization results were considered to apply for the drag force of a single particle \mathbf{F}_p in dilute conditions, there was a need to scale the drag force to multiparticle systems. A commonly used method to achieve this is by utilizing the so-called voidage function, where the drag force of a single particle is scaled with respect to the fluid volume

fraction. Of the several available models in the literature, the voidage function by Gidaspow & Ettehadieh (1983) was selected and applied, presented in Equation 42. This model is widely used in the literature and initially implemented to the fuel flow model. The selected voidage function produces a negligible effect between the Huilin-Gidaspow drag force model and characterization results presented in the following chapters.

$$\mathbf{F}_{mp} = \mathbf{F}_p \varepsilon_g^{-2.65} \quad (42)$$

The chosen voidage function assumes homogeneous fluidization, which is not true for most gas-solid fluidized beds and flow regimes due to bubbling and clustering. Nevertheless, this approach was chosen as a first stage model to expand the characterization results to conditions with multiple particles. While utilizing of a finer mesh could better support the assumption of local computational cells homogeneity, their utilization is not practical as discussed above. In later stages, the heterogeneous structures inside large computational cells could be considered with subgrid-scale models or EMMS approach, for example.

5.3 Empirical drag force model

The characterization test results were implemented in the fuel flow model as a new momentum exchange coefficient for the gas-fuel interaction. The scaling factor δ and voidage function were applied to the fractional characteristic drag coefficient β_i to form a new gas-fuel drag force model, presented in Equation 43 as momentum exchange coefficient.

$$K_{g-fu,i} = \varepsilon_g \varepsilon_{fu,i} \beta_i \delta_i \varepsilon_g^{-2.65} \quad (43)$$

Figure 19 presents a comparison of the momentum exchange coefficients between Equation 43, and the drag force models of Syamlal & O'Brien (1987) and Huilin & Gidaspow (2003) for fraction 3 of each characterized material. The average particle size and shape information was obtained from the results of the image analysis and utilized in the comparison. For highly spherical glass beads and roughly spherical quartz sand and peat, the correspondence between the models was very good, while for the highly irregular and non-spherical forest residue, larger differences in the momentum exchange coefficient could be seen, while the overall trend was similar due to the voidage function utilized. Similar results were observed in Figure 17, where the more spherical particles corresponded better with the data presented in the literature. Again, the reason lies in the inability to accurately determine and define the particle size and shape for three-dimensional, irregular, non-spherical particles with 2D image analysis.

Based on the discussion presented with Figure 17, it is concluded that due to the inability to reliably analyze the particle size for irregular non-spherical particles, the literature models produce inaccurate information about the gas-solids drag force. This can be seen in Figure 19 as poor correspondence between the literature models and the new drag force

model. The new model contains the information about the fluid and particle properties and is insensitive to their estimations. On the other hand, the new model information cannot be extended to general cases and the characterization has to be performed on every new material to be utilized.

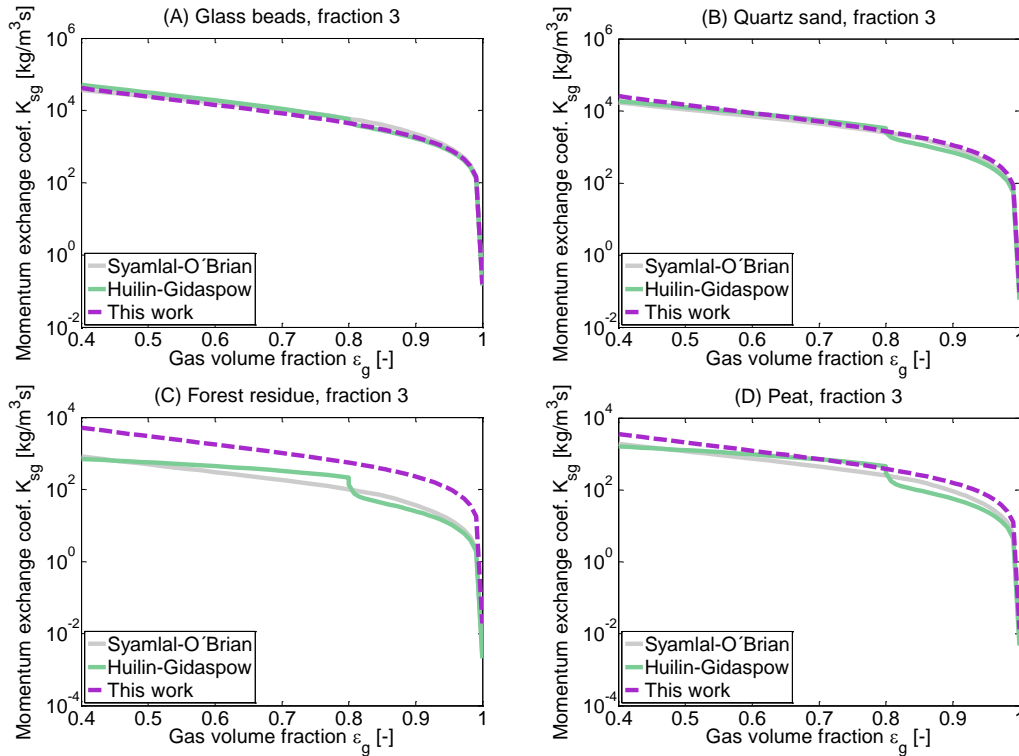


Figure 19. Comparison of the momentum exchange coefficient between the presented drag force model with the drag force models of Syamlal & O'Brien (1987) and Huilin & Gidaspow (2003) in corresponding systems of (A) Glass beads, (B) Quartz sand, (C) Forest residue, and (D) Peat. Fraction 3 is presented of each material and the temperature is 20°C in all cases.

6 Simulations of CFB furnaces

The fuel flow model was first tested by simulating a small test geometry, and the model sensitivity was analyzed for several parameters. After a qualitative validation of proper phenomenological behavior was obtained with the drag force models from the literature in a small scale, the fuel flow model was exploited in large-scale CFB furnace simulations. Later, the empirically derived gas-fuel drag force model was introduced and utilized in large-scale simulations and compared with measurement data.

6.1 Sensitivity analysis

Sensitivity analysis of the fuel flow model was performed in the first phase of model development on a small test geometry before utilizing the model in large-scale furnace analysis. The effect of mesh density, fuel feeding boundary conditions, namely inlet velocity and fuel particle size, and calculation parameters were investigated. The purpose of the sensitivity analysis was to study the behavior and validity of new fuel flow model and simulations utilized literature-based drag force models presented in chapter 2.3.3 by Huilin-Gidaspow for gas-fuel and Syamlal for bed material-fuel momentum exchange.

The effect of fuel inlet velocity as a boundary condition was found small when the magnitude of fuel velocity was varied between 0 and $\sqrt{20}$ m/s. As the fuel was fed to the bed in the lower furnace, the dampening effect of the momentum of the bed and gas flow caused the fuel to slow down rapidly towards the velocity fields of the bed and gas. It was found that the inlet boundary condition had little effect on the fuel behavior regardless of the particle size. The studies where the fuel particle size and fluidization velocity in the system were varied, portrayed a physically correct representation of the phenomena. The larger particles remained in the bed and required higher fluidization velocity for elutriation, while the fine fuel particles elutriated quickly even with low fluidization velocities.

Mesh sensitivity was studied with a simple geometry of 2 m by 2 m by 20 m presented on Figure 20 together with the inlets and outlet information. It was found that the effect of doubling or quadrupling the mesh density per axis (8 or 64 times more cells) did not change the fuel concentration (presented on Figure 21) or the reaction profiles in the semi-empirical approach significantly. Thus coarse meshes can be utilized for decreasing the computational costs with the typical cell sizes being in the order of 0.5 m per cell side.

Comparison of the previous, dispersive, and the new, convective, fuel flow models are presented in Figure 22 for all six fuel size fractions. As moisture and volatiles are released rapidly after the fuel feeding, the char profiles are used to illustrate the fuel flow. The previous model had the largest concentration of each char fraction at the grid level and the concentration was reduced with the height by the correlation relation of Johnsson & Leckner (1995) presented in Equation 26. For the new model, the highest concentration was found at the fuel inlet level and the profiles depended on the fuel particle size, the

finer particles ($d_p < 100 \mu\text{m}$) showing high concentrations in the upper furnace, while the larger particles remained in the bed at the bottom of the furnace. The results of the new model seem more physically valid than those of the previous model, especially considering the fine particles. The new model allows the formation of concentration profiles (in 3D) to form freely according to the fuel properties and the bed and gas phase flow fields, rather than being tied to fixed target profiles. More details and results of comparison between the old and new fuel flow models are presented in Publications II and III.

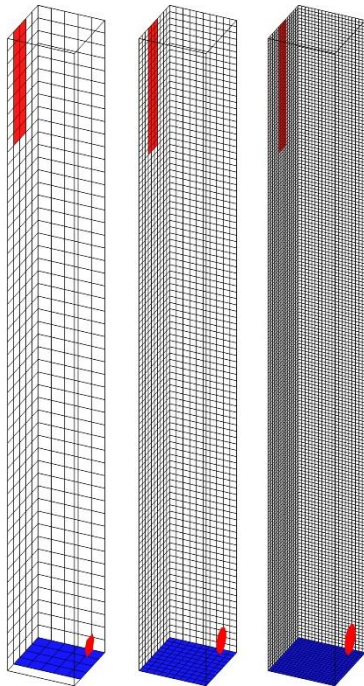


Figure 20. Meshes used in the small test geometry, coarse, medium and fine. The fluidization air inlet is highlighted at the bottom, the fuel inlet at the right hand side and the separator exit at the top left hand side.

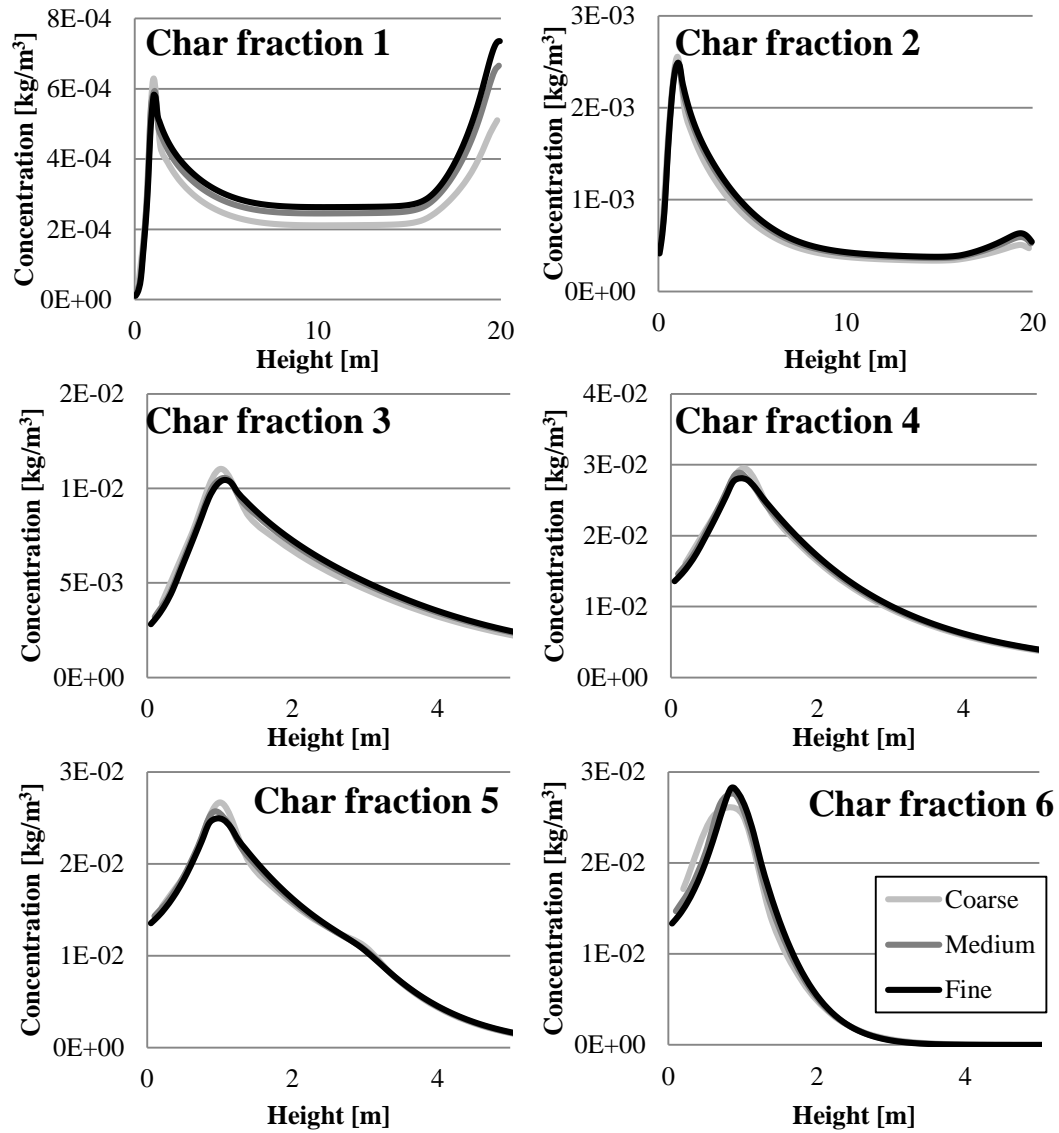


Figure 21. Effect of mesh size on char concentration profiles, fractions 1 to 6.

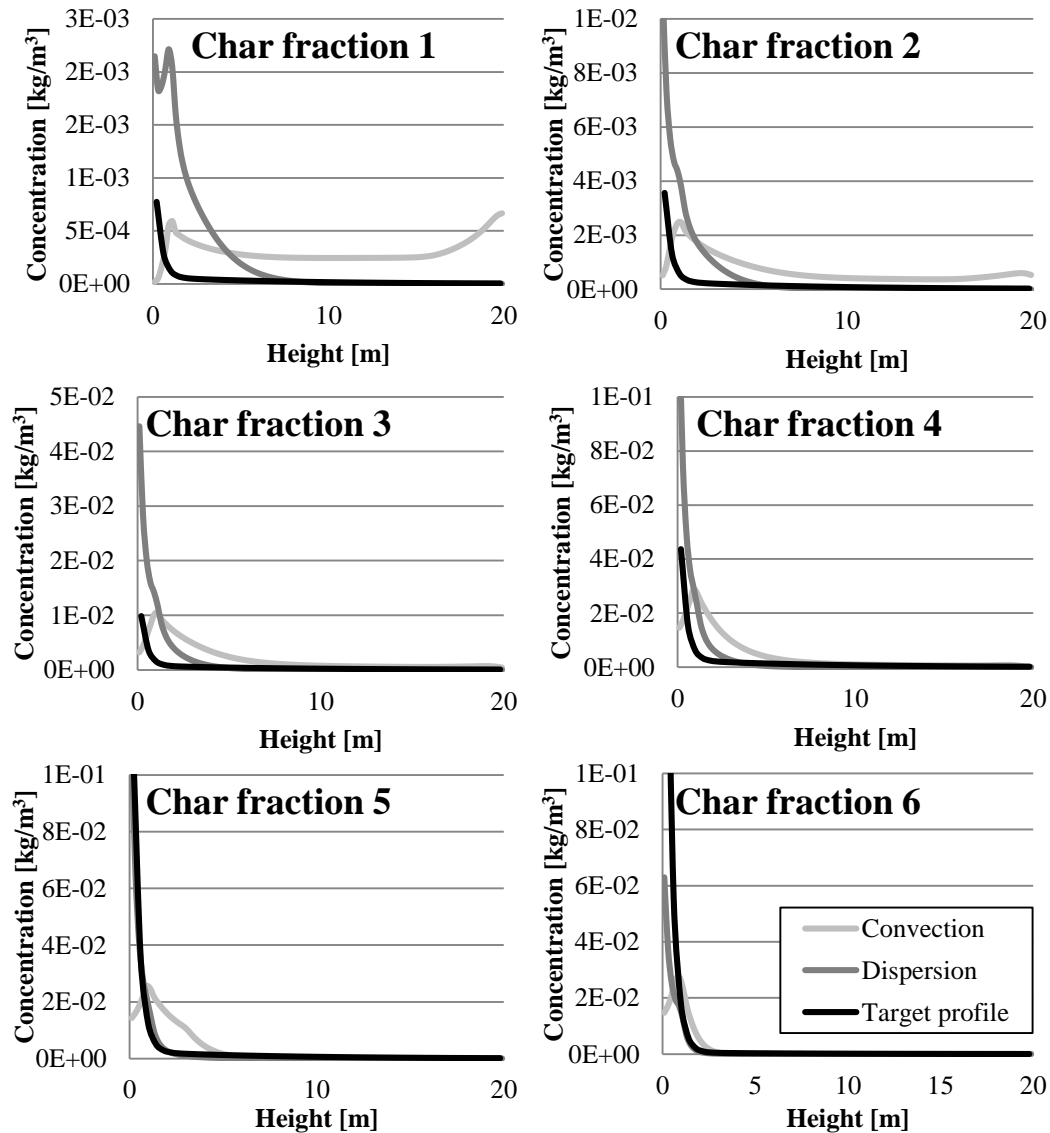


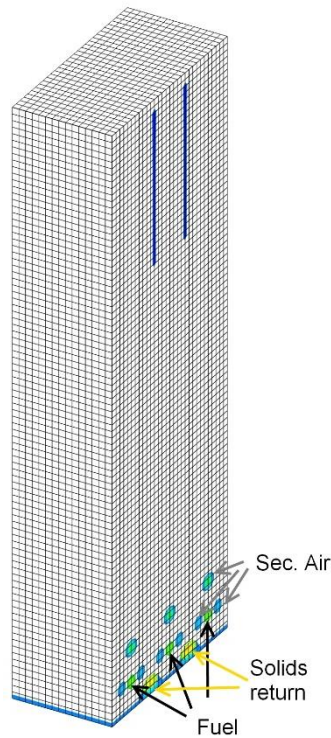
Figure 22. Comparison of the dispersive and convective approaches (previous and new model). The target profile is also illustrated, which dispersion is trying to reach, if the char is not combusted before reaching the target profile.

6.2 Large scale simulations

6.2.1 Test case

The performance of the fuel flow model was also tested in simulations of a large scale CFB furnace. These simulations utilized literature-based drag force models by Huilin-Gidaspow for gas-fuel and by Syamlal for bed material-fuel momentum exchange. A CFB furnace geometry was developed as presented in Figure 23, along with main dimensions and furnace details. The furnace was simulated with biomasses of the characterized

materials of peat and forest residue. The purpose of these simulations was to illustrate the effect of physical fuel properties (such as PSD and density) on the furnace profiles of temperature and gaseous species. That is why the chemical properties were set as identical between the biomasses. This changes the thermochemical properties of the biomass, while maintaining the flow properties. The fuel properties are presented in Table 8 and Table 9 for the test case.



Property	Unit	Value
Height	m	36
Width	m	12
Depth	m	6
Number of cells		40500
Thermal power	MW	170
Return loops		2
Bed mass	kg	106000
Fuel feeding	kg/s	20
Fuel feed points		3 + 3
Primary air	kg/s	50
Secondary air	kg/s	27

Figure 23. Large-scale imaginative CFB unit.

Figure 24 presents the concentration contours of char size fractions 1, 3 and 6 along with temperature and oxygen concentration. Due to the greater amount of fine particles and smaller density, the concentration of char fractions 1 and 3 are larger for peat on the upper furnace, leading to increased combustion and reactions there. This results in a colder bed region with larger oxygen concentrations found in the bottom of the furnace. While combustion of char contributes to the forming of temperature profiles, a stronger influence comes from combustion of volatile gases. The fuel properties determine where the volatile release occurs, and thus also contribute indirectly to the forming temperature field, as well as the profiles of gaseous species. The oxygen concentration profiles illustrate the effects of mixing and combustion. For peat, the low oxygen regions correlate well with the high concentration of fines in the upper furnace; the contours are nearly opposite. The forest residue has lower oxygen concentrations in the upper furnace, as more oxygen is consumed in the bed. In both cases, channels in which the fuel and oxygen flow separately can be detected. This indicates the importance of mixing; if the oxygen and fuel do not mix, no combustion occurs, leading to higher amounts of char and oxygen

in the upper furnace, possibly leading to combustion in the separator. More detailed results and analysis of the test case are presented in Publication III.

Table 8. Chemical properties of fuels in the test case. The proximate analysis information presented as received and the ultimate analysis of dry substance.

	Proximate analysis [%]				Ultimate analysis [%]					Other properties	
	Char	Volatiles	Moisture	Ash	C	H	N	S	O	HHV [MJ/kg]	ρ [kg/m ³]
Wood	10	39	50	1	52.92	6.15	0.39	0.02	40.52	21	500
Peat	10	39	50	1	52.92	6.15	0.39	0.02	40.52	21	300

Table 9. Particle size distribution of simulated fuels.

Fraction		1	2	3	4	5	6
Fuel particle size [μm]		32	94	153	340	1250	4000
Wood	Mass share	0.4 %	1.0 %	1.0 %	4.5 %	24.7 %	68.4 %
Peat	Mass share	2.9 %	3.7 %	14.6 %	26.3 %	21.9 %	30.6 %

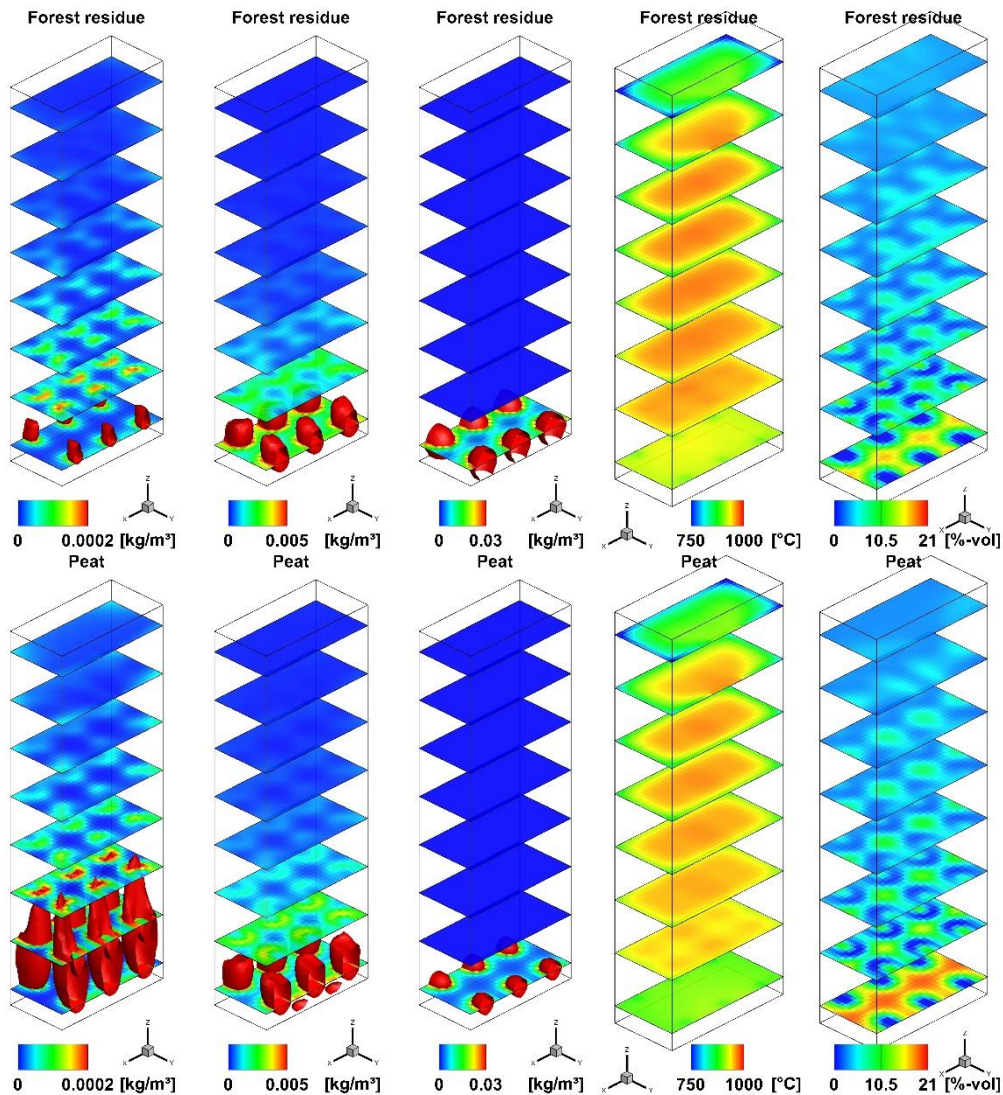


Figure 24. Test case results presenting a comparison between forest residue and peat. Data presented from left to right: the contours of char concentration for fractions 1, 3 and 6, temperature and oxygen concentration.

6.2.2 A large scale CFB unit

An operational CFB furnace firing biomass was simulated to validate the work presented above. The unit was commissioned in 2009 and fires wood-based fuel, such as bark, stumps, forest residue and industrial byproducts, and peat as a second fuel. The fuel duty of the furnace is 410 MW and it can produce 125, 152 and 110 MW of electricity, process and district heat, respectively.

Three load balances were simulated, 40, 75 and 100% of the furnace load capacity. Measurement information was obtained from the control and measurement system of the plant to determine the boundary conditions for the cases. Additionally, measurements

were taken from inside the furnace to obtain a vertical pressure profile and temperature distribution by probe measurements, which were used as validation data. The temperatures were measured at four height levels (5 m, 12 m, 20 m and 26 m) from the front wall corners and middle, and from both side walls. Two different probe lengths were used for 75% and 100% load cases.

Figure 25 presents the outline geometry of the furnace. A total of 8 fuel feeding locations are distributed on the front and rear walls, surrounded by secondary air nozzles. There are three separators, which are located on the rear wall and the material is returned to the lower furnace through external heat exchangers.

The fuel properties are presented in Table 10, and the particle size distribution in the feeding is presented in Table 11 and discussed below. Only wood fuel was used in the 40% and 75% load balance cases, while the 100% load balance was simulated with 75% of wood and 25% of peat of the total mass in the fuel feeding. The fuel inlet velocity on the feeding, given as a boundary condition of $[x,y,z]$ was $[0,1,-1]$ m/s on the front and $[0,-1,-1]$ m/s on the rear wall, and the fuel dispersion coefficients were 0.2 m/s^2 and 0.05 m/s^2 for lateral and axial directions, respectively, as presented in Publication III.

Three different cases were simulated for each load balance to compare the gas-fuel drag force models. In the first case, the Huilin-Gidaspow drag force model was applied (referred to as *H-G* in the following) with the exact fuel properties presented in Table 10. The second case applied the Huilin-Gidaspow model with reduced drag force-gravity-relation, which was obtained by increasing the fuel density to 1500 kg/m^3 . This case is below referred to as *tuned* model. In the third case, the Huilin-Gidaspow drag force model was replaced by the experimentally derived gas-fuel drag force model presented in this thesis, referred to as *new* or *this work*. The tuning of the Huilin-Gidaspow model was needed for the model to obtain good correspondence between the measured and modeled temperature profiles, which is discussed below. Tuning is required with holistic models, as many of the empirical model parameters for modeling hydrodynamics, reactions, mixing and heat transfer cannot be directly determined. (Lyytikäinen et al., 2014)

Table 10. Fuel properties. The proximate analysis information presented as received and the ultimate analysis of dry substance.

	Proximate analysis [%]				Ultimate analysis [%]					Other properties	
	Char	Volatiles	Moisture	Ash	C	H	N	S	O	HHV [MJ/kg]	ρ [kg/m ³]
Wood	9.3	33.9	55.0	1.8	53.8	6.4	0.6	0.1	39.1	20.96	510
Peat	15.3	36.2	46.4	2.0	57.0	6.0	1.9	0.2	34.9	22.26	340

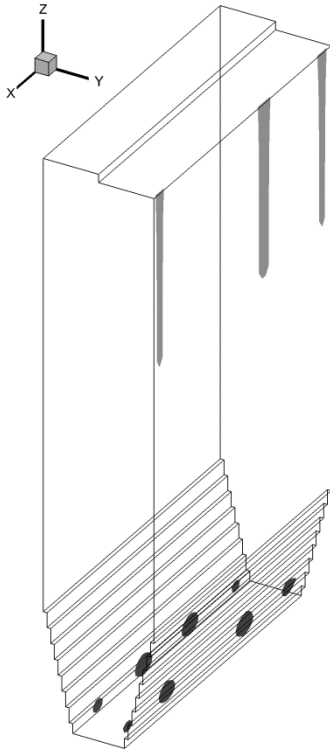


Figure 25. Simulated large-scale CFB furnace geometry. The fuel inlets are presented in the bottom furnace and the separator inlets in the upper furnace.

In the model frame, the fuel reaction model includes the particle size as a parameter. Similarly, the Huilin-Gidaspow drag force model contains the particle size, while with the new model, the characteristic drag coefficient is based on measurements in which the particles are divided into fractions by their flow properties (elutriation velocity) rather than the particle size. To be able to utilize the experimentally derived drag force model, the characteristic drag coefficient β was linked with the particle size in the modeling. Additionally, the particle size is a parameter in Equation 41 and needed in order to estimate the temperature scaling function δ value correctly. In the model frame the fuel PSD is given as an input based on the fuel sieving results and are grouped into default fractions of average particle sizes as presented in Table 9. With the characteristics model, the particle size distributions of characterized velocity fractions have been estimated by visual and image analysis and the original cumulative particle size distribution has been divided into six fractions according to particle sizes in each velocity fraction. As a result, flow of each fraction can be based on characterized drag coefficients with the new average fuel particle sizes presented in Table 11. As shown and discussed above, the literature drag force models are highly dependent on the correct particle size estimation, while the experimental drag force model was very insensitive to changes in the particle size. While it is impossible to achieve exact match between the characterization derived velocity fractions and the sieve-based size fractions, a satisfactory fit was obtained.

Table 11 presents the used fuel size fractions along with the share of fuel and the characteristic drag coefficient. Considering the coarser fuel, a better balanced distribution was achieved, describing the actual distribution more evenly, compared to the test case (Table 9). As mentioned, the fuel reaction models also depend on the particle size and therefore some adjustments to it had to be made. As the particles are non-spherical, the increase in size does not reduce the reactivity as much as it would be with spheres. However, the reaction models consider the particles as spheres, leading to significantly lower reactivity. The reaction models and equations are described by Myöhänen (2011) in greater detail. As the reactivity of the material was not studied in the scope of this work, the reactivity parameters were adjusted to correspond to the values with the particle size presented in Table 9. Reaction coefficients for evaporation, devolatilization and char combustion were 2500, 1000 and 500, and diameter exponents -1, -2 and -2, respectively.

Table 11. Fuel fractional particle size distribution with characteristic drag coefficients.

Fraction		1	2	3	4	5	6
Forest residue	Fuel particle size [mm]	0.215	0.375	0.75	1.5	3	4
	Mass share	1.6 %	3.3 %	4.8 %	6.8 %	8.5 %	75 %
	β [kg/m ³ s]	9433	3168	1915	1370	1072	887
Peat	Fuel particle size [mm]	0.188	0.375	0.75	1.5	3	4
	Mass share	24.5 %	13.4 %	16.1 %	14.1 %	14.8 %	17.0 %
	β [kg/m ³ s]	6647	6647	2216	1329	950	739

6.3 Model validation and discussion

Measurement data from within the simulated furnace and from the plant automation system were used as validation material for the simulation results for each load balance. As information on gaseous species or solids sampling measurements were not available, the fuel flow model was validated with temperature probe measurements. As the fuel flow determines where the reactions and release of energy and reaction products occur, the temperature data can be used as an indirect indicator of the fuel flow. This requires that all the other model parameters to be in the correct order of magnitude, and the comparison of simulated results and measurement data indicates a need for tuning the model parameters if the agreement is poor.

The results of 40%, 75% and 100% load cases are presented as temperature profiles with comparison to corresponding temperature probe measurements. The temperatures are presented with respect to a reference temperature T^* .

Only the tuned and new cases are presented in Figure 26 for the 40% load, as the Huilin-Gidaspow model would not converge due to strong elutriation of fuel. In this load point, the new and tuned models were in good agreement with each other and the temperature probe and average bed temperature measurements. This implies correct estimation of the fuel flow profiles in both cases. However, the new model managed to predict the average bed temperature more accurately, bearing in mind that the local temperatures in the bed deviate somewhat from the average value.

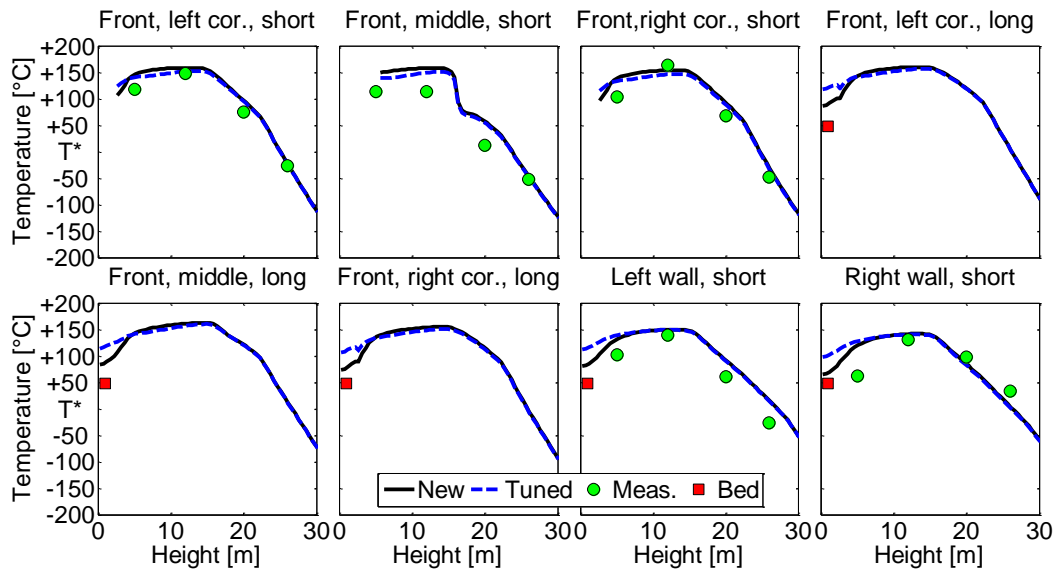


Figure 26. Comparison of measured and modeled temperature profiles at 40 % of the full load case. Wall, measurement location and probe length indicated above each figure.

Figure 27 presents a comparison of the 75% load for all the cases and measurements. The Huilin-Gidaspow model underestimated the temperature in the lower furnace in most cases, while the new and tuned models were in better agreement, similarly to the 40% load. Again, the new model without any tuning offered the best correspondence to the average bed and probe temperature measurements.

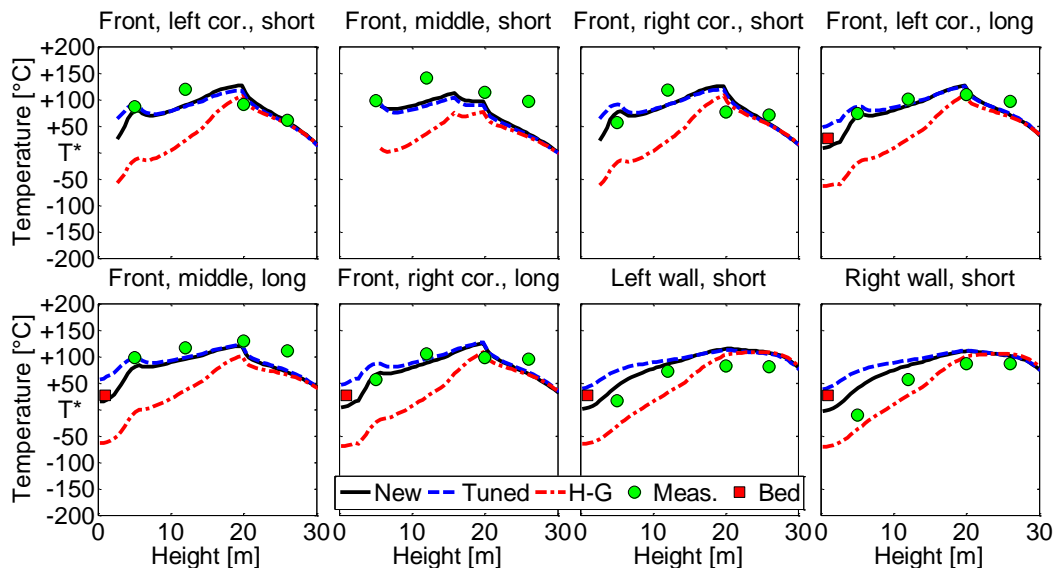


Figure 27. Comparison of measured and modeled temperature profiles of 75 % of the full load case.

For the 100% load case, peat was utilized as fuel along with forest residue, unlike with the 40% and 75% loads. This caused difficulties in the analysis as the effects of two different fuels had to be acknowledged. While good agreement was reached with the identical parameters in 40% and 75% loads between the tuned and new model, this was not the case with the 100% load. The reason for this was most likely related to the addition of peat, which has different reactivity due to chemical composition, different PSD and more spherical particle shape compared to the forest residue. As discussed above, the literature model is sensitive to the particle size, which could cause significantly different drag force for the peat than the new model. The difficulties were related to the fact that both the drag force and reactivity had an effect on the location of the reaction zones, leading to profiles of the gas species and temperature. Lower drag and higher reactivity both cause reactions to take place in the lower furnace, while a greater drag force and lower reactivity lead to reactions occurring higher in the furnace. Therefore, different combinations of the drag force model and reactivity parameters can lead to good correspondence with the measurements. The reactivity differences between the forest residue and peat would have to be studied in order to resolve the correct parameters in the modeling. Two different results could be presented for the 100% load, one with reaction parameters suitable for the tuned model and another for the new model, as is presented in Figure 28. The best agreement with measurements is found with the new model, while unlike with the previous load balances, the un-tuned Huilin-Gidaspow model offering better correspondence than the tuned one. This is likely due to the reaction parameters (in comparison to the drag force model parameter, density) used being better suited for the un-tuned case.

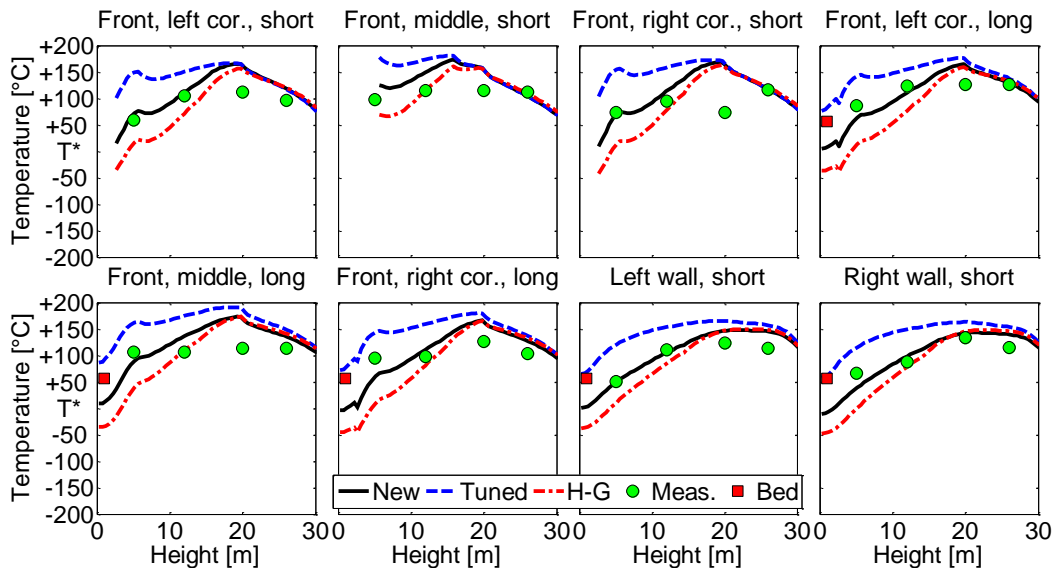


Figure 28. Comparison of measured and modeled temperature profiles of the full load case.

Figure 29 presents results of a sensitivity analysis of axial average temperature to the new drag force model for 75 % of the full load case. The characteristic drag coefficient values

were modified to correspond with -25%, -10%, +10% and +25% of the original values obtained from the analysis. The results indicate that the reduced drag force leads to increased temperature level in the furnace. This is due to lower char elutriation, leading to reactions occurring lower in the furnace. With lower drag force values, the amount of char in bottom ash is slightly increased compared to the original. The opposite is visible with the increased drag force, where more char is elutriated, reactions occur higher in the furnace, and amount of char entering the cyclone and in fly ash are increased. The high drag force profiles are similar to un-tuned Huilin-Gidaspow model results.

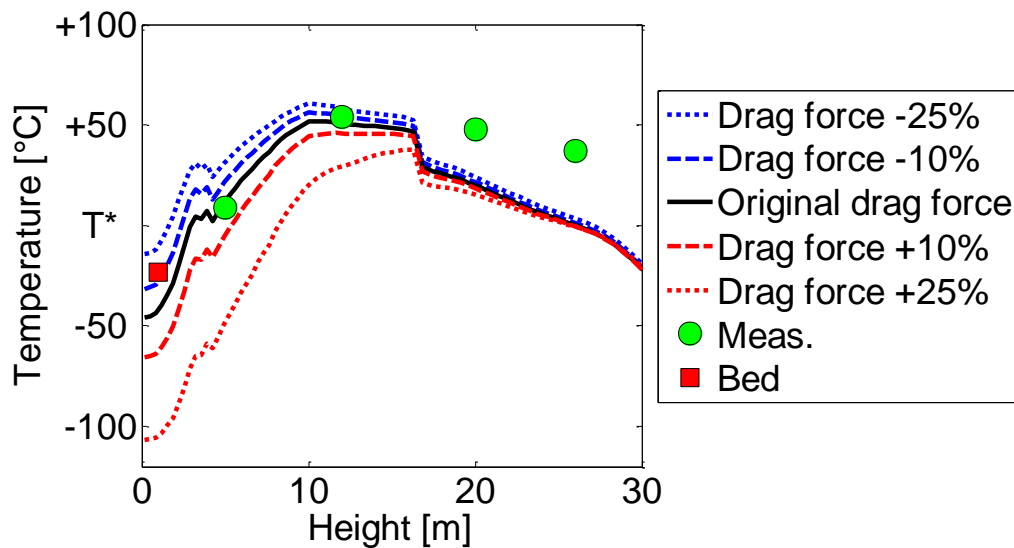


Figure 29. Sensitivity analysis of axial average temperature profile on the new drag force model with 75% load case.

Figure 30 presents a comparison of char velocity vectors and concentration contours between the three cases. The differences do not appear large due to the scale selected, but it can be seen that the concentrations of fraction 1 with the Huilin-Gidaspow model are higher in the upper furnace, while good agreement is found between the tuned and new models. For fraction 3, the reduced drag of the tuned model starts to produce lower char concentrations in the upper furnace, while higher concentrations are projected by the two other models. For fraction 6, the profiles are again similar, with slightly higher char concentrations higher with the new model. Due to the steady state flow solution and selected modeling methods in the model frame, the flow profiles of gas and solid material are rather one-dimensional, with the exception of the material inlets in the lower furnace and at the separator inlets. This leads to convective flow behavior affecting mostly in the vertical direction, and horizontal mixing being more controlled by Fick's law type of dispersion. The presented fuel flow behavior was to be expected, as the aim was to model time-average furnace performance rather than time-dependent fluctuations.

The effect of the bed material-fuel drag force was found to be small compared to the gas-fuel for the fine fuel fractions, while getting more comparable with the medium fractions and dominant for the coarse fractions. This is largely due to the utilized solids profile,

given as input based on the vertical pressure measurements from the furnace. The largest drag forces between the bed material and fuel were found at the largest concentrations of fuel and bed material, which are typically found below the fuel feeding points and close to the grid. As the bed material concentrations reduces as furnace height increases so does its drag force. The gas-fuel drag force is also reduced rapidly after the lower furnace, as the velocity of the fuel approaches to that of the gas.

Strong coupling between the concentration profiles of fuel and gas species, flow and mixing, reactions, temperature and heat transfer has to be acknowledged. Small changes in local fuel concentration may lead to large changes in the distribution of temperature and gaseous species in the furnace. Low char reactivity or poor mixing of the char with oxygen in the lower furnace causes reduced char combustion, leading to higher char and oxygen concentrations in the upper furnace. On the other hand, increased combustion in the lower furnace consumes more oxygen, leaving less of it available in the upper furnace.

As the fuel reaction rates are based on semi-empirical correlations, due to the above described coupling effects and the fact that the reactivity of the fuels was not investigated, the actual reactivity of the used fuels is unknown. Therefore in the model, the reactivity parameters of the fuel are open variables which were adjusted in minimization of the error between the modeled and measured temperature distributions. Thus the errors in the fuel flow modeling were compounded to the reaction models with the new drag force model. The reaction models assume fuel particles as spheres, while the above presented analysis of the utilized fuels clearly show that this is not true. The surface area to volume ratios of spherical and non-spherical particles are different, with non-spherical particle having more reactive surface. It is therefore reasonable to assume that adjustments are needed to achieve more realistic reaction behavior for irregular non-spherical biomass particles.

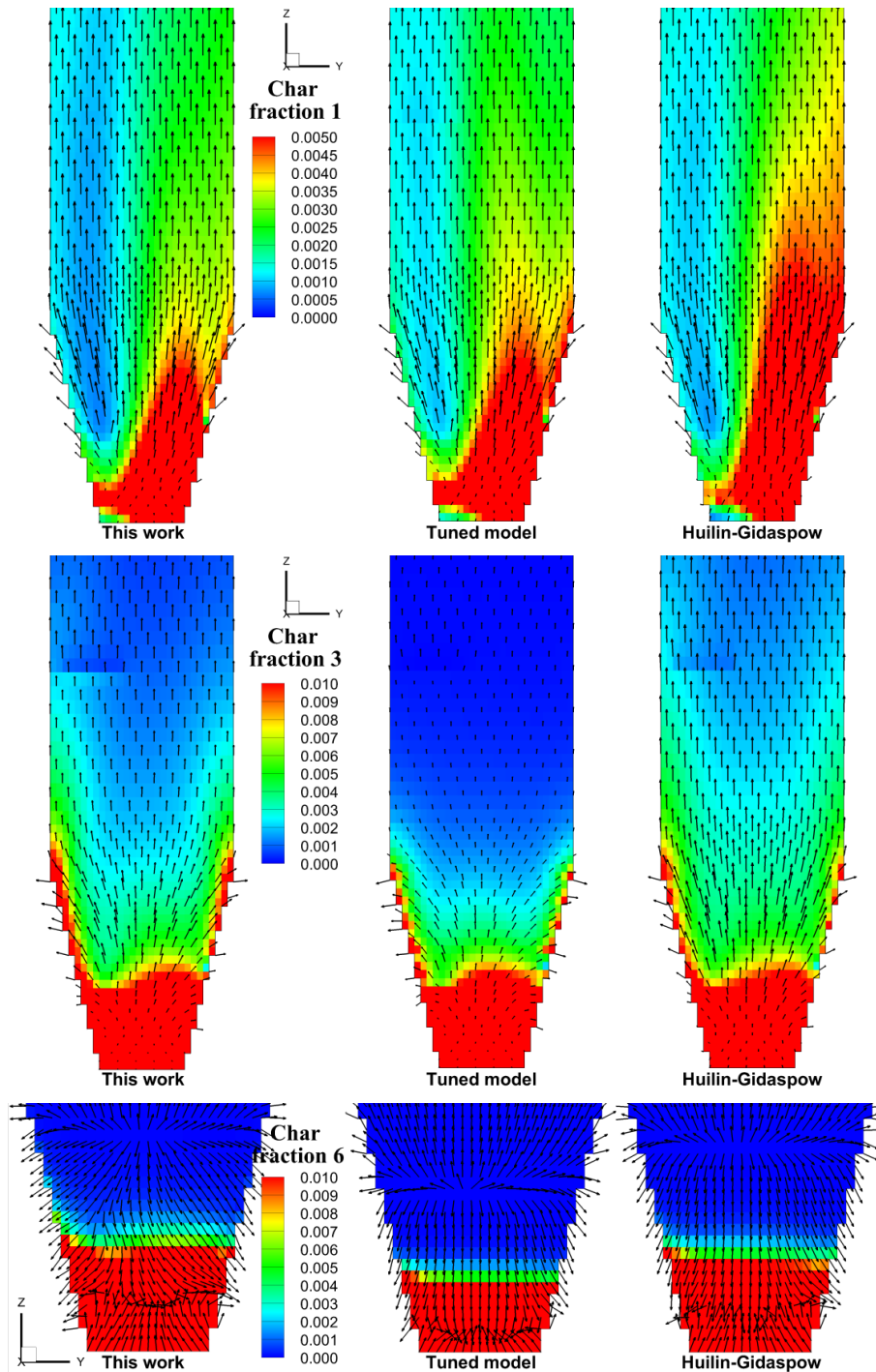


Figure 30. Concentration and velocity profiles of fuel char fractions 1, 3 and 6 for all the cases in the 75% load case. The velocity vectors of fraction 6 are magnified 8 times for better visualization of flow behavior. The concentration contours are chosen to illustrate the differences between the different cases.

As seen (and also illustrated in Publication IV), both the Huilin-Gidaspow and the new drag force models can achieve good results in the modeling of temperature distribution, which was here used as an indication of the solution quality of the fuel flow field. The difference between the models is in the level of adjustments or tuning required to be able to achieve the values measured from the actual furnace. The focus in this work was in the modeling of the fuel flow, which together with the reactions affect to all the quantity distributions in the furnace. With the new model, the gas-fuel characteristic drag coefficients were determined through measurements, leaving only the reactivity parameters open for adjustments to compensate for the larger particle size and irregular non-spherical shape in the reaction modeling. With the Huilin-Gidaspow model, in addition to the reactivity parameters, also the fuel properties related to the drag force are open for adjustments. The Huilin-Gidaspow model is typically utilized in CFD type of simulations, rather than with coarser grid semi-empirical models. Another issue is the sensitivity of the Huilin-Gidaspow model to representable size and shape information of particles, which is difficult to obtain for biomass. Therefore, it is not assumed that the Huilin-Gidaspow model could provide correct estimation of the drag force without any parameter adjustments. The drag force could be reduced in several ways to achieve good agreement with the measurement results, and in this work it was done by increasing the material density. Other options would be to modify the particle size or to add a correction factor to adjust for the particle shape or to reduce the drag force. All these options lead to either unphysical input values for the fuel or introduction of additional unknown variables which would have to be fitted to match the data. In general the modeling capability is mainly needed to analyze new furnaces or cases. For those cases, the model tuning is not possible and the significance and the contribution of the characterization method will be emphasized.

7 Conclusions

The design of new CFB furnaces is heavily affected by the fuel properties. The fuel flow determines where the thermochemical reactions take place in the furnace, affecting the temperature and gaseous species distributions, performance and efficiency of the whole boiler. Therefore, correct estimation of the fuel flow is critical in new designs and in the analysis of existing CFB furnaces. Three-dimensional modeling offers means to simulate the furnace process and fuel mixing, provided that it can consider the different fuels correctly in a reasonable timeframe. In practice, this is currently only possible with semi-empirical CFB furnace models, and the work presented in this study improves the accuracy of the flow simulations significantly.

The research in this thesis was a modeling study of the fuel flow inside large CFB furnaces with the focus on Finnish biomass fuels, with an addition of experimental investigation of the gas-solid drag force. The objective was to develop models for the fuel flow inside the CFB furnace, which acknowledge the physical properties of the fuel and the multiphase flow phenomena inside the furnace. The objective was reached, and the developed models were used successfully in the modeling of an existing large biomass-firing CFB furnace. The validity of the modeling approach was confirmed by comparing the modeling results with temperature measurement data.

One contribution of this work was the development of the new fuel flow model, where the fuel flow is solved on basis of the physical properties of the fuel and the multiphase flow phenomena inside the furnace. Compared to the previously used dispersive horizontal mixing and preset vertical concentration profiles in modeling, better results could be obtained with a momentum equation -based fuel flow model which consists of convective and dispersive flow mechanisms.

One of the major challenges in the modeling of multiphase flows is the correct estimation of interaction between the phases. This work considered a system of one gas phase and two solid phases, i.e. bed material and fuel, focusing on the momentum exchange between the phases. While the literature offers drag force models, they are generally applied in Eulerian CFD and their applicability to semi-empirical modeling is questionable. In this work, it was found that the literature models can be utilized for gas-fuel and bed material-fuel drag force modeling. While the results indicate the suitability of the used gas-fuel drag force model, data analysis in comparison with measurement data suggests that the model parameters need to be adjusted to validate the simulation results.

In the estimation of the momentum exchange between gas and fuel, the shape and size distributions of the fuel cause difficulties. Biomasses have inherently large distributions in both, thus the estimation of the drag force is limited by the correct definition of particle size and shape. In this work, information on the drag force relations of biomass and air was obtained through laboratory measurements. Instead of determining the traditional single particle drag coefficients, average characteristic drag coefficients were determined. When compared to the traditional drag coefficients, good agreement was achieved with

spherical materials, supporting the validity of the method. The main benefit of this approach was that the properties of gas and biomass particles were included in the measurement results, thus omitting their separate consideration and making the developed model insensitive to accurate determination of the physical properties of the particles. These features make the method suitable for analysis of irregular non-spherical material, such as biomass. These results were developed into a drag force model by considering the scaling from the cold experimental conditions to the hot furnace conditions. A theoretical approach was applied and found to produce comparable results with findings reported in the literature. The overall effect of the temperature scaling was small, compared to other factors. A voidage function was applied to consider the effect of packing. Other voidage functions could be utilized in the future if it could be justified that they would produce a better physical description between the packing and drag force. When the derived drag force model was applied, the results obtained showed very good correspondence with the measurement results, and unlike the used literature model, required little parameter adjustments. The adjustable parameters were related to fuel reactivity, instead of the actual drag force model.

In the future, it is recommended that more fuels are characterized and corresponding balances simulated to test and confirm the presented characterization-based drag force model approach for other fuels. The effect of other voidage functions could be studied, focusing on the non-homogeneous models. The bed material-fuel drag force was considered with a literature model and was not studied in detail. Further studies could also focus on studying the interaction between the fuel and the bed material in the lower furnace. Additionally, it is recommended that the characterization of biomass reactions and combustion is studied to develop reaction models to improve the current reaction models to apply better to non-spherical materials, and thus to require less adjustment. For better analysis and validation, also the gaseous species should be measured from the furnace to provide further information on the role of the thermochemical reactions and to help to distinguish the reactivity and drag force effects from each other.

References

- Adamczyk, W. P., Bialecki, R. A., Klimanek, A., Kozołub, P., Węcel, G., & Klajny, M. (2013). Modeling particle transport phenomena in large scale CFB boiler. In: Sahkestad, B. A., ed., *The 38th International Technical Conference on Clean Coal & Fuel Systems*, 2nd-6th June 2013. Clearwater, USA: Coal Technologies Associates.
- Adamczyk, W. P., Klimanek, A., Bialecki, R. A., Węcel, G., Kozołub, P., & Czakiert, T. (2014a). Comparison of the standard Euler–Euler and hybrid Euler–Lagrange approaches for modeling particle transport in a pilot-scale circulating fluidized bed. *Particuology*, *15*, pp. 129-137.
- Adamczyk, W. P., Węcel, G., Klajny, M., Kozołub, P., Klimanek, A., & Bialecki, R. A. (2014b). Modeling of particle transport and combustion phenomena in a large-scale circulating fluidized bed boiler using a hybrid Euler–Lagrange approach. *Particuology*, *16*, pp. 29-40.
- Alakangas, E., Hillring, B., & Nikolaisen, L. S. (2002). Trade of solid biofuels, and fuel prices in Europe. *12th European Conference and Technology Exhibition on Biomass for Energy, Industry and Climate Protection*, 17th-21st June 2002. Amsterdam.
- Alakangas, E. (2005). *Properties of wood fuels used in Finland - BIOSOUTH - project*. Jyväskylä: VTT processes.
- Alletto, M., & Breuer, M. (2012). One-way, two-way and four-way coupled LES predictions of a particle-laden turbulent flow at high mass loading downstream of a confined bluff body. *International Journal of Multiphase Flow*, *45*, pp. 70-90.
- Arsenijevic, Z. L., Grbavcic, Z. B., Garic-Grulovic, R. V., & Zdanski, F. K. (1999). Determination of non-spherical particle terminal velocity using particulate expansion data. *Powder Technology*, *103*, pp. 265-273.
- Bagheri, G. H., Bonadonna, C., Manzella, I., & Vonlanthen, P. (2015). On the characterization of size and shape of irregular particles. *Powder Technology*, *270, Part A*, pp. 141-153.
- Basu, P. (2006). *Combustion and gasification in fluidized beds*. Boca Raton: CRC/Taylor & Francis. ISBN: 0-8493-3396-2.
- Bell, R. A. (2000). *Numerical modelling of multi-particle flows in bubbling gas-solid fluidised beds*. Ph.D. thesis, Swinburne University of Technology.
- Bordbar, M. H., Myöhänen, K., & Hyppänen, T. (2015). Coupling of a radiative heat transfer model and a three-dimensional combustion model for a circulating fluidized bed furnace. *Applied Thermal Engineering*, *76*, pp. 344-356.

- Brown, R. C. (Ed.). (2011). *Thermochemical processing of biomass: Conversion into fuels, chemicals and power*. United Kingdom: John Wiley and sons.
- Bruni, G., Solimene, R., Marzocchella, A., Salatino, P., Yates, J.G., Lettieri, P., & Fiorentino, M. 2002. Self-segregation of high-volatile fuel particles during devolatilization in a fluidized bed reactor. *Powder Technology*, 128, 11-21.
- Campbell, J. E., Lobell, D. B., & Field, C. B. (2009). Greater transportation energy and GHG offsets from bioelectricity than ethanol. *Science*, 324, pp. 1055-1057.
- Cavarretta, I., O'Sullivan, C., & Coop, M. R. (2009). Applying 2D shape analysis techniques to granular materials with 3D particle geometries. In: Nakagawa, M., Luding, S., (eds), *Powders and Grains 2009: Proceedings of the 6th International Conference on Micromechanics of Granular Media, AIP Conference Proceedings 1145*, pp. 833-836. 13th–17th July 2009, Golden (Colorado).
- Chen, W., Peng, J., & Bi, X. T. (2015). A state-of-the-art review of biomass torrefaction, densification and applications. *Renewable and Sustainable Energy Reviews*, 44, pp. 847-866.
- Crowe, C., & Michaelides, E. E. (2006). Basic concepts and definitions. In: Crowe, C., ed., *Multiphase flow handbook*. CRC Press. ISBN: 978-1-4200-4047-0.
- Cui, H., & Chaouki, J. (2004a). Effects of temperature on local two-phase flow structure in bubbling and turbulent fluidized beds of FCC particles. *Chemical Engineering Science*, 59, pp. 3413-3422.
- Cui, H., & Chaouki, J. (2004b). Interparticle forces in high temperature fluidization of Geldart a particles. *China Particuology*, 2, pp. 113-118.
- Cui, H., & Grace, J. R. (2007). Fluidization of biomass particles: A review of experimental multiphase flow aspects. *Chemical Engineering Science*, 62, pp. 45-55.
- Dai, J., Cui, H., & Grace, J. R. (2012). Biomass feeding for thermochemical reactors. *Progress in Energy and Combustion Science*, 38, pp. 716-736.
- DallaValle, J. M. (1948). *Micromeritics, the technology of fine particles* (2nd ed.). New York: Pitman Publishing Corporation.
- DallaValle, J. M., & Klemin, A. (1943). *Micromeritics, the technology of fine particles* (1st ed.). New York: Pitman Publishing Corporation.
- Doroodchi, E., Zulfiqar, H., & Moghtaderi, B. (2013). A combined experimental and theoretical study on laboratory-scale comminution of coal and biomass blends. *Powder Technology*, 235, pp. 412-421.

- Ergun, S. (1952). Fluid flow through packed columns. *Chemical Engineering Progress*, 48, pp. 89-94.
- European Commission. (2005). *Communication from the commission of 7th December 2005 – biomass action plan*. Brussels: European Commission.
- European Commission. (2008). *Communication from the commission to the European parliament, the council, the European economic and social committee and the committee of the regions - 20 20 by 2020 - Europe's climate change opportunity*. Brussels: European Commission.
- European Commission. (2014). *2030 climate and energy goals for a competitive, secure and low-carbon EU economy*. Brussels: European Commission.
- Farzaneh, M., Sasic, S., Almstedt, A., Johnsson, F., & Pallarès, D. (2013). A study of fuel particle movement in fluidized beds. *Industrial and Engineering Chemistry Research*, 52, pp. 5791-5805.
- Finnish Energy Industry. (2014a). *Energy year 2013 - district heat*. Helsinki: Finnish Energy Industry.
- Finnish Energy Industry. (2014b). *Energy year 2013 - electricity*. Helsinki: Finnish Energy Industry.
- Garcia-Gutierrez, L. M., Soria-Verdugo, A., & Ruiz-Rivas, U. (2015). Optimization of the feeding ports location in a fluidized bed combustor based on Monte Carlo simulations of fuel particles motion. *Fuel*, 141, pp. 82-92.
- Garside, J., & Al-Dibouni, M. R. (1977). Velocity-voidage relationships for fluidization and sedimentation in solid-liquid systems. *Industrial & Engineering Chemistry Process Design and Development*, 16, pp. 206-214.
- Geldart, D. (1973). Types of gas fluidization. *Powder Technology*, 7, pp. 285-292.
- Gibilaro, L. G., Di Felice, R., Waldram, S. P., & Foscolo, P. U. (1985). Generalized friction factor and drag coefficient correlations for fluid-particle interactions. *Chemical Engineering Science*, 40, pp. 1817-1823.
- Gidaspow, D., Bezburuah, R., & Ding, J. (1991). Hydrodynamics of circulating fluidized beds: Kinetic theory approach. *7th International Conference on Fluidization*. 3rd-8th May 1992, Gold Coast (Australia).
- Gidaspow, D., & Ettehadieh, B. (1983). Fluidization in two-dimensional beds with a jet. 2. hydrodynamic modeling. *Industrial & Engineering Chemistry Fundamentals*, 22, pp. 193-201.

- Glicksman, L. R. (1984). Scaling relationships for fluidized beds. *Chemical Engineering Science*, 39, pp. 1373-1379.
- Green, D. W., & Perry, R. H. (Eds.). (1997). *Perry's chemical engineers' handbook* (7th ed.). USA: McGraw-Hill.
- Gudmundsson, S. (2014). Chapter 15 - aircraft drag analysis. In: Gudmundsson, S., ed., *General aviation aircraft design*. pp. 661-760. Boston: Butterworth-Heinemann. ISBN: 9780123973085.
- Guo, Q., Chen, X., & Liu, H. (2012). Experimental research on shape and size distribution of biomass particle. *Fuel*, 94, pp. 551-555.
- Guo, Z., Chen, X., Liu, H., Guo, Q., Guo, X., & Lu, H. (2014). Theoretical and experimental investigation on angle of repose of biomass-coal blends. *Fuel*, 116, pp. 131-139.
- Hartge, E., Ratschow, L., Wischniewski, R., & Werther, J. (2009). CFD-simulation of a circulating fluidized bed riser. *Particuology*, 7, pp. 283-296.
- Hill, R. J., Koch, D. L., & Ladd, A. J. C. (2001a). The first effects of fluid inertia on flows in ordered and random arrays of spheres. *Journal of Fluid Mechanics*, 448, pp. 213-241.
- Hill, R. J., Koch, D. L., & Ladd, A. J. C. (2001b). Moderate-Reynolds-number flows in ordered and random arrays of spheres. *Journal of Fluid Mechanics*, 448, pp. 243-278.
- Huilin, L., & Gidaspow, D. (2003). Hydrodynamics of binary fluidization in a riser: CFD simulation using two granular temperatures. *Chemical Engineering Science*, 58, pp. 3777-3792.
- Hyppänen, T., Lee, Y. Y., & Rainio, A. (1991). A three-dimensional model for circulating fluidized bed boilers. In: Anthony, E. J., ed., *Proceedings of the 11th International Conference on Fluidized Bed Combustion*, New York: ASME.
- Ishii, M., & Hibiki, T. (2006). *Thermo-fluid dynamics of two-phase flow*. USA: Springer Science+Business Media Inc.
- Jalali, P., & Hyppänen, T. (2010). Verification of continuum models for solids momentum transfer by means of discrete element method. *Industrial & Engineering Chemistry Research*, 49, pp. 5270-5278.
- Jalali, P., Nikku, M., & Hyppänen, T. (2013). Particle-cloud drag force in dilute particle systems: Discrete element method versus Eulerian simulations. *Industrial & Engineering Chemistry Research*, 52, pp. 4342-4350.

- Jääntti, T., Nuortimo, K., Ruuskanen, M., & Kalenius, J. (2012). Samcheok green power 4 x 550 MWe supercritical circulating fluidized bed steam generators in South Korea. *PowerGen Europe*, July 12th-14th 2012. Cologne, Germany.
- Jiliang, M., Xiaoping, C., & Daoyin, L. (2013). Minimum fluidization velocity of particles with wide size distribution at high temperatures. *Powder Technology*, 235, pp. 271-278.
- Johnsson, F., & Leckner, B. (1995). Vertical distribution of solids in a CFB-furnace. *The 13th International Conference on Fluidized Bed Combustion*. 7th-10th May 1995. Orlando, FL, USA.
- Khan, A. A., de Jong, W., Jansens, P. J., & Spliethoff, H. (2009). Biomass combustion in fluidized bed boilers: Potential problems and remedies. *Fuel Processing Technology*, 90, pp. 21-50.
- Knoebig, T., Luecke, K., & Werther, J. (1999). Mixing and reaction in the circulating fluidized bed – A three-dimensional combustor model. *Chemical Engineering Science*, 54, pp. 2151-2160.
- Koornneef, J., Junginger, M., & Faaij, A. (2007). Development of fluidized bed combustion—An overview of trends, performance and cost. *Progress in Energy and Combustion Science*, 33, pp. 19-55.
- Korhonen, H. (2012). *Characterization of fluidization properties of biomass*. Master's thesis, Lappeenranta University of Technology.
- Koski, M., Ritvanen, J., Myöhänen, K., Hyppänen, T., Palonen, J., Häkkinen, K., & Kokki, S. (2011). Three-dimensional modelling study of a circulating fluidized bed gasifier. In: Hofbauer, H., Fuchs, M., ed., *International Conference on Polygeneration Strategies 11 (ICPS 11)*, 30th August -1st September 2011. Vienna.
- Kraxner, F., Yang, J., & Yamagata, Y. (2009). Attitudes towards forest, biomass and certification – A case study approach to integrate public opinion in Japan. *Bioresource Technology*, 100, pp. 4058-4061.
- Kunii, D., & Levenspiel, O. (1991). *Fluidization engineering* (2nd ed.). Boston (Mass.): Butterworth-Heinemann. ISBN: 0-409-90233-0.
- La Nauze, R. D. (1987). A review of the fluidized bed combustion of biomass. *Journal of the Institute of Energy*, 60, pp. 66-76.
- Lapple, C. E., & Shepherd, C. B. (1940). Calculation of particle trajectories. *Industrial & Engineering Chemistry*, 32, pp. 605-617.

- Lebowitz, J. L. (1964). Exact solution of generalized Percus-Yevick equation for a mixture of hard spheres. *Physical Review*, 133, pp. A895-A899.
- Lewis, W. K., Gilliland, E. R., & Bauer, W. C. (1949). Characteristics of fluidized particles. *Industrial & Engineering Chemistry*, 41, pp. 1104-1117.
- Li, J., & Kwauk, M. (1994). *Particle-fluid two-phase flow: The energy-minimization multi-scale method*. Beijing: Metallurgical Industry Press.
- Li, J., & Kato, K. (2001). Effect of electrostatic and capillary forces on the elutriation of fine particles from a fluidized bed. *Advanced Powder Technology*, 12, pp. 187-205.
- Liu, D., & Chen, X. (2010). Lateral solids dispersion coefficient in large-scale fluidized beds. *Combustion and Flame*, 157, pp. 2116-2124.
- Loth, E. (2008). Drag of non-spherical solid particles of regular and irregular shape. *Powder Technology*, 182, pp. 342-353.
- Luecke, K., Hartge, E., & Werther, J. (2004). A 3D model of combustion in large-scale circulating fluidized bed boilers. *International Journal of Chemical Reactor Engineering*, 2. Article A11, 51 p.
- Lyytikäinen, M., Kettunen, A., Myöhänen, K., & Hyppänen, T. (2014). Utilization of a three dimensional model in designing and tuning of large scale boilers. In: Li, J., Wei, F., Bao, X. and Wang, W., ed., *Proceedings of the 11th International Conference on Fluidized Bed Technology*, 14th-17th May 2014. Beijing, China: Chemical Industry Press.
- Magdziarz, A., & Wilk, M. (2013). Thermogravimetric study of biomass, sewage sludge and coal combustion. *Energy Conversion and Management*, 75, pp. 425-430.
- Makkawi, Y. T., Wright, P. C., & Ocone, R. (2006). The effect of friction and inter-particle cohesive forces on the hydrodynamics of gas-solid flow: A comparative analysis of theoretical predictions and experiments. *Powder Technology*, 163, pp. 69-79.
- Man, Z., Rushan, B., Zezhong, Y., & Xiaoguo, J. (2010). Heat flux profile of the furnace wall of a 300 MWe CFB boiler. *Powder Technology*, 203, pp. 548-554.
- Mandø, M., & Rosendahl, L. (2010). On the motion of non-spherical particles at high Reynolds number. *Powder Technology*, 202, pp. 1-13.
- Matsen, J. M. (1982). Mechanisms of choking and entrainment. *Powder Technology*, 32, pp. 21-33.

- Mattsson, J. E. (1990). Basic handling characteristics of wood fuels: Angle of repose, friction against surfaces and tendency to bridge for different assortments. *Scandinavian Journal of Forest Research*, 5, pp. 583-597.
- Mattsson, J. E., & Kofman, P. D. (2002). Method and apparatus for measuring the tendency of solid biofuels to bridge over openings. *Biomass and Bioenergy*, 22, pp. 179-185.
- Miao, Z., Grift, T. E., Hansen, A. C., & Ting, K. C. (2011). Energy requirement for comminution of biomass in relation to particle physical properties. *Industrial Crops and Products*, 33, pp. 504-513.
- Myöhänen, K. (2011). *Modelling of combustion and sorbent reactions in three-dimensional flow environment of a circulating fluidized bed furnace*. Ph.D. thesis, Lappeenranta University of Technology.
- Myöhänen, K., & Hyppänen, T. (2011). A three-dimensional model frame for modelling combustion and gasification in circulating fluidized bed furnaces. *International Journal of Chemical Reactor Engineering*, 9. Article A25, 55 p.
- Myöhänen, K., Hyppänen, T., Eriksson, T., & Kuivalainen, R. (2014). Design and modeling of second generation oxygen-fired CFB. In: Li, J., Wei, F., Bao, X. and Wang, W., ed., *Proceedings of the 11th International Conference on Fluidized Bed Technology*, 14th-17th May 2014. Beijing, China: Chemical Industry Press.
- Nevalainen, T., Jäntti, T., & Nuortimo, K. (2012). Advanced CFB technology for large scale biomass firing power plants. *Bioenergy from Forest 2012*, 29th August 2012. Jyväskylä.
- Niemi, T., Kallio, S., Peltola, J., Nevalainen, H., & Karvonen, L. (2014). Scale-up of results from fuel characterization tests to boiler geometry. In: Li, J., Wei, F., Bao, X. and Wang, W., ed., *Proceedings of 11th International Conference on Fluidized Bed Technology*, 14th-17th May 2014. Beijing, China: Chemical Industry Press.
- Nieuwland, J. J., Huizenga, P., Kuipers, J. A. M., & van Swaaij, W. P. M. (1994). Hydrodynamic modelling of circulating fluidised beds. *Chemical Engineering Science*, 49, pp. 5803-5811.
- Nikolopoulos, A., Malgarinos, I., Nikolopoulos, N., Grammelis, P., Karrelas, S., & Kakaras, E. (2014). A decoupled approach for NO_x-N₂O 3-D CFD modeling in CFB plants. *Fuel*, 115, pp. 401-415.
- Nikolopoulos, A., Nikolopoulos, N., Charitos, A., Grammelis, P., Kakaras, E., Bidwe, A. R., & Varela, G. (2013). High-resolution 3-D full-loop simulation of a CFB carbonator cold model. *Chemical Engineering Science*, 90, pp. 137-150.

- Nikolopoulos, A., Rampidis, I., Nikolopoulos, N., Grammelis, P., & Kakaras, E. (2009). Numerical investigation of 3-D transient combustng flow in a 1.2 MWth pilow power plant. In: Yue, G., Zhang, H., Zhao, C. and Luo, Z., ed., *Proceedings of the 20th International Conference on Fluidized Bed Combustion*, 18th-21st May 2009. Beijing: Tsinghua University Press.
- Niven, R. K. (2002). Physical insight into the Ergun and Wen & Yu equations for fluid flow in packed and fluidised beds. *Chemical Engineering Science*, 57, pp. 527-534.
- Njobuenwu, D. O., & Fairweather, M. (2015). Dynamics of single, non-spherical ellipsoidal particles in a turbulent channel flow. *Chemical Engineering Science*, 123, pp. 265-282.
- Ohlrogge, J., Allen, D., Berguson, B., DellaPenna, D., Shachar-Hill, Y., & Stymne, S. (2009). Driving on biomass. *Science*, 324, pp. 1019-1020.
- Oka, S., & Anthony, E. J. (2004). *Fluidized bed combustion*. USA: Marcel Dekker. ISBN: 0-8247-4699-6.
- Olsson, J., Pallarès, D., & Johnsson, F. (2012). Lateral fuel dispersion in a large-scale bubbling fluidized bed. *Chemical Engineering Science*, 74, pp. 148-159.
- Pallarès, D., & Johnsson, F. (2006). A novel technique for particle tracking in cold 2-dimensional fluidized beds—simulating fuel dispersion. *Chemical Engineering Science*, 61, pp. 2710-2720.
- Pallarès, D., & Johnsson, F. (2008). Modeling of fuel mixing in fluidized bed combustors. *Chemical Engineering Science*, 63, pp. 5663-5671.
- Parikka, M. (2004). Global biomass fuel resources. *Biomass and Bioenergy*, 27, pp. 613-620.
- Patankar, S. V. (1980). *Numerical heat transfer and fluid flow*. USA: Hemisphere Publishing Corporation. ISBN: 0-07-048740-5.
- Peltola, J., & Kallio, S. (2013). Time-averaged simulation of the furnace of a Chinese 135MWw CFB boiler. *Finnish-Swedish Flame Days 2013*. 17th-18th April 2013. Jyväskylä. Finnish Flame Research Committee.
- Petersen, I., & Werther, J. (2005). Three-dimensional modeling of a circulating fluidized bed gasifier for sewage sludge. *Chemical Engineering Science*, 60, pp. 4469-4484.
- Poletto, M., Salatino, P., & Massimilla, L. (1993). Fluidization of solids with CO₂ at pressures and temperatures ranging from ambient to nearly critical conditions. *Chemical Engineering Science*, 48, pp. 617-621.

- Rahiala, S., Myöhänen, K., & Hyppänen, T. (2014). Modeling the behavior of limestone particles in oxy-fuel CFB processes. *Fuel*, *127*, pp. 141-150.
- Rao, P. R. (2009). *Buoyancy considerations in a fluidized bed of ground particles*. Master's thesis, The State University of New Jersey.
- Rasul, M. G. (1999). Buoyancy force in liquid fluidized beds of mixed particles. *Particle & Particle Systems Characterization*, *16*, pp. 284-289.
- Rees, A. C., Davidson, J. F., Dennis, J. S., & Hayhurst, A. N. (2005). The rise of a buoyant sphere in a gas-fluidized bed. *Chemical Engineering Science*, *60*, pp. 1143-1153.
- Rees, A. C., Davidson, J. F., Dennis, J. S., & Hayhurst, A. N. (2006). The rise of buoyant fuel-particles in a slugging gas-fluidized combustor. *Chemical Engineering Research and Design*, *84*, pp. 319-327.
- Richardson, J. F., & Zaki, W. N. (1954). Sedimentation and fluidization: Part I. *Transactions of the Institution of Chemical Engineers*, *32*, pp. 35-53.
- Rietema, K., & Piepers, H. W. (1990). The effect of interparticle forces on the stability of gas-fluidized beds—I. experimental evidence. *Chemical Engineering Science*, *45*, pp. 1627-1639.
- Riley, N. A. (1941). Projection sphericity. *Journal of Sedimentary Petrology*, *11*, pp. 94-97.
- Rosendahl, L. A., Yin, C., Kær, S. K., Friberg, K., & Overgaard, P. (2007). Physical characterization of biomass fuels prepared for suspension firing in utility boilers for CFD modelling. *Biomass and Bioenergy*, *31*, pp. 318-325.
- Rowe, P. N. (1984). The effect of pressure on minimum fluidisation velocity. *Chemical Engineering Science*, *39*, pp. 173-174.
- Schiller, L., & Naumann, Z. (1935). Über die grundlegenden Berechnungen bei der Schwerkraftaufbereitung. *Zeitschrift Des Vereines Deutscher Ingenieure*, *77*, pp. 318-320.
- Seddighi, S., Pallarès, D., Normann, F., & Johnsson, F. (2013). Progress of combustion in an oxy-fuel circulating fluidized-bed furnace: Measurements and modeling in a 4 MWth boiler. *Energy Fuels*, *27*, pp. 6222-6230.
- Sette, E., Pallarès, D., & Johnsson, F. (2014). Experimental quantification of lateral mixing of fuels in fluid-dynamically down-scaled bubbling fluidized beds. *Applied Energy*, *136*, pp. 671-681.

- Seville, J. P. K., Willett, C. D., & Knight, P. C. (2000). Interparticle forces in fluidisation: A review. *Powder Technology*, 113, pp. 261-268.
- Shabanian, J., Jafari, R., & Chaouki, J. (2012). Fluidization of ultrafine powders. *International Review of Chemical Engineering*, 4, pp. 16-50.
- Shah, S., Klajny, M., Myöhänen, K., & Hyppänen, T. (2010). Improvement of CFD methods for modeling full scale circulating fluidized bed combustion systems. In: Yue, G., Zhang, H., Zhao, C. and Luo, Z., ed., *Proceedings of the 20th International Conference on Fluidized Bed Combustion*, 18th-21st May 2009. Beijing: Tsinghua University Press.
- Shah, S., Myöhänen, K., Kallio, S., & Hyppänen, T. (2015a). CFD simulations of gas–solid flow in an industrial-scale circulating fluidized bed furnace using subgrid-scale drag models. *Particuology*, 18, pp. 66-75.
- Shah, S., Myöhänen, K., Kallio, S., Ritvanen, J., & Hyppänen, T. (2015b). CFD modeling of gas–solids flow in a large scale circulating fluidized bed furnace. *Powder Technology*, 274, pp. 239-249.
- Shuai, W., Huilin, L., Guodong, L., Zhiheng, S., Pengfei, X., & Gidaspow, D. (2011). Modeling of cluster structure-dependent drag with Eulerian approach for circulating fluidized beds. *Powder Technology*, 208, pp. 98-110.
- Singh, R. I., Brink, A., & Hupa, M. (2013). CFD modeling to study fluidized bed combustion and gasification. *Applied Thermal Engineering*, 52, pp. 585-614.
- Soria-Verdugo, A., Garcia-Gutierrez, L. M., García-Hernando, N., & Ruiz-Rivas, U. (2011). Buoyancy effects on objects moving in a bubbling fluidized bed. *Chemical Engineering Science*, 66, pp. 2833-2841.
- Statistics Finland. (2014). Energy statistics 2013. Retrieved from http://pxweb2.stat.fi/sahkoiset_julkaisut/energia2013/html/engl0021.htm
- Sternéus, J., Johnsson, F., Leckner, B., & Palchonok, G. I. (1999). Gas and solids flow in circulating fluidized beds — discussion on turbulence. *Chemical Engineering Science*, 54, pp. 5377-5382.
- Syamlal, M. (1985). *Multiphase hydrodynamics of gas-solids flow*. Ph.D. thesis, Illinois Institute of Technology.
- Syamlal, M., & O'Brien, T. (1987). *The derivation of a drag coefficient formula from velocity-voidage correlations*. National energy technology laboratory: US department of Energy, Office of Fossil Energy.

- Syamlal, M., Rogers, W., & O'Brien, T. (1993). *MFIX documentation: Theory guide*. Morgantown: Morgantown Energy Technology Center. DOE/METC-94/1004, DE94000087.
- Taivassalo, V., Peltola, J., & Kallio, S. (2012). Time averaged CFD modelling of a circulating fluidized bed combustor. *21st International Conference on Fluidized Bed Combustion Proceedings Volume 2*. Naples. 3 - 6 June 2012.
- Tanskanen, V. (2005). *CFD study of penetration and mixing of fuel in a circulating fluidized bed furnace*. Master's thesis. Lappeenranta University of Technology.
- Tee, S., Mucha, P. J., Brenner, M. P., & Weitz, D. A. (2008). Velocity fluctuations in a low-Reynolds-number fluidized bed. *Journal of Fluid Mechanics*, 596, pp. 467-475.
- Ulusoy, U., & Igathinathane, C. (2014). Dynamic image based shape analysis of hard and lignite coal particles ground by laboratory ball and gyro mills. *Fuel Processing Technology*, 126, pp. 350-358.
- Van de Velden, M., Baeyens, J., Seville, J. P. K., & Fan, X. (2008). The solids flow in the riser of a circulating fluidised bed (CFB) viewed by positron emission particle tracking (PEPT). *Powder Technology*, 183, pp. 290-296.
- Van de Velden, M., Baeyens, J., & Smolders, K. (2007). Solids mixing in the riser of a circulating fluidized bed. *Chemical Engineering Science*, 62, pp. 2139-2153.
- van der Schaaf, J., Johnsson, F., Schouten, J. C., & van den Bleek, C. M. (1999). Fourier analysis of nonlinear pressure fluctuations in gas–solids flow in CFB risers—Observing solids structures and gas/particle turbulence. *Chemical Engineering Science*, 54, pp. 5541-5546.
- Van Loo, S., & Koppejan, J. (Eds.). (2010). *The handbook of biomass combustion & cofiring*. United Kingdom: Earthscan. ISBN: 978-1-8497-1104-3.
- van Wachem, B., Zastawny, M., Zhao, F., & Mallouppas, G. (2015). Modelling of gas–solid turbulent channel flow with non-spherical particles with large stokes numbers. *International Journal of Multiphase Flow*, 68, pp. 80-92.
- Vassilev, S. V., Baxter, D., Andersen, L. K., & Vassileva, C. G. (2010). An overview of the chemical composition of biomass. *Fuel*, 89, pp. 913-933.
- Wang, W., & Li, J. (2007). Simulation of gas–solid two-phase flow by a multi-scale CFD approach—of the EMMS model to the sub-grid level. *Chemical Engineering Science*, 62, pp. 208-231.
- Weber, M. W., & Hrenya, C. M. (2006). Square-well model for cohesion in fluidized beds. *Chemical Engineering Science*, 61, pp. 4511-4527.

- Weber, M. W., & Hrenya, C. M. (2007). Computational study of pressure-drop hysteresis in fluidized beds. *Powder Technology*, *177*, pp. 170-184.
- Wei, F., & Zhu, J. (1996). Effect of flow direction on axial solid dispersion in gas—solids cocurrent upflow and downflow systems. *The Chemical Engineering Journal and the Biochemical Engineering Journal*, *64*, pp. 345-352.
- Wen, C. Y., & Yu, Y. H. (1966). Mechanics of fluidization. *Chemical Engineering Progress Symposium Series*, *62*, pp. 100-111.
- Weng, M., Nies, M., & Plackmeyer, J. (2011). Computer-aided optimization of gas-particle flow and combustion at the Duisburg circulating fluidized bed furnace. *VGB PowerTech*, *8/2011*, pp. 64-69.
- White, F. M. (2003). Flow past immersed bodies. *Fluid mechanics*. (5th ed.). pp. 451-522. Boston: McGraw-Hill. ISBN: 0072402172.
- Wischniewski, R., Ratschow, L., Hartge, E., & Werther, J. (2010). Reactive gas—solids flows in large volumes—3D modeling of industrial circulating fluidized bed combustors. *Particuology*, *8*, pp. 67-77.
- Wu, M. R., Schott, D. L., & Lodewijks, G. (2011). Physical properties of solid biomass. *Biomass and Bioenergy*, *35*, pp. 2093-2105.
- Yan, C., Fan, Y., Lu, C., Zhang, Y., Liu, Y., Cao, R., Gao, J., & Xu, C. (2009). Solids mixing in a fluidized bed riser. *Powder Technology*, *193*, pp. 110-119.
- Yang, Y. B., Sharifi, V. N., Swithenbank, J., Ma, L., Darvell, L. I., Jones, J. M., Pourkashanian, M., & Williams, A. (2008). Combustion of a single particle of biomass. *Energy & Fuels*, *11*, pp. 306-316.
- Yang, W. (2007). Modification and re-interpretation of Geldart's classification of powders. *Powder Technology*, *171*, pp. 69-74.
- Yang, W., Chitester, D. C., Kornosky, R. M., & Kearns, D. L. (1985). A generalized methodology for estimating minimum fluidization velocity at elevated pressure and temperature. *AIChE Journal*, *31*, pp. 1086-1092.
- Yates, J. G. (1996). Effects of temperature and pressure on gas-solid fluidization. *Chemical Engineering Science*, *51*, pp. 167-205.
- Ye, M., van der Hoef, M. A., & Kuipers, J. A. M. (2005). The effects of particle and gas properties on the fluidization of Geldart A particles. *Chemical Engineering Science*, *60*, pp. 4567-4580.

-
- Ye, M., Wang, J., van der Hoef, M. A., & Kuipers, J. A. M. (2008). Two-fluid modeling of Geldart A particles in gas-fluidized beds. *Particuology*, 6, pp. 540-548.
- Zhang, N., Lu, B., Wang, W., & Li, J. (2010). 3D CFD simulation of hydrodynamics of a 150 MWe circulating fluidized bed boiler. *Chemical Engineering Journal*, 162, pp. 821-828.
- Zulfiqar, M., Moghtaderi, B., & Wall, T. F. (2006). Flow properties of biomass and coal blends. *Fuel Processing Technology*, 87, pp. 281-288.

Publication I

Nikku, M., Jalali, P., Ritvanen, J. and Hyppänen, T. (2014).

Characterization method of average gas–solid drag for regular and irregular particle groups.

Reprinted with permission from
Powder Technology, 253, pp. 284-294.
© Elsevier, 2014



Characterization method of average gas–solid drag for regular and irregular particle groups

Markku Nikku*, Payman Jalali, Jouni Ritvanen, Timo Hyppänen

Lappeenranta University of Technology, LUT Energy, P.O. Box 20, Lappeenranta 53850, Finland



ARTICLE INFO

Article history:

Received 18 May 2013

Received in revised form 20 November 2013

Accepted 24 November 2013

Available online 1 December 2013

Keywords:

Fluidization

Characterization

Drag force

Size

Shape

ABSTRACT

The shape and size of particles have a major effect on the fluidization behavior of the particles through the drag force from the fluid phase. Several methods to estimate the particle size exist, but without the consideration of the particle shape of irregular particles these methods can produce varying results. The particle shape can be described in numerous ways, but currently no method can successfully describe irregular particles without ambiguity. Many computational models consider all particles as monodisperse perfect spheres, although the real particles often have size and shape distribution. Especially for biomass materials these distributions are usually wide. Disregarding this in modeling might lead to inaccurate results. Another way to describe material drag force is through experimental testing and without detailed knowledge about the material particle size and shape distribution. This paper describes a characterization method of an average drag force between gas and different materials. Material sizes and shapes are defined with optical measurements and the averaged values are combined with the characterization method for comparison with standard drag curves of single particles.

© 2013 Elsevier B.V. All rights reserved.

1. Introduction

Environmental awareness has increased the concern about greenhouse gases and their effect on global warming, leading to the demand for the reduction of CO₂ and other greenhouse gases. Biomass usage is promoted over the use of fossil fuels in the European Union [1], leading to its increased utilization and research in energy production.

A widely applied and studied field is biomass combustion in fluidized beds. Fluidized bed applications utilize a bed of solid particles driven to a fluid-like state by blowing air through the bed. The amount of fuel is small compared to the bed material and the fuel is mixed efficiently and heated up rapidly, allowing the efficient combustion of even wet and low grade fuels such as biomass. The understanding of the hydrodynamic behavior of the bed material and fuel is one of the most fundamental aspects in fluidized beds, as it determines the flow structure of fluid and solids and many aspects of the process through the mixing and flow of fuel in the furnace. The fuel flow directly determines where the fuel reactions occur, affecting to the forming temperature distribution and flue gas composition. In the fuel flow, the drag force between the fluid and the particles has the main role, and although the single particle drag force has been widely studied, comprehensive and realizable models are still not available for systems with a large number of particles found in fluidized beds.

For modeling purposes, it is preferable to have simple and robust models that can be readily applied to a variety of cases. Because of the demand for simplicity and fast computations, the parameters relating to the drag force, such as the particle size and shape, are defined by as few parameters as possible. Hence, many computational models assume particles as monodisperse perfect spheres. Taking into consideration the real shape or size distribution of the particles could provide more accurate results, but would require elaborate examination. Efforts to take into account the particle properties more accurately have been made, for example by Rosendahl et al. [2].

Another way to obtain information about the material behavior in fluidized bed conditions is through experimental methods, characterization. This approach provides information about the average behavior of particles, rather than detailed information about a single particle behavior, without detailed examination of the particle properties. This offers a clear benefit in Eulerian type modeling of large systems in which single particle information is not as easily applicable as the averaged information about the material.

This paper focuses on the role of the drag force between biomass particles and fluid flow. Experiments were performed with a characterization test device with the aims of developing a method for the characterization of materials for the modeling of fuel flow in fluidized beds. The characterization results combined with the image analysis of the particle size and shape are compared with data on a single particle drag. The results of characterization are applicable to average drag force modeling of biomass in fluidized bed applications.

* Corresponding author.

E-mail address: mnikku@lut.fi (M. Nikku).

2. Particles in fluidization process

The moving fluid exerts a drag force on the particle which consists of pressure drag and skin friction. Eq. (1) indicates that the drag force F_D is affected by the fluid density ρ_f , the fluid superficial velocity v_f relative to the velocity of the particle v_s , the particle reference area A and the drag coefficient C_D .

$$F_D = \frac{1}{2} \rho_f A C_D (v_f - v_s)^2. \quad (1)$$

The physical properties of a particle affect the drag force through the reference area and drag coefficient. The particle size and shape determine the reference area and pressure drag, while the shape of the particle surface determines the skin friction. In single particle fluidization, the drag force has to overcome the gravitational force on the particle, which is in direct relation to the particle mass. The mass can be directly measured or computed through the density and particle size, both affected by the particle shape.

In the fluidization of several solid particles, the particles cause disturbances to the fluid velocity field making the fluidization heterogeneous and transient in nature. The fluid velocity field can have high velocity regions, where the fluid is by-passing particle clusters, and low velocity wakes, similar to the boundary layer near the walls. In return, the particle flow field is affected by the changes in the fluid flow. The particles may also collide with each other and the walls. In this paper, only the drag force between the fluid and particles and the gravitational force relationship is considered and discussed.

2.1. Particle size

The determination of unambiguous characteristic dimension, the particle size, is extremely challenging for real particles [3–5], as illustrated in Fig. 1. The same 3D particle, depending on its orientation, can display several apparent sizes and shapes on a 2D projection, compared to the one produced by a sphere. Table 1 presents several characteristic dimension and their definitions, although the *diameter* is commonly used to describe the size with only one variable.

According to Yang [3] for the fluidized bed applications sieve, volume, surface and surface to volume diameters are relevant, with surface to volume diameter being the most relevant, because of its applicability to fluidization and thermo-chemical conversion descriptions [6]. All the suggested characteristic dimensions are affected by the particle shape and taking it into consideration might be difficult.

Michaelides et al. [7] used a high speed camera to measure the terminal velocities of free falling regular particles constructed from spheres and determined their drag coefficients. Tinke et al. [8] found non-spherical particles causing the widening of the particle size distribution (PSD) in laser diffraction, a problem which could be remedied with a comparison to the image analysis. Arsenijevic et al. [9] studied Geldart's method to determine the surface-to-volume diameter and obtained sphericities of over unity for glass spheres and argued the method not to be valid in all fluidization systems.

2.2. Particle shape

Mando et al. [5] presented the shape classification shown in Table 2: regular and irregular; these groups could contain spherical or non-spherical particles. Sand and pulverized coal were mentioned as irregular spherical particles, while untreated biomass particles were described as irregular non-spherical [5].

A common method to describe particle shape is to use a *shape factor*, which means that the particle is compared to a sphere and the characteristic dimension is corrected with the selected shape factor. Table 3 presents the shape factors found in literature, and Fig. 2 illustrates some of the most common dimensions of particles related to shape factors.

Cavarretta et al. [10] discussed the challenges of shape characterization between the 2D and 3D shapes, with the conclusion that 2D images are a suitable approximation for the 3D sphericity only if the particles are spherical or very needle-like (elongated and flat). Riley [11] discussed different 2D shape factor definitions and suggested his own one. Podczek [12] presented a shape factor which compares the main dimensions of a 2D shape to the basic geometrical shapes of a circle, rectangle, and triangle, and by formulating a deviation matrix and taking into consideration the number of corners in a particle, the shapes can be divided into six categories; elliptical, triangular, kite, parallelogram, trapezoidal and irregular. According to Liu et al. [13], Zingg shape factor evaluates the non-spherical particle shape well in fluidization applications. Loth [14] claimed the Corey shape factor to be the most suitable for the irregular particles and advocated its use instead of sphericity, which is widely used in the fluidization literature while being impractical to measure.

Almeida-Prieto et al. [15] presented detailed information about the functionality of image analysis software. The software measure particle projection surface area, dimensions and perimeter and use these to compute the particle shape factors. The non-standardized definitions of shape and measurement of characteristic dimensions lead to the incompatibility between different software [15]. Situations may occur



Fig. 1. The effect of three dimensional irregular shape on the two dimensional size and shape measurement.

Table 1
Characteristic dimensions of irregular particles. Adapted from [3–5].

Dimension	Definition	Equation
Volume diameter	Diameter of a sphere with the same volume as particle	$d_V = \sqrt[3]{\frac{6V_p}{\pi}}$
Surface diameter	Diameter of a sphere with the same surface area as particle	$d_S = \sqrt{\frac{S_p}{\pi}}$
Surface to volume diameter, Sauter mean diameter	Ratio of volume and surface area diameters	$d_{3-2} = \frac{6V_p}{S_p} = \frac{d_V^3}{d_S^2}$
Sieve diameter	Sieve screen opening size of which particle will not pass	NA
Free-falling diameter Stokes diameter	Diameter of a sphere with the same terminal velocity as the particle in Stokes flow ($Re < 0.3$)	$d_{St} = \sqrt{\frac{18\mu U_t}{(\rho_p - \rho_f)g}}$
Free falling diameter	Diameter of a sphere with the same terminal velocity as the particle when $Re > 0.3$	$d_{ff} = \frac{3}{4} \frac{\rho_f C_D U_t^2}{(\rho_p - \rho_f)g}$
Drag or aerodynamic diameter	Diameter of a sphere having the same drag as the particle	NA
Perimeter diameter	Diameter of a circle with the same perimeter as the particle	$d_c = \frac{P}{\pi}$
Projected area diameter, Equal circle diameter (ECD)	Diameter of a circle with the same projection surface area as the particle	$d_A = \sqrt{\frac{A_{Ap}}{\pi}}$
Feret's diameter	Mean value of distances between pairs of parallel tangents on a projection outline	NA
Martin's diameter	Mean chord length of a projection outline	NA
Laser diffraction diameter	Diameter calculated by Mie scattering or Fraunhofer diffraction theory	NA
Mass diameter	Diameter of a sphere with the same mass as the particle	$d_m = \sqrt[3]{\frac{6m}{\rho_p \pi}}$
Length Breadth Height	Dimensions of the particles major axes	NA

in which the image analysis software documentation does not describe the shape factors, measurement or calculation algorithms, leading to results which cannot be utilized with the necessary level of confidence.

Often the application dictates the definition of characteristic dimension and the shape factor to be applied [3,5]. The particle shape and size are inseparable except for particles with regular shape. The particle shape has also an effect on thermo-chemical behavior, as studied by [16] and [17]. The estimation of particles weight through volume is also affected by the shape.

2.3. Particle roughness

The particle surface texture or roughness has an effect on the particle drag, but its measurement might be challenging and it can be argued that the general shape would have a larger impact on the drag force than the skin friction. According to Loth [14], the increase in roughness will cause the flow separation in the particle's boundary layer with lower Reynolds numbers, notably reducing the drag coefficient.

Bouwman et al. [4] studied the shape and roughness of approximately 1 mm granules. They described particle surface details below 60 μm as roughness and they defined the roughness factor as the ratio between smooth and rough perimeters. They concluded both the shape and especially roughness as difficult to measure and to require a high resolution image analysis [4].

2.4. Determination of particle size and shape

The measurement of particle shape and size relies commonly on optical methods (for other techniques refer for example to Yang [3]). Typically, a 2D image analysis is used, but for irregular non-spherical particles the third dimension should also be considered. Davies [18] describes the methodology and different approaches to

Table 2
Shape categorization by [5].

	Spherical	Non-spherical
Regular	Polygons, low aspect ratio spheroids	Cubes, cylinders, disks, tetrahedrons, high aspect ratio spheroids
Irregular	Pulverized coal, sand, many powders, particulate matter	Pulverized biomass, flakes, splinters, agglomerates

size measurement. Garboczi [19] and Lin et al. [20] describe the reconstruction of the 3D shapes into 3D computer models. Dunnu et al. [21] described a method to obtain particle shape information from refuse derived fuel with image analysis, compared it to the sieve analysis and later applied the information for drag modeling [22]. Cavarretta et al. [10] measured the main axes of their elliptical particles from two 2D pictures taken with a 90 degree angle between the cameras to obtain 3D data, confirmed the measurements manually, and calculated several shape parameters along with Wadell's true sphericity. They approved with Wadell's observation that the 2D shape can give correspondence to the true 3D shape, at least with regularly shaped particles [10]. Guo et al. [23] used image analysis to compare the aspect ratios of four biomass samples after grinding them into four size classes. They found all the samples to have a needle like shape and the aspect ratios to decrease almost linearly with all samples as the particle size decreased [23].

To measure and to consider the real 3D particle shape in modeling are still too complicated and time consuming, and therefore, simpler methods like sieving and 2D image analysis are widely utilized despite their problems [5].

2.5. Drag coefficient

Drag coefficients of irregular particles are higher and their required minimum fluidization velocities can be many times lower than those of perfect spheres [24]. Various authors have studied drag coefficient of non-spherical particles [5,7,25,26]. While the effect of particle shape has been studied for long, as listed in the works of Yow et al. [25] and Chhabra et al. [26], no comprehensive theory has been published on its effect on the drag coefficient. A well known solution of drag coefficients can only be found for regular shapes for Stokes flow regime of very low Reynolds numbers [3]. For the most real applications, empirically derived correlations have to be used. Walsh et al. [27] measured the changes in gold flake settling velocity with different Corey shape factors. Dunnu et al. [22] studied the drag coefficients of solid recovered fuel with similar method as presented in this work. Chhabra et al. [26] reviewed current drag coefficient models for non-spherical particles. Hilton et al. [28] studied the effect of particle shape in pneumatic conveying. Cui et al. [29] reviewed existing research on biofuel hydrodynamics. Zastawny et al. [30] used DNS simulations to model flows around non-spherical particles and suggested new drag and lift force correlations. Qi et al. [31] measured the settling velocities

Table 3
List of shape factors and definitions.

Shape factor	Definition	Equation	Reference
Sphericity	Wadell's degree of true sphericity: area of sphere with same volume as particle divided by the actual particle area	NA	[25,5,10]
	Wadell's degree of sphericity	$\varphi_W = 2\sqrt{\frac{A_p}{\pi}}d_{0,\min}^{-1}$	[10]
	Sympatec (2007)	$\varphi_S = \frac{2\sqrt{A_p\pi}}{P}$	[10]
	Cho et al. (2006): ratio of min. circumscribed to max. inscribed circle diameter	$\varphi_C = \frac{d_{i,\max}}{d_{o,\min}}$	[10]
Roundness or projection sphericity	Ratio of the average radius of curvature of the corners to the radius of the largest inscribed circle	NA	[5]
	Pentland	$R_P = \frac{4A_p}{\pi d_{\max}^2}$	[38,11]
	Tickell	$R_T = \frac{A_p}{0.25\pi d_{o,\min}^2}$	[11]
	Riley (inscribed circle sphericity)	$R_R = \sqrt{\frac{d_{i,\max}}{d_{o,\min}}}$	[11]
	Wadell	$R_W = \frac{\pi CD}{d_{o,\min}}$	[11]
Circularity (ISO 9276-6/2006) or Cox's roundness	Ratio of area and perimeter	$C = 4\pi \frac{A_p}{P^2}$	[10,11,38]
Aspect ratio	Ratio of minimum and maximum dimensional distances	$AR = \frac{d_{\max}}{d_{\min}}$	[38]
Stokes shape factor	Ratio of mass diameter to Stoke's diameter	$\Psi_{St} = \frac{d_{ms}}{d_m}$	[4]
Mass shape factor	Ratio of mass diameter to projection area diameter	$\Psi_m = \frac{d_m}{d_p}$	[4]
Podczek shape factor	Deviation of main dimensions from basic 2D shapes (circle, square, triangle), particle aspect ratio and number of corners	$NS = Co + \det[M]$	[12]
Corey shape factor	Three dimensional. Ratio of the smallest principal length axis of the particle to the square root of the intermediate and longest principle length axis. Note: $\Psi_C = 1$ for spheres and cubes.	$\Psi_C = \frac{d_{\min}}{\sqrt{d_{\text{mean}}d_{\max}}}$	[5,27]
Zingg shape factor or Coefficient of flattening	Three dimensional. Note: $\Psi_Z = 1$ for spheres and cubes.	$\Psi_Z = \frac{LH}{B^2}$	[13,27]
Flatness factor	Three dimensional. Average of two largest dimensions divided by smallest dimension. Note: $\Psi_F = 1$ for spheres and cubes.	$\Psi_F = \frac{(L+H)}{2B}$	[27]
Volumetric shape factor	Ratio of the volume of the particle to the diameter of a sphere with the same projected area as the particle cubed	$V = \Psi_V d_p^3$	[5]
Heywood's shape factor	Analog to volumetric shape factor, but projection area is defined as rectangle of two main dimensions L and H.	$\Psi_H = \frac{V}{(\frac{\sqrt{LH}}{\pi})^3}$	[27]

and the orientation of fibers in dilute conditions with particle tracking velocimetry and calculated the fiber characteristic dimension (equivalent diameter) based on the obtained drag force.

Loth [14] and Klinzing et al. [24] reported the effect of turbulence on a single particle drag force. Similar to roughness, the increasing turbulence lowers the critical Reynolds number for the flow separation.

2.6. Characterization of fluidization properties

An extensive review on the characterization of fluidization behavior of different systems has been reported by Kunii et al. [33], while the applicability of the majority of them is limited only to certain systems and operational conditions.

Geldart's [34] classification of powders in fluidization by considering the material's mean particle size and density. One of the materials used, plastic molding powder was stated to consist of spherical particles, while for the two cracking catalysts the shape was not described, they can be assumed spherical.

Grace published the characterization of fluidization regimes using dimensionless particle size and fluidization velocity as parameters. Later, this characterization has been extended by several authors, giving the approach a wide range of applications and operational conditions. This regime mapping is also linking the Geldart particle groups to different fluidization regimes [32,33]. The effect of particle shape seems to have been neglected.

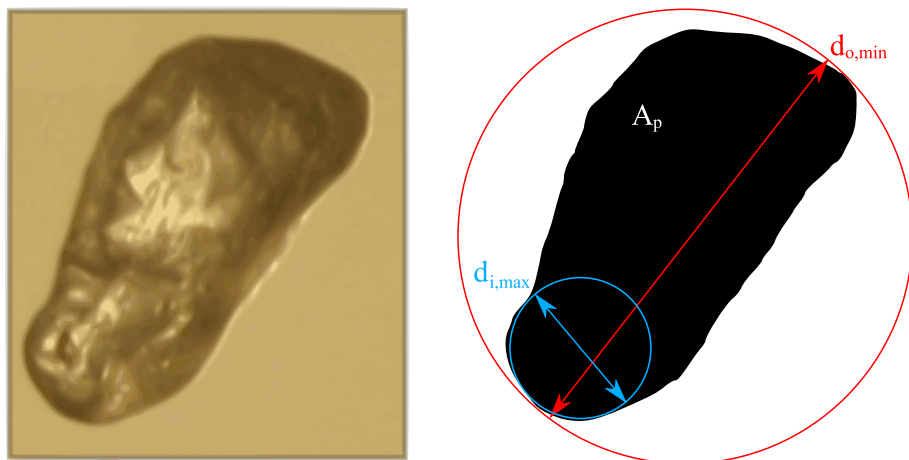


Fig. 2. Image and illustration of the measurements of a single sand grain.

Haider and Levenspiel used the dimensionless particle size and fluidization velocity in their method to determine the particle terminal velocity using sphericity to describe the particle shape [33].

Fluidization state diagram by Reh provides not only the fluidization state in known regimes, but also the estimation of the mean bed voidage and the minimum and the maximum fluidization velocities for the known material size. The diagram allows the investigation of changes in fluidization with the respect to changes in material properties (particle density, size) or the operational parameter (fluidization velocity) [35].

Arsenijevic et al. [9] used the method proposed by Grbavcic to measure the minimum fluidization velocity and determined the “effective” terminal velocity from the dimensionless number of $U_{mt}^2/U_{t\epsilon_{mf}}^3$. They summarized the particle expansion method to be useful, since detailed knowledge of particle size and shape is not needed [9].

3. Experimental study

Characterization of material fluidization properties was performed in order to investigate average gas–solid particle drag force without having detailed information about the material properties. Experimental investigation was executed with fluidization characterization test device, illustrated in Fig. 3 [36]. The device was operated with compressed air in ambient pressure and temperature, and it consists of a glass tube riser to allow visual inspection of fluidization behavior, followed by a U-bend to down comer. The total riser height is 2.3 m with an internal diameter of 0.11 m and the device is capable of producing superficial air velocities between 0.3 and 10.5 m/s. The solid material sample was placed to the bottom of the riser above a fine mesh grid, fluidized and a part of the sample was elutriated from the riser. In the down comer, the pipe diameter is increasing to lower the flow velocity and a T-intersection was used to separate the elutriated sample from the air. The sample was collected in the collection vessel while air and the finest particles were led to a cyclone separator containing a bag filter. The flow rate in the test device was controlled with a mass flow controller and the

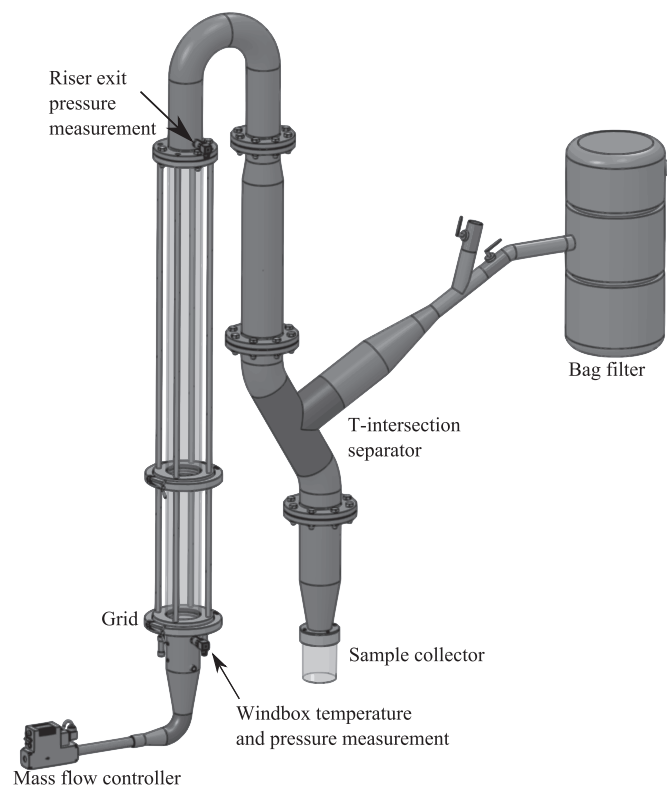


Fig. 3. Fluidization test device CAD drawing.

Table 4
Material sample properties.

	Sand	Peat	Forest residue	Silica
Sample mass m_i [g]	1873	121	110	1093
Material density ρ_{sg} [kg/m ³]	2415	340	510	2730

pressure drop over the riser was measured from below the grid and before the U-bend. The temperature of the fluidizing air was measured before the grid to determine the correct fluidization air density.

Four dried samples of different materials were used in the tests: glass beads (silica), quartz sand, peat and forest residue from South-Eastern Finland. The glass beads represent nearly spherical particles. Sand represents a common make up material in circulating fluidized bed boilers. The two biomass samples were provided by a local power plant. The sample material properties are presented in Table 4. Densities of biomass samples were measured in fine powder, and in water for sand and the glass beads density was provided by the supplier. The lower sample mass of biomasses is caused by the lower material densities and the wide PSD which causes the biomass samples to take significantly more space in the bottom of the riser. The initial material PSD for biomass samples was determined by sieving a part of the sample, for sand the PSD was provided by the supplier and mean diameter of glass beads was reported to be 250 μm by the manufacturer.

The sand and biomass samples were fluidized for several minutes with steady superficial air velocity ranging from 1 to 5 m/s with 1 m/s increments and for the forest residue an additional velocity of 6 m/s was used. For the glass beads velocities from 0.5 to 2.0 m/s with 0.5 m/s increments were used. The elutriated samples were collected, weighed to obtain the mass loss with each fluidization velocity, photographed and image analyzed. The particles were spread out and photographed at their presumed maximum surface area by using a systems camera for large particles and a microscope for small particles. The glass beads and quartz sand particles were slightly transparent, but this did not interfere with the image analysis. Commercial software was used to detect and determine the particle shape and sizes, although later several other shape factors were calculated from the measurement results due to the insufficient documentation of software on the shape determination. The roundness by Pentland was chosen as the shape factor for the analysis and data comparison. Although the particle thickness was not measured, a visual observation of the sample thickness was made.

The image analysis is sensitive to the total amount of pixels in each particle and the initial data suffered from a large scatter due to very small particles with too few pixels. For a more reliable shape analysis, detected particles with the projection surface area under 1 mm² for the systems camera and under 0.01 mm² for the microscope photographs were

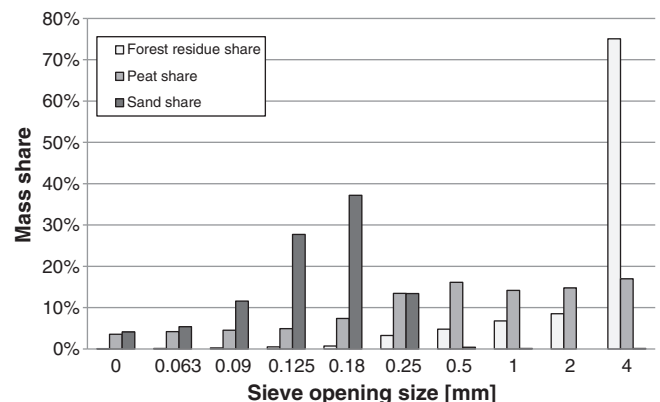


Fig. 4. Sieve analysis on particle size distribution.

Table 5
Sieved biomass size and shape information including standard deviation.

Sieve opening size [mm]	Sample mass [% of total]	Particle count	Filt. aver. diameter [mm]			Diameter standard deviation			Median diameter [mm]			Average values			
			max	mean	min	max	mean	min	max	mean	min	AR	st.dev	R _p	st.dev
Forest residue															
4.000	75.04	101	64.431	58.267	26.337	44%	44%	47%	58.371	53.251	26.378	2.768	52%	0.235	66%
2.000	8.51	305	9.986	8.899	4.418	64%	66%	46%	8.445	7.303	4.258	2.283	44%	0.371	49%
1.000	6.76	364	6.989	6.246	2.823	75%	77%	64%	5.146	4.526	2.266	2.504	45%	0.309	65%
0.500	4.80	502	3.225	2.861	1.508	81%	85%	62%	2.272	1.961	1.252	2.132	52%	0.432	50%
0.250	3.26	203	0.678	0.598	0.379	55%	55%	44%	0.611	0.543	0.370	1.820	32%	0.445	38%
0.180	0.69	326	0.499	0.442	0.264	57%	58%	34%	0.439	0.387	0.262	1.909	43%	0.452	38%
0.125	0.49	181	0.388	0.343	0.186	60%	62%	34%	0.324	0.283	0.173	2.097	43%	0.425	43%
Peat															
4.000	16.99	277	9.600	8.639	6.740	71%	70%	63%	8.329	7.550	6.258	1.459	24%	0.656	22%
2.000	14.77	344	5.366	4.740	3.393	43%	43%	37%	5.337	4.744	3.520	1.633	30%	0.567	27%
1.000	14.15	557	3.488	3.045	1.982	51%	52%	40%	3.149	2.783	1.930	1.779	33%	0.502	33%
0.500	16.12	664	2.066	1.807	1.185	37%	37%	24%	1.827	1.601	1.156	1.791	37%	0.535	32%
0.250	13.44	222	0.644	0.567	0.329	56%	56%	52%	0.626	0.550	0.333	2.019	39%	0.370	42%
0.180	7.38	341	0.479	0.422	0.247	48%	48%	45%	0.448	0.394	0.243	2.029	35%	0.364	47%
0.125	4.91	473	0.365	0.323	0.188	50%	52%	44%	0.318	0.282	0.172	2.043	41%	0.383	43%
0.090	4.51	783	0.268	0.236	0.140	43%	43%	35%	0.237	0.205	0.128	1.956	35%	0.423	41%
0.063	4.19	341	0.252	0.222	0.124	40%	41%	36%	0.218	0.191	0.113	2.118	35%	0.359	47%

excluded. This reduced the scatter dramatically. The filter sizes were determined by particles' projection surface area; if several particles had equal areas, it was deemed that in their detection, too few pixels had been used.

Static electricity caused some adhesion problems during the test runs, especially with sand, as small, charged particles made contact with the glass tube and would not detach even when brushed. The amount of material on the riser walls was small compared to the overall mass in the system, but the results showed that a small amount of fine quartz sand particles were present in the higher flow velocities, likely to have been detached from the walls. Small fractions of biomass attached to the sieve sides due to static electricity.

Steady fluidization of biomass samples was more difficult than that of the more spherical and homogeneous sand and glass beads. The fluidization regimes varied during the biomass experiments due to the wide PSD; irregular shape and large particles having a trapping effect that made fluidization of smaller particles difficult. This might have caused smaller particles to elutriate at a higher fluidization velocity than they would in the absence of larger particles. It is difficult to estimate the amount of error caused by this, as the average particle sizes increase monotonically with the fluidization velocity.

4. Results and analysis

4.1. Sieve analysis

Fig. 4 presents the results of the preliminary sieving for quartz sand, peat, and forest residue. From Fig. 4, it can be seen that peat is quite evenly distributed on each sieve. Forest residue has the majority of the sample, 75%, deposited on the 4 mm sieve, which was the largest sieve used. The quartz sand shows a Gaussian distribution with the majority of the sample deposited on the 0.125 and 0.18 mm sieves, 28% and 37% respectively.

Table 5 presents the image analysis data for sieved biomass samples. An image analysis of sieved forest residue indicates that larger particles have lower roundness values and the deviation of shape is reduced as the particle size reduces. The opposite is observed with peat, with which the coarse sieved particles are rounder and having smaller deviation than that of the fine particles. For forest residue, all filtered average minimum dimensions are higher than the previous sieve opening size, but for peat only half were higher. One explanation is that the fibrous material can bend and penetrate the sieve and bend back to its original shape and dimensions. On the other hand, flat disks, needle or

stick shaped particles can find orientation, which is a combination of the smallest dimensions of the particle, allowing them to pass through the rectangular sieve. It can be concluded that the biomass samples portray wide size and shape distributions making them unsuitable for sieving.

4.2. Fluidization analysis

The results of fluidization experiments are presented in Fig. 5 as a cumulative mass loss for each fluidization velocity. In Fig. 5, glass beads data is presented with the same interval as the other samples, more details on all samples are presented in Table 6 along with the averaged measurement data.

Seen in Fig. 5, the glass beads and peat were elutriated readily even with low fluidization velocities, while the forest residue was difficult to elutriate, with little material elutriated with the two lowest fluidization velocities. Similarly, little sand was elutriated with the 1 m/s velocity, but a significant increase was visible after 2 m/s. The narrow PSD of glass beads is visible as almost all material has left the device by 2 m/s, while the wider PSD of other samples distributes their elutriation velocity among all fluidization velocities.

Sample images of the materials are presented in Fig. 6 with the fluidization velocity of 2 m/s. These images illustrate the shape and size distribution and their relation between the materials; spherical and dense glass

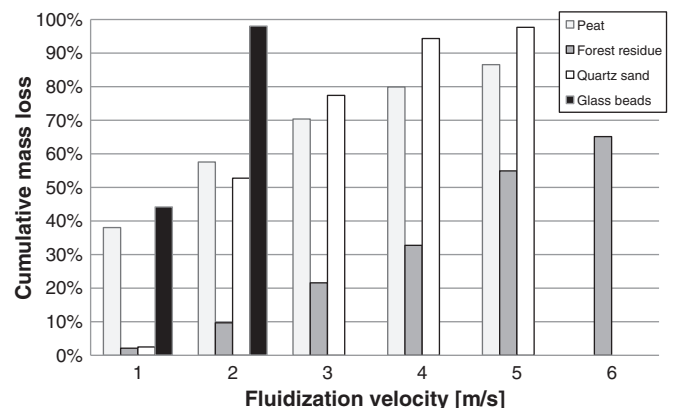


Fig. 5. Cumulative mass loss of tested materials with fluidization velocity.

Table 6
Measured size information and calculated shape parameters for test materials in with every fluidization velocity including standard deviation.

Fluidization velocity U_f [m/s]	Sample mass [% of total]	Particle count	Filt. aver. diameter [mm]			Diameter standard deviation			Median diameter [mm]			Averaged shape with standard deviation			
			max	mean	min	max	mean	min	max	mean	min	AR	st.dev	R_p	st.dev
<i>Forest residue</i>															
1.0	2.1	347	2.858	2.518	1.405	51%	52%	50%	2.390	2.100	1.220	2.174	43%	0.378	51%
2.0	7.6	844	3.686	3.248	1.800	68%	69%	71%	2.936	2.604	1.474	2.187	49%	0.376	50%
3.0	11.9	338	13.191	11.768	5.793	85%	86%	92%	10.793	9.649	4.538	2.426	50%	0.273	66%
4.0	11.2	250	21.551	19.420	9.028	67%	68%	80%	18.268	16.568	7.280	2.689	53%	0.264	65%
5.0	22.1	177	27.799	24.911	11.695	80%	80%	82%	26.464	23.705	10.640	2.584	57%	0.288	65%
6.0	10.2	61	25.786	23.368	11.147	90%	92%	84%	23.935	21.092	9.664	2.318	56%	0.400	46%
<i>Peat</i>															
1.0	38.0	313	0.269	0.236	0.143	43%	43%	35%	0.237	0.206	0.131	1.931	33%	0.378	41%
2.0	19.5	800	3.249	2.852	1.787	61%	62%	52%	2.799	2.417	1.520	1.871	38%	0.483	37%
3.0	12.8	846	4.215	3.725	2.679	52%	51%	48%	3.661	3.184	2.303	1.615	31%	0.579	26%
4.0	9.5	436	5.916	5.291	3.943	59%	59%	59%	5.279	4.721	3.616	1.570	36%	0.616	26%
5.0	6.7	250	7.576	6.762	4.849	71%	72%	62%	6.616	5.856	4.442	1.596	32%	0.590	29%
<i>Quartz sand</i>															
1.0	2.5	348	0.202	0.181	0.140	19%	18%	19%	0.195	0.176	0.138	1.460	19%	0.639	17%
2.0	50.3	221	0.260	0.235	0.189	22%	21%	21%	0.246	0.226	0.182	1.390	15%	0.665	14%
3.0	24.6	90	0.633	0.573	0.459	25%	24%	22%	0.610	0.551	0.449	1.392	19%	0.672	15%
4.0	16.9	436	0.839	0.758	0.611	22%	22%	21%	0.831	0.752	0.605	1.382	13%	0.676	13%
5.0	3.4	176	0.530	0.478	0.384	74%	74%	75%	0.279	0.255	0.204	1.412	15%	0.664	15%
<i>Glass beads</i>															
1.0	43.7	26	0.216	0.211	0.204	13%	12%	13%	0.214	0.211	0.204	1.060	1.5%	0.926	2.2%
1.5	52.1	4	0.247	0.242	0.234	5.9%	5.8%	5.6%	0.243	0.238	0.230	1.053	1.0%	0.942	0.4%
2.0	1.7	16	0.256	0.250	0.242	6.8%	6.8%	7.0%	0.260	0.253	0.242	1.060	1.7%	0.926	2.6%

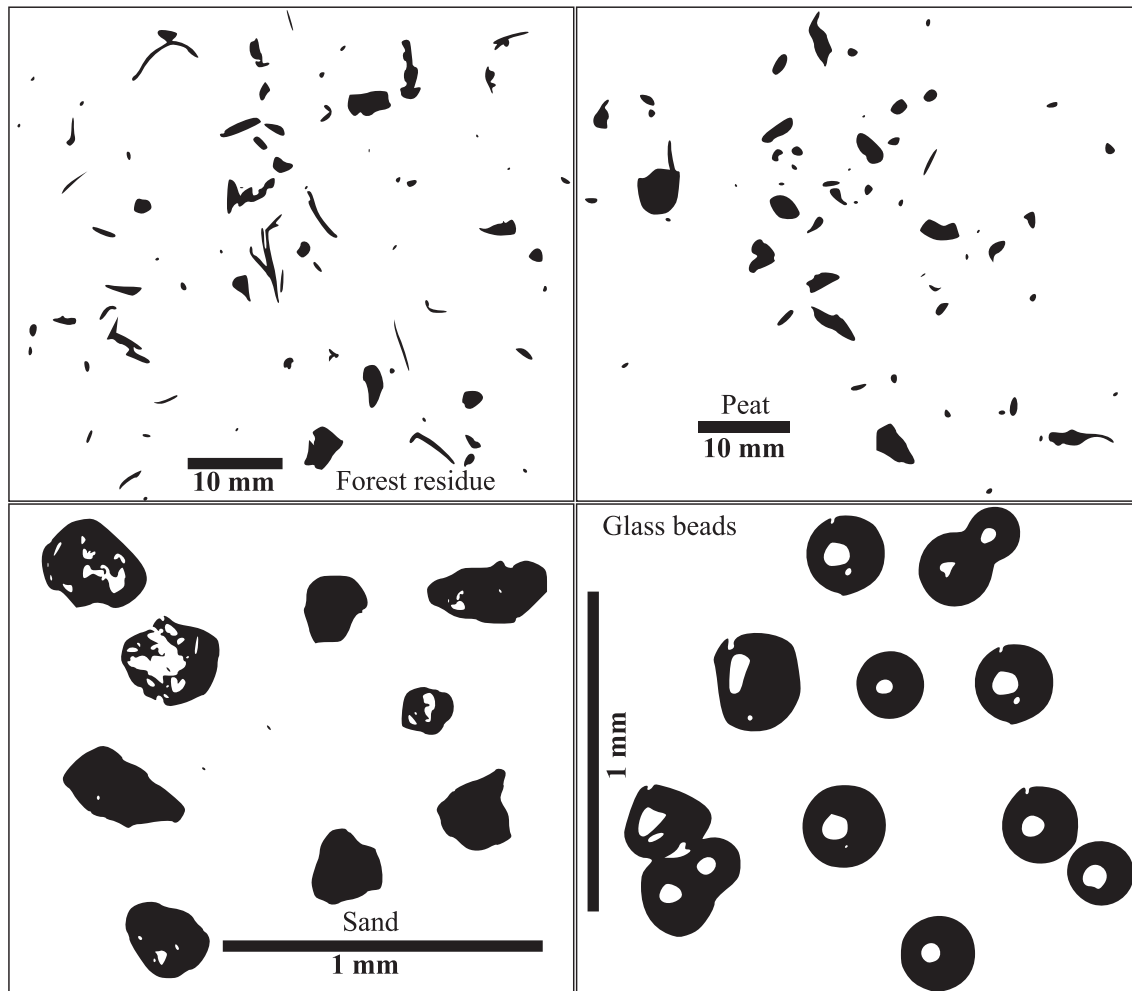


Fig. 6. Material samples with the fluidization velocity of 2 m/s.

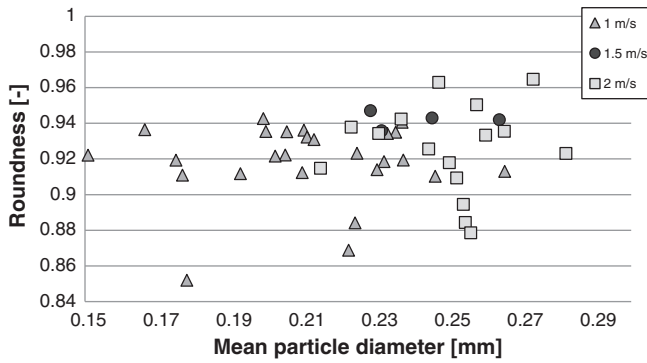


Fig. 7. Glass bead roundness versus mean particle diameter.

beads and sand particles are several times smaller than the non-spherical peat and forest residue particles. The biomass samples also have larger range of shapes and sizes, unlike the glass beads and sand.

Figs. 7, 8, 9 and 10 illustrate the relation of the mean diameter to roundness with individual data points of glass beads, quartz sand, forest residue and peat respectively.

The 2D shape of silica glass beads (Fig. 7) was found to be close to circle and very consistent, as expected. The average roundness for all samples was 0.93 with the standard deviation of 1.8% with a very narrow shape and size distribution as seen in Fig. 7. An increase in the fluidization velocity leads to a slight increase in the mean particle size and the average roundness, though no defined conclusions can be made due to the scatter and number of particles in the image analysis. The glass beads rolled and formed groups of particles on the microscope glass plate. Due to this, the count of single particles in the image analysis was very low and data is not statistically valid for detailed conclusions, but qualitative comparison can be made. Glass beads had suffered some fragmentation either during the fluidization, storage time or both. This was visible in the images as small and larger fragments that were elutriated and some part of the size and shape scatter can be linked to them. The effect of fragments on characterization results is difficult to estimate.

The average roundness of quartz sand particle (Fig. 8) was found to remain almost constant throughout the fluidization experiments, with the mean of 0.66 from all filtered data points. Standard deviation of quartz sand roundness was low, 16% on the average. The data for 1 m/s and 2 m/s are overlapping, with same sized particles having higher roundness in the 2 m/s fraction, due to the larger drag force being exerted to more non-spherical particles. For higher fluidization velocities the particle mean diameter increases more significantly with the increase of fluidization velocity except with the highest velocity. In the fluidization velocity of 5 m/s, some of the finer particles, which were attached to the device walls by static electricity, were detached and elutriated, leading to a bimodal particle size distribution, lowering the average particle size and increasing the standard deviation significantly (around 75%, with the rest being around 20%).

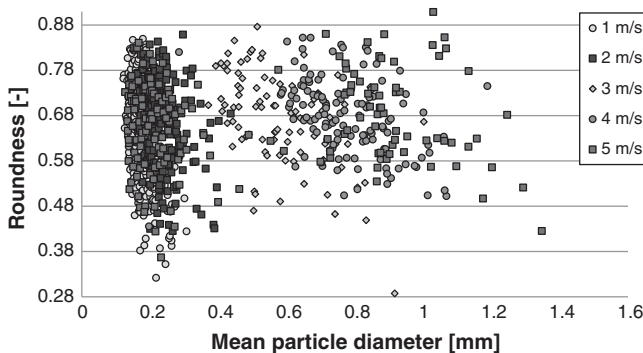


Fig. 8. Quartz sand roundness versus mean particle diameter.

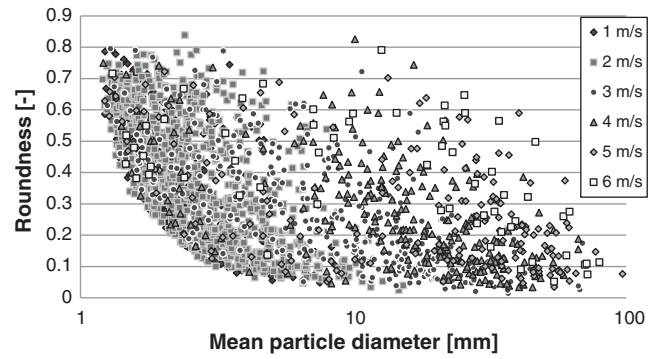


Fig. 9. Forest residue roundness versus mean particle diameter.

For forest residue (Fig. 9), the results show large deviations of size and shape. Overall mean roundness is in the order of 0.33 with the deviation of 57%. The roundness is decreasing with the mean particle diameter with exponential relation, supporting the findings of Guo et al. [23]. The effect is most visible with small fluidization velocities. Effect of filtering on this was investigated and found negligible. The data points were very scattered and the effect of increasing the fluidization velocity was less obvious as the standard deviation and scatter increased. As the fluidization was affected by large particles, the two lowest fluidization velocities had similar particles and their regions overlap in Fig. 9, though this might also be related to the increase in thickness as well as shape. Some small particles were also elutriated during the higher fluidization velocities. This could be due to static electricity or small particles being trapped by the larger particles. The sieving results indicated that the largest particles had the lowest roundness (half of the average), supported by the roundness in fluidization results being lowest with velocities of 3, 4 and 5 m/s. The roundness values were significantly higher for 6 m/s than for 5 m/s while the particle sizes were very similar. This would indicate the difference between the elutriation velocities coming from the different particle shape.

Wide size and shape distributions were also found for peat, Fig. 10, though the average roundness of smaller particles was lower than that of larger particles. This is in good agreement with the sieving results. In the visual inspection, especially the larger peat chunks appeared to be quite spherical, while the lower velocity samples contained more fibrous particles. Overall mean roundness was in the order of 0.53 with the standard deviation of 32%. The similar asymptotical behavior of shape and size of forest residue is also observed with peat. First fluidized peat sample was analyzed with a microscope, due to very fine particles, and the mean particle diameter was significantly smaller than for the rest of the samples photographed with a systems camera. This switching of method combined with filtering most likely explains the gap in Fig. 10 between sample fractions and in reality the particle size distribution is continuous.

The averaged shape and size information for all materials is presented in Fig. 11. The results indicate that for nearly mono-sized

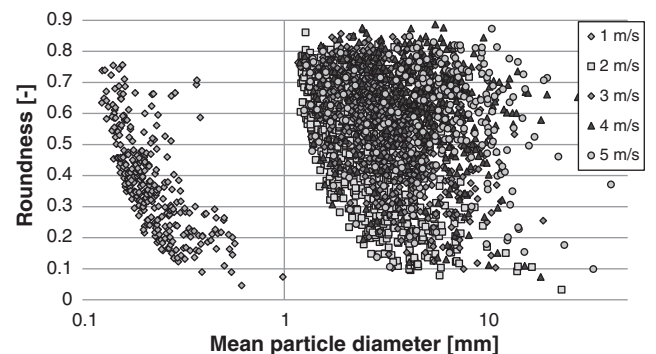


Fig. 10. Peat roundness versus mean particle diameter.

and shaped glass beads, small changes in shape and size will affect their elutriation. For roughly constant particle shapes as quartz sand, the mean particle size determines the elutriation. For biomass samples, the analysis is difficult to make without knowledge of the particle thickness. For peat the roundness is increasing, but for forest residue it is decreasing with the averaged mean particle size.

All averaged dimensions of peat particles in Table 6 seem to increase more evenly as fluidization velocity increases, unlike the forest residue with which the maximum and mean diameters grow more rapidly than the minimum diameter. This could indicate the role of thickness. On inspection of samples, the forest residue thickness was not increasing with the same rate as other dimensions, and most forest residue particles were quite flat. For peat, the particle thickness increase was almost comparable with the projected dimensions. On this basis it could be deemed that for forest residue, the effect of particle shape is dominant and for peat the increasing of size is a more dominant term in determination of elutriation. Forest residue, the mean roundness actually increases and average size slightly decreases between samples of 5 and 6 m/s velocities. The key issue here is the 3D shape in the form of thickness, which was observed to be higher in the 6 m/s sample.

By comparing information about different material fractions between materials in Table 6 and Figs. 7 to 11, several effects can be noted. With the velocities of 1 and 2 m/s, the image analysis yields smaller diameters for less round quartz sand particles than for nearly spherical glass beads, whereas the opposite is expected as more spherical particles have lower drag coefficients than the non-spherical ones. A wider PSD of sand and a large difference in the number of particles are the most likely reasons for this result. The effect of material density is visible when comparing biomass particles to sand or glass beads. Significantly smaller sand and glass beads have several times higher material densities along with their more spherical shape, causing higher gravitational force than for lighter and more irregular biomass particles. Higher gravitational force also explains the difference between the forest residue and peat particle sizes, as the peat particles are thicker and more spherical, their mass is larger compared to the relatively thin, but in other dimensions larger forest residue particles.

4.3. Characterization

Characterization test is used to describe material elutriation without detailed information about the material particle size (or shape) distribution or even density. It is assumed that given enough time of fluidization with steady gas velocity, all particles will experience enough time in dilute condition to be free of the effect of other particles. In these conditions, all the particles of which the terminal velocity exceeded, are elutriated from the system due to a drag force larger than the particle's gravitational force. Material samples can be divided into fractions based on their fluidization velocities

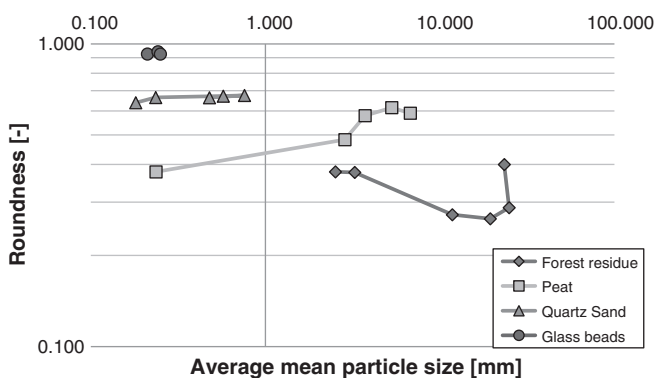


Fig. 11. Average particle shape and diameter.

Table 7
Material fractions, average velocity and material specific drag coefficient.

Class beads fraction	Fraction mass share	Average fluidization velocity	β	Peat fraction	Fraction mass share	Average fluidization velocity	β
1	0.437	0.60	27.058	1	0.380	0.5	39.240
2	0.521	1.24	6.357	2	0.195	1.5	4.360
3	0.017	1.74	3.243	3	0.128	2.5	1.570
				4	0.095	3.5	0.801
				5	0.067	4.5	0.484
Quartz sand fraction	Fraction mass share	Average fluidization velocity	β	Forest residue fraction	Fraction mass share	Average fluidization velocity	β
1	0.025	0.5	39.240	1	0.021	0.5	39.240
2	0.503	1.5	4.360	2	0.076	1.5	4.360
3	0.246	2.5	1.570	3	0.119	2.5	1.570
4	0.169	3.5	0.801	4	0.112	3.5	0.801
5	0.034	4.5	0.484	5	0.221	4.5	0.484
				6	0.102	5.5	0.324

in which they are elutriated, but in the analysis an average velocity is used since the exact terminal velocity is not known. Eq. (2) describes the relation of the specific drag force f_D with the average fluidization velocity \bar{v} as comparable to the gravitational specific force for each fraction.

$$f_D(\bar{v}) = g. \quad (2)$$

We then postulate that for a single particle Eq. (3) is valid, where the classical drag force (Eq. (1)) can be expressed as a function of particle mass m and the characteristic drag coefficient β .

$$F_D = \frac{1}{2} \rho_f A C_D (v_f - v_s)^2 \cong m \beta (v_f - v_s)^2. \quad (3)$$

Material specific drag coefficient β contains the information about the particle shape and size (A) as well as fluid properties (ρ_f) and drag force. When the particle and fluid properties remain constant, i.e. the same solid material and fluid are used, the drag force is a function of the fluidization velocity and therefore needs further description. We then extend this approach from a single particle to a group of particles (fractions), and after combining Eqs. (2) and (3) and obtain:

$$g = \beta_i (v_f - v_s)^2. \quad (4)$$

As the fluid velocity exceeds the terminal velocity, the particle velocity is positive. Taken that we are only interested in the elutriation threshold, we assume solids velocity v_s as 0 in the force balance

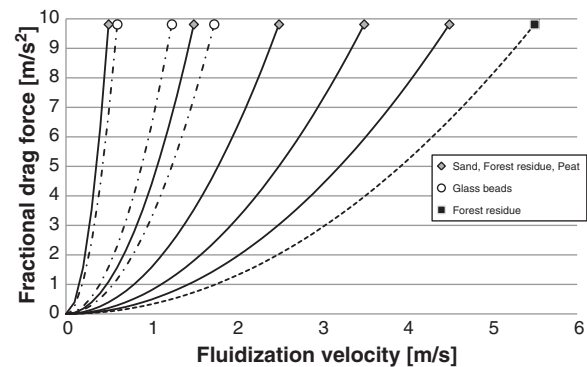


Fig. 12. Characteristic drag force of glass beads, quartz sand, peat and forest residue. The data points and curves (based on Eq. (5)) of sand, peat and forest residue overlap, with forest residue having an additional fraction presented as a separate curve and data point.

situation and solve the fractional characteristic drag coefficient as presented in Eq. (5).

$$\beta_i = \frac{g}{V_f^2} \quad (5)$$

Based on Eq. (5), Fig. 12 presents characteristic drag force curves (lines in Fig. 12) plotted for each material fraction presented in Table 7. Data points from characterization are presented as symbols on the graph. The curves present the characteristic drag for each fraction for gas velocities lower than the elutriation velocity (the symbols). As the used velocities in the experiments were same for many of the samples, the symbols and curves overlap. The mass share of the elutriated sample fraction is acknowledged in order to portray the materials fluidization behavior. Fig. 13 presents the characteristic drag coefficient as a function of material mass share of each fraction. Curve fit lines are added to Fig. 13 to illustrate an apparent trend, which seems to be present for each material. The best curve fitting functions for glass beads is quadratic, logarithmic for quartz sand and power function for biomasses peat and forest residue. The higher the β and mass share values are, the easier it is to elutriate the material, as seen with glass beads. The smallest β values can be found along with the lowest mass shares in forest residue, which was difficult to fluidize and elutriate. The data presents all the material fractions, portraying the behavior of the whole material sample. While the sand and forest residue share a common point, the other fractions behave very differently.

4.4. Fractional drag coefficient

Combining the information from characterization with the image analysis results, it is possible to obtain an average drag coefficient for each fraction. This can be considered as a comparison between the single particle approach and averaged fractional approach of characterization method, which highlights the benefits of the characterization.

The estimation of an average single particle mass is presented in Eq. (6). At this point, the particles are considered as spheres.

$$m_p = \rho_p V_p = \rho_p \left(\frac{4}{3} \pi \frac{d_p^3}{8} \right) \quad (6)$$

The ratio of the volume to cross-sectional area of sphere is presented with Eq. (7).

$$\frac{V_p}{A_p} = \frac{2d_p}{3} \quad (7)$$

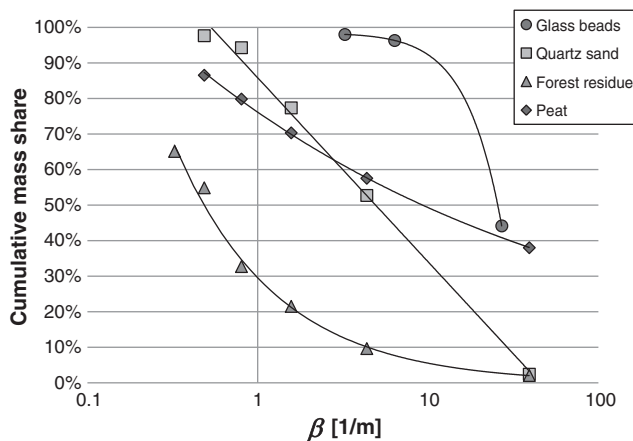


Fig. 13. Cumulative mass share and characteristic drag coefficient.

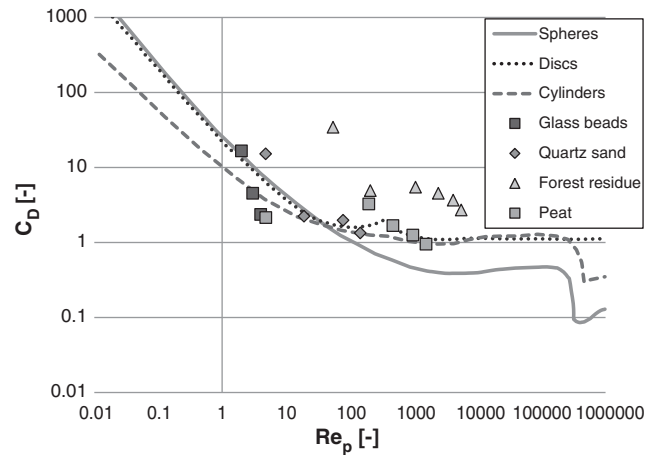


Fig. 14. Calculated fractional average drag coefficients with standard drag curves by [37].

To correct the particle shape assumption from spherical to non-spherical, Eq. (8) enables the usage of roundness by Pentland. Since the roundness is area based, the square root of roundness is used with the mean diameter of a non-spherical particle.

$$d_p = \sqrt{R_p} d_{mean} \quad (8)$$

Combining Eq. (3) with the equations above, a fractional average drag coefficient can be computed from Eq. (9). The results are presented in Fig. 14.

$$C_{D,i} \approx \frac{4\rho_p}{3\rho_f} \sqrt{R_p} d_{mean} \beta_i \quad (9)$$

In Fig. 14, the averaged fractional drag coefficients seem to behave quite well compared to the standard drag curves by [37], especially considering the irregular non-spherical shapes. Only the largest fraction of glass beads is on the standard drag curve of spheres. This might be caused by the averaging and estimation of many variables as well as the low count of glass beads particles yielded by the image analysis. The agreement of peat and drag curve of disks and cylinders is reasonably good. Considering the results in Fig. 14, almost all non-spherical particles are above the drag curve of spheres as expected because their drag coefficient is higher.

Based on these results it can be concluded that the characterization method gives a clear indication of the material characteristic drag force without detailed information on the particle size, shape and density. While this method is not absolutely accurate and valid for a single particle, it can be utilized in representing the average drag force exerted on a group of particles.

5. Conclusions

Four different materials were fluidized with a characterization test device and two biomass samples were also sieved. The shape and size information of the samples was determined with commercial image analysis software.

For irregular, non-spherical particles sieving is not a valid method of obtaining the PSD, as indicated by the image analysis results of the sieved material. Irregularly shaped particles can find orientations which allow them to pass through the sieve sizes smaller than the apparent projection size of the particles.

In fluidization, the shape and size affect the force balance between drag and gravitational forces. For nearly constant shaped and sized glass beads, small changes in shape can affect the elutriation velocity. With roughly constant shape quartz sand, the elutriation velocity was more clearly determined by the particle size. For biomasses, the distribution

of size and shape is wide and a combination of the two parameters determine the elutriation; ie. the larger and spherical the particle, the larger the elutriation velocity. For irregular and non-spherical materials such as biomass, all the dimensions of particles have to be considered, ie. three dimensional shape and size analyses are needed for a systematic analysis. This is not currently feasible for a large amount of irregular particles.

A characterization method was described to determine the material average gas–solid drag force without having detailed knowledge of the particle properties. This approach was adopted because of an infeasible measurement of shape and size for materials with large particle size and shape distributions, such as biomass. The authors aim to apply the characterization results in modeling of biomass material flow in fluidized beds process modeling.

Comparison of the characterization results and with averaged image analysis results reveals that characterization alone cannot provide full information about the single particle drag coefficients. The results are in right order of magnitude, but without having full details about the particles size and shape distribution, the comparison is only qualitative.

Nomenclature

A	Reference area	[m ²]
A_p	Cross sectional area of particle	[m ²]
Ar	Archimedes number	[–]
AR	Aspect ratio	[–]
B	Breadth	[m]
C	Circularity	[–]
C_D	Drag coefficient	[–]
CO	Number of corners	[–]
d_{3-2}	Volume-to-surface diameter	[m]
d_A	Projected area diameter	[m]
d_C	Perimeter diameter	[m]
d_{ff}	Free falling diameter	[m]
$d_{i,max}$	Diameter of maximum inscribed circle	[m]
d_m	Mass diameter	[m]
d_{min}	Minimum diameter	[m]
d_{mean}	Mean diameter	[m]
d_{max}	Maximum diameter	[m]
$d_{o,min}$	Diameter of minimum circumscribed circle	[m]
d_p	Particle diameter	[m]
d_s	Surface diameter	[m]
d_{St}	Stokes diameter	[m]
d_V	Volume diameter	[m]
ECD	Equal circle diameter	[m]
F_D	Drag force	[N]
$f_{D,i}$	Fractional drag force	[m/s ²]
g	Gravitational acceleration	[m/s ²]
H	Height	[m]
L	Length	[m]
M	Podczek's deviation matrix	[–]
m	Mass	[kg]
NS	Podczek's shape factor	[–]
P	Perimeter of particle	[m]
R_p	Roundness by Pentland	[–]
R_R	Roundness by Riley	[–]
R_T	Roundness by Tickell	[–]
R_W	Roundness by Wadell	[–]
S_p	Surface area of particle	[m ²]
V_p	Volume of particle	[m ³]
v_f	Fluid superficial velocity	[m/s]
U_t	Terminal velocity of particle	[m/s]
U_{min}	Minimum fluidization velocity	[m/s]
β_i	Fractional, material specific drag coefficient	[1/m]
ε	Void fraction	[–]
μ	Viscosity of fluid	[Pa s]
ρ_f	Density of fluid	[kg/m ³]
ρ_p	Density of particle	[kg/m ³]
ϕ_W	Wadell's degree of sphericity	[–]
ϕ_S	Sphericity by Sympatec	[–]
ϕ_C	Sphericity by Cho et al.	[–]
ψ_C	Corey shape factor	[–]
ψ_{Ht}	Heywood's shape factor	[–]
ψ_V	Volume shape factor	[–]
ψ_Z	Zingg shape factor	[–]

References

- [1] European Commission, Communication from the Commission of 7 December 2005–Biomass Action Plan, 2013, 2009.
- [2] L.A. Rosendahl, C. Yin, S.K. Kaer, K. Friborg, P. Overgaard, Physical characterization of biomass fuels prepared for suspension firing in utility boilers for CFD modelling, *Biomass Bioenergy* 31 (2007) 318–325.
- [3] W. Yang, Particle characterization and dynamics, in: W. Yang (Ed.), *Handbook of Fluidization and Fluid-Particle Systems*, CRC Press, 2003.
- [4] A.M. Bouwman, J.C. Bosma, P. Vonk, J.A. Wesselingh, H.W. Frijlink, Which shape factor(s) best describe granules? *Powder Technol.* 146 (2004) 66–72.
- [5] M. Manda, L. Rosendahl, On the motion of non-spherical particles at high Reynolds number, *Powder Technol.* 202 (2010) 1–13.
- [6] E. Michaelides, C. Crowe, *Basic Concepts and Definitions*, CRC Press, 2005, 1-1–1-79.
- [7] S. Tran-Cong, M. Gay, E.E. Michaelides, Drag coefficients of irregularly shaped particles, *Powder Technol.* 139 (2004) 21–32.
- [8] A.P. Tinke, A. Carnicer, R. Govoreanu, G. Scheltjens, L. Lauwersen, N. Mertens, K. Vanhoutte, M.E. Brewster, Particle shape and orientation in laser diffraction and static image analysis size distribution analysis of micrometer sized rectangular particles, *Powder Technol.* 186 (2008) 154–167.
- [9] Z.L. Arsenijevic, Z.B. Grbavcic, R.V. Garic-Gulovic, F.K. Zdzanski, Determination of non-spherical particle terminal velocity using particulate expansion data, *Powder Technol.* 103 (1999) 265–273.
- [10] I. Cavaretta, C. O'Sullivan, M.R. Coop, Applying 2D shape analysis techniques to granular materials with 3D particle geometries, *AIP Conf. Proc.* 1145 (2009) 833–836.
- [11] N.A. Riley, Projection sphericity, *J. Sediment. Petrol.* 11 (1941) 94–97.
- [12] F. Podczek, A shape factor to assess the shape of particles using image analysis, *Powder Technol.* 93 (1997) 47–53.
- [13] B. Liu, X. Zhang, L. Wang, H. Hong, Fluidization of non-spherical particles: sphericity, Zingg factor and other fluidization parameters, *Particology* 6 (2008) 125–129.
- [14] E. Loth, Drag of non-spherical solid particles of regular and irregular shape, *Powder Technol.* 182 (2008) 342–353.
- [15] S. Almeida-Prieto, J. Blanco-Méndez, F.J. Otero-Espinar, Microscopic image analysis techniques for the morphological characterization of pharmaceutical particles: Influence of the software, and the factor algorithms used in the shape factor estimation, *Eur. J. Pharm. Biopharm.* 67 (2007) 766–776.
- [16] S.R. Gubba, L. Ma, M. Pourkashanian, A. Williams, Influence of particle shape and internal thermal gradients of biomass particles on pulverised coal/biomass co-fired flames, *Fuel Process. Technol.* 92 (2011) 2185–2195.
- [17] H. Lu, E. Ip, J. Scott, P. Foster, M. Vickers, L.L. Baxter, Effects of particle shape and size on devolatilization of biomass particle, *Fuel* 89 (2010) 1156–1168.
- [18] R. Davies, Size measurement, in: H. Yoshida, H. Masuda, K. Higashitani (Eds.), *Powder Technology, Fundamentals of Particles, Powder Beds and Particle Generation*, CRC Press, 2006, pp. 13–32.
- [19] E.J. Garboczi, Three dimensional shape analysis of JSC-1A simulated lunar regolith particles, *Powder Technol.* 207 (2011) 96–103.
- [20] C.L. Lin, J.D. Miller, 3D characterization and analysis of particle shape using X-ray microtomography (XMT), *Powder Technol.* 154 (2005) 61–69.
- [21] G. Dunnu, T. Hilber, U. Schnell, Advanced size measurements and aerodynamic classification of solid recovered fuel particles, *Energy Fuels* 20 (2006) 1685–1690.
- [22] G. Dunnu, J. Maier, U. Schnell, G. Scheffknecht, Drag coefficient of solid recovered fuels (SRF), *Fuel* 89 (2010) 4053–4057.
- [23] Q. Guo, X. Chen, H. Liu, Experimental research on shape and size distribution of biomass particle, *Fuel* 94 (2012) 551–555.
- [24] G.E. Klinzing, F. Rizk, R. Marcus, L.S. Leung, *Fluid and particle dynamics, Pneumatic Conveying of Solids*, 8th ed., Springer, Netherlands, 2010.
- [25] H.N. Yow, M.J. Pitt, A.D. Salman, Drag correlations for particles of regular shape, *Adv. Powder Technol.* 16 (2005) 363–372.
- [26] R.P. Chhabra, L. Agarwal, N.K. Sinha, Drag on non-spherical particles: an evaluation of available methods, *Powder Technol.* 101 (1999) 288–295.
- [27] D.E. Walsh, P.D. Rao, A study of factors suspected of influencing the settling velocity of fine gold particles, *MIRL Report* 1988.
- [28] J.E. Hilton, P.W. Cleary, The influence of particle shape on flow modes in pneumatic conveying, *Chem. Eng. Sci.* 66 (2011) 231–240.
- [29] H. Cui, J.R. Grace, Fluidization of biomass particles: a review of experimental multiphase flow aspects, *Chem. Eng. Sci.* 62 (2007) 45–55.
- [30] M. Zastawny, G. Mallouppas, F. Zhao, B. van Wachem, Derivation of drag and lift force and torque coefficients for non-spherical particles in flows, *Int. J. Multiphase Flow* 39 (2012) 227–239.
- [31] G.Q. Qi, G.J. Nathan, R.M. Kelso, PTV measurement of drag coefficient of fibrous particles with large aspect ratio, *Powder Technol.* 229 (2012) 261–269.
- [32] J. Grace, J. Zhu, B. Leckner, Y. Cheng, Fluidized beds, in: C.T. Crowe (Ed.), *Multiphase Flow Handbook*, CRC Press, 2005, pp. 5-1–5-93.
- [33] D. Kunii, O. Levenspiel, *Fluidization Engineering*, 2nd ed. Butterworth-Heinemann, Boston (Mass.), 1991.
- [34] D. Geldart, Types of gas fluidization, *Powder Technol.* 7 (1973) 285–292.
- [35] J. Werther, Fluidized-bed reactors, *Ullmann's Encyclopedia of Industrial Chemistry*, Wiley-VCH Verlag GmbH & Co. KGaA, 2000.
- [36] H. Korhonen, Characterization of Fluidization Properties of Biomass, Master's thesis Lappeenranta University of Technology, 2012.
- [37] C.E. Lapple, C.B. Shepherd, Calculation of particle trajectories, *Ind. Eng. Chem.* 32 (1940) 605–617.
- [38] W.S. Rasband, ImageJ, U. S. National Institutes of Health, Bethesda, Maryland, USA, 1997–2012. (<http://imagej.nih.gov/ij/>).

Publication II

Nikku, M., Myöhänen, K., Ritvanen, J. and Hyppänen, T. (2014).
Modeling of fuel flow in circulating fluidized bed furnaces.

Reprinted with permission from
Proceedings of 11th International Conference on Fluidized Bed Technology,
© Chemical Industry Press, 2014

MODELING OF FUEL FLOW IN CIRCULATING FLUIDIZED BED FURNACES

Markku Nikku, Kari Myöhänen, Jouni Ritvanen, Timo Hyppänen

Lappeenranta University of Technology, LUT Energy, PL 20, 53851 Lappeenranta, Finland

Abstract – Modeling of biomass combustion in fluidized beds is challenging due to varying chemical and physical properties of biomass particles. Physical properties such as low density, wide particle size and shape distribution have a major effect on the drag force. In this work a characterization method is presented to experimentally obtain an average drag force for solid materials and a new approach to modeling of fuel flow is introduced into an existing holistic three dimensional CFB furnace model in order to better predict and analyze biomass fuel flow.

INTRODUCTION

Biomass particles have been shown to have wide particle size distribution (PSD) as well as deviating shape. The irregular shape increases the drag force of the particle significantly compared to a sphere and because of this, the effect of shape has to be included when modeling the fluid dynamics of biomass. For an accurate representation, the 3D geometry of the individual particles would need to be considered, but this is impractical for industrial scale studies (Mandø, Rosendahl 2010, Rosendahl et al. 2007, Nikku et al. 2013).

An alternative approach to estimate the drag force between biomass and fluid is experimental characterization. In this paper, this approach has been utilized to obtain average drag force on a group of particles. The benefit of the approach is that it does not require detailed information on the particle properties, such as shape and size and the characteristic properties can be determined by a simple and fast experiment.

Modeling of commercial scale CFB furnaces is still mainly performed with semi-empirical codes (Myöhänen, Hyppänen 2011, Knoebig, Luecke & Werther 1999, Luecke, Hartge & Werther 2004, Wischnewski et al. 2010). The application of fundamentals-oriented CFD codes for modelling of combustion in a large scale CFB is rare, due to high computational costs (Adamczyk et al. 2013). The current semi-empirical models consider fuel flow and mixing with simplified semi-empirical approaches without solution of momentum equations. (Pallarès, Johnsson, 2008b, Wischnewski et al. 2010). The following paper presents a fuel convection model, which has been implemented to an existing model frame in order to improve prediction of flow dynamics of fuel, especially for biomass.

CHARACTERIZATION

Experimental investigation of the average momentum exchange force between gas and solid particles was executed with fluidization characterization test device, illustrated in Fig 1 (a).

Four dried samples of different materials were used in the tests: glass beads (silica), quartz sand, peat and forest residue from South-Eastern Finland. The glass beads represent nearly spherical particles. Sand represents a common make-up material in circulating fluidized bed boilers. The two biomass samples were provided by local power plant. The material density was 2730 kg/m³ for glass beads, 2415 kg/m³ for sand and 340 kg/m³ and 510 kg/m³ for peat and forest residue, respectively.

The sand and biomass samples were fluidized for several minutes with steady superficial air velocity ranging from 1 to 5 m/s with 1 m/s increments and for the forest residue an additional velocity of 6 m/s was used. For the glass beads velocities from 0.5 to 2.0 m/s with 0.5 m/s increments were used. The materials are divided into fractions based on their elutriation velocity. The elutriated samples were collected, weighed to obtain the mass loss with each fluidization velocity, photographed and image analyzed. Filtering was used to remove the particles with too few pixels and agglomerated and overlapping particles. Due to clustering of glass beads, the individual particle count was low, making the results statistically invalid but suitable for qualitative comparison. Fig 1 (b) presents a comparison of 2 m/s fractions of every material. There are significant differences in particle sizes between biomass and sand and glass beads, explained by the large difference in the material densities.

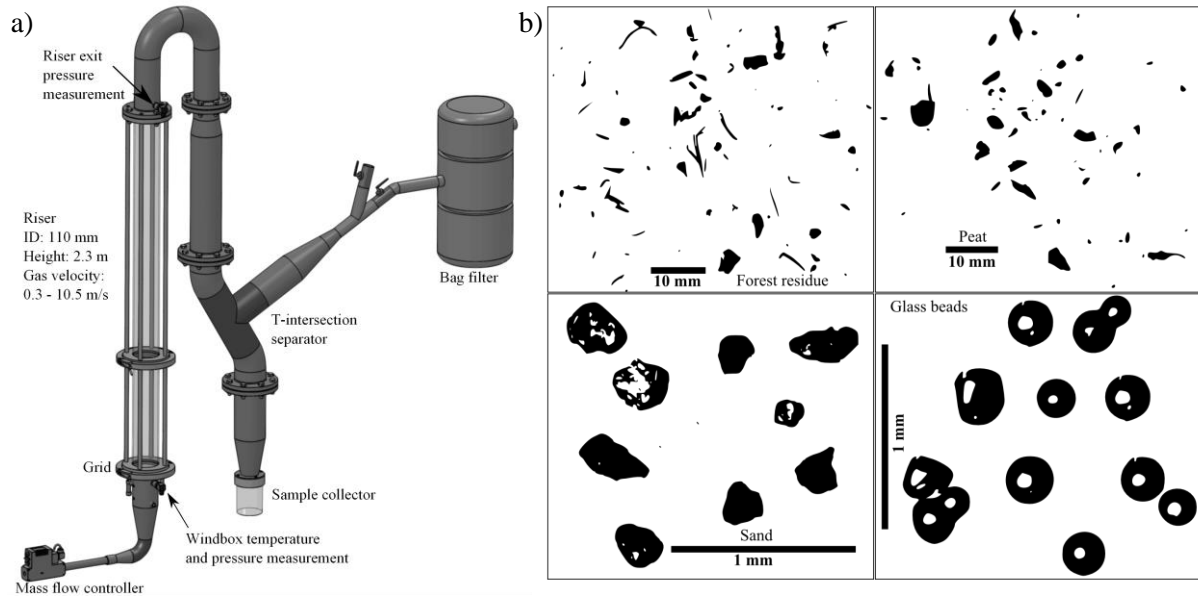


Fig 1. a) The fluidization test device and its main parameters. b) The sample images of material for image analysis with fluidization velocity 2 m/s.

The image analysis results are presented in Table 1. The particle shape is presented with roundness R by Pentland (1927), described in Eq. (1). A wide size and shape distribution can be observed for biomass while spherical glass beads have a narrow size and shape distribution. The shape of quartz sand is roughly constant between different fractions while the mean diameter monotonically increases, except for the 5 m/s fraction, where a significant number of small particles were present, causing large deviation in mean diameter. These small particles were previously attached to the riser walls by static electricity and were only detached into this fraction. The size of peat and forest residue particles increases with the fractions. Only for the fraction 6 m/s for forest residue, the mean diameter is smaller than for the previous fraction. The roundness of this fraction is significantly higher than the previous, which explains the difference between fractions. For forest residue, the shape is increasingly non-spherical as the particle size increases, while the opposite is observed with peat. The larger peat particles are quite spherical, while the larger forest residue particles are cylindrical or flat in shape.

$$R = \frac{4A}{\pi d_{\max}^2} \quad (1)$$

Table 1. Image analysis results of fluidized samples.

	Forest residue						Peat					Quartz Sand					Glass beads		
	1	2	3	4	5	6	1	2	3	4	5	1	2	3	4	5	1	1.5	2
v_g [m/s]	1	2	3	4	5	6	1	2	3	4	5	1	2	3	4	5	1	1.5	2
Sample mass [%]	2.1	7.6	11.9	11.2	22.1	10.2	38.0	19.5	12.8	9.5	6.7	2.5	50.3	24.6	16.9	3.4	43.7	52.1	1.7
Particle count	347	844	338	250	177	61	313	800	846	436	250	318	221	90	436	176	26	4	16
d [mm]	2.52	3.25	11.77	19.42	24.91	23.37	0.236	2.85	3.73	5.29	6.76	0.181	0.235	0.573	0.758	0.478	0.211	0.242	0.25
St. Dev. [%]	52	69	86	68	80	92	43	62	51	59	72	18	21	24	22	74	12	5.80	6.80
R [-]	0.378	0.376	0.273	0.264	0.288	0.4	0.378	0.483	0.579	0.616	0.59	0.639	0.665	0.672	0.676	0.664	0.926	0.942	0.926
St.Dev [%]	51	50	66	65	65	46	41	37	26	26	29	17	14	15	13	15	2.20	0.40	2.60

It is assumed that during the fluidization, each particle will experience enough time free from the influence of other particles, in order for it to be considered as a single particle. For a single particle in fluidization Eq. (2) presents the drag force from gas phase and its relation to the particle mass m and characteristic drag coefficient β . The term β describes all the properties of fluidization gas and the particle. Considering the threshold of elutriation, the fluid velocity has to exceed particle's terminal velocity, at which the particle velocity is zero. At this point, the drag force is equal to gravitational force. The characteristic drag coefficient for each velocity range, fraction i , can be described with Eq. (3) as average fluidization velocity of the range in relation to gravitational acceleration g . The characteristic drag force relation to cumulative share of each material is plotted in Fig 2 (a). The lines presented are curve fits with of the most suitable

function form. The results portray the materials fluidization, the lower the β and the mass share, the harder it is to elutriate the material. This is seen with forest residue, while the opposite is observed with glass beads.

$$F_D = \frac{1}{2} \rho_g A C_D (v_g - v_s)^2 \cong m \beta (v_g - v_s)^2 \quad (2)$$

$$\beta_i = \frac{\mathbf{g}}{v_g^2} \quad (3)$$

The characteristic drag coefficient β can be compared with the average drag coefficient C_D of the fraction with Eq. (4). The average shape of the particles is considered with roundness R as correction to particle mean diameter d . The standard drag curves presented by (Lapple, Shepherd 1940) serve as a comparison to results in Fig 2 (b). The correspondence of peat to the drag curves of discs and cylinders is quite good, while this could as coincidental. Also the correspondence of roughly constant shaped sand is good. Only the smallest fraction of glass beads matches with the drag curve of spheres, this could be at least partially explained by the clustering issues in their image analysis. The forest residue data portrays similar shape to the drag curves, but the C_D values are significantly higher, as expected for highly non-spherical particles. It can be concluded that the characterization results are comparable to average drag coefficient of the material fractions.

$$C_{D,i} = \frac{4}{3} \frac{\rho_f}{\rho_g} \sqrt{R} d \beta_i \quad (4)$$

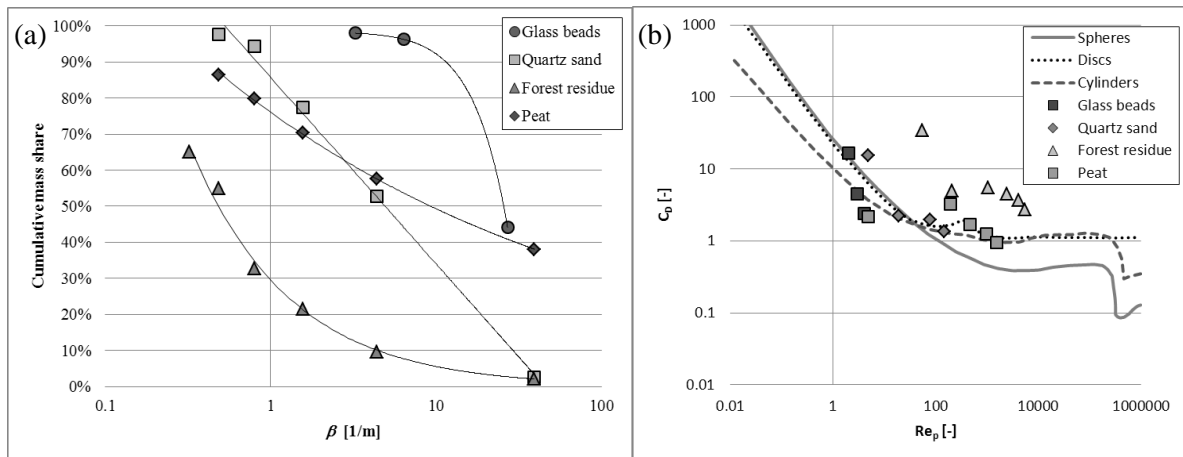


Fig 2. (a) Cumulative mass as a function of characteristic drag force for each sample fraction. (b) Comparison of characteristic drag force to fraction average drag coefficient. Drag curves by (Lapple, Shepherd 1940).

MODELING OF FUEL FLOW

The existing CFB model frame (Myöhänen, Hyppänen 2011) was modified to include a momentum equation based solution for the fuel flow in order to improve the modeling capability of biomass. The model frame is steady state and semi-empirical, for the vertical density profile of solid material is determined experimentally or by literature correlation. The model frame contains a solution of reactions of fuel, sorbent and various gaseous species, fragmentation of solid material, convective and radiative heat transfer and flow dynamics. All solid materials are divided into six size fractions, and fuel consists of char, volatiles, moisture and ash. When the fuel is fed into the furnace model, it dries and releases the volatile material according to the reaction models, leaving the char and inert ash to the fuel particle.

In the previous model (later named as “dispersion model”), the mixing of fuel was defined by a diffusive flux towards an empirical target profile and the convective flux was neglected (Myöhänen, Hyppänen 2011). In the presented model (“convective model”), a simplified momentum equation (Eq. 5) is defined for the fuel, i.e. matrix consisting of char, volatiles, moisture and ash. The considered forces (Fig 3 (a)) include inertia, gravity, buoyancy, and momentum exchange between fuel and gas and fuel and solids. The model parameters are presented in Table 2, Eq. (7-13). The convective velocity field is solved for each particle size fraction of fuel.

Due to different reaction rates, the continuity equations are defined separately for char, volatiles, and moisture in fuel. Eq. (6) presents the continuity equation for char, size fraction i . The format is similar for

volatiles and moisture. The convective velocity field and the dispersion coefficients are the same for each of these reacting species.

$$\oint_A \varepsilon_{f,i} \rho_f v_{f,i} v_{f,i} dA = \int_V \varepsilon_{f,i} (\rho_f - \rho_{\text{susp}}) \mathbf{g} dV + \int_V K_{g-f} (\mathbf{v}_g - \mathbf{v}_f) dV + \int_V K_{s-f} (\mathbf{v}_s - \mathbf{v}_f) dV \quad (5)$$

$$\oint_A \varepsilon_{f,i} \rho_f v_{f,i} dA - \oint_A D_{f,i} f_{0,i} \left(\frac{\varepsilon_{f,i} \rho_f}{f_{0,i}} \right) dA = \int_V \psi_{f,i} dV - \int_V \sum_{j,j \neq i} k_{f,ij} \varepsilon_{f,i} \rho_f dV + \int_V \sum_{j,j \neq i} k_{f,ji} \varepsilon_{f,j} \rho_f dV \quad (6)$$

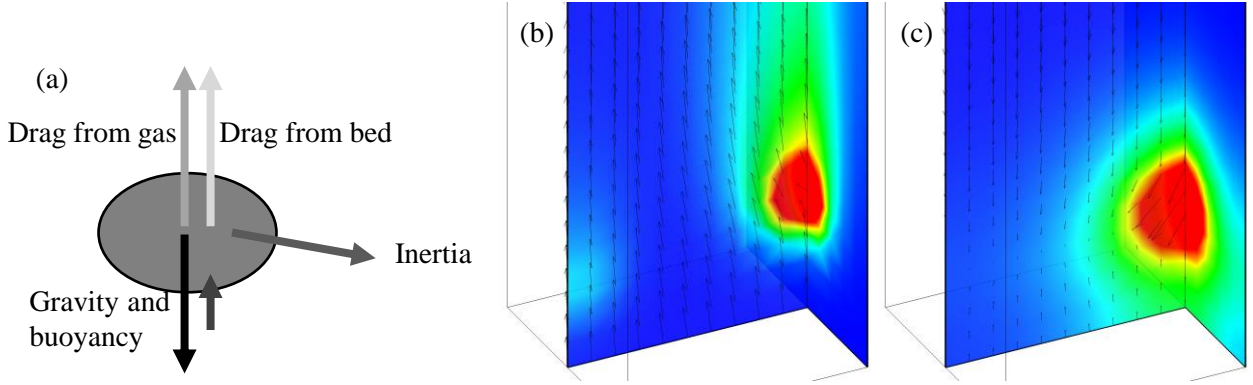


Fig 3. (a) Considered force balance for the fuel momentum equation. Example of contours and velocity vectors (not in scale) of finest (b) and coarsest (c) char fraction.

Table 2. Gas and solids drag model equations. (Huilin, Gidaspow 2003, Shuai et al. 2011, Syamlal, Rogers & O'Brien 1993, Gidaspow, Bezburuah & Ding 1991)

$K_{WY} = \frac{3}{4} C_D \frac{\varepsilon_g \varepsilon_{f,i} \rho_g u_{f,i} - u_g }{d_{f,i}} \varepsilon_g^{-2.65} \quad \varepsilon_g > 0.8$	(7)
$K_E = 150 \frac{\varepsilon_{f,i} (1 - \varepsilon_g) \mu_g}{\varepsilon_g d_{f,i}^2} + 1.75 \frac{\rho_g \varepsilon_{f,i} u_{f,i} - u_g }{d_{f,i}} \quad \varepsilon_g \leq 0.2$	(8)
$K_{g-f} = \phi K_E + (1 - \phi) K_{WY}$	(9)
$\phi = \arctan[150 \cdot 1.75 (0.2 - \varepsilon_s)] \pi^{-1} + 0.5$	(10)
$C_D = \begin{cases} \frac{24}{\text{Re}} (1 + 0.15 \text{Re}^{0.68}) & \text{Re} \leq 1000 \\ 0.44 & \text{Re} > 1000 \end{cases}$	(11)
$K_{s-c} = \frac{3(1+e)(\pi/2 + C_f \pi^2/8) \varepsilon_s \varepsilon_{f,i} \rho_s \rho_f (d_s + d_{f,i})^2 g_0 \mathbf{v}_s - \mathbf{v}_{f,i} }{2\pi(\rho_s d_s^3 + \rho_f d_{f,i}^3)}$	(12)
$g_0 = \frac{1}{\varepsilon_g} + \frac{3d_s d_{f,i}}{\varepsilon_g^2 (d_s + d_{f,i})} \sum_{i=1}^M \frac{\varepsilon_i}{d_i}$	(13)

An imaginary 170 MW_{th} CFB furnace was simulated with dispersion and convection models to demonstrate the differences between the models. The layout and parameters are thought to present a typical CFB furnace, while not corresponding to any manufacturer design. Unfortunately, the results cannot be validated due to lack of reference measurements.

Dispersion coefficient of 0.1 m/s² for lateral and 0.2 m/s² for axial were used. The peat type fuel was used similar to the characterization peat. 6 fuel inlets were located at 1.8 m from grid on front and rear walls, feeding total of 20 kg/s and fuel inlet velocity [x,y,z] was [1,0,-1] m/s on the front and [-1,0,-1] m/s on the rear wall. Table 3 presents the fuel fractions. Examples of char fractional behavior are presented in Fig 3 (b) where the drag forces dominate the flow of the finest fuel fraction, elutriating it directly from the fuel feed point. The largest fraction in Fig 3 (c), is fed towards the bed and disperses in the bottom furnace. The gravitational force of large particles is comparable to drag and the char remain in the bed. The velocity

vectors in the below the feed point indicate the flow is slowly moving upwards due to buoyancy effect. Above the feed point, the fuel vectors indicate the flow to be towards the bottom as drag forces alone cannot keep the char flowing upwards.

Table 3. Fuel particle size distribution on fractions.

Fractions of fuel	Fraction particle size [mm]	Mass share of fraction [%]
1	32	2.9
2	94	3.7
3	153	14.6
4	340	26.3
5	1250	21.9
6	4000	30.6

Fig 4 presents the char and temperature distributions between the convection and dispersion models. The convection model allows the finer fractions of char to be elutriated by the rising suspension and char is combusted higher in the furnace, while the target profile of dispersion forces the char to mainly remain in the bed. This leads to higher bed temperatures for the dispersion case, while the convection model predicts upper furnace to have higher temperatures than the bottom region. The flow of fuel (and gas) determines where the reactions occur, leading to temperature and gas component distributions.

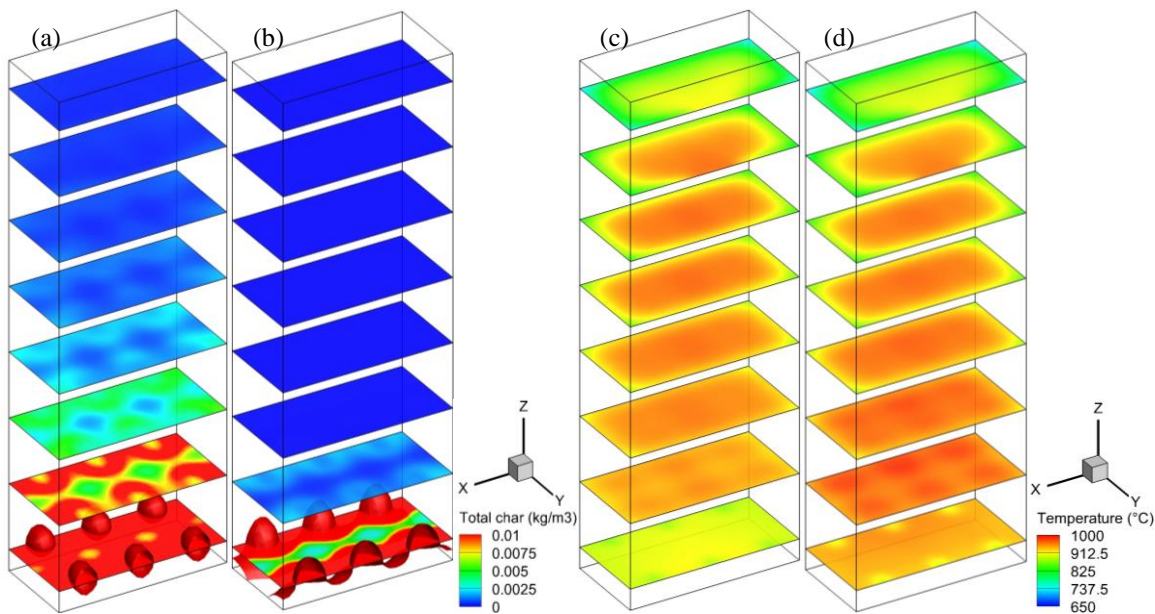


Fig 4. The char distribution for (a) convection and (b) dispersion models and the temperature distribution for (c) convection and (d) dispersion models.

CONCLUSIONS

The presented characterization method provides average information about the material fluidization properties without detailed knowledge about the particle properties. When combined with information about the average particle shape, size and density, the computed drag coefficients are comparable to those of average single particle.

A convective solution approach to fuel flow was introduced into an existing holistic CFB model frame in order to be able to utilize the characterization results. The new model defines a simplified momentum balance from which the convective velocity field for each particle size fraction of fuel is solved. The new approach was shown to improve the modeling biomass compared to the dispersion approach. In future, the characterization method approach is aimed to be linked to the model frame as a drag model for the fuel – gas phase.

Notation

A	Surface area, m^2	K	Momentum exchange coefficient, kg/m^3s
C_D	Drag coefficient, -	R	Roundness, -
C_f	Friction coefficient, -	Re	Reynolds number, -
D	Diffusion / dispersion coefficient, m^2/s	V	Volume, m^3

d	Diameter, m	β	Characteristic drag coefficient, 1/m
e	Coefficient of restitution, -	ε	Volume fraction, -
f	Target solid concentration, kg/m ³	φ	Switching function, -
g	Gravitational acceleration, m/s ²	μ	Viscosity of fluid, Pa s
g_0	Radial dispersion coefficient, -	ρ	Density, kg/m ³
k	Comminution coefficient, kg/s	ψ	Reaction source term, kg/m ³ s
m	Mass, kg		
v	Velocity, m/s		

Subscripts

E	Ergun	ij	indexes
WY	Wen-Yu	max	maximum
f	fuel	s	solid
g	gas	susp	suspension

References

- Adamczyk, W.P., Bialecki, R.A., Klimanek, A., Kozolub, P., Węcel, G. & Klajny, M. 2013, "Modeling particle transport phenomena in large scale CFB boiler", *The 38th International Technical Conference on Clean Coal & Fuel Systems* Clearwater, USA, 2nd-6th June 2013.
- Gidaspow, D., Bezburuah, R. & Ding, J. 1991, "Hydrodynamics of circulating fluidized beds: Kinetic theory approach.", *7th international conference on fluidization, Gold Coast (Australia)*, 3rd-8th May 1992.
- Huilin, L. & Gidaspow, D. 2003, "Hydrodynamics of binary fluidization in a riser: CFD simulation using two granular temperatures", *Chemical Engineering Science*, vol. 58, no. 16, pp. 3777-3792.
- Knoebig, T., Luecke, K. & Werther, J. 1999, "Mixing and reaction in the circulating fluidized bed – A three-dimensional combustor model", *Chemical Engineering Science*, vol. 54, no. 13–14, pp. 2151-2160.
- Lapple, C.E. & Shepherd, C.B. 1940, "CALCULATION OF PARTICLE TRAJECTORIES", *Industrial & Engineering Chemistry*, vol. 32, no. 5, pp. 605-617.
- Luecke, K., Hartge, E. & Werther, J. 2004, "A 3D Model of Combustion in Large-Scale Circulating Fluidized Bed Boilers", *International Journal of Chemical Reactor Engineering*, vol. 2, no. A11.
- Mandø, M. & Rosendahl, L. 2010, "On the motion of non-spherical particles at high Reynolds number", *Powder Technology*, vol. 202, no. 1–3, pp. 1-13.
- Myöhänen, K. & Hyppänen, T. 2011, "A Three-Dimensional Model Frame for Modelling Combustion and Gasification in Circulating Fluidized Bed Furnaces", *International Journal of Chemical Reactor Engineering*, vol. 9, no. 1.
- Nikku, M., Jalali, P., Ritvanen, J. & Hyppänen, T. 2014 "Characterization method of average gas-solid drag for regular and irregular particle groups", *Powder Technology*, vol 253, pp.284-294.
- Pallarès, D., Johnsson, F. & Palonen, M. 2008a, "A comprehensive model of CFB combustion", *Proceedings of the 9th International Conference on Circulating Fluidized Beds*, pp. 577-582. Hamburg: TuTech Innovation.
- Pallarès, D. & Johnsson, F. 2008b. "Modeling of fuel mixing in fluidized bed combustors". *Chemical Engineering Science*, vol. 63, pp. 5663-5671.
- Rosendahl, L.A., Yin, C., Kær, S.K., Friborg, K. & Overgaard, P. 2007, "Physical characterization of biomass fuels prepared for suspension firing in utility boilers for CFD modelling", *Biomass and Bioenergy*, vol. 31, no. 5, pp. 318-325.
- Shuai, W., Huilin, L., Guodong, L., Zhiheng, S., Pengfei, X. & Gidaspow, D. 2011, "Modeling of cluster structure-dependent drag with Eulerian approach for circulating fluidized beds", *Powder Technology*, vol. 208, no. 1, pp. 98-110.
- Syamlal, M., Rogers, W. & O'Brien, T. 1993, *MFIX Documentation: Theory Guide*, DOE/METC-94/1004, DE94000087, Morgantown, WV.
- Wischniewski, R., Ratschow, L., Hartge, E. & Werther, J. 2010, "Reactive gas–solids flows in large volumes—3D modeling of industrial circulating fluidized bed combustors", *Particuology*, vol. 8, no. 1, pp. 67-77.

Publication III

Nikku, M., Myöhänen, K., Ritvanen, J. and Hyppänen, T. (2014).

**Three-dimensional modeling of fuel flow with
a holistic circulating fluidized bed furnace model.**

Reprinted with permission from
Chemical Engineering Science, 117, pp. 352-363.
© Elsevier, 2014



ELSEVIER

Contents lists available at ScienceDirect

Chemical Engineering Science

journal homepage: www.elsevier.com/locate/ces

Three-dimensional modeling of fuel flow with a holistic circulating fluidized bed furnace model



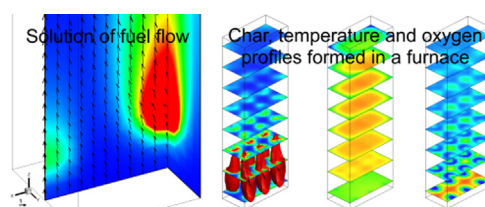
Markku Nikku*, Kari Myöhänen, Jouni Ritvanen, Timo Hyppänen

LUT Energy, Faculty of Technology, Lappeenranta University of Technology, PO Box 20, FI-53851 Lappeenranta, Finland

HIGHLIGHTS

- New fuel flow model was introduced to an existing CFB model frame.
- Fuel flow profiles determined by the physical properties of the fuel.
- Presented model improves comparison of different fuels.

GRAPHICAL ABSTRACT



ARTICLE INFO

Article history:

Received 13 February 2014

Received in revised form

27 May 2014

Accepted 21 June 2014

Available online 7 July 2014

Keywords:

Circulating fluidized bed

Fuel

Flow

Modeling

ABSTRACT

To study the mixing and flow of fuel inside commercial scale circulating fluidized bed (CFB) furnaces, a new model was introduced to solve the flow of fuel in an existing semi-empirical, steady state, three-dimensional Eulerian model frame. The fuel flow model is a simplified momentum equation which is based on the momentum balance considering the fuel inertia, gravity, and drag force from gaseous and solid phase. The model improves the prediction capabilities of fuel flow patterns in the existing model frame for conventional and especially renewable fuels, such as biomass. The fuel flow model improves the analysis of CFBs and can be utilized in the design and development of commercial CFB units.

© 2014 Elsevier Ltd. All rights reserved.

1. Introduction

1.1. Overview

As the computational capabilities have developed, the usage of computational fluid dynamics (CFD) has increased significantly in the modeling of industrial applications. CFD is increasingly used as a

Abbreviations: CFB, circulating fluidized bed; CFD, computational fluid dynamics; DEM, discrete element method; DNS, direct numerical simulation; EMMS, energy minimization multi-scale; LBM, Lattice-Boltzmann method; LES, large eddy simulation; MP-PIC, multiphase particle-in-cell; PSD, particle size distribution; RANS, Reynolds averaged Navier–Stokes

* Corresponding author at: LUT Energy, Faculty of Technology, Lappeenranta University of Technology, PO Box 20, FI-53851 Lappeenranta, Finland.
Tel.: +358 40 501 5201.

E-mail address: mnikku@lut.fi (M. Nikku).

<http://dx.doi.org/10.1016/j.ces.2014.06.038>

0009-2509/© 2014 Elsevier Ltd. All rights reserved.

supportive tool for research and development as well as in the design and dimensioning of existing and new products. CFD is especially useful in applications in which comprehensive measurements are not possible or are impractical, as in large industrial furnaces, for example.

When considering industrial furnace applications, the combustion air and flue gas form one phase, with species of gas components. The fuel, liquid or solid, is considered as its own phase. In fluidized bed furnaces, the vast amount of bed material particles (mostly fuel ash, sorbent, and make-up sand) forms the third phase. In a multiphase system, the fundamental conservation equations of mass, species, momentum, and energy have to be described for each phase.

The fluidized bed combustion is a complex and interconnected process of fluidization hydrodynamics and mixing of gas, bed material, and fuel (all forming the suspension), reactions, and heat transfer in and between the suspension and surfaces. In fluidization, the fluid (gas) flows through a bed of solid particles setting the bed to a fluid-like state. Depending on the fluid flow rate

and bed particle properties, the fluidized bed can demonstrate different behavior, from static packed to bubbling or circulating fluidized bed (CFB), all the way to pneumatic transport. The state of fluidization affects the mixing between the materials and reactants in the furnace.

There are several approaches to the modeling of phenomena related to fluidized bed processes as summarized by Singh et al. (2013). For the computations of flows, reactions, and heat transfer, several different methods and models are available which add to the computational costs of the holistic modeling of fluidized bed processes. Here, discussion is limited to the approaches relating to the solution of the momentum equation and to the modeling of the fuel flow.

Since commercial CFB furnaces are significantly larger than laboratory equipment, the computational costs of having an academic level, three-dimensional detailed resolution in the commercial scale simulations is not yet practical for engineering purposes. Simplified models, often with empirical background, are used to achieve good results in acceptable computational times for large units.

Often in works published on holistic three-dimensional CFB model frames, the multiphase and fuel flow are handled with semi-empirical and dispersion driven approach (Knoebig et al., 1999; Koski et al., 2011; Luecke et al., 2004; Myöhänen and Hyppänen, 2011; Myöhänen, 2011; Pallarès and Johnsson, 2008; Pallarès et al., 2008; Petersen and Werther, 2005; Wischnewski et al., 2010), which can produce good results with previously known, tested and more homogeneous material pairs, such as bed material and coal. For heterogeneous material pairs, such as a mixture of denser bed material and low density biomass, the previously used approach may not be suitable. Additionally, for new types of fuels, empirical parameters are required in the models, which might be difficult to obtain without actually measuring those parameters from an existing CFB unit firing the new fuels.

In this paper, an existing holistic, steady-state, three-dimensional CFB furnace model frame has been modified to include a more detailed solution of the momentum equation of fuel. The introduced model utilizes the physical properties of the fuel in the solution of the fuel flow field rather than empirically determined information. The aim of this work was to obtain and introduce a more accurate and more physical estimation of fuel flow and mixing inside the furnace. The new model is presented and compared with the previous modeling approach to highlight the differences with unconventional fuels especially for biomass, which has been shown to differ significantly from conventional fuels.

1.2. Modeling of flows in circulating fluidized beds

1D and 1.5D models of CFB are suitable for simplified mass and energy balance solutions for the process simulation or design, and 2D simulations have their place in the modeling of mainly vertical flow and mixing. Lateral mixing of fuel is especially important in large scale furnaces and requires the use of 3D modeling. (Basu, 1999; Nikolopoulos et al., 2013) The CFB furnace hydrodynamics make the process inherently fluctuating, and on this basis, transient modeling would be logical. However, transient simulation in 3D leads to long computational times (Adamczyk et al., 2013; Pallarès and Johnsson, 2006), and for this reason, the most comprehensive 3D CFB furnace models are steady-state models (Hyppänen et al., 1991; Knoebig et al., 1999; Pallarès and Johnsson, 2008).

Fluidized beds are multiphase flow systems in which at least two phases have to be considered: the fluid phase, consisting of air and flue gas in a typical combustion process, and the particulate phase, consisting typically of fuel ash or make up material. Also additional fluid or solid phases can be included, such as gaseous, liquid or solid fuel, or sorbent for sulfur capture.

The modeling approaches for these phases are discussed later in greater detail.

Another important approach to consider is the coupling, i.e. how to consider the interaction of the phases. This interaction has to be taken into account in all of the conservation equations: mass (such as evaporation and condensation), momentum (drag), or energy (heat transfer). In one-way coupling, one phase affects another without being affected back, while in two-way coupling, true interaction is considered (Crowe and Michaelides, 2006). According to Alletto and Breuer (2012), the two-way coupling should be taken into account after the particle phase volume fraction exceeds 10^{-6} , which means that the flow is still quite dilute and the particle–particle interaction can be neglected. As the particle volume fraction exceeds 10^{-3} , the flow can be considered to be in transition towards dense, and the particle collisions should be included with four-way coupling (Alletto and Breuer, 2012). The fuel and sorbent phases are minor phases in CFB furnaces, which gives justification for one-way momentum coupling, i.e. gas and bed material affect the flow of fuel and sorbent without changing the flows of gas and bed material substantially. One-way coupling reduces the computational costs significantly.

The following chapters discuss the available methods for the modeling of gas and particulate phases. Different methods can provide varying levels of details having varying computational costs. The study of the fine details of the flow phenomena leads to small spatial and temporal scales, while the simulation of the whole furnace process requires the balancing of the available computational resources and calculation time.

1.3. Gas modeling approaches

In fluidized beds, the gaseous phase is always modeled as a continuous, i.e. the Eulerian phase. The more cells in the discretization of the computational domain, the higher the resolution and level of detail. Drawbacks include higher memory requirements and longer computational times. Further consideration of the gas phase modeling leads to the choice of how to close the momentum equation regarding turbulence. Many of the models for the gas phase are computationally too expensive for commercial scale furnaces.

Various models have been used in fluidized bed simulations with Eulerian–Eulerian and Eulerian–Lagrangian approach from direct numerical simulation (DNS) (Duret et al., 2012; Duret et al., 2013; Gui et al., 2010; Puragliesi et al., 2011; Ström and Sasic, 2013; Xiong et al., 2012) and Lattice–Boltzmann method (LBM) (van der Hoef et al., 2006). Their high resolution and computational costs limit their use to microscale. Large eddy simulation (LES) has been successfully utilized in the modeling of the hydrodynamics of small fluidized beds in 2D and 3D, but currently commercial scale is not yet feasible (Alletto and Breuer, 2012; Gui et al., 2008; Luo et al., 2013; Zhou et al., 2007).

Reynolds averaged Navier–Stokes (RANS) is currently the most widely used approach in CFD to tackle simulating of gas flow in industrial scale problems. The level of detail obtained is limited, with averaging procedure and modeling of small scale flow phenomena. Several authors (Al-Rashed et al., 2013; Li et al., 2011; Liu et al., 2011; Shah et al., 2012; Taivassalo et al., 2012) have used RANS in their fluidized bed related research.

1.4. Particle modeling approaches

Similarly to the fluid flow, there are several approaches to the modeling of the particle phase with a varying level of accuracy and need for computational resources. The particulate phase can be considered as a continuous, Eulerian phase or as a Lagrangian phase consisting of single or groups of particles. The Lagrangian phase does not require the discretization of the computational

domain as the Eulerian phase does. Every particle position and interaction between other particles and domain walls are recorded and used to compute a new state of motion for each particle for each time step, as Lagrangian models are transient. As the number of individual particles increases, so do the computational costs.

Several methods have been applied to fluidized beds, from single particle level discrete element method (DEM) combined with LES (Alobaid et al., 2013; Gui et al., 2008, 2010; Luo et al., 2013; Zhou et al., 2004) and RANS (Alobaid et al., 2013; Patankar and Joseph, 2001b) in small scale, to particle grouping method of multiphase parcel-in-cell (MP-PIC) (Karimipour and Pugsley, 2012; Li et al., 2012; Patankar and Joseph, 2001a).

In the Eulerian phase approach, single particles are not considered, allowing a large number of particles to be modeled, which is desirable especially in the simulation of large scale applications. Various authors (Al-Rashed et al., 2013; Li et al., 2011; Liu et al., 2011; Shah et al., 2012; Taivassalo et al., 2012) have utilized the Eulerian–Eulerian or two-fluid model in their research.

In order to improve the Eulerian–Eulerian modeling of a particulate phase, the Energy minimization multi-scale (EMMS) approach improves the model predictability by taking into account the heterogeneous flow structure of fluidized beds. The approach considers the interaction between gas and particles in both dilute and dense (cluster) phase (Li et al., 2012; Shuai et al., 2011; Shuai et al., 2012; Wang et al., 2008).

1.5. Large scale CFB studies

Ravelli et al. (2008), Taivassalo et al. (2012), Adamczyk et al. (2013), (2014) used commercial CFD codes with the Eulerian approach to the model the gas and bed phases and additionally the Lagrangian approach in the modeling of fuel flow of refuse-derived fuel (waste material) and coal, respectively, and recently (Adamczyk et al., 2014) used a hybrid Euler–Lagrange approach in their work for coal combustion in CFB furnace. While realizable and detailed, the computational times and costs are still beyond engineering purposes.

Several authors (Knoebig et al., 1999; Koski et al., 2011; Luecke et al., 2004; Myöhänen and Hyppänen, 2011; Myöhänen, 2011; Pallarès and Johnsson, 2008; Pallarès et al., 2008; Petersen and Werther, 2005; Wischniewski et al., 2010) have used the semi-empirical approach in which empirical correlations are partially or completely used instead of the detailed and computationally expensive solution of conservation equations or their different terms. The fuel flow behavior in these works is handled through the dispersion/diffusion type mixing, modeled with dispersion coefficients and a predefined axial concentration profile for the fuel is utilized.

Compared to commercial CFD codes, the resolution of semi-empirical codes is smaller, but simulations are faster to perform with less computational resources. Good agreement between results and measurement information have been reported with both modeling methods. Often the drawback is the need for experimental data for the semi-empirical models and their applicability in new geometries and furnace conditions.

2. Three-dimensional CFB model frame

In previous works (Hyppänen et al., 1991; Koski et al., 2011; Myöhänen and Hyppänen, 2011; Myöhänen, 2011) the three-dimensional CFB model frame has been utilized to study combustion, gasification, and sorbent reactions in commercial and pilot scale CFB units, and they can be referred to for a more detailed description of the model frame. The model frame is steady-state and semi-empirical containing a solution of reactions of fuel, sorbent and various gaseous

species, fragmentation of solid material, convective and radiative heat transfer, and flow dynamics. Solid materials are divided into six size fractions, and fuel material consists of char, volatiles, moisture, and ash. When the fuel is fed into the furnace model, it dries and releases the volatile material according to the reaction models, leaving the char to the fuel particle. The inert fuel ash is handled separately in the code. The model frame utilizes a uniform block mesh with typical mesh sizes in order of 100,000 cells for commercial CFB units. A single core desktop PC can be utilized in the simulations and with typical simulation times in order of hours.

2.1. Models for gas and solids flow

The flow field of solids is solved with semi-empirical approach. The pressure profile form presented by Johnsson et al. (2004) is used for the axial concentration profile of each particle size fraction. The axial profiles give the uniform solids concentration in the core at each height, whereas the dense wall-layer is handled with superimposed wall-layer model for internal circulation in the furnace. The velocity field of all solid material for each fraction is solved with potential flow approach.

The gas pressure and velocity fields are solved with total gaseous material continuity and simplified momentum equation where only the macroscopic drag force between gas and solid phase is considered with pressure and velocity terms. The conservation of species is modeled separately utilizing a dispersive modeling for mixing. For more detailed information please refer to Myöhänen and Hyppänen (2011), Myöhänen (2011).

2.2. Model for fuel flow

The utilized model frame employs an empirical target profile for all solid material for solution of solids velocity. Additional target concentration profiles are used for fuel fractions and dispersion is directing the materials towards their respective targets. This approach is better suitable when the physical properties related to fluidization, such as particle size, density, and shape, are comparable between solid phases. Comparing conventional and widely utilized solid fuels such as coal to biomass, several physical and chemical differences can be found. Biomass presents a challenge since it is lighter than the bed material, and the particle size distribution (PSD) can be significantly wider and especially the finer fractions of low density biomasses might behave very differently from denser and/or larger fuel particles. Also for new types of fuel, the target profile determination might prove challenging.

In this work, the fuel phase momentum equation is developed to enable a more detailed solution of the fuel flow field from the physical properties of the fuel. The model is based on fuel force balance considering inertia, gravity, and drag force from the gaseous and solid phases. The momentum exchange is one-way coupled; the fuel phase has no effect on the flow of gas and bed material. This new model is later referred to as the *convection model*, whereas the old model is called the *dispersion model* to distinguish them when comparing the results.

Eq. (1) presents the continuity equation for the fuel fraction i . The first term on the left hand side is convective and the second term diffusive, which represents the turbulent mixing. In the dispersion model, the convective term is neglected and the diffusion is directing the fuel towards a predetermined and fixed axial target profile with the fractional target function $f_{0,i}$. For the convection model, a separate momentum equation for fuel is introduced and the term $f_{0,i}$ is given the value 1, leading to the Fick's law type of diffusion. The terms on the right hand side are, from left to right, (volumetric) source and sink terms and

comminution between the size fractions i and j .

$$\oint_A \varepsilon_{f,i} \rho_f \mathbf{v}_{f,i} \cdot d\mathbf{A} - \oint_A D_{f,i} \nabla \left(\frac{\varepsilon_{f,i} \rho_f}{f_{0,i}} \right) \cdot d\mathbf{A} = \int_V \phi_{f,i} dV - \int_V R_{f,i} dV - \int_V \sum_{j \neq i} k_{f,ij} \varepsilon_{f,i} \rho_f dV + \int_V \sum_{j \neq i} k_{f,ji} \varepsilon_{f,j} \rho_f dV \quad (1)$$

where variables are ε_f is the volume fraction, ρ_f , the density, \mathbf{v}_f , the velocity, A , the surface area of computational cell faces, D_f , the dispersion coefficient, ϕ_f , the source term, V , the computational cell volume, R_f , the reaction source term and k_f , the comminution coefficients from fraction i to j and vice versa.

The momentum equation for the fuel fraction i is presented in Eq. (2). The term on the left hand side is the inertia, with gravity, buoyancy, and drag from gas and solids, respectively, on the right hand side of Eq. (2).

$$\oint_A \varepsilon_{f,i} \rho_f \mathbf{v}_{f,i} \mathbf{v}_{f,i} \cdot d\mathbf{A} = \int_V \varepsilon_{f,i} (\rho_f - \rho_{\text{susp}}) \mathbf{g} dV + \int_V K_{g-f} (\mathbf{v}_g - \mathbf{v}_f) dV + \int_V K_{s-f} (\mathbf{v}_s - \mathbf{v}_f) dV \quad (2)$$

where variables are \mathbf{g} , the gravitational acceleration, K_{g-f} and K_{s-f} , the momentum exchange coefficient between gas and fuel, and solids and fuel, \mathbf{v}_g and \mathbf{v}_s , the gas and solids velocities, respectively. The buoyancy is considered with the suspension density $\rho_{\text{susp}} = \varepsilon_g \rho_g + (1 - \varepsilon_g) \rho_s$ to include the effect of both gas and bed material phases. For the drag force between the gas and fuel phases, Huilin and Gidaspow (2003) drag model is utilized, with switching function (Table 1 Eq. (6)) was used to handle the discontinuity between the Wen and Yu (1966) (Eq. (3)) and

Table 1
Gas and solids drag model equations.

$$K_{WY} = \frac{3}{4} C_D \frac{\varepsilon_g \varepsilon_{f,i} \rho_g |\mathbf{v}_{f,i} - \mathbf{v}_g|}{d_{f,i}} \varepsilon_g^{-2.65} \quad \varepsilon_g > 0.8 \quad (3)$$

$$K_E = 150 \frac{\varepsilon_{f,i} (1 - \varepsilon_g) \mu_g}{\varepsilon_g d_{f,i}^2} + 1.75 \frac{\rho_g \varepsilon_{f,i} |\mathbf{v}_{f,i} - \mathbf{v}_g|}{d_{f,i}} \quad \varepsilon_g \leq 0.2 \quad (4)$$

$$K_{g-f} = \varphi K_E + (1 - \varphi) K_{WY} \quad (5)$$

$$\varphi = \arctan[150 \times 1.75 (0.2 - \varepsilon_s)] \pi^{-1} + 0.5 \quad (6)$$

$$C_D = \begin{cases} \frac{24}{Re} (1 + 0.15 Re^{0.68}) & Re \leq 1000 \\ 0.44 & Re > 1000 \end{cases} \quad (7)$$

$$K_{s-f} = \frac{3(1 + e)(\pi/2 + C_f \pi^2/8) \varepsilon_s \varepsilon_{f,i} \rho_s \rho_f (d_s + d_{f,i})^2 g_0 |\mathbf{v}_s - \mathbf{v}_{f,i}|}{2\pi(\rho_s d_s^3 + \rho_f d_{f,i}^3)} \quad (8)$$

$$g_0 = \frac{1}{\varepsilon_g} + \frac{3d_s d_{f,i}}{\varepsilon_g^2 (d_s + d_{f,i})} \left(\frac{\varepsilon_s}{d_s} + \frac{\varepsilon_{f,i}}{d_{f,i}} \right) \quad (9)$$

Table 2
Small and large scale unit data.

Property	Small scale	Large scale
Height [m]	20	36
Width [m]	2	12
Depth [m]	2	6
Number of cells used	1250 ^a /10,000 ^b /80,000 ^c	40,500
Thermal power [MW]	10	170
Return loops	1 (rear wall)	2 (rear wall)
Bed mass [kg]	4000	106,000
Fuel feeding [kg/s]	1.3	20
Fuel feed points	1 (front wall)	3/3 (front/rear wall)
Primary/secondary air [kg/s]	4.8/0	50/27

^a Coarse.

^b Medium.

^c Fine mesh.

Ergun (1952) (Eq. (4)) models, leading to Eq. (5) for the gas–solid momentum exchange coefficient. Schiller–Naumann drag correlation (Schiller and Naumann, 1935) (Eq. (7)) is used by the Wen–Yu model.

For the solid phase drag force, Syamlal equation (Syamlal et al., 1993) (Eq. (8)) was used with the radial distribution function (Eq. (9)) by Lebowitz (1964). The chosen models were taken from literature, and the particles were modeled as perfect spheres. While this approach might not be well suited for biomass (Nikku et al., 2014), it is selected here to demonstrate the fuel flow model. The model parameters can be adjusted and corrected for non-spherical particles and new models introduced and tested in further works.

2.3. Simulations

The model functionality and parameter sensitivity were tested with two arbitrary geometries: small test geometry and commercial scale CFB unit. These furnaces are not based on any existing boiler or design; therefore, only qualitative validation can be performed. Model parameters and input values are presented in Table 2 and geometries in Fig. 1 for both furnaces.

The pressure profile presented by Johnsson et al. (2004) was adopted for the bed material axial density profile. The fuel inlets were located at the height of 1.8 m from the grid level in both furnaces and symmetrically to the front and rear walls in the commercial scale. Fuel inlet velocity $[x,y,z]$ in the feed cells,

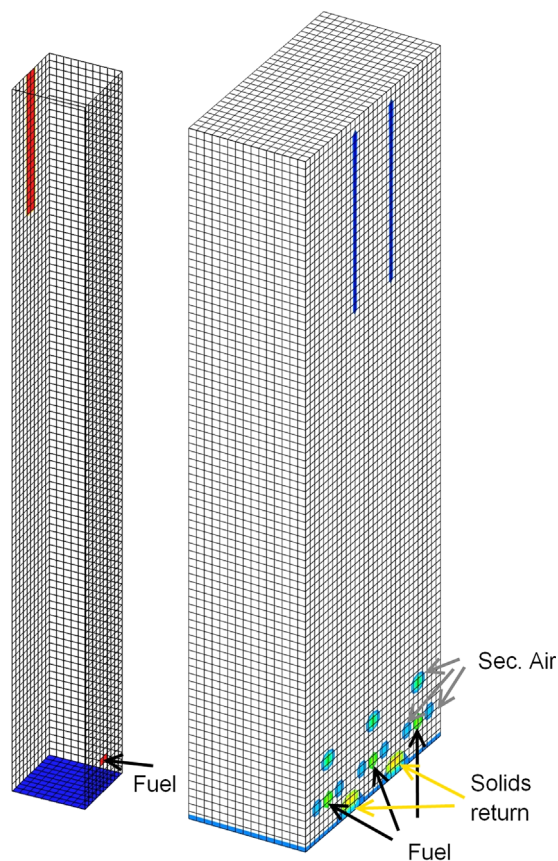


Fig. 1. Small and commercial scale CFB geometries (not in scale). Visible in the figures are separator inlets, and the circulating material is returned to the bottom part of the furnace through the openings directly below the separator inlets. In the large scale unit, the lower furnace contains 3 identical sections having an upper secondary air port above and lower secondary air ports on both sides of the fuel feeding points.

Table 3
Chemical properties of fuels.

Higher heating value	21 MJ/kg	Carbon content	52.92%
Moisture content	50%	Hydrogen content	6.15%
Volatile content	39%	Nitrogen content	0.39%
Char content	10%	Sulfur content	0.02%
Ash content	1%	Oxygen content	40.52%

Table 4
Particle size distribution of simulated fuels.

Fractions of fuel	Particle size [μm]	Share of fraction, forest residue [mass%]	Share of fraction, fuel peat [mass%]
1	32	0.4	2.9
2	94	1.0	3.7
3	153	1.0	14.6
4	340	4.5	26.3
5	1250	24.7	21.9
6	4000	68.4	30.6

[0,1,−1] m/s on the front wall and [0,−1,−1] m/s on the rear wall, was selected as the boundary condition for fuel. The secondary air ports were located around the fuel feeding points as visible in Fig. 1.

The full fuel reaction chemistry of the model frame was used, including evaporation, devolatilization, char combustion, and gasification reactions. Two types of biofuel were utilized, later referred to as *forest residue* and *peat*. The chemical properties of these fuels (Table 3) were set to be identical to better illustrate the effect of the fuel particle size distribution (Table 4) and density on the furnace process. The material densities of forest residue and peat were 500 kg/m^3 and 300 kg/m^3 , respectively.

Lateral dispersion coefficient of $0.12 \text{ m}^2/\text{s}$ was used by Petersen and Werther (2005), while Xiao et al. (1998) reported values ranging from approximately 0.09 to $0.14 \text{ m}^2/\text{s}$ for the velocity range of 3.4 to 5.25 m/s. In this work, the coefficients of $0.1 \text{ m}^2/\text{s}$ for lateral dispersion and $0.2 \text{ m}^2/\text{s}$ for axial dispersion were chosen and used.

3. Results and analysis

3.1. Mesh study in the small scale

The total char concentration on the bottom of the furnace is illustrated for each mesh size of the test geometry in Fig. 2. The coarse mesh contours are jagged compared to the smoother contours of medium and fine meshes due to the difference in the number of cells. The overall concentration levels are in good agreement.

Fig. 3 presents the averaged axial profile of each char fraction for the small scale geometry. The profiles are averaged from the whole furnace cross-section for each height. The results show good agreement with all the used meshes. The applied semi-empirical approach does not significantly benefit from having a finer mesh size, at least when the cell sizes are comparable. On this basis the coarse meshes are preferable due to shorter computational times.

3.2. Comparison of the new and old model

Table 5 presents a comparison of typically reported operational parameters of CFB furnaces for each mesh size and also the corresponding dispersion model simulations. The different meshes

for the convection and dispersion simulations have minor differences for example in heat recovery or bed temperature, but the differences are not significant. In comparison between the dispersion and convection results, the bed temperature is higher with the dispersion model, in which the majority of the char resides and combusts in the bed. While the overall circulation mass flow to the separator is virtually the same in the models, the char behavior is dramatically different. In the convection simulations, the main way for the char to leave the system is through the separator as fly ash, which occurs through the set separator model quite eagerly (on average 4.6% of the char), whereas the dispersion model predicts mere fractions of this (on average 1E−5%). In the dispersion simulations, the only mechanism available for char losses is through bottom ash removal with the average of 0.04% compared to 0.009% of the convection cases.

Fig. 4 presents a comparison of the averaged axial char profiles between the dispersion and convection model results in the medium mesh. With the convection model, the highest char concentrations are found near fuel feeding points, while the dispersion model tries to achieve the set target profile for char, which has similar shape as the bed material presented by Johnsson et al. (2004). The finer fractions of fuels are clearly more affected by the selection of the model and portray the effect of the dominance of drag forces over the gravitational force, causing the char to elutriate immediately at the fuel feeding. With the larger fractions, the gravitational force is more comparable to the drag forces, and they are distributed over the lower furnace more evenly. In this case, the dispersion model could not predict the behavior of small fractions, which led to the differences visible in Table 5. The fuel profiles are computed with the convection model, and they are not as heavily dependent on the semi-empirical parameters, such as the axial solid concentration target profile which could be difficult to estimate for new types of fuels.

To illustrate the phenomena and different behavior of fuel fractions, Fig. 5 presents char concentration contours and velocity vectors for fuel fractions 1, 3, and 6. Fine particles of fraction 1 are immediately elutriated upwards by the drag forces, which are significantly higher than the gravitational or inertia force of light weight particles. For fraction 3, the forces are more comparable with each other, and the fuel can penetrate further into the furnace before being elutriated by the drag forces. The largest particles, fraction 6, have a high gravitational force, and coupled with the inertia from fuel feeding, drop towards the grid. At some point, due to the bed material concentration, the buoyancy force and drag forces in the bottom bed start to lift the fuel upwards. The lift effect vanishes below the fuel feed point level, and the velocity vectors indicate the stagnation point above which the vectors point downwards, causing the large fuel particles to “float” on the top of the bed. For the smaller fractions, the convective transport is dominant, whereas the larger fractions are dominated by the diffusion due to lower fuel velocities.

The observed behavior of the fractions seems logical considering the phenomena modeled and the current knowledge on fluidized bed processes. Especially the increased entrainment of finer fractions is a clear improvement compared to the old model. The convection model allows the finer fraction concentration to remain steady or increase with height, which couldn't be obtained with dispersion model. Pallarès and Johnsson (2008) published experimental and simulation findings on fuel concentration distribution near fuel feeding point (Fig. 7 of Pallarès and Johnsson, 2008) similar to simulated results in the small scale geometry (Fig. 5 fraction 6). The char concentration and size profiles they presented also indicated the biomasses of having flatter concentration profiles than coal and upper furnace of having smaller mass-averaged particle size. Both of these findings support the convection modeling results on similar fuels. The results obtained in the small scale

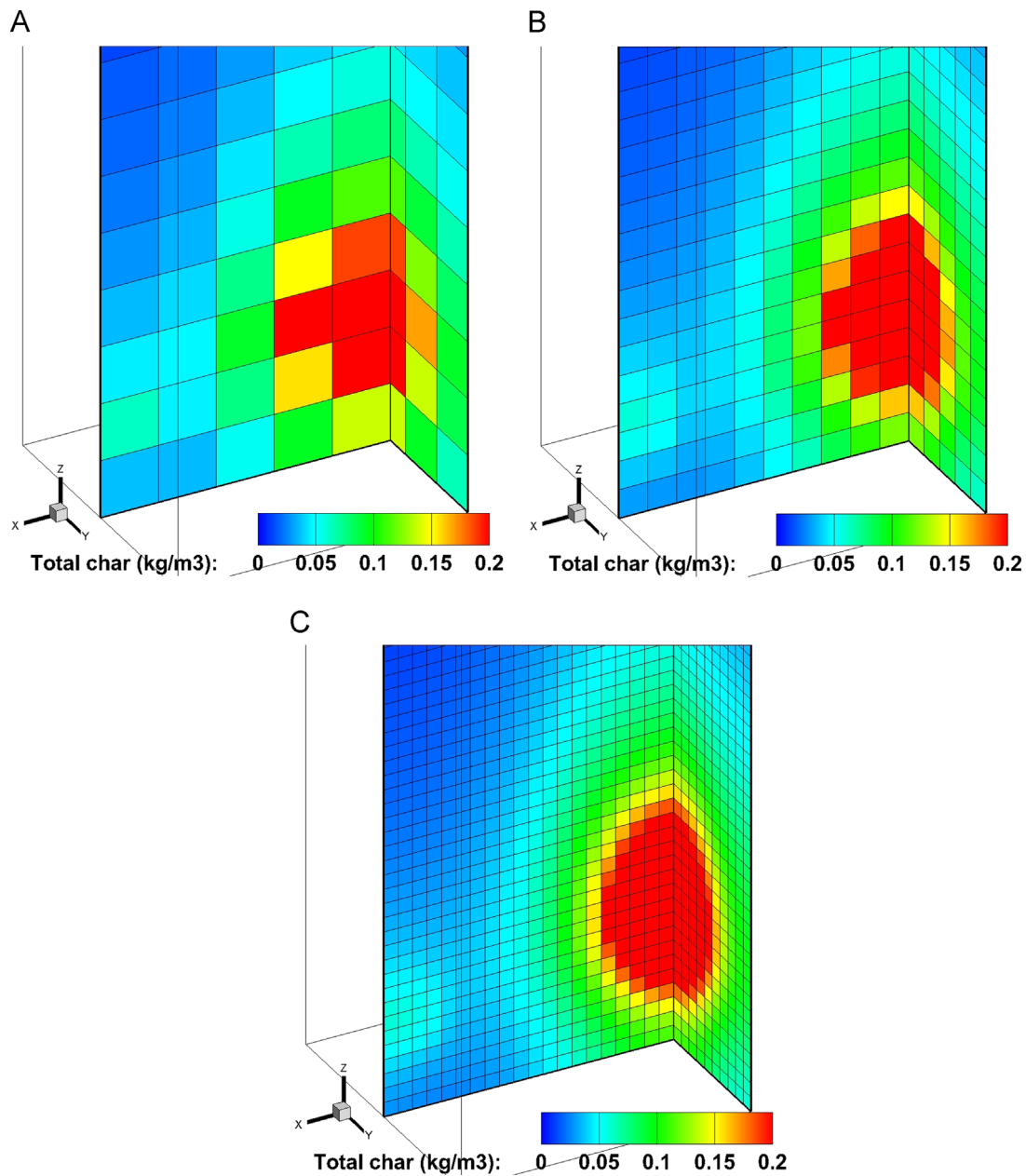


Fig. 2. Concentration profiles of total char for peat in coarse, medium and fine meshes.

can be considered as qualitative validations of the convection model, until validation can be performed on existing CFB unit with measured data.

3.3. Commercial scale results

Commercial scale furnace, presented in Section 2.3, was simulated by using both fuels, and the results are presented in Table 6 for the typical operational parameters. The heat balance of both fuels is almost identical due to the same chemical composition. For forest residue, the bed temperature is approximately 20 °C higher, while the furnace exit temperatures are nearly identical. The mass balances are also very similar, with forest residue having a slightly larger bottom ash removal rate and peat having a slightly higher circulation mass flow rate to the separators. The char distribution is different because of the different fuel PSD and density: the finer peat has more char elutriated to the separator and in the fly ash, while the coarser forest residue has more char in the bottom ash.

Even though the char and oxygen distribution in the furnace are different, the flue gas compositions are highly similar, with only 0.2% more oxygen with the forest residue. This is also largely related to the identical chemical composition.

Fig. 6 presents the char fractions 1, 3, and 6, the oxygen concentrations, and the furnace temperature contours. Peat has a significantly larger amount of fines compared to forest residue, which can be seen from the char concentration profiles. The fines are elutriated from the feeding and combusted when enough oxygen is present. Peat has also larger concentrations of fraction 3 in the upper furnace than forest residue, similarly because of the larger share of the fraction. Forest residue has a significantly larger amount of fraction 6, which is mainly located around and below the fuel feeding points. The bed temperature of forest residue is higher because of the higher rates of combustion in the lower bed, compared to peat. The higher temperatures in the bed in turn enhance the fuel reactions. For peat, the temperature distribution is more even because of the combustion also occurring higher in

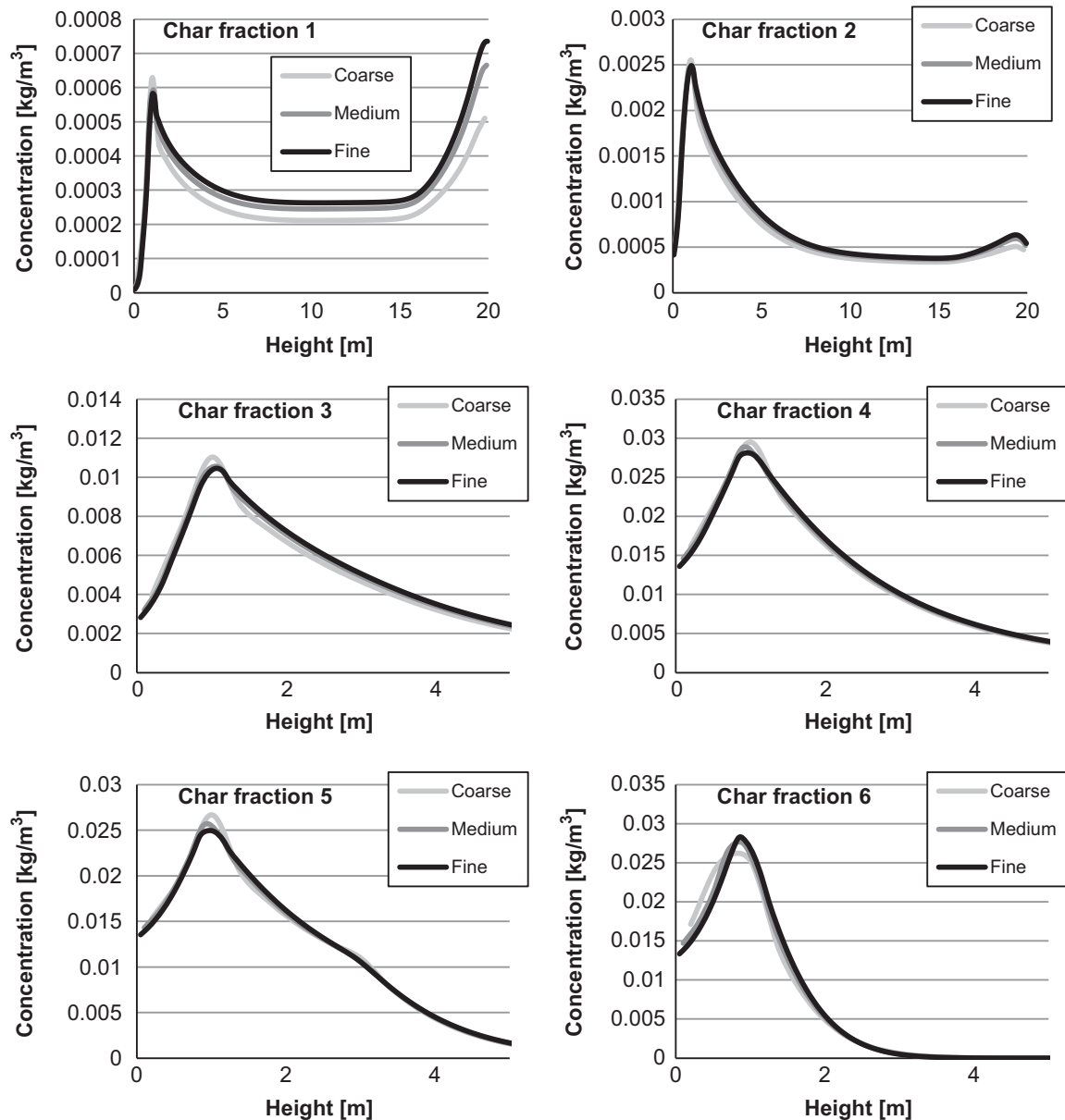


Fig. 3. Comparison of the cross-sectional average of fractional char profiles of peat between different meshes in the small scale geometry. The lines are overlapping with only minor differences in bed region and top of the furnace.

the furnace. The oxygen concentration profiles illustrate the effects of mixing and combustion. For peat, the low oxygen regions correlate well with the high concentration of fines in the upper furnace; the contours are nearly opposite. The forest residue has lower oxygen concentrations in the upper furnace as more oxygen is consumed in the bed. In both cases, channels in which fuel and oxygen flow separately can be detected. This indicates the importance of mixing; if the oxygen and fuel do not mix, no combustion occurs, leading to higher amounts of fly ash and oxygen in the back pass, possibly leading to combustion in the separator.

The mixing in the convection model is mainly handled by the dispersion as the steady-state flow fields of gas and solids phase are nearly one-dimensional with material flowing upwards. This is a clear limitation in the lower furnace and near the material inlets, but otherwise the time-averaged CFB flow fields are also rather one-dimensional.

The chemical properties of the fuel and the reactions also affect the formation of fuel concentration profiles. More reactive fuels

spread less as they are more rapidly burned out if oxygen is available, while less reactive fuels need longer exposure to oxygen in sufficiently high temperatures in order to burn out. In the presented cases the chemical properties and reactivity of fuels are set to be identical, while with real fuels the comparison would also be strongly affected by the chemical properties and reactivity.

Fig. 7 presents cumulative relative release profiles for fuel components for small and commercial scale simulations for forest residue. Both cases portray the fuel phenomena that the fuel particles experience, from drying, to devolatilization and char combustion in the correct order and demonstrate that these processes are overlapping. The presented results are similar to [Pallarès and Johnsson \(2008\)](#), though this could be coincidental, since the fuel chemical and physical properties, reaction rates, model parameters, the boundary conditions and simulated geometry are different. A comparison to the small scale results illustrate the effect of mixing, which is significantly better in a small scale where cross-sectional areas are smaller. This allows the volatile gas species and char to mix more efficiently with oxygen

Table 5

The effect of mesh size on the overall furnace performance with peat. The differences are negligible in most cases, and individual differences between the meshes can be explained through the normal variation of values between iterations.

	Convection			Dispersion		
Sensible heat (MW)	Coarse	Medium	Fine	Coarse	Medium	Fine
Total in	1.58	1.58	1.58	1.58	1.58	1.58
Reaction heat (MW)	10.8	10.8	10.8	10.84	10.74	10.65
Heat recovery (MW)	5.72	5.59	5.54	5.65	5.51	5.40
Temperatures (°C)						
Bed	948	945	951	968	967	964
Separator inlet	814	824	829	820	825	829
Separator gas exit	812	822	828	819	823	827
Mass flows (kg/s)						
Bottom ash	0.446	0.446	0.445	0.446	0.446	0.446
Fly ash	0.074	0.075	0.075	0.071	0.071	0.071
Circ. to separator	15.5	15.3	15.4	15.5	15.3	15.3
Char in ash (mass%)						
Bottom ash	0.010	0.008	0.008	0.041	0.044	0.047
Fly ash	4.22	4.99	4.69	1.45E–05	1.21E–05	1.15E–05
Circ. to separator	0.171	0.185	0.172	4.42E–07	3.68E–07	3.42E–07

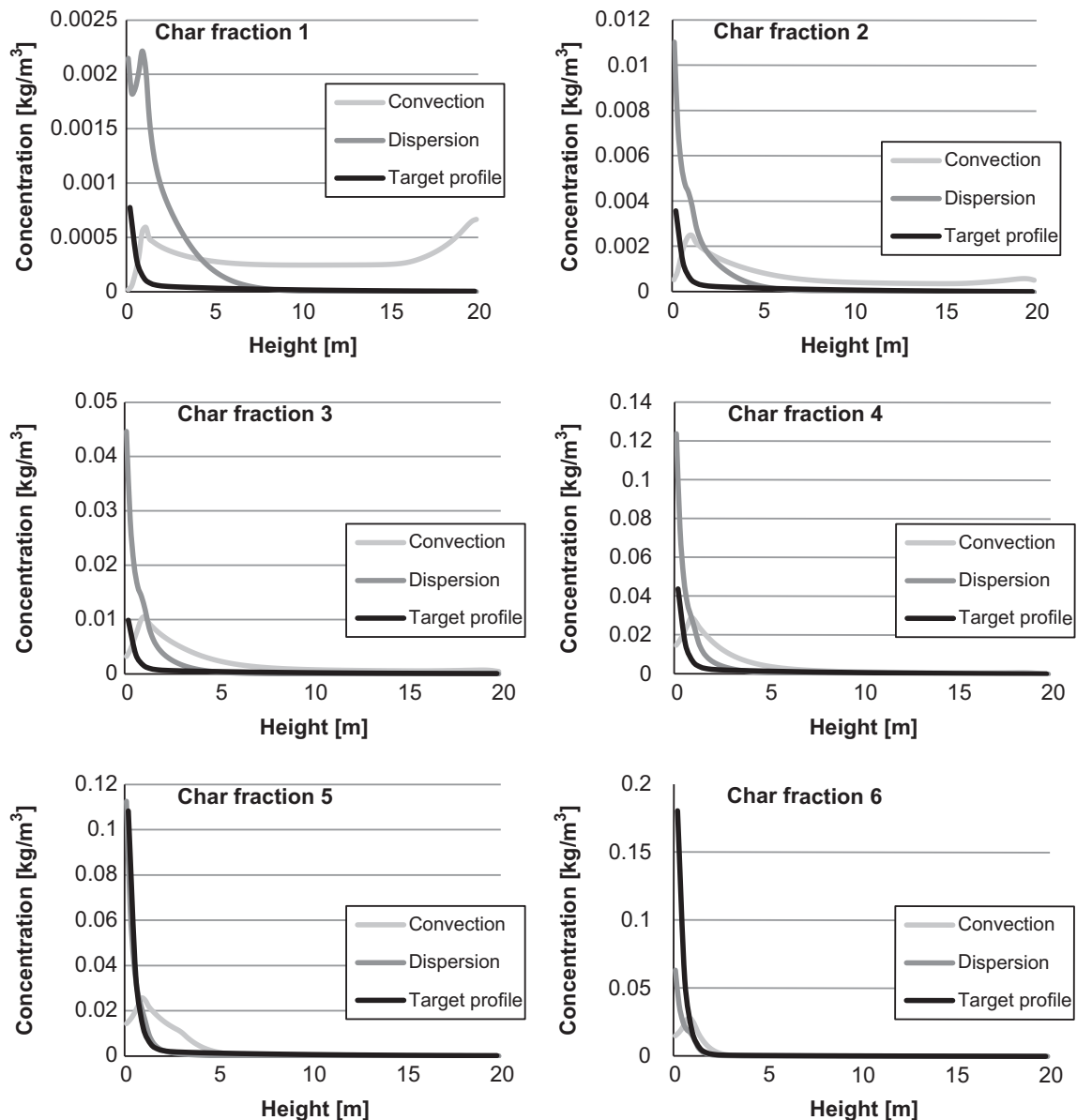


Fig. 4. Fractional comparison of the cross-sectional average char concentrations profiles of forest residue between the convection and dispersion model. The target profile for the dispersion model is also presented.

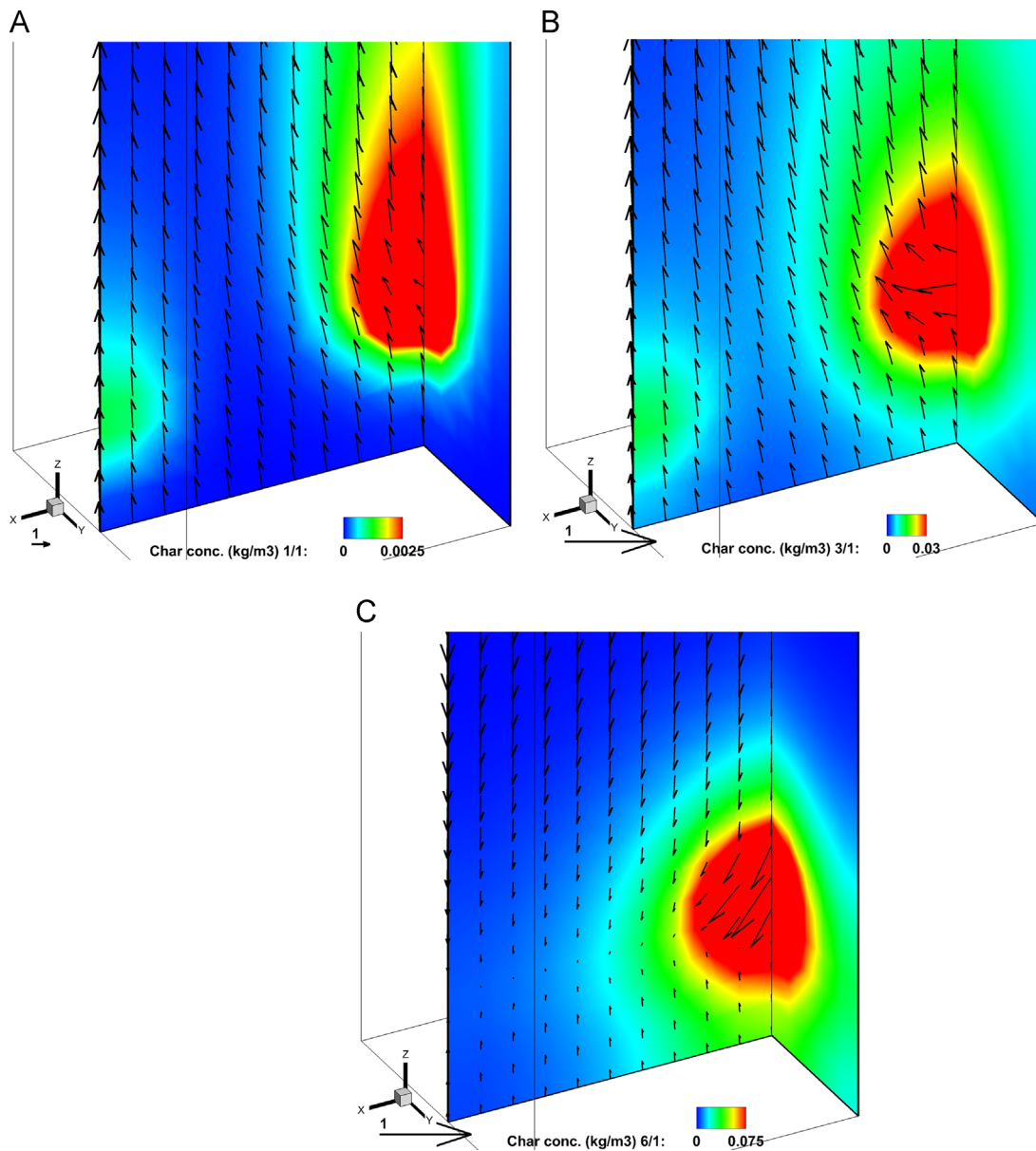


Fig. 5. Concentration contours and velocity vectors of char fractions 1, 3, and 6 respectively, simulated in the medium mesh for peat. It is clearly visible how the smallest fraction 1 is almost directly elutriated, while fraction 3 is able to penetrate further into the furnace. Particles of fraction 6 are large and mix and remain in the lower furnace.

and the reactions can take place lower in the furnace. The air to fuel ratio in the small case simulation was slightly higher and the same dispersion coefficients were used in both cases, which might be slightly too high for the small case. Still combustion of finer char fractions can be observed occurring higher in the furnace for the reasons discussed earlier.

4. Conclusions

An existing three-dimensional model frame was modified to include a fuel flow model based on the force balance. The model considers inertia force, gravity, and drag force from gaseous and solids phase. The model functionality was demonstrated in a small geometry and mesh dependency was studied. The semi-empirical model frame allows the utilization of a coarser mesh size compared to conventional CFD, which reduces the computational costs significantly. The new model was compared with the previous, target profile and dispersion

based model, and the improvements were illustrated. In the new fuel flow model, dispersion is still applied in the modeling of fuel mixing.

The introduced model allows predictions of fuel flow fields based on the fuel properties, mainly particle size and density, without preliminary assumptions about the fuel concentration profiles. The improved prediction of the fuel flow enables the better prediction of reaction zones resulting in temperature and gas concentration profiles which are typically measured in commercial furnaces. Ultimately better prediction of the fuel flow allows improved understanding of the whole furnace process.

Two commercial scale simulation results with the same chemical properties but with different fuel density and particle size distributions were presented to illustrate the effect of fuel physical properties on the process parameters and distributions of different quantities inside the furnace. The two simulated fuels both have low material density and similar particle size distribution, and small changes were observed in the general process parameters. More significant changes would likely be observed if comparison were made with for example coals. The model was shown to

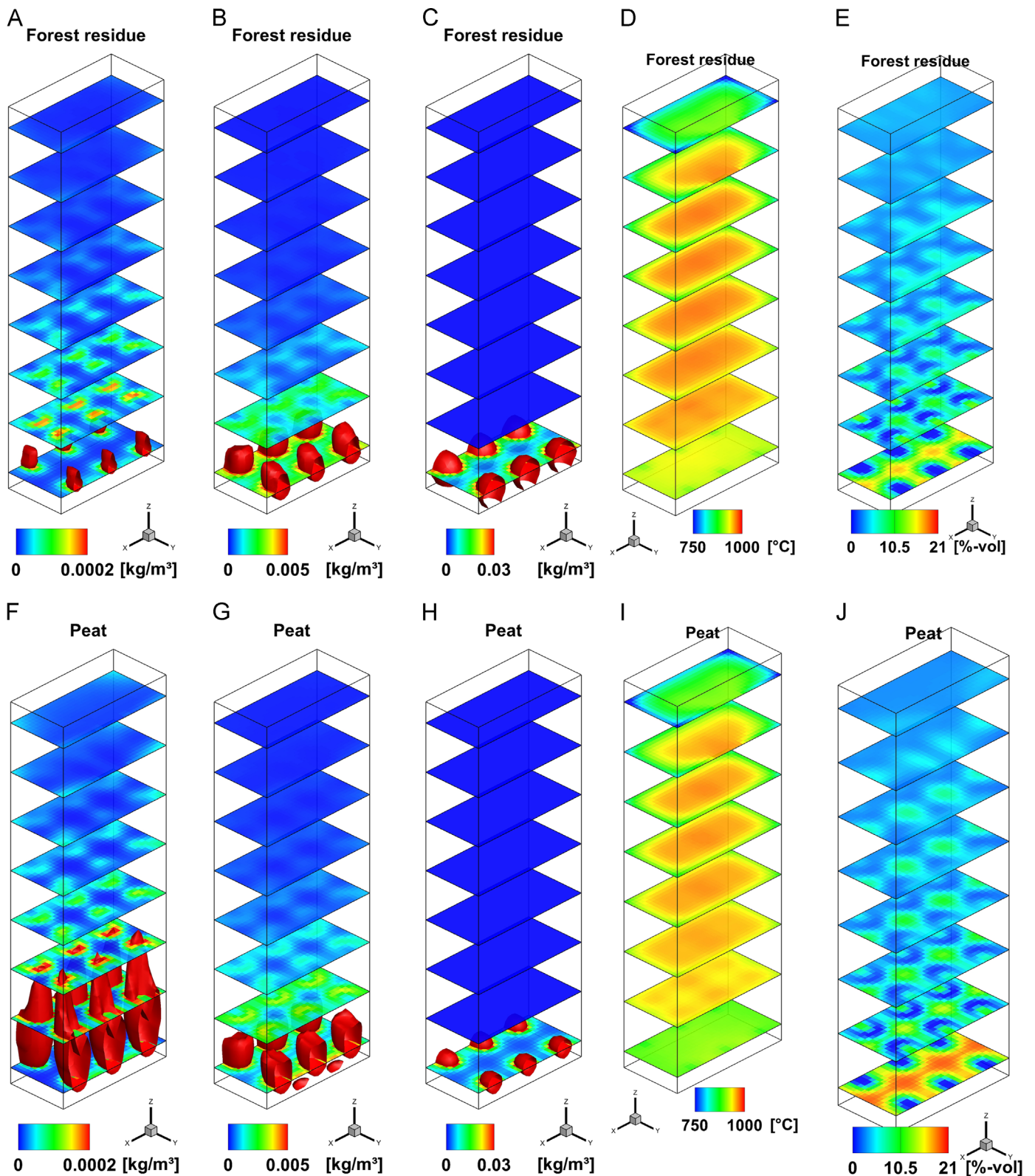


Fig. 6. Concentration contours of cross-sections from commercial scale forest residue (above) and peat (below) fired cases, from left to right: char fractions 1, 3, and 6, temperature and oxygen.

improve the modeling of smaller and lighter fuel particles compared to the previous dispersion type model. The developed model can be utilized in the modeling of real commercial scale CFB furnaces on a desktop computer with reasonable computational times.

For large scale CFB furnaces, suitable validation data is not available in open literature. This is the reason for the selection of two arbitrary geometries to introduce the model and demonstrate its potential. The model presented in this study gives qualitatively reasonable results and modeling capability has improved

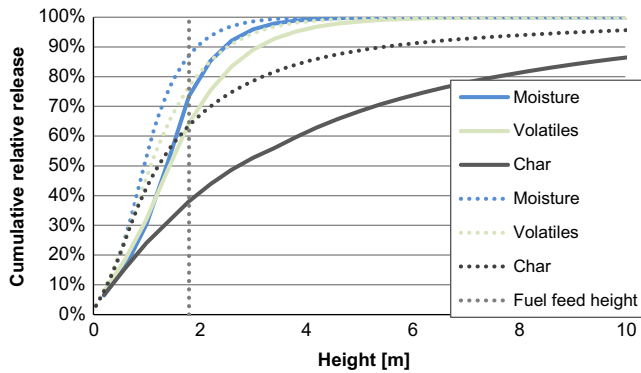


Fig. 7. Cumulative relative release profiles of moisture, volatiles and char for small scale (dotted lines) and large scale simulations (solid lines) for forest residue. The height is limited to 10 m to better illustrate the reactions in the lower furnaces.

Table 6
Furnace performance comparison between the fuels.

Sensible heat (MW)	Peat	Forest residue
Total in	26.1	26.1
Flue gas	117.7	117.7
Fly ash	0.556	0.511
Bottom ash	0.177	0.226
Reaction heat	168.8	168.5
Heat recovery	76.5	76.2
Temperatures (°C)		
Bed	898	922
Separator inlet	927	927
Separator gas exit	920	921
Separated solids	929	929
Mass flows (kg/s)		
Bottom ash	0.185	0.229
Fly ash	0.566	0.520
Circ. to separator	392.6	383.6
Char in ash (mass%)		
Bottom ash	0.0011	0.0031
Fly ash	0.531	0.302
Total ash discharge	0.401	0.211
Circ. to separator	0.023	0.013
Flue gas composition		
O ₂ (vol%,wet)	3.80	3.82
CO ₂ (vol%,wet)	11.59	11.58
H ₂ O (vol%,wet)	23.15	23.10
SO ₂ (vol%,wet)	0.0017	0.0017
CO (vol%,wet)	0.0009	0.0005
N ₂ (vol%,wet)	61.43	61.47

especially for finer fuel fractions. Authors aim to publish results on model validation when suitable validation material can be obtained. The presented model terms for momentum interchange are literature based assuming spherical particle shape. Authors aim to improve the model frame by including new models in the future to consider the momentum exchange and to include the particle shape and obtain publishable measurement data for validation.

Nomenclature

A	surface area [m ²]
C_D	drag coefficient [-]
C_f	friction coefficient [-]
D	diffusion/dispersion coefficient [m ² /s]
K	momentum exchange coefficient [kg/m ³ s]
R	reaction source term [kg/m ³ s]

Re	Reynolds number [-]
V	volume [m ³]
d	diameter [m]
e	coefficient of restitution [-]
f	target solid concentration [kg/m ³]
g	gravitational acceleration [m/s ²]
g_0	radial dispersion coefficient [-]
k	comminution coefficient [kg/s]
v	velocity [m/s]
ε	volume fraction [-]
φ	switching function [-]
ϕ	source term [-]
μ	viscosity of fluid [Pa s]
ρ	density [kg/m ³]

Subscripts

O	target
f	fuel
g	gas
ij	indexes
s	solid
WY	Wen–Yu
E	Ergun

Acknowledgments

This work was performed with funding from the project ERA-NET Biomodelling—Advanced biomass combustion modeling for clean energy production within the framework of ERA-NET Bioenergy Joint Call on Clean Biomass Combustion.

References

- Adamczyk, W. P., Bialecki, R. A., Klimanek, A., Kozolub, P., Węcel, G., Klajny, M. 2013. Modeling particle transport phenomena in large scale CFB boiler. In: The 38th International Technical Conference on Clean Coal & Fuel Systems, Clearwater, USA.
- Adamczyk, W.P., Węcel, G., Klajny, M., Kozolub, P., Klimanek, A., Bialecki, R.A., 2014. Modeling of particle transport and combustion phenomena in a large-scale circulating fluidized bed boiler using a hybrid Euler–Lagrange approach. *Particology* (2014), <http://dx.doi.org/10.1016/j.partic.2013.10.007>.
- Alletto, M., Breuer, M., 2012. One-way, two-way and four-way coupled LES predictions of a particle-laden turbulent flow at high mass loading downstream of a confined bluff body. *Int. J. Multiphase Flow* 45 (0), 70–90.
- Alobaid, F., Ströhle, J., Epple, B., 2013. Extended CFD/DEM model for the simulation of circulating fluidized bed. *Adv. Powder Technol.* 24 (1), 403–415.
- Al-Rashed, M., Wójcik, J., Plewik, R., Synowiec, P., Kuś, A., 2013. Multiphase CFD modeling: fluid dynamics aspects in scale-up of a fluidized-bed crystallizer. *Chem. Eng. Process.* 63 (0), 7–15.
- Basu, P., 1999. Combustion of coal in circulating fluidized-bed boilers: a review. *Chem. Eng. Sci.* 54 (22), 5547–5557.
- Crowe, C., Michaelides, E.E., 2006. Basic concepts and definitions. In: Crowe, C. (Ed.), *Multiphase Flow Handbook*. CRC Press, United States.
- Duret, B., Luret, G., Reveillon, J., Menard, T., Berlemont, A., Demoulin, F.X., 2012. DNS analysis of turbulent mixing in two-phase flows. *Int. J. Multiphase Flow* 40 (0), 93–105.
- Duret, B., Reveillon, J., Menard, T., Demoulin, F.X., 2013. Improving primary atomization modeling through DNS of two-phase flows. *Int. J. Multiphase Flow* 55 (0), 130–137.
- Ergun, S., 1952. Fluid flow through packed columns. *Chem. Eng. Prog.* 48 (2), 89–94.
- Gui, N., Fan, J.R., Chen, S., 2010. Numerical study of particle–particle collision in swirling jets: a DEM–DNS coupling simulation. *Chem. Eng. Sci.* 65 (10), 3268–3278.
- Gui, N., Fan, J.R., Luo, K., 2008. DEM–LES study of 3-D bubbling fluidized bed with immersed tubes. *Chem. Eng. Sci.* 63 (14), 3654–3663.
- Huilin, L., Gidaspow, D., 2003. Hydrodynamics of binary fluidization in a riser: CFD simulation using two granular temperatures. *Chem. Eng. Sci.* 58 (16), 3777–3792.
- Hyppänen, T., Lee, Y.Y., Rainio, A. 1991. A three-dimensional model for circulating fluidized bed boilers. In: Anthony, E.J. (Ed.), *Proceedings of the 11th International Conference on Fluidized Bed Combustion*. New York, p. 439.

- Johnsson, F., Johansson, A., Sternéus, J., Leckner, B., Hartge, E., Budinger, S., Fehr, M., Werther, J., Sekret, R., Bis, Z., Nowak, W., Borovec, K., Ochodek, T., Noskiewicz, P., Gadowski, J., Jablonski, J., Walkowiak, R., Kallner, P., Strömberg, L., Kettunen, A., Hyppänen, T., 2004. An experimental study of in-furnace processes and dynamic behaviour of a 235 MWe CFB boiler. *VGB PowerTech* 84 (3), 82.
- Karimipour, S., Pugsley, T., 2012. Application of the particle in cell approach for the simulation of bubbling fluidized beds of Geldart A particles. *Powder Technol.* 220 (0), 63–69.
- Knoebig, T., Luecke, K., Werther, J., 1999. Mixing and reaction in the circulating fluidized bed—a three-dimensional combustor model. *Chem. Eng. Sci.* 54 (13–14), 2151–2160.
- Koski, M., Ritvanen, J., Myöhänen, K., et al. 2011. Three-dimensional modelling study of a circulating fluidized bed gasifier. In: Hermann Hofbauer, M.F. (Ed.), *International Conference on Polygeneration Strategies 11 (ICPS 11)*. p. 251.
- Lebowitz, J.L., 1964. Exact solution of generalized Percus-Yevick equation for a mixture of hard spheres. *Phys. Rev.* 133 (4A), A895–A899.
- Li, F., Song, F., Benyahia, S., Wang, W., Li, J., 2012. MP-PIC simulation of CFB riser with EMMS-based drag model. *Chem. Eng. Sci.* 82 (0), 104–113.
- Li, T., Dietiker, J., Zhang, Y., Shahnam, M., 2011. Cartesian grid simulations of bubbling fluidized beds with a horizontal tube bundle. *Chem. Eng. Sci.* 66 (23), 6220–6231.
- Liu, Y., Liu, X., Kallio, S., Zhou, L., 2011. Hydrodynamic predictions of dense gas-particle flows using a second-order-moment frictional stress model. *Adv. Powder Technol.* 22 (4), 504–511.
- Luecke, K., Hartge, E., Werther, J., 2004. A 3D model of combustion in large-scale circulating fluidized bed boilers. *Int. J. Chem. Reactor Eng.* 2 (A11).
- Luo, K., Fang, M., Yang, S., Zhang, K., Fan, J., 2013. LES-DEM investigation of an internally circulating fluidized bed: effects of gas and solid properties. *Chem. Eng. J.* 228 (0), 583–595.
- Myöhänen, K., 2011. *Modelling of Combustion and Sorbent Reactions in Three-dimensional Flow Environment of a Circulating Fluidized Bed Furnace* (Ph.D. Thesis). Lappeenranta University of Technology.
- Myöhänen, K., Hyppänen, T., 2011. A three-dimensional model frame for modelling combustion and gasification in circulating fluidized bed furnaces. *Int. J. Chem. Reactor Eng.* 9, 1.
- Nikku, M., Jalali, P., Ritvanen, J., Hyppänen, T., 2014. Characterization method of average gas-solid drag for regular and irregular particle groups. *Powder Technol.* 253 (0), 284–294.
- Nikolopoulos, A., Nikolopoulos, N., Charitos, A., Grammelis, P., Kakaras, E., Bidwe, A.R., Varela, G., 2013. High-resolution 3-D full-loop simulation of a CFB carbonator cold model. *Chem. Eng. Sci.* 90 (0), 137–150.
- Pallarès, D., Johnsson, F., 2008. Modeling of fuel mixing in fluidized bed combustors. *Chem. Eng. Sci.* 63 (23), 5663–5671.
- Pallarès, D., Johnsson, F., 2006. Macroscopic modelling of fluid dynamics in large-scale circulating fluidized beds. *Prog. Energy Combust. Sci.* 32 (5–6), 539–569.
- Pallarès, D., Johnsson, F., Palonen, M., 2008. A comprehensive model of CFB combustion. In: Werther, J., Nowak, W., Wirth, K., Hartge, E. (Eds.), *Proceedings of the Ninth International Conference on Circulating Fluidized Beds*. Hamburg.
- Patankar, N.A., Joseph, D.D., 2001a. Lagrangian numerical simulation of particulate flows. *Int. J. Multiphase Flow* 27 (10), 1685–1706.
- Patankar, N.A., Joseph, D.D., 2001b. Modeling and numerical simulation of particulate flows by the Eulerian-Lagrangian approach. *Int. J. Multiphase Flow* 27 (10), 1659–1684.
- Petersen, I., Werther, J., 2005. Three-dimensional modeling of a circulating fluidized bed gasifier for sewage sludge. *Chem. Eng. Sci.* 60 (16), 4469–4484.
- Puragliesi, R., Dehbi, A., Leriche, E., Soldati, A., Deville, M.O., 2011. DNS of buoyancy-driven flows and Lagrangian particle tracking in a square cavity at high Rayleigh numbers. *Int. J. Heat Fluid Flow* 32 (5), 915–931.
- Ravelli, S., Perdichizzi, A., Barigozzi, G., 2008. Description, applications and numerical modelling of bubbling fluidized bed combustion in waste-to-energy plants. *Prog. Energy Combust. Sci.* 34 (2), 224–253.
- Schiller, L., Naumann, Z., 1935. A drag coefficient correlation. *Z. Ver. Dtsch. Ing.*, 77–318.
- Shah, S., Ritvanen, J., Hyppänen, T., Kallio, S., 2012. Space averaging on a gas-solid drag model for numerical simulations of a CFB riser. *Powder Technol.* 218 (0), 131–139.
- Shuai, W., Guodong, L., Huilin, L., Pengfei, X., Yunchao, Y., Gidaspow, D., 2012. A cluster structure-dependent drag coefficient model applied to risers. *Powder Technol.* 225 (0), 176–189.
- Shuai, W., Huilin, L., Guodong, L., Zhiheng, S., Pengfei, X., Gidaspow, D., 2011. Modeling of cluster structure-dependent drag with Eulerian approach for circulating fluidized beds. *Powder Technol.* 208 (1), 98–110.
- Singh, R.I., Brink, A., Hupa, M., 2013. CFD modeling to study fluidized bed combustion and gasification. *Appl. Therm. Eng.* 52 (2), 585–614.
- Ström, H., Sasic, S., 2013. A multiphase DNS approach for handling solid particles motion with heat transfer. *Int. J. Multiphase Flow* 53 (0), 75–87.
- Syamlal, M., Rogers, W., O'Brien, T., 1993. *MFIX Documentation: Theory Guide*.
- Taivassalo, V., Peltola, J., Kallio, S., 2012. Time averaged CFD modelling of a circulating fluidized bed combustor. In: *21st International Conference on Fluidized Bed Combustion Proceedings Volume 2*, 891.
- Wang, J., Ge, W., Li, J., 2008. Eulerian simulation of heterogeneous gas-solid flows in CFB risers: EMMS-based sub-grid scale model with a revised cluster description. *Chem. Eng. Sci.* 63 (6), 1553–1571.
- Wen, C.Y., Yu, Y.H., 1966. *Mechanics of fluidization*. *Chem. Eng. Prog. Symp. Ser.* 62, 100–111.
- Wischniewski, R., Ratschow, L., Hartge, E., Werther, J., 2010. Reactive gas-solids flows in large volumes—3D modeling of industrial circulating fluidized bed combustors. *Particuology* 8 (1), 67–77.
- Xiao, P., Yan, G., Wang, D., 1998. Investigation on horizontal mixing of particles in dense bed in circulating fluidized bed (CFB). *J. Therm. Sci.* 7 (2), 78–84.
- Xiong, Q., Li, B., Zhou, G., Fang, X., Xu, J., Wang, J., He, X., Wang, X., Wang, L., Ge, W., Li, J., 2012. Large-scale DNS of gas-solid flows on mole-8.5. *Chem. Eng. Sci.* 71 (0), 422–430.
- Zhou, H., Flamant, G., Gauthier, D., 2007. Modelling of the turbulent gas-particle flow structure in a two-dimensional circulating fluidized bed riser. *Chem. Eng. Sci.* 62 (1–2), 269–280.
- Zhou, H., Flamant, G., Gauthier, D., 2004. DEM-LES of coal combustion in a bubbling fluidized bed. Part I: Gas-particle turbulent flow structure. *Chem. Eng. Sci.* 59 (20), 4193–4203.
- van der Hoef, M.A., Ye, M., van Sint Annaland, M., Andrews, A.T., Sundaresan, S., Kuipers, J.A.M., 2006. Multiscale modeling of gas-fluidized beds. *Adv. Chem. Eng.* 31, 65–149.

Publication IV

Nikku, M., Myöhänen, K., Ritvanen, J., Hyppänen, T. and Lyytikäinen, M. (2015).
Modelling and validation of fuel flow in CFB furnace.

Reprinted with permission from
Proceedings of 22th conference of Fluidized Bed Conversion,
© Åbo Akademi University, 2015

Modelling and validation of fuel flow in CFB furnace

Markku Nikku¹, Kari Myöhänen¹, Jouni Ritvanen¹, Timo Hyppänen¹, Marko Lyytikäinen²

¹*Lappeenranta University of Technology, P.O. box 20, 53851 Lappeenranta, Finland*

²*Amec Foster Wheeler, P.O. box 201, 78201 Varkaus, Finland*

Tel. +358 40 501 5201, Fax. +358 5 411 7201, mnikku@lut.fi

Abstract

Semi-empirical models are currently widely used in holistic modelling of circulating fluidized bed (CFB) furnaces, as detailed computational fluid dynamics are still computationally very expensive and unfeasible as engineering tools for furnace design and performance analysis. Previously the semi-empirical models have utilized a fixed vertical fuel concentration profile with dispersive type of mixing in the modelling of fuel distributions. This approach might not be suitable for all types of fuels, such as light and fine fractions of biomass. The approach also requires knowledge of the axial fuel concentration profile, which might be unavailable for new fuels or mixtures.

A model for fuel flow in CFB presented by Nikku et al [1] is validated using measurement data from large scale boiler firing biomass. The validation relies on temperature measurements from the furnace, as well as overall performance information.

Keywords: CFB, fuel flow, modelling

1 Introduction

The application of commercial computational fluid dynamics (CFD) software for modelling of combustion in large scale CFB furnaces is rare, due to high computational costs as recently reported by Adamczyk et al [2]. This is the main reason why large scale CFB furnaces are still mainly modelled with semi-empirical codes [3-6].

In order to cut down the computational costs, the semi-empirical models aim to solve the whole furnace process with coarser resolution, while typically the high resolution CFD analysis often focus on the solution of the multiphase flow neglecting the reactions and heat transfer. Semi-empirical codes also offer only a steady state solution and they require additional input parameters for the semi-empirical parts, which typically are multiphase flow related, such as the solution of the vertical particle concentration profile, for example. These parameters can be obtained from correlations or directly from furnace measurements. Also the consideration of fuel flow and mixing is simplified in semi-empirical approaches and fuel mixing is modelled with only dispersion and without separate momentum equation for fuel. [6,7].

Lyytikäinen et al [8] presented how a semi-empirical CFB furnace model can be utilized in furnace design and analysis and referred to need for model parameter tuning to achieve model validity. Recently Nikku et al [1] presented a momentum equation based fuel flow model and modelled a fictive CFB furnace to demonstrate the model applicability. In this work, the previously presented fuel flow model is used to simulate a large, biomass firing CFB furnace and the model is validated against measurement data.

2 Methods

2.1 Model description

The holistic model frame solves conservation equations of mass, species, momentum and energy in three dimensions and in steady state, and includes semi-empirical components in the modelling of hydrodynamics and chemical reactions. The model frame contains a solution of reactions of fuel, sorbent and various gaseous species, fragmentation of solid material, convective and radiative heat transfer and flow dynamics. The furnace is discretized with a hexahedral block mesh and 0D-models are utilized for separators and external heat exchangers, which are linked to the furnace model. The

vertical density profile of solid material is determined by literature correlation or from measurements, as was done in the presented case. The model frame has been utilized in modeling of combustion, oxycombustion, gasification and sorbent reactions by [8-12]. New fuel flow model was presented by Nikku et al [1] to improve the modelling capabilities in cases of new and especially biomass fuels.

Eq. (1) presents a simplified momentum equation for the fuel, which is divided into char, volatiles, moisture and ash. The momentum equation considers inertia, gravity, buoyancy, and momentum exchange between fuel and gas and fuel and solids. The model parameters for momentum exchange between the phases are Huilin-Gidaspow [13] for gas-fuel and Syamlal [14] for solid-fuel interaction, and they are presented in Table 2, Eq. (3-9). The velocity field is solved for each particle size fraction of each fuel. The continuity equation is defined separately for char, volatiles, and moisture in fuel. Eq. (2) presents the continuity equation for char, size fraction i and the equation form is similar for volatiles and moisture.

$$\oint_A \varepsilon_{f,i} \rho_f \mathbf{v}_{f,i} \mathbf{v}_{f,i} dA = \int_V \varepsilon_{f,i} (\rho_f - \rho_{\text{susp}}) \mathbf{g} dV + \int_V K_{g-f} (\mathbf{v}_g - \mathbf{v}_{f,i}) dV + \int_V K_{s-f} (\mathbf{v}_s - \mathbf{v}_{f,i}) dV \quad (1)$$

$$\oint_A \varepsilon_{f,i} \rho_f \mathbf{v}_{f,i} dA - \oint_A D_{f,i} f_{0,i} \left(\frac{\varepsilon_{f,i} \rho_f}{f_{0,i}} \right) dA = \int_V \psi_{f,i} dV - \int_V \sum_{j,j \neq i} k_{f,ij} \varepsilon_{f,i} \rho_f dV + \int_V \sum_{j,j \neq i} k_{f,ji} \varepsilon_{f,j} \rho_f dV \quad (2)$$

The convective part of the fuel flow is solved with the momentum equation, while the continuity equation handles the dispersive/diffusive mixing with diffusion coefficient D . f_0 is a target profile term, which is needed if the fuel flow model is not used and the fuel is spreading by dispersion towards a vertical concentration profile. When the fuel flow model is applied, the term f_0 is given value 1, which disables any effect of predetermined concentration profiles, and the fuel can flow “freely” according to the momentum equation and mixing.

In CFD, Huilin-Gidaspow model is widely used in simulation of fluidized bed hydrodynamics, but with significantly finer meshes than utilized in this work. With coarse meshes, the model cannot accurately predict the drag force as it cannot account for heterogeneous mesoscale phenomenon of particle clustering, at least without utilization of a subgrid scale model [15]. In this work, no subgrid scale drag model was implemented. The model validation and method is further discussed on chapter 3.

Table 1. Gas and solids drag model equations. [13,14,16]

$$K_{\text{WY}} = \frac{3}{4} C_D \frac{\varepsilon_g \varepsilon_{f,i} \rho_g |\mathbf{v}_{f,i} - \mathbf{v}_g|}{d_{f,i}} \varepsilon_g^{-2.65} \quad \varepsilon_g > 0.8 \quad (3)$$

$$K_E = 150 \frac{\varepsilon_{f,i} (1 - \varepsilon_g) \mu_g}{\varepsilon_g d_{f,i}^2} + 1.75 \frac{\rho_g \varepsilon_{f,i} |\mathbf{v}_{f,i} - \mathbf{v}_g|}{d_{f,i}} \quad \varepsilon_g \leq 0.2 \quad (4)$$

$$K_{g-f} = \varphi K_E + (1 - \varphi) K_{\text{WY}} \quad (5)$$

$$\varphi = \arctan[150 \cdot 1.75 (0.2 - \varepsilon_s)] \pi^{-1} + 0.5 \quad (6)$$

$$C_D = \begin{cases} \frac{24}{\text{Re}} (1 + 0.15 \text{Re}^{0.68}) & \text{Re} \leq 1000 \\ 0.44 & \text{Re} > 1000 \end{cases} \quad (7)$$

$$K_{s-c} = \frac{3(1+e)(\pi/2 + C_f \pi^2/8) \varepsilon_s \varepsilon_{f,i} \rho_s \rho_f (d_s + d_{f,i})^2 g_0 |\mathbf{v}_s - \mathbf{v}_{f,i}|}{2\pi(\rho_s d_s^3 + \rho_f d_{f,i}^3)} \quad (8)$$

$$g_0 = \frac{1}{\varepsilon_g} + \frac{3d_s d_{f,i}}{\varepsilon_g^2 (d_s + d_{f,i})} \sum_{i=1}^M \frac{\varepsilon_i}{d_i} \quad (9)$$

2.2 Furnace description and case setup

The simulated furnace utilizes wood (bark, stumps, and forest residue) and peat in generation of process and district heat, and electricity with 262MW_{th} and 125MW_{e} duty respectively. A layout of the furnace is presented in Figure 1 and dimensions and the fuel properties in Table 2. The furnace has three separators, each equipped with an external heat exchanger in the solids return loop. Fuel is fed through 8 points, 4 on front and back walls, with secondary air inlets placed around the fuel inlets. Dispersion coefficient of 0.2 m/s^2 for lateral directions and 0.05 m/s^2 for axial direction were used for the fuel and boundary condition for fuel inlet velocity $[x,y,z]$ was $[1,0,-1]\text{ m/s}$ on the front and $[-1,0,-1]\text{ m/s}$ on the rear wall.

Measurement information was obtained from the plant, probe temperature measurements within the furnace, pressure measurements to determine the vertical pressure profile and plant automation system measurements which were used to determine necessary inputs and additional measurement information for validation.

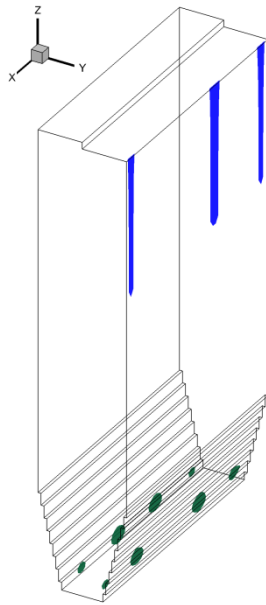


Figure 1. Layout of the simulated furnace. Fuel and separator inlets marked with green and blue, respectively.

Table 2. Furnace and fuel properties.

	Dimension	Number of cells
Height (Z)	40 m	80
Width (X)	21 m	50
Depth (Y)	7.5 m	30
Volume	5810 m^3	120 000

	Wood	Peat
Mass share in fuel feeding	76 %	24 %
Proximate analysis		
Char content	9.3 %	15.3 %
Volatile content	33.9 %	36.2 %
Moisture content	55.0 %	46.4 %
Ash content	1.8 %	2.0 %
Ultimate analysis		
Carbon	53.8 %	57.0 %
Hydrogen	6.4 %	6.0 %
Nitrogen	0.6 %	1.9 %
Sulfur	0.1 %	0.2 %
Oxygen	39.1 %	34.9 %
Higher heating value [kJ/kg]	20960	22260
Material density [kg/m³]	510	340

Fraction	Fuel particle size [mm]	Wood	Peat
1	0.03	0.4 %	2.9 %
2	0.094	0.5 %	3.7 %
3	0.15	1 %	14.6 %
4	0.34	4.4 %	26.3 %
5	1.25	20.7 %	21.9 %
6	4	73 %	30.6 %

3 Results and discussion

Figure 2 presents measured and modelled temperatures from the front wall and Figure 3 the furnace average vertical temperature profile and measurement data.

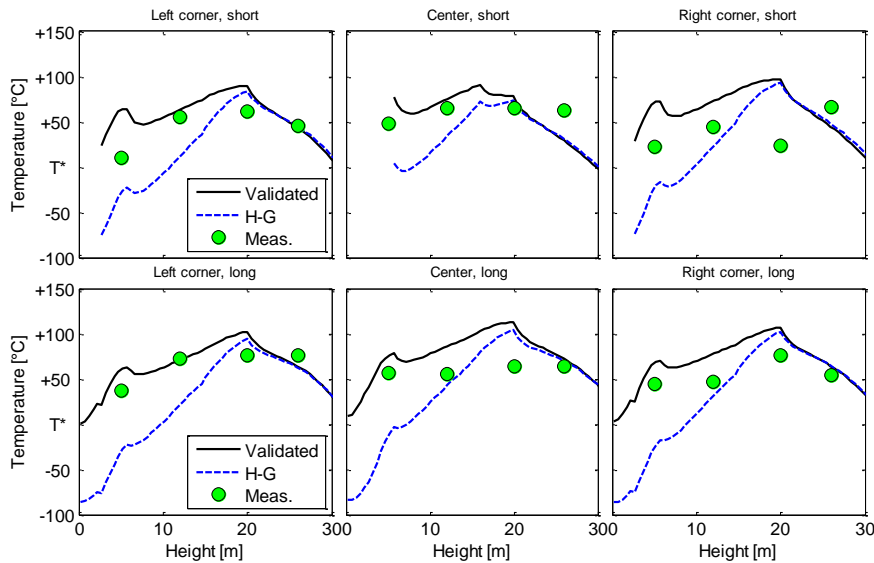


Figure 2. Modelled temperature profiles from the front wall and short and long probe measurements, presented in respect to a reference temperature T^* . H-G refers to Huilin-Gidaspow.

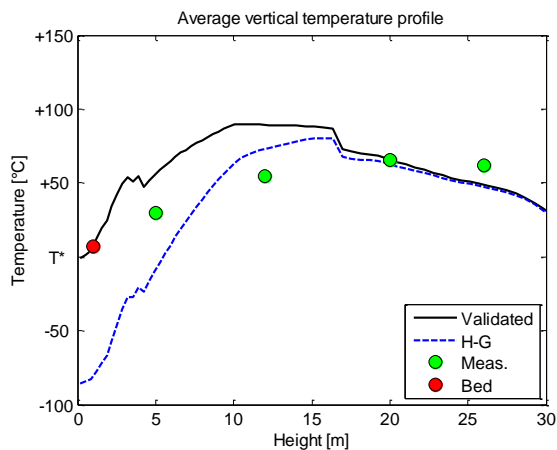


Figure 3. Averaged vertical profiles of modelled and measured temperatures, presented in respect to a reference temperature T^* . H-G refers to Huilin-Gidaspow.

From the results, it is clearly visible that the *Huilin-Gidaspow* model with the measured fuel parameters as input values, predicts too high gas – fuel drag force (illustrated in Figure 4), resulting in quite different temperature profile than the measured values. The bed region and lower furnace are especially significantly colder than the measurements indicate. To improve the situation, the gas – fuel drag force was reduced by utilizing a higher fuel density than measured, thus in this *validated* model, fuel density of 1500 kg/m^3 was used.

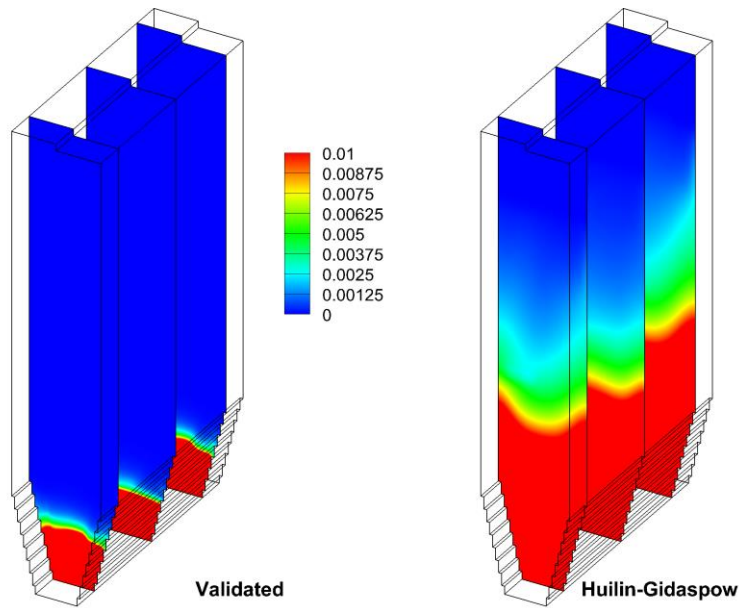


Figure 4. Comparison of drag force per volume [N/m^3] for wood fuel fraction 5.

Compared to Huilin-Gidaspow model, the validated model significantly improves the prediction of temperature in the bed and lower furnace. Partially the local temperature can now be overestimated compared to measurements, but qualitatively the results are better. The validated model results capture the rising temperature profile presented by the measurements, which is largely the result of volatile combustion in the middle furnace rather than in the bed or higher in the furnace as is the case with the Huilin-Gidaspow model. The validated model also captures the average bed temperature with good accuracy. Figure 5 illustrates the combustion regions of char and volatile material.

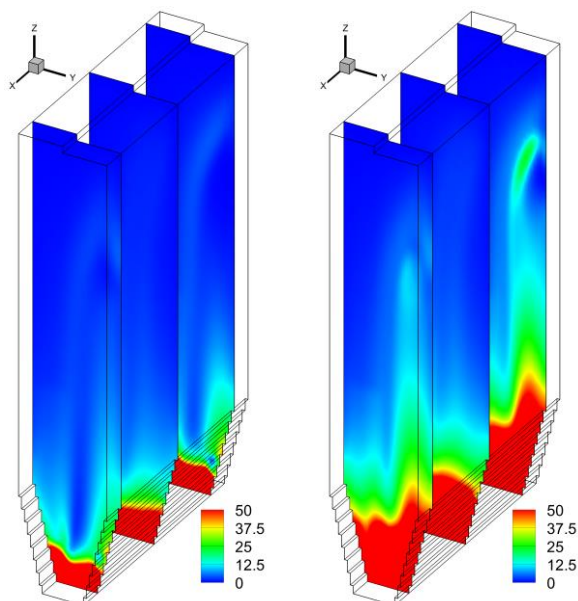


Figure 5. Heat released by char (on the left) and gas combustion (on the right) in the validated model.

Figure 6 illustrates the char flow of three different fractions in the furnace with the validated model. The finest fraction is elutriated directly from the fuel feeding by the relatively high gas drag force and remains close to the wall, while the medium and coarse fractions penetrate deeper and mix in the bed, spreading more evenly. The medium fraction 3 is somewhat elutriated and also found in the upper furnace, while the coarsest fraction 6, char particles (size of 4 mm) remains in the bed.

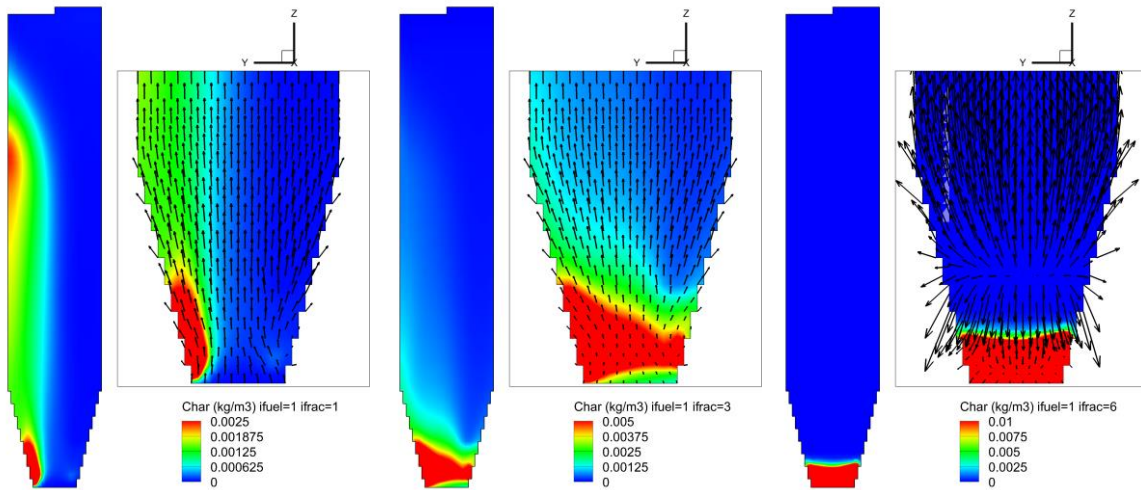


Figure 6. Char fractional distributions with velocity vectors in lower furnace. Char fractions (from left to right) 1, 3 and 6. Vector lengths not in scale.

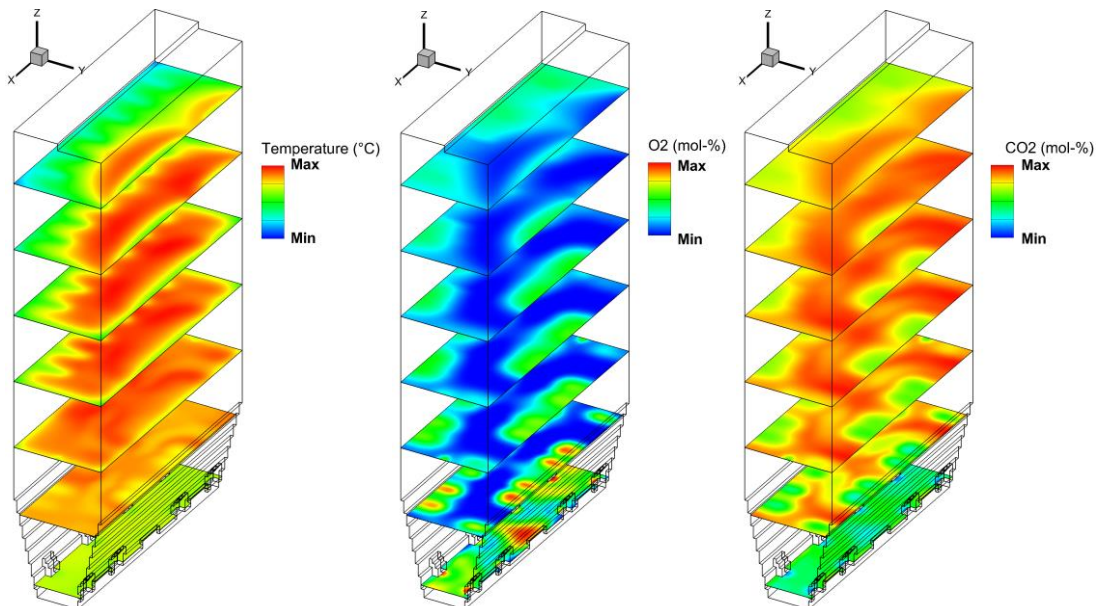


Figure 7. Temperature, oxygen and carbon dioxide profiles of the validated model.

Figure 7 presents temperature, oxygen and carbon dioxide distributions and analysed together with previously presented results, several conclusions can be made. The biomasses fired contain large share of moisture and volatiles, which is visible as large share of heat produced by volatile combustion in the freeboard. The majority of the fuel char is rather coarse and remains and combusts in the lower furnace. Fuel and oxygen mixing is not complete in furnaces with large cross-sections. The finer fuel fractions (or secondary air) do not mix evenly across the cross section and rising columns can form with relatively little combustion, due to limited mixing. As the flow turns towards the separator inlets, modelling results indicate local combustion zones with unburned volatiles and char coming in contact with oxygen. From the separator, the majority of unburned char is returned to the bed region via solids return system to ensure more complete combustion. The modelled results at the separator exit indicate a flue gas oxygen concentration of 3 %-volume on dry basis, and negligible amounts of volatiles and unburned char in the fly ash. These results indicate very good overall combustion efficiency with good overall air-to-fuel ratio as the material circulation remedies the shortcomings limited local mixing. The mixing of bed material, on the other hand is efficient, leading to relatively even temperature field across the furnace, maximum difference of 70°C between the measured values. Also the modelled results show highly uniform temperature distributions, with lower temperatures found near the cooled furnace walls.

4 Conclusions

A new fuel flow model was previously introduced in to a three-dimensional, holistic CFB furnace model. A large scale biomass firing CFB furnace was simulated and validated with measurement information. The gas-fuel drag model based on literature was found to overestimate the gas drag force, and the drag force was reduced by increasing the fuel material density to reach better agreement with the measurements. The model predictions of the furnace temperature field were able to model the trend and level of the rising vertical temperature profile with good agreement. The validated model can be utilized in furnace analysis and as a tool for design.

To achieve good correspondence between the model predictions and measurements results, model parameters have to be adjusted to account for phenomena occurring in the furnace, which are difficult to take into account accurately without detailed measurement information. Typically these parameters and phenomena include reactions, multiphase flow and mixing and heat transfer. The model validation was achieved by reducing the gas – fuel drag force predicted by the Huilin-Gidaspow drag model. This was achieved by increasing the fuel density. Huilin-Gidaspow model is typically utilized in higher resolution CFD simulations, and it is not expected to work well with coarse mesh simulations, such as utilized in this work. Still, with proper adjustments, the model can be utilized to achieve good agreement with measurement data, especially considering that steady state coarse mesh simulations can only demonstrate large scale phenomena, and not highly local small scale or transient phenomenon. The modified parameter used in this work can be used in simulation of different scenarios of the current furnace or similar geometries with similar fuels in order to estimate their performance. While the parameter tuning is typically furnace and load sensitive, often satisfactory accuracy can be achieved with “default” parameter values found through validation of similar furnaces.

A method that could be utilized in fuel flow modelling, which would simulate the gas-fuel drag force more accurately with coarse meshes, would reduce the need for tuning the drag force by modifying the fuel parameters or the drag force. Research related to developing a new gas-fuel drag force model is ongoing and aims to improve the utilization of actual fuel properties without a need for tuning.

Nomenclature

CFB	Circulating fluidized bed	H-G	Huilin-Gidaspow model
CFD	computational fluid dynamics		

Notation

A	Surface area, m^2	f_0	Target solid concentration, kg/m^3
C_D	Drag coefficient, -	g	Gravitational acceleration, m/s^2
C_f	Friction coefficient, -	g_0	Radial dispersion coefficient, -
D	Diffusion / dispersion coefficient, m^2/s	k	Comminution coefficient, $1/s$
K	Momentum exchange coefficient, kg/m^3s	m	Mass, kg
T	Temperature, $^{\circ}C$	\mathbf{v}	Velocity, m/s
R	Roundness, -	ε	Volume fraction, -
Re	Reynolds number, -	ϕ	Switching function, -
V	Volume, m^3	μ	Viscosity of fluid, $Pa \cdot s$
d	Diameter, m	ρ	Density, kg/m^3
e	Coefficient of restitution, -	ψ	Reaction source term, kg/m^3s

Subscripts and superscripts

E	Ergun	max	maximum
WY	Wen-Yu	min	minimum
f	fuel	s	solid
g	gas	susp	suspension
i, j	indices	*	reference

References

- [1] Nikku M, Myöhänen K, Ritvanen J, Hyppänen T, Three-dimensional modeling of fuel flow with a holistic circulating fluidized bed furnace model, *Chemical Engineering Science* 117(0) (2014) p. 352-363.
- [2] Adamczyk WP, Bialecki RA, Klimanek A, Kozołub P, Węcel G, Klajny M, Modeling particle transport phenomena in large scale CFB boiler, *Modeling particle transport phenomena in large scale CFB boiler*, The 38th International Technical Conference on Clean Coal & Fuel Systems; 2nd-6th June 2013; Clearwater, USA; 2013.
- [3] Myöhänen K, Hyppänen T, A Three-Dimensional Model Frame for Modelling Combustion and Gasification in Circulating Fluidized Bed Furnaces, *International Journal of Chemical Reactor Engineering* 9(1) (2011) .
- [4] Luecke K, Hartge E, Werther J, A 3D Model of Combustion in Large-Scale Circulating Fluidized Bed Boilers, *International Journal of Chemical Reactor Engineering* 2(A11) (2004) .
- [5] Knoebig T, Luecke K, Werther J, Mixing and reaction in the circulating fluidized bed – A three-dimensional combustor model, *Chemical Engineering Science* 54(13–14) (1999) p. 2151-2160.
- [6] Wischniewski R, Ratschow L, Hartge E, Werther J, Reactive gas–solids flows in large volumes—3D modeling of industrial circulating fluidized bed combustors, *Particuology* 8(1) (2010) p. 67-77.
- [7] Pallarès D, Johnsson F, Modeling of fuel mixing in fluidized bed combustors, *Chemical Engineering Science* 63(23) (2008) p. 5663-5671.
- [8] Lyytikäinen M, Kettunen A, Myöhänen K, Hyppänen T, Utilization of a three dimensional model in designing and tuning of large scale boilers, In: Li J, Wei F, Bao X, Wang W, editors. 11th International Conference on Fluidized Bed Technology; 14th-17th May 2014; Beijing, China: Institute of Process Engineering, Chinese Academy of Sciences; 2014.
- [9] Koski M, Ritvanen J, Myöhänen K, et al, Three-Dimensional Modelling Study of a Circulating Fluidized Bed Gasifier, In: Hermann Hofbauer MF, editor. International Conference on Polygeneration Strategies 11 (ICPS 11); 30.8.-1.9.2011; ; 2011.
- [10] Myöhänen K, Hyppänen T, Eriksson T, Kuivalainen R, Design and modeling of second generation oxygen-fired CFB, In: Li J, Wei F, Bao X, Wang W, editors. Proceedings of the 11th International Conference on Fluidized Bed Technology; 14th-17th May 2014; Beijing, China; 2014.
- [11] Rahiala S, Myöhänen K, Hyppänen T, Modeling the behavior of limestone particles in oxy-fuel CFB processes, *Fuel* 127(0) (2014) p. 141-150.
- [12] Ylätaalo J, Parkkinen J, Ritvanen J, Tynjälä T, Hyppänen T, Modeling of the oxy-combustion calciner in the post-combustion calcium looping process, *Fuel* 113(0) (2013) p. 770-779.
- [13] Huilin L, Gidaspow D, Hydrodynamics of binary fluidization in a riser: CFD simulation using two granular temperatures, *Chemical Engineering Science* 58(16) (2003) p. 3777-3792.
- [14] Syamlal M, Rogers W, O'Brien T. MFIx Documentation: Theory Guide. 1993;.
- [15] Benyahia S, Sundaresan S, Do we need sub-grid scale corrections for both continuum and discrete gas-particle flow models? *Powder Technology* 220(0) (2012) p. 2-6.
- [16] Gidaspow D, Ettehadieh B, Fluidization in two-dimensional beds with a jet. 2. Hydrodynamic modeling, *Ind.Eng.Chem.Fund.* 22(2) (1983) p. 193-201.

ACTA UNIVERSITATIS LAPPEENRANTAENSIS

606. JUVONEN, PASI. Learning information technology business in a changing industry landscape. The case of introducing team entrepreneurship in renewing bachelor education in information technology in a university of applied sciences. 2014. Diss.
607. MÄKIMATTILA, MARTTI. Organizing for systemic innovations – research on knowledge, interaction and organizational interdependencies. 2014. Diss.
608. HÄMÄLÄINEN, KIMMO. Improving the usability of extruded wood-plastic composites by using modification technology. 2014. Diss.
609. PIRTTILÄ, MIIA. The cycle times of working capital: financial value chain analysis method. 2014. Diss.
610. SUIKKANEN, HEIKKI. Application and development of numerical methods for the modelling of innovative gas cooled fission reactors. 2014. Diss.
611. LI, MING. Stiffness based trajectory planning and feedforward based vibration suppression control of parallel robot machines. 2014. Diss.
612. KOKKONEN, KIRSI. From entrepreneurial opportunities to successful business networks – evidence from bioenergy. 2014. Diss.
613. MAIJANEN-KYLÄHEIKO, PÄIVI. Pursuit of change versus organizational inertia: a study on strategic renewal in the Finnish broadcasting company. 2014. Diss.
614. MBALAWATA, ISAMBI SAILON. Adaptive Markov chain Monte Carlo and Bayesian filtering for state space models. 2014. Diss.
615. UUSITALO, ANTTI. Working fluid selection and design of small-scale waste heat recovery systems based on organic rankine cycles. 2014. Diss.
616. METSO, SARI. A multimethod examination of contributors to successful on-the-job learning of vocational students. 2014. Diss.
617. SIITONEN, JANI. Advanced analysis and design methods for preparative chromatographic separation processes. 2014. Diss.
618. VIHAVAINEN, JUHANI. VVER-440 thermal hydraulics as computer code validation challenge. 2014. Diss.
619. AHONEN, PASI. Between memory and strategy: media discourse analysis of an industrial shutdown. 2014. Diss.
620. MWANGA, GASPER GODSON. Mathematical modeling and optimal control of malaria. 2014. Diss.
621. PELTOLA, PETTERI. Analysis and modelling of chemical looping combustion process with and without oxygen uncoupling. 2014. Diss.
622. NISKANEN, VILLE. Radio-frequency-based measurement methods for bearing current analysis in induction motors. 2014. Diss.
623. HYVÄRINEN, MARKO. Ultraviolet light protection and weathering properties of wood-polypropylene composites. 2014. Diss.

624. RANTANEN, NOORA. The family as a collective owner – identifying performance factors in listed companies. 2014. Diss.
625. VÄNSKÄ, MIKKO. Defining the keyhole modes – the effects on the molten pool behavior and the weld geometry in high power laser welding of stainless steels. 2014. Diss.
626. KORPELA, KARI. Value of information logistics integration in digital business ecosystem. 2014. Diss.
627. GRUDINSCHI, DANIELA. Strategic management of value networks: how to create value in cross-sector collaboration and partnerships. 2014. Diss.
628. SKLYAROVA, ANASTASIA. Hyperfine interactions in the new Fe-based superconducting structures and related magnetic phases. 2015. Diss.
629. SEMKEN, R. SCOTT. Lightweight, liquid-cooled, direct-drive generator for high-power wind turbines: motivation, concept, and performance. 2015. Diss.
630. LUOSTARINEN, LAURI. Novel virtual environment and real-time simulation based methods for improving life-cycle efficiency of non-road mobile machinery. 2015. Diss.
631. ERKKILÄ, ANNA-LEENA. Hygro-elasto-plastic behavior of planar orthotropic material. 2015. Diss.
632. KOLOSENI, DAVID. Differential evolution based classification with pool of distances and aggregation operators. 2015. Diss.
633. KARVONEN, VESA. Identification of characteristics for successful university-company partnership development. 2015. Diss.
634. KIVYIRO, PENDO. Foreign direct investment, clean development mechanism, and environmental management: a case of Sub-Saharan Africa. 2015. Diss.
635. SANKALA, ARTO. Modular double-cascade converter. 2015. Diss.
636. NIKOLAEVA, MARINA. Improving the fire retardancy of extruded/coextruded wood-plastic composites. 2015. Diss.
637. ABDEL WAHED, MAHMOUD. Geochemistry and water quality of Lake Qarun, Egypt. 2015. Diss.
638. PETROV, ILYA. Cost reduction of permanent magnet synchronous machines. 2015. Diss.
639. ZHANG, YUNFAN. Modification of photocatalyst with enhanced photocatalytic activity for water treatment. 2015. Diss.
640. RATAVA, JUHO. Modelling cutting states in rough turning of 34CrNiMo6 steel. 2015. Diss.
641. MAYDANNIK, PHILIPP. Roll-to-roll atomic layer deposition process for flexible electronics applications. 2015. Diss.
642. SETH, FRANK. Empirical studies on software quality construction: Exploring human factors and organizational influences. 2015. Diss.
643. SMITH, AARON. New methods for controlling twin configurations and characterizing twin boundaries in 5M Ni-Mn-Ga for the development of applications. 2015. Diss.